Patient-Specific Rib Cage and Thoracic Volume Reconstruction in Spine Patients Using Biplanar Radiographs

A DISSERTATION
SUBMITTED TO THE FACULTY OF THE GRADUATE SCHOOL
OF THE UNIVERSITY OF MINNESOTA
BY

Po-Chih Lee

IN PARTIAL FULFILLMENT OF THE REQUIREMENTS
FOR THE DEGREE OF
DOCTOR OF PHILOSOPHY

Arthur G. Erdman Ph.D.

June, 2019

Acknowledgements

Firstly, I would like to give the upmost thanks to my advisor, Dr. Arthur Erdman. It has been my great honor and fortune to do my Ph.D. research and learn the correct attitude toward executing good research under his supervision. He not only gave me the freedom to discover my research direction but also provided me with many valuable suggestions and feedback when I faced difficulties. I am also grateful that he was always willing to spend time advising me in professional knowledge, research writing, and career development.

I would also like to express my appreciation to my dissertation committee members, Dr. William Durfee, Dr. Paul Iaizzo, and Dr. James Van de Ven, for their mentorship and feedback on my research work. In particular, I am very grateful to Dr. Paul Iaizzo and the Visible Heart Lab for collecting the CT scan data from the cadavers. My appreciation also goes to Dr. David Polly, Dr. Charles Ledonio, and Dr. Noelle Larson, who gave me the interdisciplinary insights and expertise in the orthopedic field and provided me with many spine patients' data.

The customized medical software for the dissertation would not have been possible without the generous help of Dr. Evan Bollig from the Minnesota Supercomputing Institute. Evan was very passionate about our project and his motivation was a blessing. He contributed many hours to helping us create the customized software and maintain its stability. I would specially like to acknowledge Dr. Arin Ellingson for his kind inspiration and recommendations for my research. In addition, I want to express my gratitude to the volunteers, Adrian Houston, Giuliana Giannelli, Hannah Simerly, and Katherine Hayes, for their hard work to perform the usability test for validating the developed software.

I would like to extend my special thanks to Dr. Chi-Lun Lin for his advice and discussion about the qualifying and preliminary exams. He gave me much help when I came to the U.S. to pursue my degree. Also, I am very lucky to have several best friends in my life, including Chun-Hung Chou, Fang-Chieh Chen, Chun-Sheng Chen, Kuan-Yu Lin, and

Jyun-Yu Lin. Even though they all work in Taiwan, they still care about my family and me.

Last but not least, I would like to express my sincere love to my wife, Ya-Chu Chang. I have never thought I would have that fortune to fall in love while studying abroad. I would not be able to accomplish this research without her unconditional encouragement, patience, and support.

This Ph.D. research was funded by the Pediatric Device Innovation Consortium (PDIC project No. 00025240), a fellowship from Mr. Wendell Hung and research assistantships from Dr. Arthur Erdman and Dr. David Polly.

Dedication

I dedicate this dissertation to my dear parents, Chung-Ching Lee and Yi-Mei Chao, whose endless love, support and encouragement throughout my entire life have made me the person I am today.

This dissertation is specially dedicated to the memory of my beloved father. Although he is definitely my greatest motivation in finishing this dissertation, he is unable to witness my graduation.

This is for you, Dad.

Abstract

Spine deformity dysfunctions, including scoliosis, osteoporosis, and Scheuermann's kyphosis, are common among different age cohorts. Progressive deformities of the spine curvature can deform the rib cage and lead to complications, such as cardiopulmonary disorders, back pain or even mortality. Traditionally, a severe spine deformity has a negative influence on patients' pulmonary function, because the limited thoracic volume restricts the expansion space of the lungs. Hence, the volume of the thoracic cavity can help doctors infer the lung volume in spine patients. To evaluate spine patients' respiratory function, some orthopedic doctors use pulmonary function tests to measure the lung volume and function, and some utilize the CT scan as a gold standard to reconstruct and compute the lung volume. Since a pulmonary function test highly relies on patients' understanding of the test instructions, its results might be inaccurate when the instructions are not followed correctly. For the CT scan, it is often criticized for its high-dose radiation, and exposure to CT scans significantly increases the risk of cancer, especially in pediatric patients. As a result, there is an unmet medical need to find an alternative to measure the volume of the thoracic cavity.

In this study, the concept of the thoracic volume was introduced and the definition of the thoracic volume boundary was also demonstrated for normal and abnormal subjects. Measuring thoracic volume is an alternative way to follow up spine patients' lung capacity. To avoid using high-radiation-dose CT scans, a simulation method and workflow to reconstruct and measure the thoracic volume were proposed. The simulation method shows how to develop semi-automatic software (named thoracic volume estimator) that can leverage low-dose frontal and lateral radiographs to reconstruct patient-specific rib cages and further reconstruct and measure the thoracic volume for spine patients. The developed medical software includes a user friendly interface and an add-on package for Blender software, which facilitate the reconstruction of the rib cage and thoracic volume via biplanar radiographs. To validate the developed software, five volunteers were recruited and trained to perform usability testing, which assessed the accuracy and precision of the rib cage and thoracic volume reconstruction, and reconstruction time. In the usability test, there were 15 datasets, including 7 children and 8 adults, and 11 of them possessed spine

deformity symptoms and the other 4 did not. With the rib cage and thoracic volume reconstruction for 15 datasets, the results from the developed software were compared to those from the gold standard CT scan. Furthermore, the thoracic volume results were compared to those calculated by the existing methods, which also utilized the X-rays to measure the thoracic volume.

A case study was demonstrated using the developed software to monitor the thoracic volume variation during the growing rod surgical treatments for six pediatric scoliosis patients. The benefit of the growing rod surgery was discussed in those young patients. In addition, thoracic volumes of 10 adult scoliosis patients with different spine treatments during their adolescence, including physical bracing and surgical intervention, were correlated to the parameters gained from the pulmonary function test. An investigation of the correlation between thoracic volume and the one-dimensional spinal parameters was conducted in pediatric and adult patients. Those studies imply the thoracic volume can be a surrogate for the prediction of the pulmonary function for spine patients.

With our customized program, two quantitative studies were performed via virtual spine patients having osteoporosis and Scheuermann's kyphosis symptoms. The potential risk of the pulmonary dysfunction in osteoporosis and Scheuermann's kyphosis patients with the vertebral wedging fractures or wedging deformities was mentioned in the previous literature. However, the influence of the wedging location and wedging numbers on thoracic volume changes was seldom discussed. Hence, a simulation workflow was proposed to create virtual spine patients, and it can be duplicated and adjusted for future clinical usages. In the quantitative study, I generated 126 virtual osteoporosis patients with vertebral wedging fractures and 30 virtual Scheuermann's kyphosis patients with vertebral wedging deformities. These studies reveal that the vertebral wedging deformities increase the spine curvature and reduce the thoracic volume. Altogether, the virtual spine patients can be employed in educational training and surgical planning for medical professionals in future clinical settings.

Contents

List of Tables

List of Figures

Chapter 1

Introduction

1.1 Motivation

Spine deformity is a disorder of the spine which produces a side-to-side curvature (e.g., scoliosis) or a back-to-front curvature (e.g., kyphosis, Scheuermann's kyphosis, and osteoporosis). Severe or progressive spine deformity symptoms may lead to immobility, cardiopulmonary complication (e.g., restrictive lung disease), or back pain. Orthopedic doctors may follow up the pulmonary function of the spine patients to determine the timing for the intervention of the spine curvature through physical or surgical treatments. Pulmonary function testing includes many important parameters, and those parameters can be used as indicators to evaluate the lung function or monitor the disease progression.

A pulmonary function test is a non-invasive evaluation for humans' respiratory system (lung capacity), and its development may date back to the 1840s. The first pulmonary function testing device (or spirometer) was invented by John Hutchinson [1], a British surgeon. The spirometer can detect the respiratory parameters, such as forced vital capacity and forced expiratory volume in 1 second, which are commonly used to assess the lung function. However, if the patients are too young (i.e., under age 5), they may have difficulty following the instructions during the pulmonary function test. If so, then the results cannot accurately represent their real lung function [2].

Since the X-ray radiation was discovered by Wilhelm Röntgen, it has been widely applied in medical imaging technologies. Those technologies, like X-ray, fluoroscopy and CT scan machines, possess the ability to pass through the human body to help doctors diagnose the disorder or disease for spine patients. In recent decades, radiologists have utilized the patients' CT scan imaging results to reconstruct the pathological spine and

measure the lung volume/capacity. However, the high-dose radiation from a CT scan can cause significant risk of cancer. During the spine deformity treatment, doctors may periodically examine the spine curvature every six months. Unless necessary, putting spine patients into a CT scan to follow up the alteration of the spine curvature is too risky, especially for pediatric patients [3]. Currently, most of the spine examinations still rely on plain X-rays due to their low-dose radiation compared to a CT scan (average chest examination radiation: 0.1mSv vs. 7mSv [4]). Another issue of the CT scan is that the examination cost is higher than regular X-rays.

To overcome the disadvantages of the pulmonary function test and the high-dose radiation problem, this study relies on the plain frontal and lateral X-rays to reconstruct the pathological spine and the thoracic volume in 3D. One motivation is that most doctors still depend on the low-dose radiation device, X-rays, to inspect the variation of the spine curvature in patients periodically before and after the treatments. Another motivation is to involve the concept of thoracic volume to avoid inaccurate or misleading outcomes of the pulmonary function tests obtained from patients who cannot properly perform the tests. Then, a simulation method and workflow are created to design a strategy to reconstruct the rib cage and the thoracic volume for spine deformity patients. Measuring thoracic volume via traditional X-rays can be a potential surrogate to monitor the pulmonary function variation of the spine deformity patients. The only required information from the spine patients is the frontal and lateral chest X-rays with full inhalation during the X-ray screenings. Our developed program (named thoracic volume estimator) is capable of reconstructing and calculating the thoracic volume via biplanar X-rays.

1.2 Definition of Thoracic Volume Boundary

In the past decade, thoracic volume or chest volume has seldom been mentioned in the literature, but most of the research investigated the human lung volume or pulmonary function (total lung capacity) instead [5–14]. An early article that discussed the thoracic/chest volume dates back to 1933, when Hurtado et al. [7] utilized the lung area (the area of the heart was also included) and lateral diameter viewed from the frontal and

lateral radiographs to calculate the chest volume. In 1960, the term, thoracic volume, was first introduced by Barnhard et al. [15]; they defined the boundary of the thoracic volume and also provided a method to compute the thoracic volume through parameters, which could be directly measured via frontal and lateral radiographs. In 1990, Dimeglio and Bonnel [16] were the first to document the thoracic volume values from birth to adolescence (0~18 yrs) of different genders.

Thoracic volume is the region of the mediastinum, cardiopulmonary system, and part of the abdominal cavity. Its boundary is outlined by the sternum, costal cartilages, superior T1 group (T1 vertebra and its adjacent two ribs) and the most downward ribs at the cross-section area, as shown in Figure 1.1. If the patient has scoliosis, the right side and left side of the ribs may not be symmetric. In that way, the top boundary of the thoracic volume will be defined by the connection of the inner apex of the T1 ribs (the two blue points on the top in Figure 1.2(a)), and the bottom boundary will be defined by the connection between the most downward ribs of the right and left rib cages (the two blue points on the bottom in Figure 1.2(a)).

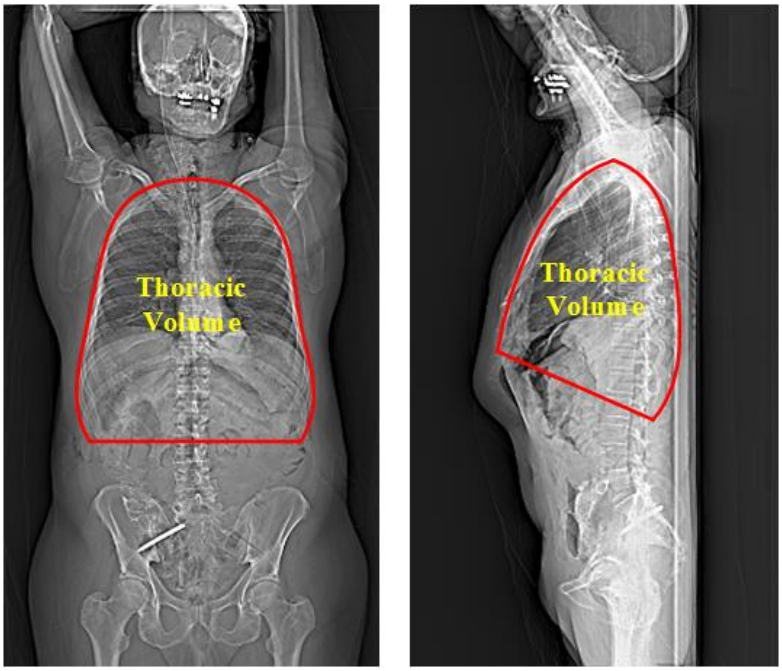

(a) frontal X-ray (b) lateral X-ray

Figure 1.1 Thoracic volume boundary of a non-spine deformity subject

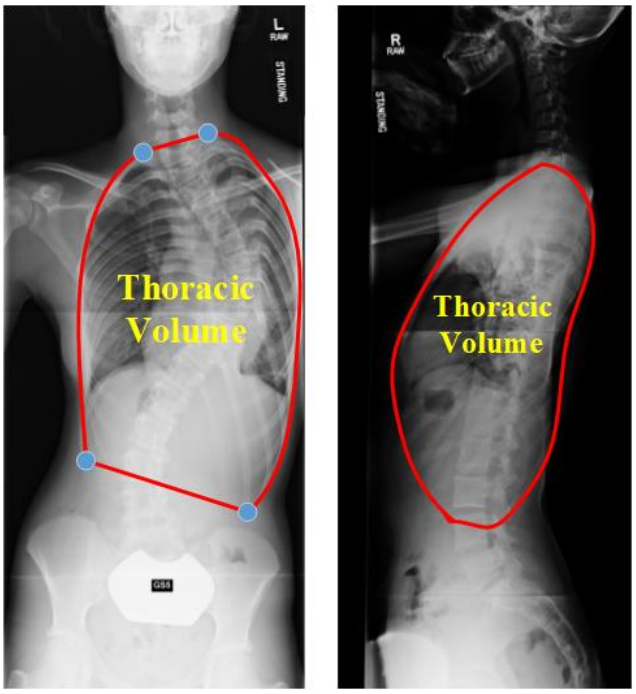

(a) frontal X-ray (b) lateral X-ray

Figure 1.2 Thoracic volume boundary of a spine deformity subject

1.3 Summary

There are several ways to predict and track the lung function of the spine patients, including pulmonary function tests or lung reconstruction by different medical imaging technologies. In my study, I use low-dose X-rays as an alternative to reconstruct and measure the thoracic volume after considering the shortcomings of the pulmonary function tests and the radiation dose of the medical devices. In addition, I define the thoracic volume boundary, which is the space inside the thoracic rib cage. We believe the thoracic volume could be a useful indicator to predict lung function of the spine deformity patients, especially the patients who are unable to routinely perform pulmonary function tests. Also, the orthopedic doctors can track the thoracic volume variation of the spine patients through chest X-rays to implement surgical planning and decide the best treatments.

In Chapter 2, I review the existing literature concerning the human rib cage and thoracic volume reconstruction through different technologies. In Chapter 3, a simulation method and workflow are proposed to develop a medical software to reconstruct the thoracic rib

cage and thoracic volume via biplanar (frontal and lateral) X-rays. Chapter 4 performs a usability testing study and its results are used to validate the reconstruction accuracy and precision through the developed software (thoracic volume estimator) mentioned in Chapter 3. In Chapter 5, I apply our customized software to reconstruct the rib cages and thoracic volumes for various age cohorts of the spine patients and correlate the pulmonary function parameters to the thoracic volume in adult scoliosis patients. Chapter 6 quantitatively studies the effect of the wedging deformity (local deformity or fracture on the vertebra) on thoracic volume change by virtual spine patients.

Chapter 2

Literature Review

Two main focuses of this dissertation are the rib cage and thoracic volume reconstruction. To present the status of the related research, the literature review is divided into two sections. In Section 2.1, the past methods to reconstruct the thoracic rib cages are reviewed. The existing tools and platforms to reconstruct the pathological spine using plain X-rays are investigated. In Section 2.2, the research on thoracic volume related to the lung volumes through different medical imaging techniques is reviewed.

2.1 Rib Cage Reconstruction Literature

Thoracic rib cage deformity is a combined disorder between ribs and vertebrae, which can develop into spine syndromes, such as scoliosis, Scheuermann's kyphosis and osteoporosis. In current clinical settings, medical doctors employ the CT scan to diagnose the spinal deformities or estimate the thoracic volume due to its accuracy and convenience [5,17,18]. CT scans produce multiple cross-section two-dimensional images, which can be used to reconstruct the thoracic rib cage or the lungs through computer software, such as Mimics [19], OsiriX [20], and 3D Slicer [21]. Therefore, 3D reconstruction of the human spine is helpful in spine deformity assessment and assists doctors in performing surgical planning in a routine hospital setting. In addition, the volumes of the rib cage or the lungs can be further extracted [5,22,23], and the accuracy of the CT scan makes it the gold standard [24–26]. However, the high-dose radiation of the CT scan technique is one critical issue which doctors are mostly concerned about [27]. That is, the radiation dose for each patient per year should be regulated and limited. Another problem with the CT scan technique is related to the diagnosis of the actual spine curvature of the spine patient. Yazici

et al. [28] pointed out that the deformation of the spine is affected by patients' postures, because the spinal curvature alters when patients lie down without the effect of gravity. To take CT scans, spine patients need to be in the supine posture, which will lead to the underestimate of the deformed spine curvature and a bias toward the assessment.

In contrast to the CT scan technique, magnetic resonance imaging (MRI) and ultrasounds are two commonly used medical imaging devices without radiation concerns. Neither of them has significant side effects for the patient, and some medical professionals have incorporated them to inspect the curvature of the spine. For the MRI, several articles discussed its possibility to reconstruct the lumbar spine [29–31], but none of them used the MRI to do the rib cage or thoracic volume reconstruction. The MRI can easily identify the soft tissue injuries and joint effusion in the human body [32]. Despite the absence of radiation exposure, one drawback of the MRI is that the osseous anatomy obtained from the MRI is inferior to that from the CT scan. In addition, the MRI scan time is long, the cost is high, it is not recommended for the patients with surgical implants, and the MRI is not suitable for the patient with obesity or claustrophobia [24]. As for the ultrasound technique, it is a low-cost and easily portable imaging device in comparison with a CT scan and an MRI, and ultrasound produces almost no contraindications. Based on this promising application, a pilot study [33] employed real-time ultrasound imaging to reconstruct the scoliotic spine. The user needed to manually digitize the surface contour of each vertebra in different frames to transform the vertebra from the two-dimensional surface contour into a three-dimensional image. After obtaining the three-dimensional contour, the authors did the contour triangulation between two consecutive frames to form the 3D mesh, and finally applied the surface rendering to the triangular surface. However, they pointed out several shortages of the current spine reconstruction by the ultrasound. For example, the quality of the ultrasound image is not as good as that of the CT scan and MRI due to its shallow penetration ability for the bone, and more patients' data are needed to validate the accuracy of the spine reconstruction. Apparently, utilizing ultrasounds to perform spine reconstruction is not viable yet.

Over the past decades, using the postero-anterior (PA) and lateral (LAT) radiographs has still been the preferred approach to help doctors directly evaluate spine deformities. Due to the low-dose radiation of the radiograph compared with the CT scan machine, more researchers employed the radiographs to restructure the human vertebral columns. Among previous articles, some took advantage of the two-dimensional X-rays to reconstruct the vertebrae [34–38], and others used X-rays to reconstruct the ribs [39–45]. Overall, most of the researchers utilized two orthogonal (PA and LAT) X-rays as the reference to perform the reconstruction [34,35,37,38,40,42,44,45], but several of them used only two frontal X-rays [39,41,43] or multiple X-rays instead [34,36].

For the vertebrae reconstruction, scientists have developed several methodologies to approach the reconstruction through the X-ray technique in recent decades. The main differentiation of those studies lies in the reconstruction method and algorithm. Aubin et al. [34] utilized a direct linear transformation (DLT) algorithm alone in generating the 3D points from the stereo-corresponding landmarks of the projected radiographs, and it was necessary to identify six stereo-corresponding points for each vertebra before the reconstruction process. In addition, the dual kriging algorithm [46], consisting of geometric transformations, interpolation, and extrapolation techniques, was utilized to deform each vertebra to fit the six reconstructed landmarks. The reconstruction accuracy was evaluated through in vitro studies. The conclusion of this research revealed two concepts: the pedicles are the most efficient landmarks to reconstruct the spine, and the orthogonal PA and LAT views of the radiographs are the optimal choices to reconstruct the spine. In 2000, Mitton et al. [35] manually identified the 2D landmarks on PA and LAT X-rays. Then, they adopted a DLT algorithm to calibrate the X-ray sources and used the non-stereo-corresponding points (NSCP) method to transform the 2D landmarks into 3D points. In this paper, a generic model for three different levels of cervical vertebrae was established by averaging topology of six cadaveric specimens, and the cervical vertebrae were also deformed using the dual kriging algorithm [46]. However, the authors only concentrated on rebuilding the cervical spine instead of the thoracic spine, and the processing time was not mentioned. Delorme et al. [36] proposed a high-resolution geometric modeling for the

human trunk, which was reconstructed by means of three digital radiographic images of PA, PA-20^0 (X-ray source was tilted 20 degrees down), and LAT views. All radiographs were calibrated by a positioning apparatus; custom-designed software could implement the detection of the landmarks on the apparatus and allow users to register six stereo-corresponding and eight non-stereo-corresponding anatomical points for later reconstruction. A model-based adaptation of the DLT algorithm was incorporated to reconstruct the spine. The deformation of the vertebrae was based on the dual kriging algorithm, a generalized interpolation and extrapolation. Also, a validation for reconstructing the scoliotic spine was carried out in vivo. A weakness of this research was that the radiology technician needed to spend 2 hours placing all of the anatomical landmarks on the radiographs, which increased the time for the whole reconstruction procedures. In [37], Kadoury et al. developed a portable system without the need of calibrating the orthogonal radiographs, and the system could reconstruct the 3D anatomical landmarks based on a self-calibration algorithm and the weak-perspective method. They also involved a stereo-triangulation method in reconstructing the spine. In clinical assessment, they performed the validation using 60 subjects, including 51 scoliotic and 9 non-scoliotic patients with an average Cobb angle of 25^0. In that article, they also suggested the reduction of errors resulting from the manual identification of the landmarks for future work. Humbert et al. [38] employed a semi-automatic reconstruction method to reconstruct the spine from biplanar X-rays, and they divided the reconstruction process into two different levels: level 1 for clinical usage and level 2 for dealing with more complex pathologies. Level 1 was merely utilized for clinical measurements, so the reconstruction time was short (less than 3 minutes); but additional adjustments were required for different spinal deformities, such as lordosis, kyphosis, and scoliosis. In contrast, the accuracy of Level 2 was superior to that of Level 1 and the thoracic and lumbar spine was reconstructed in 10 minutes during Level 2. Their method highly depended on the parametric database of the vertebrae by longitudinal and transversal inferences. Nonetheless, the authors did not indicate during which steps the operator could intervene, and the manual operation time

was not provided. In brief, most of the recent research increasingly relied on the spine databases (statistical spine models) to accurately reconstruct the spine.

As for the rib reconstruction, the common issue is that it is hard to imagine the actual geometry shape, deformation, and orientation of the three-dimensional ribs via PA and LAT X-rays. As a result, the reconstruction of the ribs, especially for the deformed rib cage, is absolutely necessary when doctors and technicians want to visualize the 3D geometric profile of the ribs. To tackle this problem, some researchers required that users register points (2D landmarks) on the radiographs, then discretize the marked points and interpolate extra points to build the midline of each rib for further reconstruction [39,40], while others adopted different methods, such as edge detection [41,42]. In 1988, Dansereau and Stokes [39] discussed the reconstruction of the ribs via radiographs, and they employed two different PA views, oriented toward the subjects at 0^0 and 20^0 from the horizontal, in order to visualize the shape of the ribs in vivo. Before the reconstruction by DLT method, they needed to manually register 11 points along the midline of each rib on each X-ray image, and the points were digitized and then fitted by the cubic splines. Then, up to 60 points, which were interpolated by 2D cubic splines, were discretized along each spline, and those 2D points were transformed into 3D points through the DLT method. Additionally, the authors validated the results of 10 subjects without spine deformities. The accuracy of this method was further improved by considering the respiration movement of the patient when the patient took radiographs [43]. Mitton et al. [40] used the non-stereo-corresponding contours (NSCC) algorithm [47] and a generic rib cage object to reconstruct the midlines of the ribs into 3D after manually identifying the rib cage boundary for the rib reconstruction. In the study, they also showed the 3D reconstruction of the sternum, but they did not explain how to reconstruct it in detail. In addition, the reconstruction accuracy was only assessed for the ribs (between T2 and T10 levels) in vitro by comparing their results with the CT scan reconstruction. Jolivet et al. [44] proposed a fast 3D reconstruction for the ribs. They developed a pre-personalized rib cage model which was reconstructed according to the bivariate cubic spline. The pre-personalized model was deformed using the NSCP method to generate a subject-specific rib cage model. Due to the pre-

personalized deformed object, the reconstruction time (including the operation time) was approximately 3 minutes. They did the in vivo reproducibility study for 15 healthy subjects and the accuracy was compared with that of the gold standard CT scan. The authors pointed out two limitations of their proposed method. Once the rib cage was deformed and reconstructed, the rib cage could not be adjusted even if the user was not satisfied with the result. In addition, it is necessary to validate the accuracy using the pathological rib cage for future efforts. In the studies of Seoud et al. [45], users manually registered 11 anatomical points on the PA view for each rib, and they did the refinement by only registering three specific points on the LAT view for each rib. These three points included the two most extreme points and the one most lateral point (referred from the PA view) of the rib. They validated 13 patients with scoliosis symptoms and compared the results with those from the previous method using two frontal X-rays. Their reconstruction results only focused on the lower section of the ribs (T5-T12 of the thoracic levels) due to the limitation of the resolution of the LAT radiograph. In 2012, Plourde et al. [41] proposed a semi-automatic (edge detection) method for the scoliotic rib borders through a single frontal chest radiograph, either PA-0^0 or PA-20^0 (X-ray tube was oriented down toward the subject at 20 degrees from the horizontal). Four starting points were manually selected for each rib on a PA-0^0 or PA-20^0 X-ray. Several parameters on the ribs would be automatically derived and the borders (dorsal and ventral portions) of each rib were detected based on the information of the four registered points, and the interaction time the user spent on two X-rays was under 12 minutes. After that, they involved three users to validate their proposed method by reconstructing 994 ribs from scoliotic patients. 93 percent of the ribs were successfully reconstructed; however, the authors mentioned the algorithm divergence problem might need to be overcome in the future. Overall, one thing worthy of emphasis is that the reconstruction for the ribs is more complicated than the vertebrae through PA and LAT X-rays, because it is hard to visualize the boundary of each rib on the LAT view. Compared to vertebrae and the ribs, the reconstruction of the sternum was discussed by only a few papers [39,40] which did not explain the reconstruction procedure in detail. More recently, one new low-dose X-ray imaging system, EOS^{TM} [48], has been applied to

orthopedic diagnosis and examinations of the human spine. Several articles [38,44] utilized this system to do the calibration for the biplanar X-rays before reconstructing the spine due to its high-quality images with less irradiation. However, this system is not capable of measuring the thoracic volume and it only reconstructs the vertebrae, pelvis, and lower-limb skeletons, excluding the ribs and the sternum.

2.2 Thoracic Volume Reconstruction Literature

Most of the literature discussed how to measure the lung volume/total lung capacity or chest wall volumes using different techniques, such as CT scans [5,6], X-rays [7–12], and the optical reflectance system [13,14]. However, no papers mention how to measure lung volume or thoracic volume using MRI or ultrasound. No matter what techniques are used to measure these volumes, it is necessary to have accuracy lower than 3% error for the volume estimation to be clinically useful based on the suggestions of the American Thoracic Society in 1994 [49]. The thoracic volume (or chest volume) estimation through routine radiographs dates back to 1933. Hurtado and Fray [7] were the pioneers to adopt frontal chest radiographs in order to calculate the lung volume. They measured the area of the lungs and multiplied it by the external posterior-anterior diameter of the chest to further infer the lung volumes for 50 healthy males. In 1996, Cala et al. [13] first described how to set up a system, called optical reflectance, to measure the chest volume with the help of the placement of infrared reflective markers on the chest wall. In contrast, the previous literature seldom defined the boundary of the thoracic volume, and the calculation of the thoracic volume was less addressed or validated relatively [15,17,50–58]. Like the lung volume calculation, the thoracic volume can be derived through CT scans [17,51–53], X-rays [15,54–57], and the optical reflectance system [13,50]. Pierce et al. [51] involved the CT scan concept in calculating the volume inside the thoracic cage. They presented an equation for the cross-section area and added all divided cross-section areas to obtain the thoracic volume.

Koehler and Wischgoll [57] used frontal and lateral X-rays to reconstruct the lung volume and thoracic volume in 3D. The authors reconstructed the lung and thoracic

volumes for five patients and compared their results with those gained from the CT scan. Courvoisier et al. [58] reconstructed the rib cage through orthogonal frontal and lateral X-rays, and they mentioned the thoracic volume could be extracted by joining the surface obtained from the rib reconstruction. In addition, they reconstructed the thoracic volume for twenty-two idiopathic scoliosis patients and involved three users in performing usability testing. However, they did not point out the specific boundary of the thoracic volume. Charles et al. [50] utilized the Orten optical system [59], which needed to attach several markers to the outer surface of the torso, to measure the thoracic volume of 130 children with different scoliosis symptoms. Because the markers are attached to the human body, the thoracic volume they obtain will be larger than the real one.

Herein, I focus on the research which clearly defines the boundary of the thoracic volume and explains how to measure the thoracic volume via plain radiographs. In 1956, Kovach et al. [54] viewed the thoracic volume as a paraboloid shape and tried to calculate the lung volumes through X-rays for healthy adults. To do that, they firstly derived an equation to calculate the volume inside the chest wall (thoracic volume) and subtracted the heart volume and diaphragmatic dome volume. They only relied on the frontal X-rays to estimate the thoracic volume for healthy subjects in their study. In 1960, Barnhard et al. [15] defined the thoracic volume as the summation of five elliptical cylindroids, and each elliptical cylindroid was computed based on their derived equation. Their ultimate goal was to find out the total lung capacity for healthy subjects and patients with emphysema using frontal and lateral X-rays. In 1966, Loyd et al. [55] used a similar equation that Barnhard derived to measure the thoracic volume inside the rib cage. In 1985, Stolle [56] et al. also took advantage of frontal and lateral X-rays to construct an equation to help estimate the thoracic volume and the total lung capacity. Later on, their equation to measure thoracic volume was employed by Kovac et al. [60] to track the thoracic volume variations in adolescent scoliosis patients before and after their surgical operations. The thoracic volume accuracy of the above-mentioned literature depended only on the correlation of their methods with other methods, such as gas dilution or plethysmography. In other words, their

methods were not validated or compared with any gold standard method in the orthopedic field.

2.3 Summary of the Literature Review

As mentioned above, there are several imaging devices which can be used to visualize and reconstruct the spine, including CT scans, MRIs, ultrasounds, and X-rays. Each device has its advantages and disadvantages, so I summarize their pros and cons in Table 2.1.

Table 2.1 Pros and cons of four commonly used medical imaging technologies

Imaging Device	Advantages	Disadvantages
Computed Tomography (CT) scan	Spine reconstruction accuracy (gold-standard)	1. High-dose radiation (chest CT scan: 7 mSv [4]) compared to other devices 2. Not suitable for pediatric patients 3. Higher cost
Magnetic Resonance Imaging (MRI)	No significant side effects	1. Highest cost 2. Long scanning time 3. Inferior to CT scan in bone image display 4. Not recommended for patients with surgical implants
Ultrasound	1. Lower cost 2. No radiation 3. No contraindications 4. Easy portability	1. Inferior to CT scan or MRI in bone display 2. Still immature and seldom used to reconstruct spines
X-ray	1. Low-dose radiation (chest X-ray: 0.1 mSv [4]) 2. Commonly used for spine deformity inspection 3. Short filming time 4. Lowest cost	1. Rib cage overlap problem 2. Error due to patients' postures

Previous studies mainly focused on obtaining an accurate reconstruction of the vertebrae or ribs using different technologies, and they seldom indicated how to measure

or estimate the thoracic volume/cavity, which is related to the pulmonary function, for the spine patients. Thoracic volume can be a potential reference to predict the pulmonary function [22,23,61] for orthopedic doctors to determine the timing for spine corrections. This dissertation not only describes the processes to reconstruct the thoracic rib cage but also explains how to measure the thoracic volume with the help of traditional biplanar X-rays. To be clinically useful, this dissertation discusses the accuracy of the developed program and studies if the process satisfies the 3% error recommended by the American Thoracic Society [49].

In Chapter 3, a simulation method will be proposed to demonstrate the key components to reconstruct the rib cage through frontal and lateral X-rays and present how to reconstruct/measure the thoracic volume after rib cage reconstruction. In addition, my designed workflow based on the proposed method is illustrated and discussed in detail, and the workflow can be duplicated by the engineer to develop medical software to achieve rib cage and thoracic volume reconstruction.

In Chapter 4, I will perform usability testing by using our customized program to reconstruct the rib cage and thoracic volume. Then, I will validate the accuracy and precision of the rib cage reconstruction and compare our results to the previous literature and the results gained from CT scans (gold standard). From the comparison, I can assess whether our developed program is comparable to the exiting methods. For the thoracic volume, most of the researchers defined the thoracic volume boundary and parameters that can be easily observed on the plain radiographs, and then they further built equations for computing the thoracic volume. Other literature may have different definitions for the thoracic volume, and most of them did not validate the accuracy of the results they got through their derived equations. Hence, I will compare our results with the previous literature using their derived equations to estimate the thoracic volume. Our thoracic volume results are also compared to the results gained from CT scans (gold standard). These comparisons find that the outcome of our method is better than the previous research and the thoracic volume measurement using the developed program meets the American Thoracic Society standard.

Chapter 3

Simulation Workflow and Methodology for Thoracic Rib Cage and Thoracic Volume Reconstruction Using Biplanar Radiographs

This chapter proposes a simulation method for developing software (i.e., thoracic volume estimator) to reconstruct thoracic rib cage and thoracic volume using biplanar X-rays. Then, the detailed workflow to create a semi-automatic program (including a graphical user interface and the Blender add-on package) to reconstruct the rib cage and thoracic volume using the proposed method is presented. The thoracic volume measurement is also calculated. The advantages and the application of the thoracic volume estimator are pointed out in the results and conclusion sections.

3.1 Software Developing Method for Rib Cage and Thoracic Volume Reconstruction

3D reconstruction for the human thoracic rib cage and thoracic volume is becoming more important to assist doctors to visually inspect and identify a spine deformity. However, it still takes doctors a long time to apply the current spine reconstruction technique in the routine clinical setting, not to mention the lack of thoracic volume reconstruction to predict pulmonary function for spine patients. In order to tackle those problems, a simulation method is suggested to help engineers develop appendable and portable medical software

for the reconstruction of the patient-specific rib cage and the thoracic volume. The end goal of the developed software is to accurately reconstruct the thoracic volume in 3D and measure its volume. It is necessary to firstly reconstruct the thoracic rib cage, which defines the boundary of the thoracic volume. We rely on the biplanar/orthogonal X-rays to reconstruct the thoracic rib cage due to its benefit of low-dose radiation. Over the past few decades, scientists have employed the radiographs to conduct the spine reconstruction through rib cage databases (statistical shape model) [62,63], including the geometric structure of the spine gained from pathological or non-pathological patients. However, getting access to those databases is not necessarily easy for doctors or even for engineers. Instead, my proposed method only needs one intact adult thorax model (the adult can be a male or a female but a child's spine is not recommended due to bone immaturity) to implement the spine and the thoracic volume reconstruction.

I present a general method in Figure 3.1 to demonstrate the key components and processes to create a software/program that can implement the thoracic rib cage and thoracic volume reconstruction using traditional biplanar/orthogonal X-rays. An important first step is the pre-processing stage, where one intact/healthy rib-cage is used to reconstruct the rib cage as a template for spine patients. To that end, one non-spine deformity adult's CT scan DICOM images need to be segmented and reconstructed into a 3D rib cage as a template, using any image processing software. The rib cage template will be imported to the software environment (e.g., computer-aided design and computer graphics software) to conduct the patient-specific rib cage reconstruction with the help of the anatomical information gained in the graphical user interface. Once the patient-specific rib cage is completed, the thoracic volume can be reconstructed and computed in the software environment. In the following section, I will explain how to perform each component of the proposed method in detail.

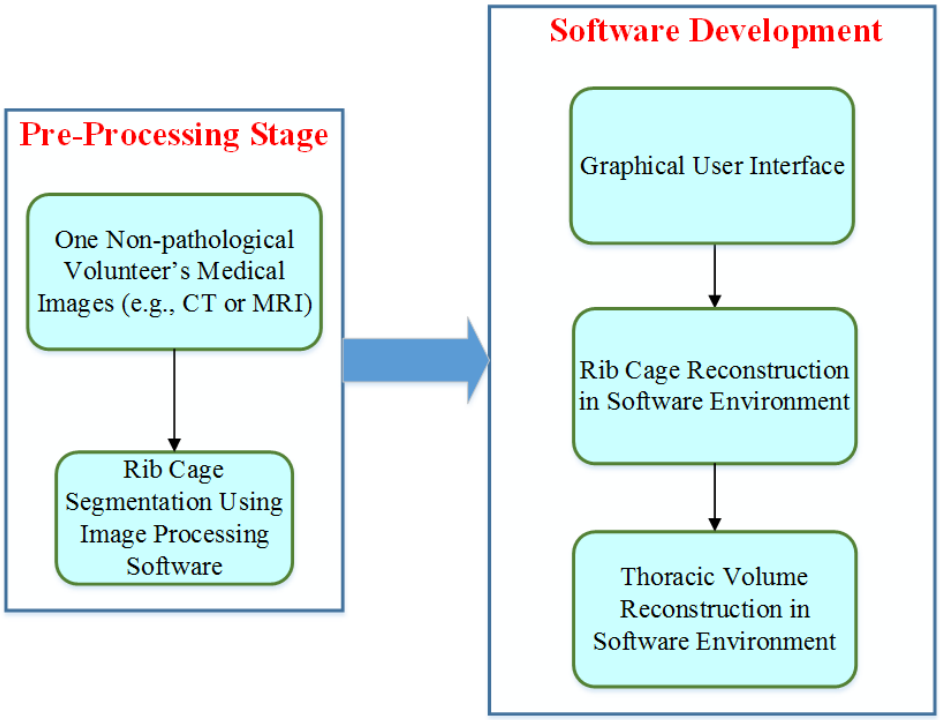

Figure 3.1 Simulation method to develop software for rib cage and thoracic volume reconstruction

3.2 Semi-automatic Software to Reconstruct Rib Cage and Thoracic Volume Based on the Proposed Method

With the proposed simulation method shown in Figure 3.1, Figure 3.2 shows a simulation workflow to implement our software development for the thoracic rib cage and thoracic volume reconstruction. After getting biplanar X-rays from spine patients, there is a need to develop a graphical user interface (GUI) software to load the X-ray images. Through the GUI, clinical users can apply their medical knowledge to identify 2D anatomical landmarks based on the spine on the biplanar radiographs to reconstruct the rib cage. The role of the GUI software will act as a connecting platform that can activate the rib cage template and then load the template into the software environment, using a computer-aided design (CAD) or computer graphics (CG) software. In the CAD or CG environment, the rib cage

template will be positioned and oriented according to the 3D anatomical landmarks based on the data in the GUI software. During this stage, the patient-specific thoracic rib cage is generated. Actually, the reconstructed thoracic rib cage model outlines and defines the boundary for the thoracic volume reconstruction. Next, the software engineers need to build the thoracic-volume-like contour based on the rib cage boundary reconstructed in the CAD or CG environment. Besides, the thoracic-volume contour needs to be fitted inside the rib cage boundary. Most doctors or clinicians have no experience in operating a rib cage or thoracic volume reconstruction in the CAD or CG software environment. Thus, some manual procedures need to be simplified and automated so that the non-expert users can easily reconstruct and calculate the thoracic volume. For example, the software can allow the user to set up the number of times for iteration and then it automatically iterates and refines the thoracic-volume contour.

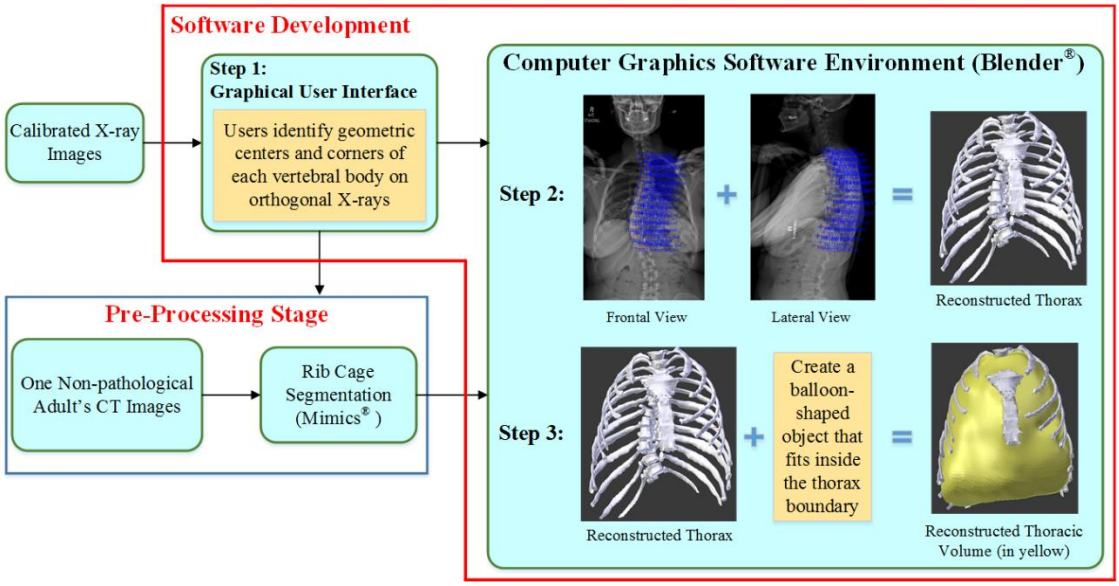

Figure 3.2 The simulation workflow to develop software for rib cage and thoracic volume reconstruction using biplanar X-rays

3.2.1 Calibrated X-ray Images and Pre-Processing Stage

There are two tasks that need to be accomplished before developing the reconstruction software. One is the calibration for the biplanar X-rays from spine patients, and the other is the acquisition of the intact thoracic rib-cage model from non-spine deformity persons. For the first task, the frontal and lateral X-rays of the spine patients are stored as DICOM (Digital Imaging and Communications in Medicine) image formats, so the scale of the images has already been calibrated by the X-ray machine. I utilized the open-source software Surgimap®, version 2.2.14 (Surgimap Spine Software, Nemaris Inc., New York, NY) to read out the actual size of the DICOM image and transfer the existing information in the DICOM image to the bitmap (BMP) image format. That is, all of the pixels' distance in the DICOM image was scaled to the actual distance before exporting it as a BMP image format. As a consequence, the BMP images were imported to the GUI and developed software for later use.

As for the other task, Figure 3.3 demonstrates my workflow to gain the rib cage template. One male adult without a spine deformity was scanned by a CT scan with 1 mm slice thickness (1 mm distance between each slice), and his de-identified CT scan DICOM images were collected from the Fairview Hospital at the University of Minnesota. Once the CT scan DICOM images were obtained, I imported them to the image processing software, called Mimics® (version 19.0, Materialise Inc., Belgium). In the environment of Mimics, the non-pathological thoracic rib cage can be automatically segmented and reconstructed by tuning the image threshold of the pixel value. Sometimes the information, like the tissues, organs (lungs and heart), and muscles, may also be included. As a consequence, it is necessary to manually retrieve the geometric information of the bones we want, such as vertebrae, ribs, and sternum; Mimics allows the user to select the region of interest to do the segmentation. In order to separate the vertebrae, ribs, and sternum, I employed several functions in Mimics: crop function to cut each portion, cavity fill function to fill up the unexpected holes on the bone's surface manually, and smoothening function to get rid of some surface noise on the bone. After manual segmentation, the rib cage template, including 12 vertebrae (T1-T12), 24 ribs, and 1 sternum in Figure 3.4, was

reconstructed, smoothened, and exported respectively as the stereolithographic (STL) file. The STL file is a standard format and displays three-dimensional objects with triangular surfaces under the Cartesian coordinate system. The rib cage template will be exported to Blender software and be used to reconstruct the patient-specific rib cages for spine patients in the Blender environment. Based on the proposed simulation workflow in Figure 3.2, we can focus on the software development (in the following two sections) which includes a graphical user interface and the logic that can reconstruct the rib cage and thoracic volume.

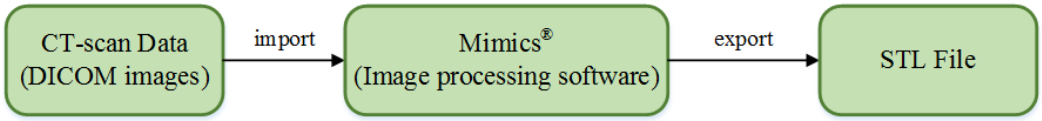

Figure 3.3 Workflow to gain rib cage template

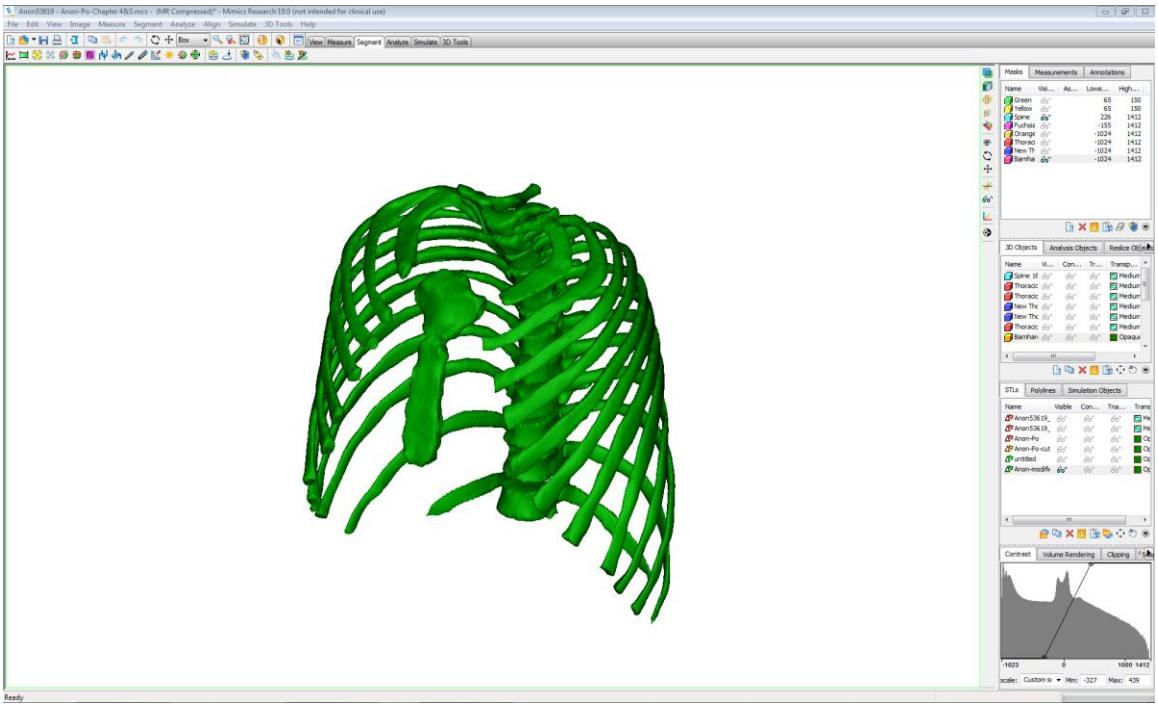

Figure 3.4 Segmentation and reconstruction of the rib cage template using Mimics®

3.2.2 Development of the Graphical User Interface Platform

After the biplanar image calibrations and pre-processing stage, I now discuss the development of the GUI platform for the purpose of rib cage reconstruction. The Python GUI platform with Tkinter was coded in Python 3.4. The GUI allows the user to import the calibrated frontal and lateral X-ray images. With the help of GDCM library (cross-platform open-source library written in C++), the GUI can support DICOM images and common image formats, such as JPEG, TIFF, BMP, and PNG.

After importing the biplanar X-rays as the BMP format, the true scale of the frontal and lateral images needs to be provided by users. In addition, users have to register five specific landmarks for each vertebra in each X-ray image, including the top and bottom endplates of the vertebral body (four landmarks), and the centroid of the vertebral body (one landmark), to help the program identify the location, orientation, and potential wedging/local deformity of each bone segment. In Figures 3.5 (a) and 3.5 (b), I show an example of a scoliosis patient to demonstrate the registration landmarks on each vertebral body in the GUI environment.

In Figure 3.5 (a), the GUI presents the pixel coordinates of the four 2D landmarks on the top and bottom endplates of the vertebral body. The users can easily compute the frontal and lateral rotation angles of the vertebral body based on the pixel coordinates to determine whether the vertebra has wedging fractures or not. As for the axial rotation angle of the vertebral bodies, this angle can be computed and inferred with the assistance of the open-source software, SCODIAC, developed by Cerny et al. [64]. They used the six anatomical landmarks (four landmarks on the corner of the vertebral body and two landmarks on the inner edge of the pedicle) in the frontal view of the vertebral body to compute the axial rotation angle. In Figure 3.6, six red crosses on the vertebral body are the anatomical landmarks used for deriving the axial rotation of the vertebra. The vertebra in this figure has an axial rotation of 1.6 degrees with respect to the negative Z-axis.

In order to make the GUI more user-friendly, we created some functions, such as zoom-in/zoom-out features, pixel intensity adjustment (pixel contrast), and pixel brightness in Figure 3.5 (a). Those functions allow users to visibly identify the anatomic landmarks on

the frontal and lateral X-rays. The 2D anatomical landmarks of the centroids of the vertebral bodies that users mark on both X-rays need to be stored and transformed into the landmarks in 3D space. In Figure 3.5 (c), I present the results of the 2D anatomical landmarks of the centroid vertebral bodies and their merged/transformed 3D anatomical landmarks. The first and the third columns show the 2D landmarks on the frontal and lateral X-rays respectively, and the second column shows the 3D landmarks which are merged using the 2D landmarks on biplanar X-rays. Those 3D landmarks are the reference coordinates to align the rib cage template acquired from a non-spine deformity subject. Once users finish registering anatomical landmarks in the GUI (Step 1), those 2D and 3D landmarks will be stored as the JSON file, which is originally a subset of JavaScript but becomes a language-independent format supported by many different application programming interfaces (also called APIs).

The advantage of the GUI platform is that it can trigger Blender software and automatically load the rib cage template (12 vertebrae, 24 ribs, 1 sternum), obtained in the pre-processing stage, into Blender software; users do not need to import all bones one by one to Blender. Then, the GUI will use the rib cage template in the Blender environment to automatically reconstruct and align the patient's rib cage depending on users' registration information in the JSON file. In the next section, I will address the development of the semi-automatic add-on package for Blender software, as can be seen in Steps 2 and 3 of Figure 3.2.

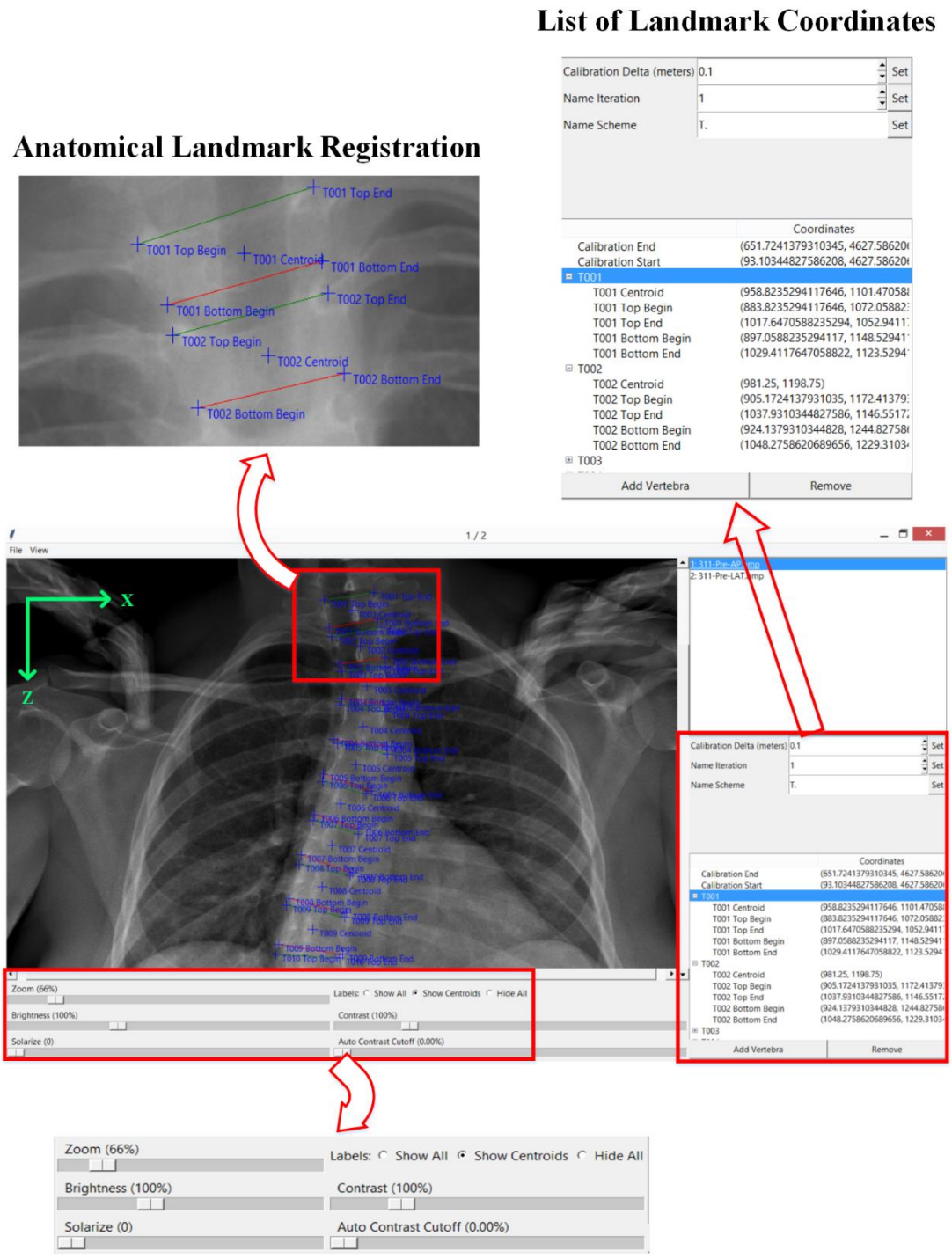

(a) Frontal X-ray in the GUI

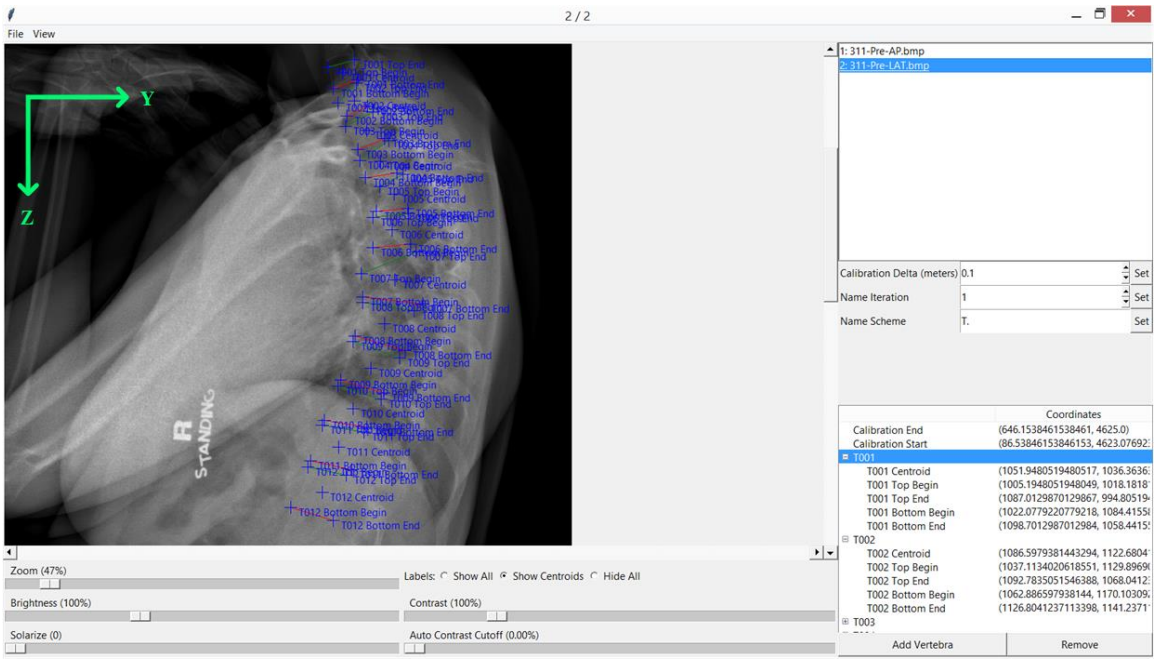

(b) Lateral X-ray in the GUI

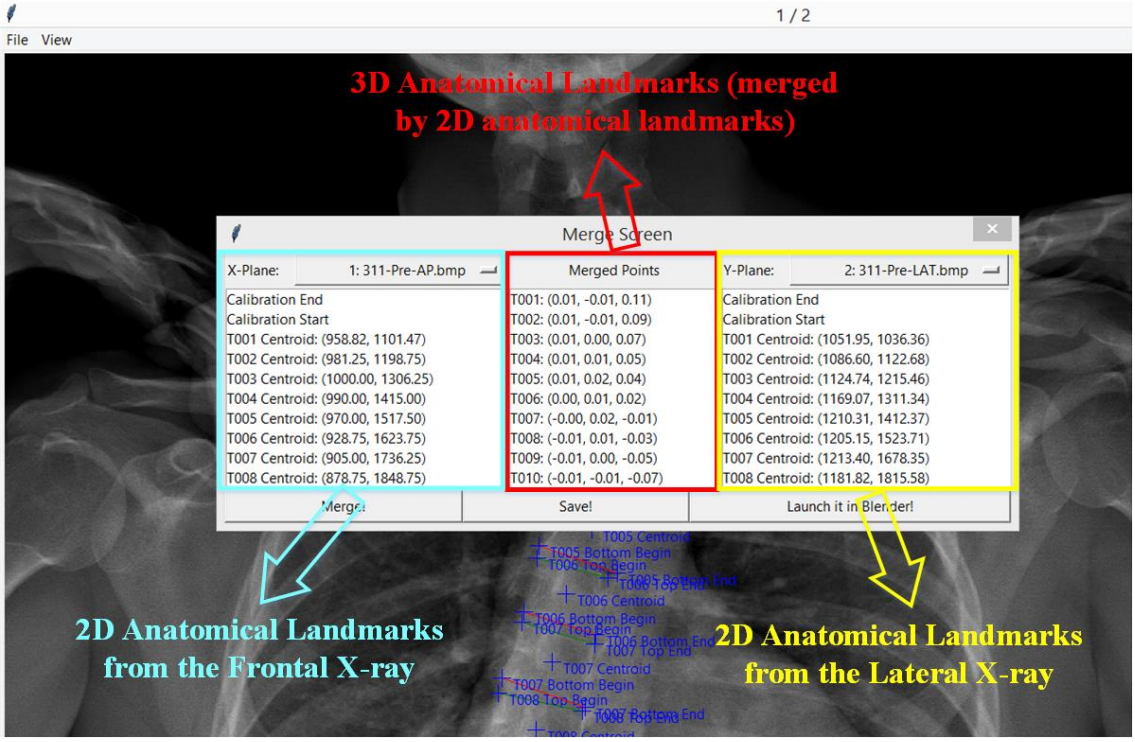

(c) Transforming 2D landmarks (unit: pixel) into 3D landmarks (unit: meter) on the merge screen

Figure 3.5 Graphic user interface environment of the thoracic volume estimator

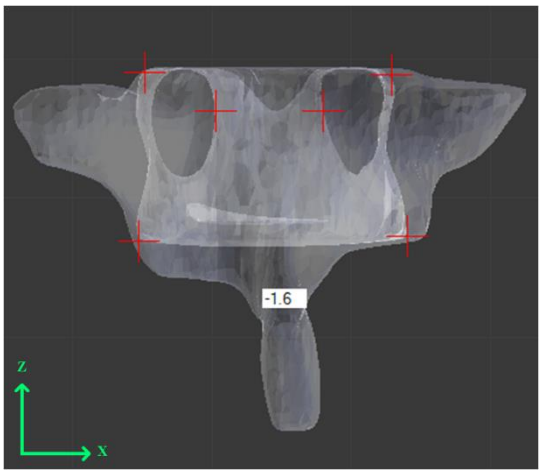

Figure 3.6 Demonstration of six landmarks (labelled in red crosses) on the vertebral body for calculating axial rotation angle of the vertebra by Cerny's method

3.2.3 Development of the Blender Add-on Package

As for the software development, I focused on creating a semi-automatic add-on (plugin) package that can be implemented in the Blender environment to reconstruct the patient-specific rib cage and further reconstruct and compute the thoracic volume. The reason why we call it semi-automatic is that the user can manually intervene and calibrate the rib cage and thoracic volume reconstruction. Steps 2 and 3 in Figure 3.2 depict the simulation workflow to reconstruct the rib cage and thoracic volume separately in Blender software. Python scripts (free open-source) are a powerful way to extend the functionality of Blender software; they are used to develop the Blender plugin package. There are two main tasks for the plugin package; one is rib cage reconstruction and the other is thoracic volume reconstruction and measurement.

For the rib cage reconstruction, it includes the automatic, semi-automatic, and manual processes. The semi-automatic processes indicate that the program can automatically finish some processes for users but the results might not be accurate enough. Therefore, the program still needs users' input to improve the accuracy of the results. Figure 3.7 shows the detailed processes to reconstruct the rib cage in Blender. The yellow and green blocks

stand for the automatic and semi-automatic processes done by my program respectively; the blue blocks represent the manual processes. The Blender plugin needs to load the rib cage template gained from the non-spine patient and read in the JSON file, which stores the 3D anatomical landmarks transformed through the developed GUI program. In addition, the frontal and lateral X-ray image (BMP format) should be imported to Blender, and the developed add-on package also has a custom icon to import the images that users use for the landmark registration in the GUI. The size of the frontal and lateral X-rays needs to be scaled manually based on the information in the Surgimap software. Once the rib cage template and JSON file are loaded to Blender, the thoracic vertebrae (T1-T12) are aligned and positioned automatically on the basis of the registration landmarks that the user marks in the GUI environment. After that, the user has to manually adjust the scales and the rotations of the vertebrae; the scales can be completed with the help of the background X-rays in Blender, and the rotations can be derived through the pixel coordinates of the vertebrae in the GUI. In order to shorten the manual operation time for the user, each vertebra is automatically connected to three Lattices (function in Blender) when the rib cage template is semi-automatically imported to Blender. The Lattice is a structure which is constructed by multiple vertices, and it can be used to deform and manipulate a complex mesh (e.g., human bones) in a non-destructive way. Figure 3.8 (a) demonstrates a thoracic vertebra connected to three Lattices (front, back, and whole Lattices) in the frontal and lateral views in Blender. The whole Lattice is used to manipulate rotation and scale for the vertebra; when the user rotates and scales the whole Lattice, the vertebra will be rotated and scaled identically. The front Lattice is bonded to the vertebral body while the back Lattice is bonded to the rest of the vertebra portion. Both Lattices are utilized to deform the morphology of the vertebrae. For example, once the user notices the vertebrae have wedging deformities, the front Lattice can be used for manual modification of the vertebral morphology. In Figure 3.8 (b), the top vertices on the frontal Lattice rotate 15 degrees with respect to the Y-axis in Blender, which leads to a 15-degree wedging vertebra relative to Figure 3.8 (a). Additionally, the number of vertices inside the Lattice can increase if the user requires a more detailed reconstruction for a specific region of the bone.

As for the ribs, when they are imported to Blender semi-automatically, the locations of the ribs are automatically attached to their adjacent vertebra (pair ribs are attached to two conjunction joints, costotransverse and costovertebral joints, on their vertebra structurally). Thus, the user needs to alter the orientations and the dimensions for the ribs according to the background X-ray images in Blender. As can be seen in Figure 3.8 (c), each rib is also bonded to a Lattice structure for the purpose of manual adjustment, and each Lattice can be used to adjust the dimensions and the orientations of the bonded rib. Also, the increased vertices in the Lattice structure can be employed for shape morphology calibration. Like the vertebrae and ribs, the orientations and the dimensions of the sternum should be manually adjusted by the user through the Lattice function.

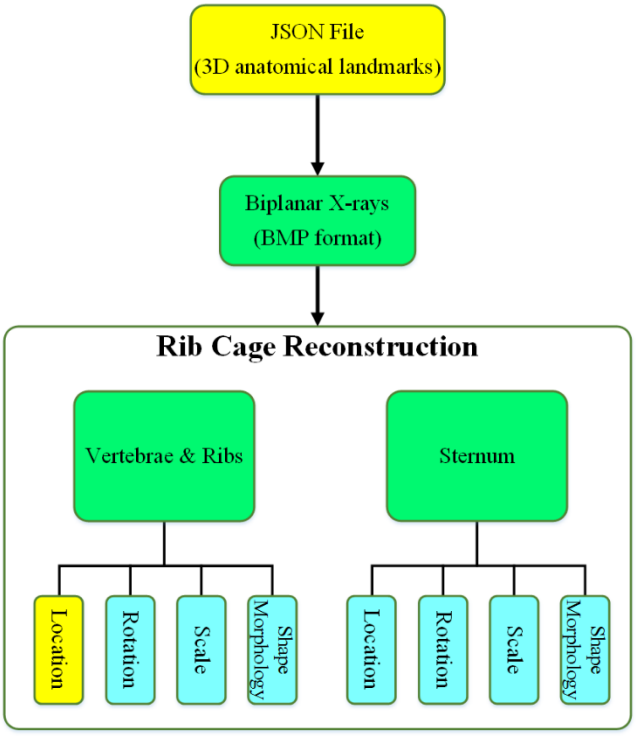

Figure 3.7 Step-by-step processes for rib cage reconstruction in Blender

Yellow, green, blue blocks represent automatic, semi-automatic, and manual processes respectively.

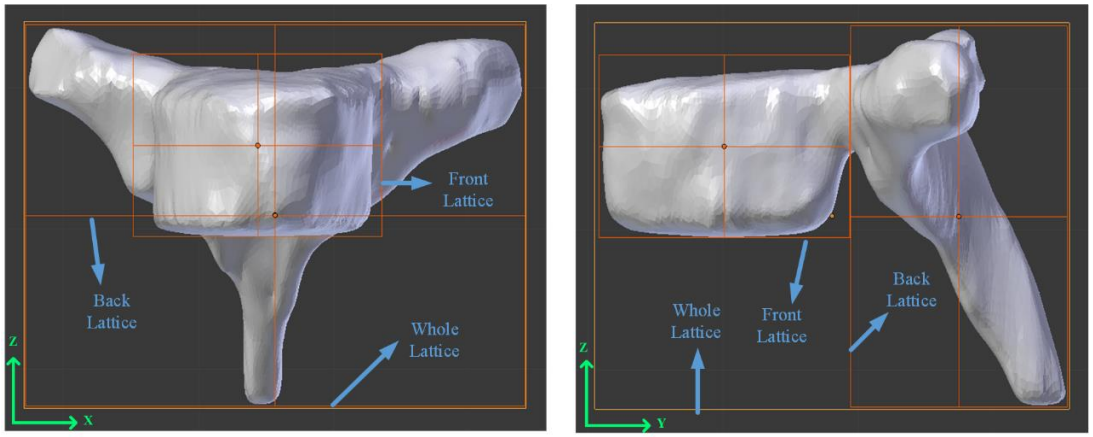

(a) Vertebra with three Lattices (whole, front, and back)

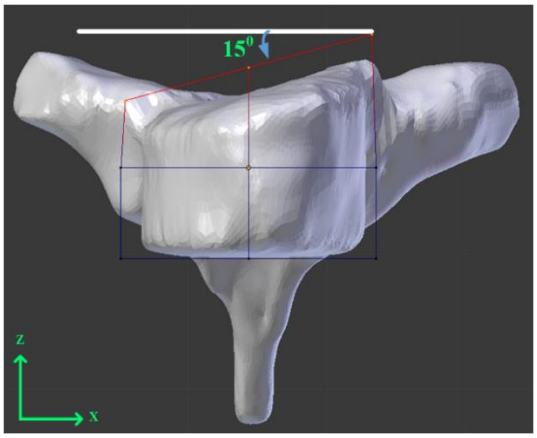

(b) Demonstration of using front Lattice for wedging deformity (front Lattice rotates 15 degrees relative to 3.8 (a))

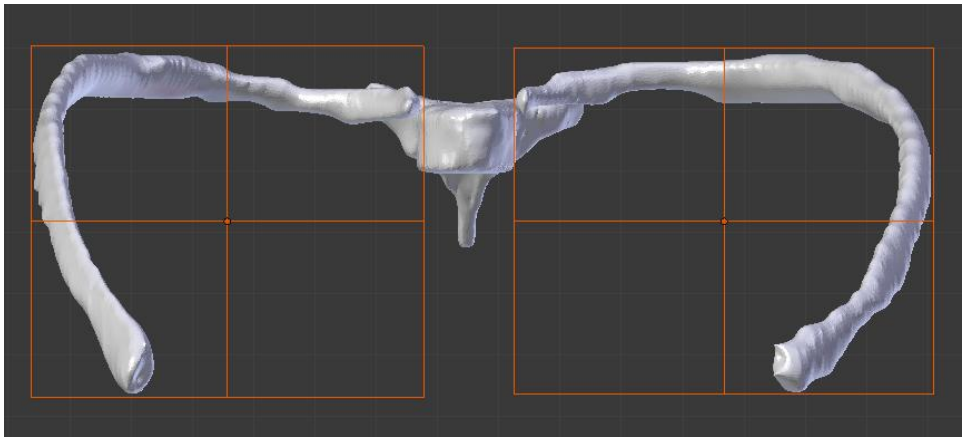

(c) Ribs with Lattices

Figure 3.8 Vertebrae and ribs bonded to Lattices function in Blender

Regarding the thoracic volume reconstruction, none of the previous literature investigated how to reconstruct the thoracic volume in 3D. As soon as the rib cage reconstruction is done, the next step (Step 3 in Figure 3.2) is to work on thoracic volume reconstruction and measurement. Therefore, I have to build a balloon-shaped object and modify its shape until it perfectly fits inside the reconstructed rib cage. In this process, I need to utilize some functions in Blender, and I list the terms of these functions and their purposes as follows [65]:

1. **Join**: to merge and combine multiple objects into one single object.
2. **ConvexHull**: to take a point cloud (vertices) as an input and then output the smallest convex hull which surrounds those vertices.
3. **ShrinkWrap**: to allow an object to be shrunk to the outer surface of another object.
4. **SubSurf**: (also called Subdivision Surface) to split the faces of a mesh into smaller faces, giving a smooth appearance.
5. **Smooth**: to smooth the selected vertices by averaging the angles between the faces, and to decrease the surface noise of the object.
6. **Remesh**: to create new mesh topology. The output object follows the surface curvature of the input object, but its topology contains only cube-like shapes. This function normally controls a parameter, called Octree Depth, to create the new mesh topology. An Octree is a common way to partition a three-dimensional object by recursively subdividing it into eight regular hexahedrons. A low Octree Depth value will generate larger faces relative to the input object, and a higher value will generate a denser output object.

To reconstruct the thoracic volume, four abovementioned functions, including **ShrinkWrap**, **SubSurf**, **Smooth**, and **Remesh**, need to be iterated for the balloon-shaped object. That is, those functions have to be repeatedly performed until the reconstructed thoracic volume fully fits inside the thoracic cavity. However, we integrated several repetitive processes and functions to automatically approach the thoracic volume reconstruction in the thoracic volume estimator. The automation of those repetitive processes replaces the manual operation which took an average of an hour for the user to perform the thoracic volume reconstruction in Blender. We developed a Blender add-on

package (coded in Python 3.4) and appended it to the Blender environment. This add-on package is part of the thoracic volume estimator and can automatically build a convex-hull object inside the reconstructed rib cage and further iterate the object to match the boundary of the reconstructed rib cage with the help of above-mentioned Blender functions.

Our Blender plugin generates an approximation for the thoracic volume algorithmically after the 3D thoracic volume is reconstructed. The algorithm for the thoracic volume reconstruction and computation is expressed as the following pseudo-code:

Input: $\{O\}_{i=1}^{N}$ mesh objects represent the rib cage, including all vertebrae, ribs, and sternum.

Output: the approximate thoracic volume, *V*.

User Input Data:

- Volume Convergence: $\in$
- Volume Refinement Iterations: *refineIter*
- Max Smooth Iterations: *smoothIter*
- Max Octree Depth: *ocDepth*

Begin
  $\hat{O}$ = **Join** ($\{O\}_{i=1}^{N}$);
  C = **ConvexHull** ($\hat{O}$);
  repeat
    W = **ShrinkWrap** (C, $\hat{O}$);
    S = **SubSurf** (W, 2);
    T = **Smooth** (S, *smoothIter*);
    R = **Remesh** (T, *ocDepth*);
    V_{new} = CalcVolume (R);
    $C = R$;
  until ($|V_{new} - V_{old}| < \in$) or (iteration > refineIter);
  $V_{old} = V_{new}$;
end

Algorithm 1: Pseudo-code for automatic thoracic volume reconstruction and calculation

As shown in Algorithm 1, the **Join** function is used to merge all meshes from individual objects (bones) in $\{O\}_{i=1}^{N}$ into a single object (rib cage), $\hat{O}$. The **ConvexHull** function, *C*, will generate the smallest convex set of vertices to surround $\hat{O}$. The purpose of the mesh *C* in this algorithm is to minimize the number of vertices managed by Blender during volume calculation, because each vertex and edge will be repeatedly projected, shrunk, and smoothed. With $\hat{O}$ and *C* calculated, the crux of the algorithm then repeats a process of projecting all vertices in *C* onto the surface of the rib cage, $\hat{O}$, with the **ShrinkWrap** function. This step introduces concavity to the projected mesh as projections can be either inward or outward of the rib cage's surface depending on whether *C* is outside or inside the rib cage. Next, the projected mesh is sub-divided (i.e., each edge is split, which increases more new vertices on the existing object) with the **SubSurf** function, and new vertices are nudged toward the interior of $\hat{O}$ through the **Smooth** function. Due to the utilization of orthogonal vertex projection in the **ShrinkWrap** function, vertices tend to cluster on the outer surface of $\hat{O}$. In response to this problem, the algorithm uses the **Remesh** function to replace the mesh with a new version constructed based on a high resolution Octree, which automatically distributes the clustered vertices more uniformly to represent the thoracic-volume shape. We find that this combination of projecting, sub-dividing, smoothing and re-meshing methods using the Blender functions leads to a thoracic-volume mesh object that is nicely contained in the interior of the reconstructed rib cage, as though a balloon is inflated to fill the interior of the rib cage.

Finally, the algorithm not only automatically reconstructs and calculates the volume of the Octree-produced mesh, but also tests if either of the two criteria (volume refinement iterations and volume convergence) is satisfied. The criteria of the volume refinement iterations contain the user's inputs, with which the user wants the program to repeatedly run the four functions, including **ShrinkWrap**, **SubSurf**, **Smooth**, and **Remesh**. The criteria of the volume convergence are to compare the thoracic volume value between different iterations, and check if the newest iterated thoracic volume value is larger than the previous value by a specific amount. If either of the criteria is met, then the program will automatically stop iterating and refining the thoracic volume. On the other hand, if

neither of the criteria is met, the algorithm automatically repeats the entire refinement process using the most recent Octree mesh, *R*, as input.

In the developed thoracic volume estimator, the volume calculation methodology and function in Blender are directly employed. Specifically, the value of thoracic volume (*R*) is approximated as the sum of the volumes from multiple signed triangle pyramids in Blender. To perform this calculation, Blender automatically converts the thoracic volume model to a triangular mesh object, and each surface normal must be consistent (i.e., pointed away from the centroid of the thoracic volume model). In this case, the triangle pyramids are constructed by connecting the vertices of the *M* triangle faces to the centroid in the thoracic volume model. Then, the thoracic volume (*TV*) [66] value is given by:

$$TV = \frac{1}{3}\sum_{j=1}^{M} A_j \cdot (\overrightarrow{C_j} \cdot \overrightarrow{N_j}) \tag{3.1}$$

where A_j is the area of the *j*-th triangle on the thoracic volume model, $\overrightarrow{C_j}$ is the vector between the centroid of the *j*-th triangle on the thoracic volume model and the centroid of the thoracic volume model, and $\overrightarrow{N_j}$ is the surface normal of the *j*-th triangle. For a clear explanation, a sphere shape on the left side of Figure 3.9 represents the thoracic volume model which is made up of multiple triangle pyramids. Enlarging one of the pyramids, we get the right figure, where the area of the selected triangle abc is A_1, the vector between point O (centroid of the sphere) and point P (centroid of the triangle abc) is $\overrightarrow{C_1}$, and the surface normal of the selected A_1 triangle is $\overrightarrow{N_1}$. In Blender, the way to get the volume of an object is to compute and accumulate volumes of multiple triangle pyramids inside that object.

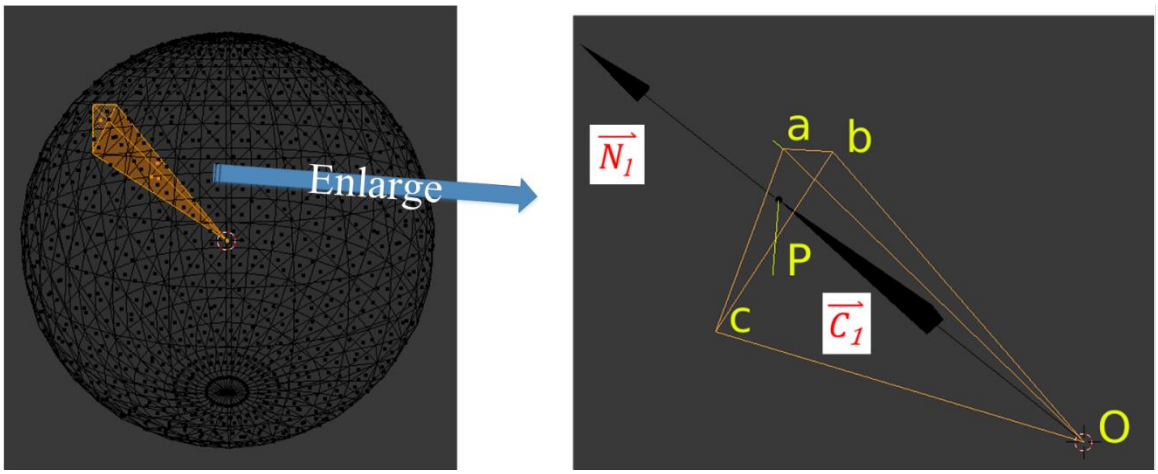

Figure 3.9 Demonstration of a sphere-shaped object with a highlighted triangle pyramid and the symbols used for explaining the thoracic volume calculation in Blender

3.3 Results and Discussion

In Figure 3.10 (a), I highlight the add-on package in red, which is appended to the Blender environment. This semi-automatic package includes the four panels for the rib cage reconstruction, thoracic volume reconstruction, and thoracic volume measurement. With the enlargement, Figure 3.10 (b) shows these four add-on panels, i.e., Status, Volume Calculation Interface, Volume Construction Parameters, and Extras panels. The user can click the Import Thorax and Add Images icons, belonging to the Volume Calculation Interface panel, to import the information (JSON file) gained from the GUI and the biplanar X-rays to Blender separately. After that, the rib cage template will be aligned based on the information stored in the JSON file, and the user can adjust each bone (including orientation and shape morphology) for more accurate rib cage reconstruction. Once the rib cage reconstruction is completed, the user can select the rib cage and the program will recognize that the user wants to reconstruct and measure the inner volume surrounded by the rib cage. The user can set up the parameters at the Volume Construction Parameters panel, and then click the Build Hull and Refine Volume icons for thoracic volume reconstruction. Next, the thoracic volume will be iterated automatically until it fulfills the

parameter settings in the Volume Construction Parameters panel. The final result of the thoracic volume measurement will be presented at the top of the Status panel.

The advantage of the add-on package is that it provides some changeable parameters, such as smooth iteration, octree depth, and volume refinement iteration. The smooth iteration parameter can smoothen the surface noise. The max octree depth parameter can vary the resolution of the reconstructed thoracic-shape volume (it is worthwhile to mention that this parameter will significantly lead to the increase of the computational time if the setting is larger than 7). In addition, the volume refinement iteration parameter can repeatedly implement the **ShrinkWrap**, **SubSurf**, **Smooth**, and **Remesh** functions for iterating and calibrating the thoracic-shaped volume until either of the criteria (volume refinement iterations or volume convergence criteria) is satisfied, as shown in the Volume Construction Parameters panel in Figure 3.10 (b). With the help of these changeable parameters, the user can cut down the reconstruction time for refining the thoracic volume reconstruction. Most important of all, the functionality of the rib cage and the thoracic volume reconstruction contained in our add-on package is separately developed. In other words, if there is a 3D rib cage reconstructed by any other software in the STL or OBJ format, the user can load it into Blender and use the add-on package to reconstruct and compute the thoracic volume.

From Step 1 to Step 2 in Figure 3.2, it takes on average 5 hours to reconstruct the patient-specific rib cage with detailed bone morphology through our semi-automatic program. As for Step 3 in Figure 3.2, it takes an average of 23 minutes (*SD* 6 minutes) for thoracic volume reconstruction and calculation. The reconstruction time for the rib cage and thoracic volume by our thoracic volume estimator will be compared with that by other image processing software which adopts high-dose CT scan images to perform the rib cage and thoracic volume reconstruction.

In the following chapter, the software requires reconstruction accuracy and precision checking through model validations by five independent participants who do not have the Blender or anatomical background. They will be trained to operate our semi-automatic program to reconstruct a patient-specific rib cage and thoracic volume for both spine and

normal subjects. Then, the reconstructed rib cage will be compared with the results gained from the CT scan, including position, orientation, and shape morphology of all bones, belonging to the rib cage structure. In addition, the reconstructed thoracic volume will be compared not only with CT scan's results but also with the methods proposed in the previous literature, which directly develop the equations to calculate the thoracic volume through the plane X-ray. The entire validation processes for the thoracic volume estimator are discussed and executed in Chapter 4.

The importance of the thoracic volume is that it can be a vital alternative used to predict the pulmonary function. Our thoracic volume estimator uses traditional orthogonal X-rays to reconstruct and calculate the thoracic volume. With the application of the thoracic volume estimator, I will correlate the thoracic volume with the parameters in the pulmonary function test for the spine deformity patients in Chapter 5. The wedging deformity commonly happens in spine deformities, such as scoliosis, Scheuermann's kyphosis, and osteoporosis. Thus, I will use the virtual patients to simulate pathological rib cage and further measure the thoracic volume through our thoracic volume estimator in Chapter 6.

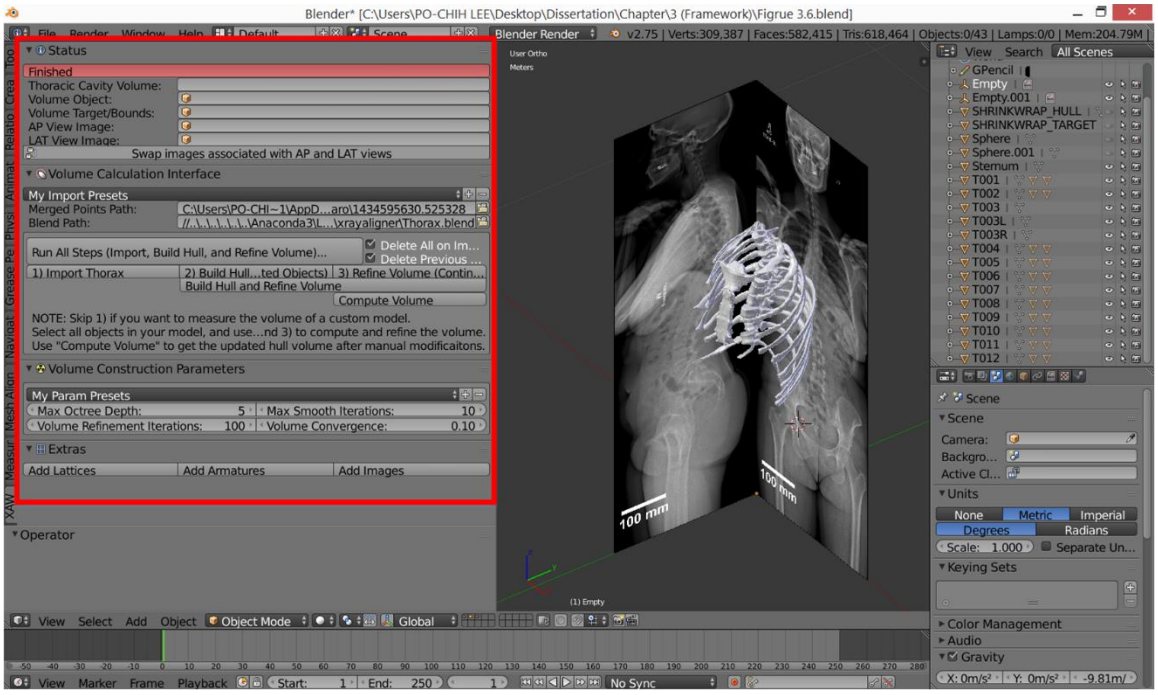

(a) Rib cage reconstruction and four add-on panels in Blender

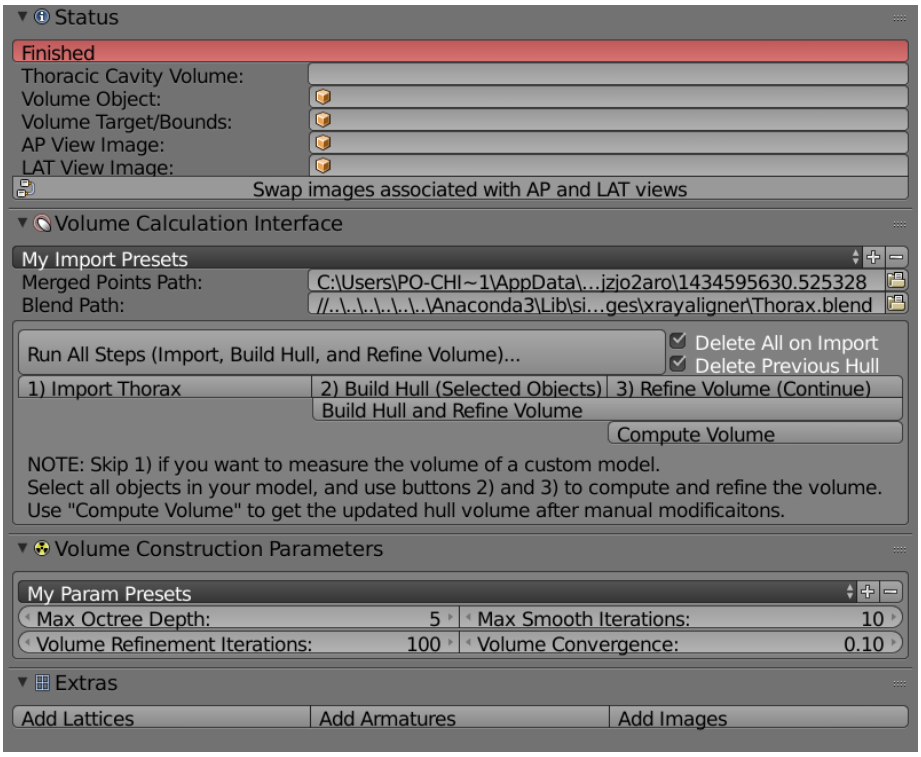

(b) Enlargement of four add-on panels

Figure 3.10 Results of the software development (add-on panels) in Blender

3.4 Conclusion

I proposed a general simulation method to describe how to use the biplanar X-rays to reconstruct a patient-specific rib cage and thoracic volume. This method can be duplicated and used for developing medical software for orthopedic applications. In the pre-processing stage, retrieving the CT scan data of one healthy subject is an important step, because this subject's rib cage is taken as the template to carry out the rib cage reconstruction during software development. Some previous literature involved a statistical method, which required a large amount of data collection from spine patients or healthy subjects in order to accurately reconstruct the vertebrae or ribs [62,63]. Instead, my method only required one rib cage template for software development in view of the limited data source. To create the semi-automatic software for the rib cage and thoracic volume reconstruction, there are several key components in the proposed method that help the

program developer: the developed software (thoracic volume estimator) can be utilized to do the three-dimensional rib cage reconstruction first and then move on to the thoracic volume reconstruction based on the resulting rib cage structure. Therefore, the method provides a general concept to accurately reconstruct and compute the thoracic volume with the help of the rib cage structure.

Following the proposed method, a semi-automatic program (thoracic volume estimator) which consisted of a GUI platform and an add-on package for Blender software was designed. The GUI could load the X-ray images and it played a role in collecting the medical information, such as image scale and anatomical landmarks, which is inputted by the users. The information was read into Blender software, whose features we relied on to do the 3D rib cage reconstruction. In Blender, we created an add-on package that could load the information stored in the GUI, and we took advantage of several Blender functions to help the program and users perform the rib cage reconstruction. Most importantly, I introduced an algorithm for the thoracic volume reconstruction, which was not proposed before. The algorithm was programmed into part of the Blender add-on package to reduce the user's operation time. Once the rib cage was reconstructed, the add-on package was capable of executing the thoracic volume reconstruction based on the inner boundary of the reconstructed rib cage; that is, a thoracic-volume-like object was iterated and refined through the user's input parameters until the object fully fitted inside the previously reconstructed rib cage to represent the thoracic volume. In summary, our thoracic volume estimator is semi-automatic, since the user still can interact with the program to do more accurate rib cage reconstruction and thoracic volume reconstruction/iterations. In other words, the users can always intervene in the program and Blender to help calibrate the rib cage and thoracic volume reconstruction whether they need an accurate or a rough reconstruction for the rib cage and thoracic volume.

Chapter 4

Validation of the Thoracic Volume Estimator for Thoracic Rib Cage and Thoracic Volume Reconstruction Based on the Proposed Method

4.1 Overview

This chapter focuses on validating the accuracy and precision of the rib cage and the thoracic volume using the developed program. The gold standard rib cage and thoracic volume models reconstructed by the CT scan data are employed to validate the accuracy and precision of the models reconstructed by our thoracic volume estimator, which is operated by the five recruited participants. Also, the precision of the rib cage and thoracic volume reconstruction is validated between each participant's models. The inter-observer reproducibility for the rib cage reconstruction and the thoracic volume measurement is also investigated. In addition, I compare our thoracic volume reconstruction results with the previous methods which use equations to calculate the thoracic volume through radiographs. Actually, the previous literature [7,15,54,56] seldom mentioned the term thoracic volume, because their ultimate goal was to calculate the lung volumes. Since the lung volume corresponds to one of the portions inside the thoracic volume/chest volume, there is still a need to measure the total thoracic volume first through X-rays. To that end, some researchers generated the equations for the thoracic volume, and the accuracy of the thoracic volume measured by those equations was also studied. Because previous

researchers set different boundaries for the thoracic volume from mine, I adjust our thoracic volume models and the CT scan models in order to make a more direct comparison between the models. Finally, some discussions and conclusions about the accuracy and precision of the rib cage and thoracic volume reconstruction are made.

4.2 Usability Testing

In this section, I first introduce the source information of the datasets utilized to implement the usability testing to validate the developed program. Next, the processes to simulate the frontal and lateral fluoroscopy images and to reconstruct the gold standard models by the image processing software are explained. In addition, the training tasks and time for the participants to operate the developed software are estimated, and the results of the user testing are presented.

4.2.1 Datasets' Information and Image Data for Reconstruction

There are 15 human datasets (including seven children and eight adults) involved in the usability testing for validating rib cage and thoracic volume reconstruction through our developed program and Blender add-on package. The University of Minnesota IRB determined this study was not human subject research. Table 4.1 lists all datasets' ages, genders, spine deformity symptoms, scoliotic Cobb angles, and kyphotic angles. The developed software uses orthogonal anterior-posterior (AP) and lateral thoracic radiographs to implement the rib cage and thoracic volume reconstruction. In order to validate the developed software, it is necessary to retrieve these subjects' biplanar X-rays and CT scan data. Four of them are cadavers from the Visible Heart Lab at the University of Minnesota and eleven de-identified subjects are spine deformity patients whose medical record, CT scan data, and frontal and lateral X-rays are collected from the Fairview Hospital at the University of Minnesota. These spine patients are subjected to radiographs in a standing position because their spine deformities are not severe. When undergoing the CT scan, patients need to lie down in a supine position no matter what degree the spine deformity is. In fact, spine curvature is anticipated to be amended and corrected due to a

supine position [28,67]. Some researchers have suggested that comparing different imaging technologies in different postures is impractical [58]. In order to circumvent this problem, I found an alternative to avoid directly comparing the results from the lying down CT scan with the results from traditional standing X-rays. That is, I decide to compare the lying down CT scan with the lying down fluoroscopy images. To do that, the first step is to use the CT scan data to reconstruct the thoracic rib cages for all fifteen datasets in Mimics. Then, I utilize the simulation modules in Mimics, called fluoroscopy module, to simulate AP and lateral fluoroscopy images for all datasets' thoracic rib cages. Hence, I replace the traditional standing X-rays with the lying down simulated fluoroscopy images to perform the rib cage and thoracic volume reconstruction. Figure 4.1 demonstrates the simulated AP and lateral fluoroscopy images of Dataset 13. The developed software can also load the fluoroscopy images to perform the reconstruction. For the fluoroscopy image, the bone structure and heart become black, and the lungs become white in Figure 4.1. After simulating the biplanar fluoroscopy images in Mimics, the images can be loaded into the program to do the rib cage and thoracic volume reconstruction.

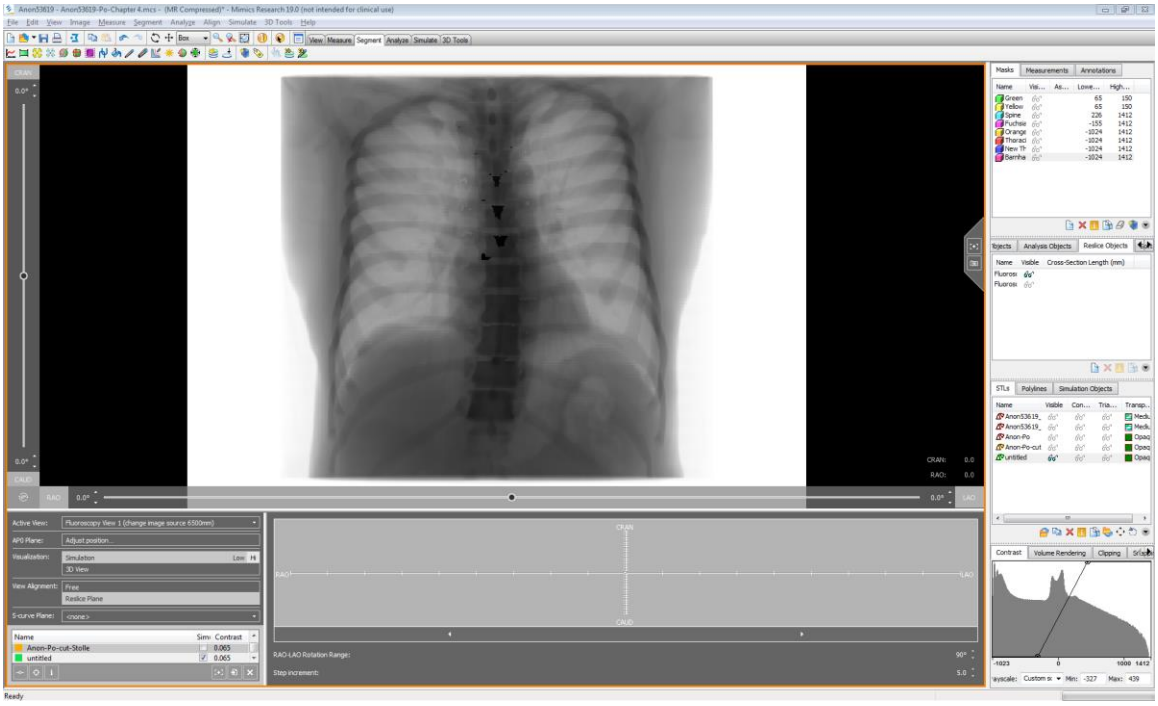

(a) Frontal view

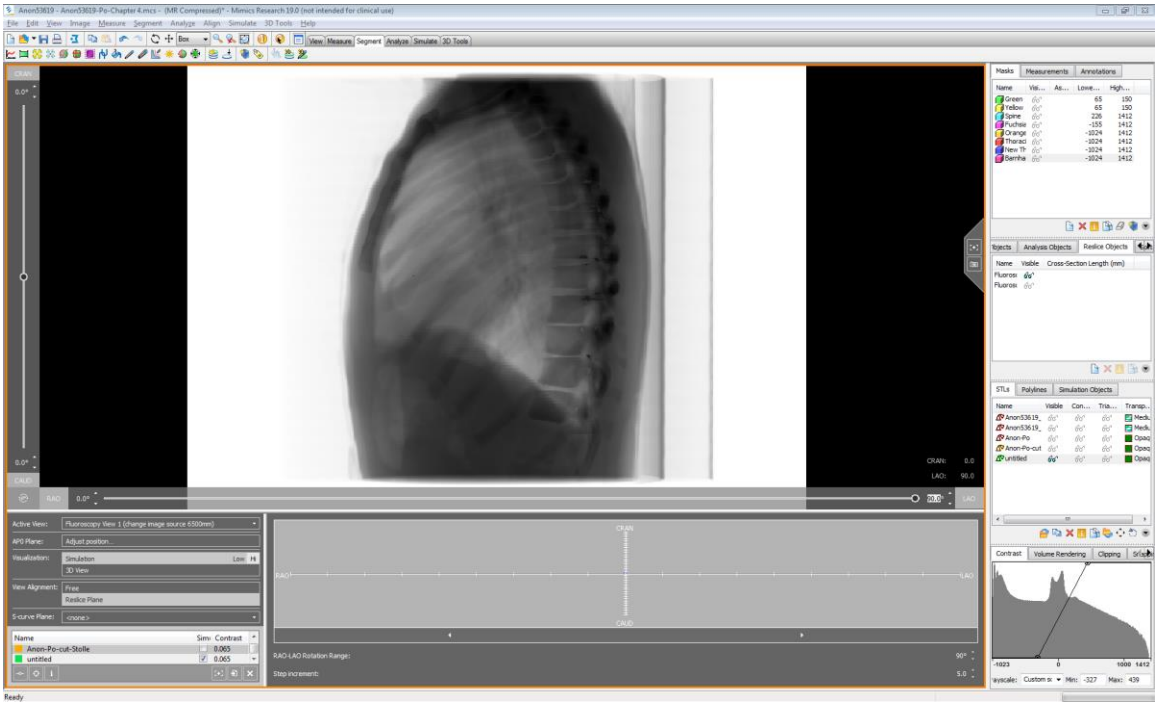

(b) Lateral view

Figure 4.1 Simulated frontal and lateral fluoroscopy images for Dataset 13 in Mimics

Table 4.1 Dataset information for validation and usability testing

Dataset No.	Gender	Age (years)	Spine deformity symptom	Cobb angle (deg) and location	Kyphotic angle (deg)	Notes
1	F	2	Yes; severe scoliosis	78.8 (T6-T12)	35.4 (T4-T12)	Patient
2	F	4	Yes; severe scoliosis & severe kyphosis	92.3 (T5-T12)	75.3 (T7-T12)	Patient
3	F	5	Yes; severe scoliosis & mild kyphosis	73.8 (T1-T8)	54.0 (T1-T12)	Patient
4	F	5	Yes; severe scoliosis & severe kyphosis	84.4 (T9-T12)	73.6 (T1-T12)	Patient
5	F	7	Yes; severe scoliosis & severe kyphosis	96.3 (T6-T12)	84.1 (T3-T12)	Patient
6	F	8	Yes; severe scoliosis	60.5 (T6-T12)	32.4 (T5-T12)	Patient
7	M	10	Yes; severe scoliosis	92.9 (T3-T12)	22.2 (T4-T10)	Patient
8	M	23	Yes; mild scoliosis	15.9 (T3-T11)	42.7 (T1-T12)	Patient
9	F	34	Yes; moderate scoliosis & mild kyphosis	44.8 (T6-T11)	55.7 (T3-T12)	Patient
10	M	54	No	< 10*	32.1 (T1-T12)	Cadaver
11	M	62	No	< 10*	29.8 (T3-T12)	Cadaver
12	M	69	Yes; mild kyphosis	< 10*	53.7 (T1-T12)	Patient
13	M	74	Yes; mild scoliosis	10.6 (T1-T11)	42.3 (T1-T12)	Patient
14	M	75	No	< 10*	26.2 (T1-T12)	Cadaver
15	F	87	No	< 10*	35.4 (T3-T12)	Cadaver

*Cobb angle less than 10 degrees is not considered as scoliosis

4.2.2 Rib Cage Segmentation and Thoracic Volume Reconstruction Using CT Scan as the Gold Standard

The CT scan imaging technique is commonly used as a "gold standard" to assess the lung morphology [25], and it is also widely used in the orthopedic field to help diagnose spine deformity patients [68]. In addition, a CT scan is featured as a gold standard to evaluate the 3D reconstruction of the spine [68]. In order to generate the gold standard model for validation, I load CT scan data of the fifteen datasets to Mimics, which can semi-automatically isolate the bone structure, including vertebrae, ribs and sternum. When the pixel threshold value is set properly, Mimics will select the area that I want to segment. If some bone structure cannot be automatically isolated due to the image quality of the CT scan data, I need to manually select the region/bone of each cross section that I want to segment for my datasets. An example in Figure 4.2 (a) shows the cross section at the level of T7 and T8 vertebrae for Dataset 5, who has a severe scoliosis problem, and the cross-section location along the rib cage is also shown. The bony structure is highlighted in green, and the specific locations of the vertebrae, ribs and sternum are labeled as well. In Figure 4.2 (b), I present the rib cage segmentation results of Dataset 5. The red bones are 12 thoracic vertebrae, the green shows the 24 ribs, and the blue is the sternum. In Mimics, the semi-automatic reconstruction for the thoracic rib cage of one dataset takes approximately 8 to 10 hours depending on the quantity of the slices (transverse layers) of the CT scan data. Generally, the more cross-section slices of the CT scan images there are, the less time the reconstruction will take because the time for the manual reconstruction decreases. After the segmentation of the thoracic rib cage, I manually select the region layer by layer which belongs to the inner boundary of the rib cage. In Figure 4.3 (a), the area of the thoracic volume at a selected cross section of the rib cage is highlighted in yellow. After selecting all cross-section areas of the thoracic volume, I reconstruct the three-dimensional thoracic volume model serving as the gold standard thoracic volume model for Dataset 5, shown in Figure 4.3 (b). The mean reconstruction time of the thoracic volume for each of the fifteen datasets is about 35 minutes. In Mimics, the value of the gold standard thoracic volume is equivalent to the summation of all cross-section area slices inside the rib cage.

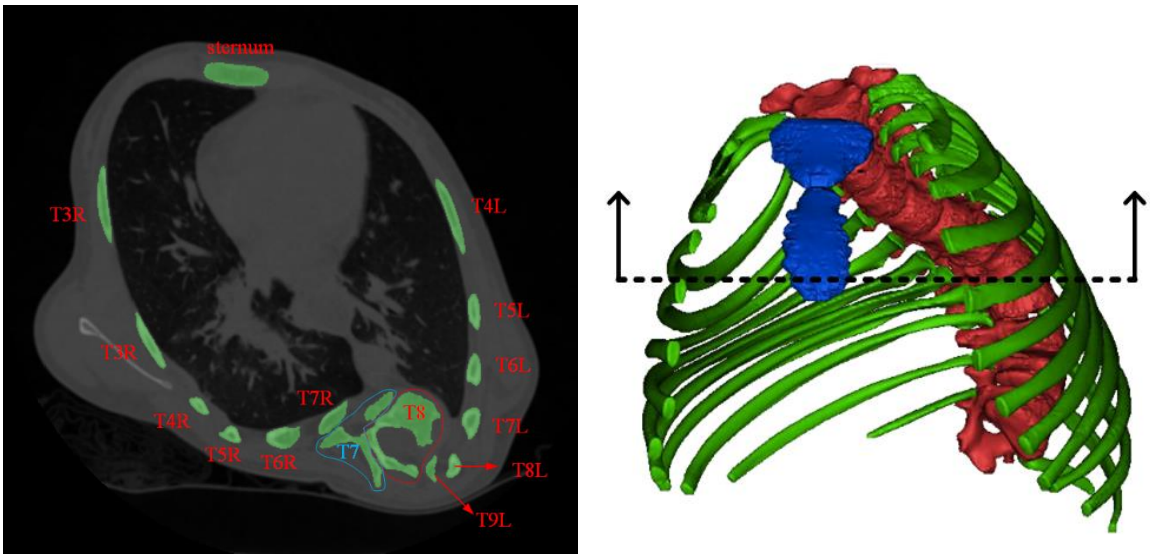

(a) Cross section of the rib cage at T7/T8 level

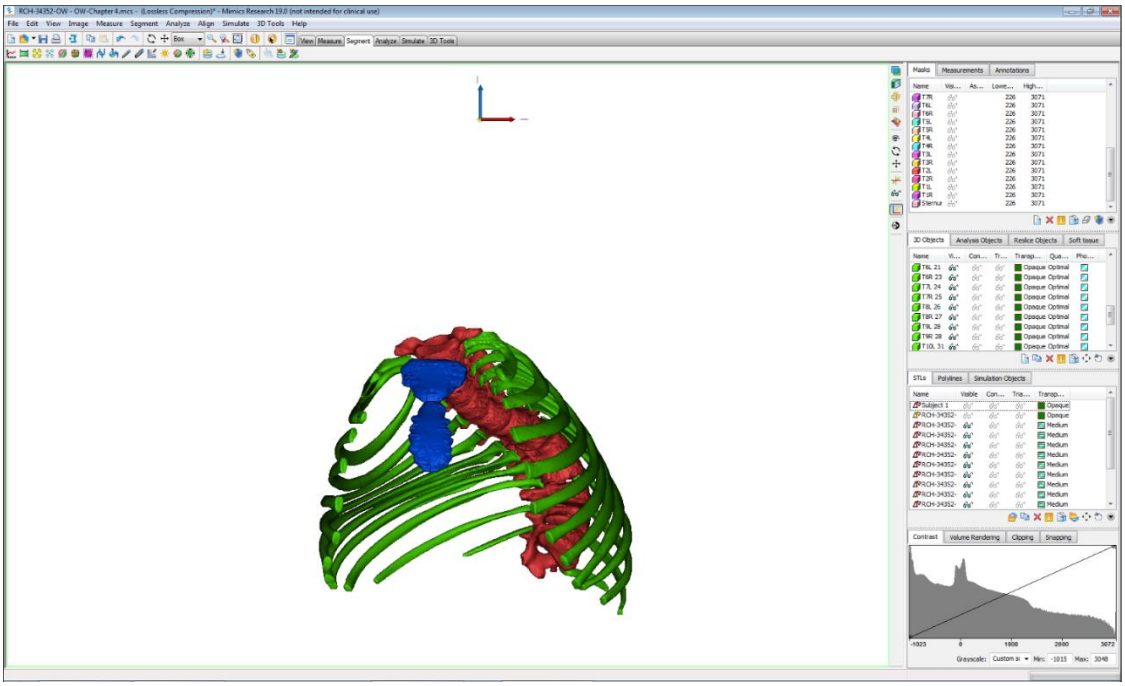

(b) Rib cage reconstruction result

Figure 4.2 Thoracic rib cage segmentation for Dataset 5 in Mimics

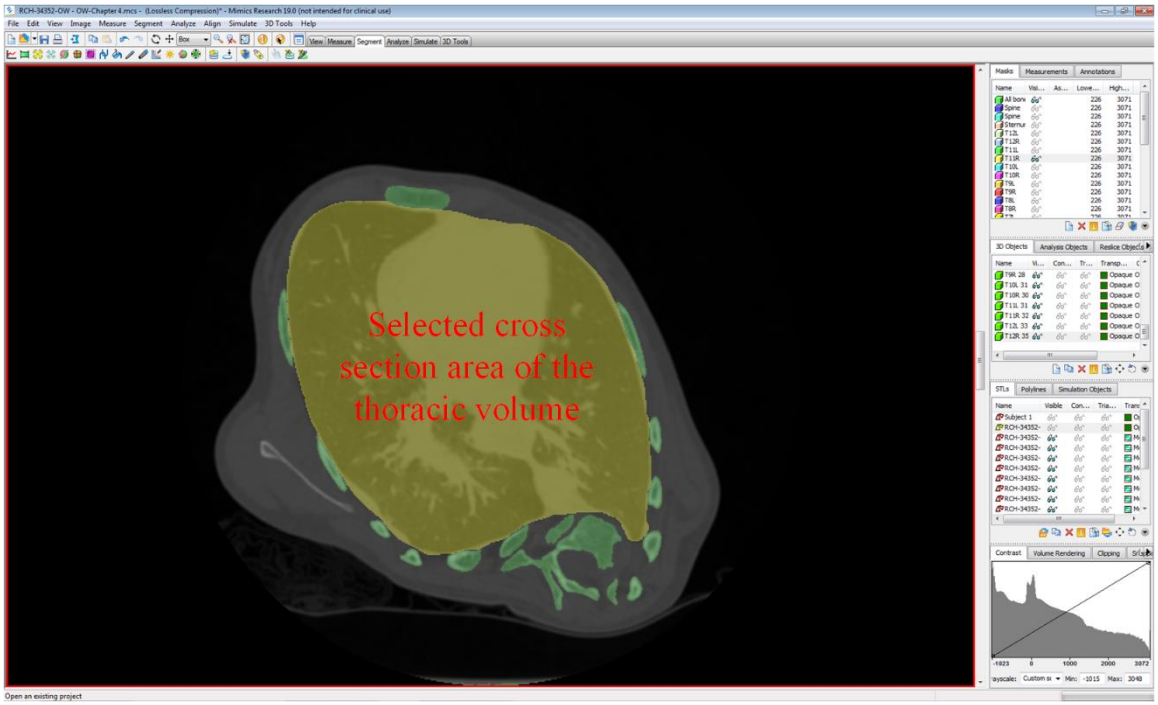

(a) Selected cross section of the thoracic volume (yellow) at T7/T8 level

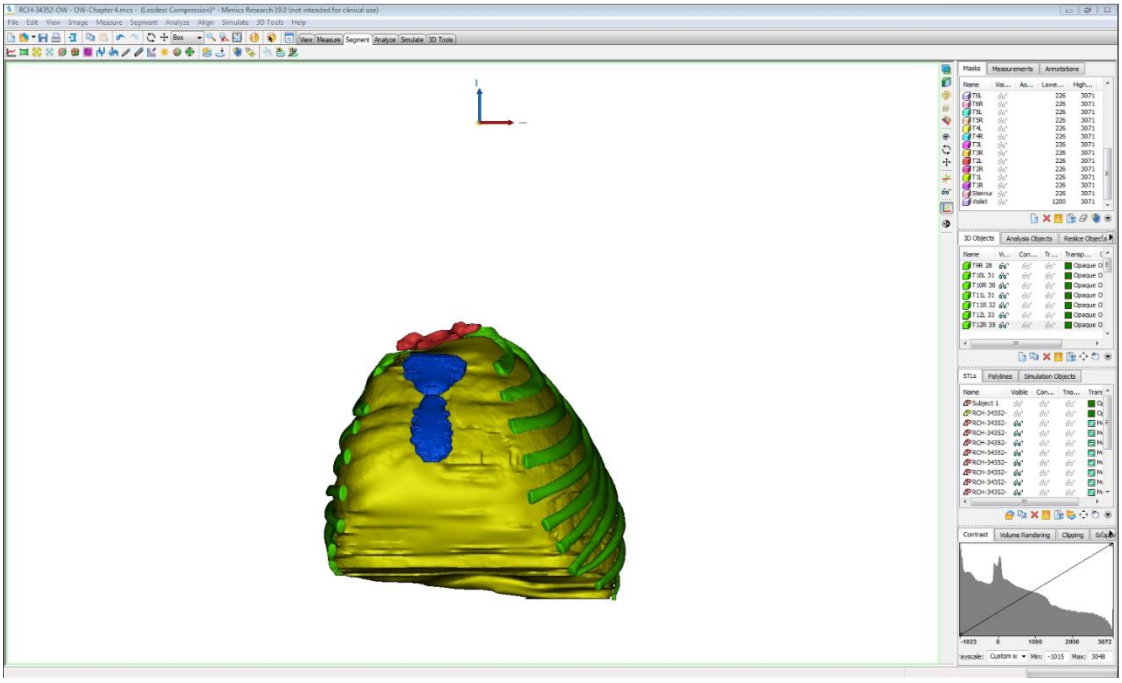

(b) Rib cage and thoracic volume (yellow) reconstruction

Figure 4.3 Thoracic volume reconstruction for Dataset 5 in Mimics

4.2.3 Training Processes for the Usability Testing

The University of Minnesota IRB determined this usability testing study was not human subject research. There were five participants, two males and three females, involved in the usability testing for the developed program. Among them, three undergraduates and one graduate student were recruited through the University of Minnesota, and one undergraduate was recruited from the University of Notre Dame. All the participants majored in the College of Science and Engineering, and none of them had a background in orthopedics or human anatomy before they were trained to use our developed program. The training processes included the following five main tasks:

1. Understand and identify the spine deformity (scoliosis) through frontal and lateral X-rays.
2. Register anatomical points for each vertebra in the graphical user interface (GUI).
3. Transfer GUI information/data to Blender software.
4. Know how to perform the basic operation in Blender software.
5. Perform rib cage and thoracic volume reconstruction with the help of the customized add-on program in Blender.

Before performing the usability testing for the thoracic volume estimator, all participants spent 10 hours per week doing the training for a duration of 6 weeks to become familiar with the anatomical structure of the rib cage viewed from biplanar X-rays, graphical user interface, and add-on package and functions of Blender. A more detailed description of the sub-tasks in the usability test and the training timeline is documented in Table 4.2. Also, Table 4.3 shows the average work time of the five participants for each dataset using the developed program, including the time for GUI operation, the rib cage reconstruction, and thoracic volume reconstruction in the Blender environment. During the usability testing, the mean operation time was 9 minutes (*SD* 2 minutes) in the GUI, 4 hours and 15 minutes (*SD* 32 minutes) for reconstructing rib cages in Blender, and 23 minutes (*SD* 6 minutes) for measuring thoracic volumes in Blender. Overall, it took each participant an average of 72 hours to finish the reconstruction of the rib cage and thoracic volume for

15 datasets, and their results were collected for further analyzing the performance of the developed thoracic volume estimator.

Table 4.2 Timeline of training processes for participants

Main Tasks	Sub-tasks	Duration
1. Read the information on frontal and lateral chest X-rays & fluoroscopy images	(a) Identify the bone structure on the fluoroscopy images (b) Diagnose scoliosis and kyphosis symptoms (c) Identify the rotation (axial, frontal, and lateral) of the vertebrae in the scoliosis patient (d) Determine the boundary of the thoracic volume	1 week
2. Learn how to operate the developed graphical user interface (GUI)	(a) Load frontal and lateral fluoroscopy images to the GUI (b) Register 2D anatomical points for each vertebra in the GUI and save points as JSON file (c) Obtain the rotation angles of the vertebrae from the GUI	1 week
3. Transfer information/data from the GUI to Blender software	(a) Reconstruct the 2D registration points from the GUI into the 3D points in Blender (b) Import frontal and lateral fluoroscopy images to Blender (c) Import the vertebrae and ribs from the stored template in Blender	0.5 week
4. Basic operation in Blender software	(a) Move/rotate/scale the bone structure (b) Deform the vertebrae to mimic the wedging vertebrae (c) Use the lattice function in Blender to adjust the morphology of the bones	2 weeks
5. Perform rib cage and thoracic volume reconstruction with the customized add-on package in Blender	(a) Manually adjust the posture for the vertebrae, ribs, and sternum (b) Select the boundary of the thoracic volume and iterate the volume inside the chest wall (c) Manually trim the volume, which is outside the thoracic volume boundary	1.5 weeks

Table 4.3 Average reconstruction time for 15 datasets

Dataset No.	Creation of JSON file by graphical user interface	Rib cage reconstruction in Blender*	Thoracic volume reconstruction using Blender add-on package*
1	14 minutes	4 hours and 55 minutes	28 minutes
2	10 minutes	4 hours and 36 minutes	30 minutes
3	11 minutes	4 hours and 48 minutes	29 minutes
4	11 minutes	4 hours and 41 minutes	27 minutes
5	14 minutes	5 hours and 7 minutes	34 minutes
6	10 minutes	3 hours and 55 minutes	24 minutes
7	8 minutes	4 hours and 44 minutes	28 minutes
8	8 minutes	4 hours and 5 minutes	20 minutes
9	7 minutes	4 hours and 19 minutes	22 minutes
10	7 minutes	3 hours and 50 minutes	18 minutes
11	8 minutes	3 hours and 37 minutes	16 minutes
12	8 minutes	4 hours and 15 minutes	19 minutes
13	7 minutes	3 hours and 24 minutes	18 minutes
14	8 minutes	3 hours and 30 minutes	17 minutes
15	9 minutes	4 hours and 5 minutes	19 minutes

*Time for rib cage and thoracic volume reconstruction, including time spent on manually calibrating the models

4.3 Accuracy and Precision of the Rib Cage Reconstruction

In this section, I study the accuracy and precision of our developed software to reconstruct the thoracic rib cage. For accuracy, I validate the thoracic rib cage reconstruction by comparing the usability test results with the gold standard CT technique. For precision, I compare the reconstruction results from each participant to investigate the reproducibility and replication. Then, I rely on the MATLAB to validate and compare the postures (positions and rotations) of each bone belonging to the rib cage structure. Also, Cloudcompare is used to validate the accuracy of the shape morphology (surface structure) of the thoracic spine, ribs and the sternum. The rib cage reconstruction results are compared to the existing methods proposed by other researchers. Finally, absolute mean errors, mean absolute maximal errors, root mean square errors, and 95% Confidence Intervals (CIs) are calculated and these statistical results are discussed.

4.3.1 Processes of Rib Cage Validation

In order to perform rib cage validation, I first export the rib cage model reconstructed by Mimics and by the five participants to the open-source CloudCompare software [69]. CloudCompare is a 3D point cloud processing software that can execute model registration, distance computation (shape morphology comparison), statistics computation, etc. Figure 4.4 demonstrates the entire processes of rib cage validation. Once all models are imported into CloudCompare, it is necessary to conduct the registration (also called alignment) for each dataset to align participants' reconstructed models with the gold standard CT model reconstructed by Mimics. The purpose of aligning the participants' models with the Mimics model is to eliminate the operation error that occurs when the participants position or scale the biplanar X-rays in Blender. Utilizing the iterative closest point algorithm [70], CloudCompare can automatically position and rotate the participants' models to align with the Mimics model for each dataset. When the alignment is completed, CloudCompare will provide a transformation matrix which is used to validate the postures (3 positions and 3 rotations) of each bony structure, including 12 vertebrae, 24 ribs, and 1 sternum in

MATLAB. The validation process in MATLAB consists of two main procedures, accuracy and precision. Generally, the measurement errors can be divided into two components, random error and systematic error. Good accuracy and precision mean low systematic error and low random error, and they are references to evaluate the performance of our software. For the accuracy of our software, I validate the rib cage reconstruction between the gold standard CT and the five participants' results. For precision, I hope to explore the reproducibility performed by our thoracic volume estimator, so I compare the results among the five participants.

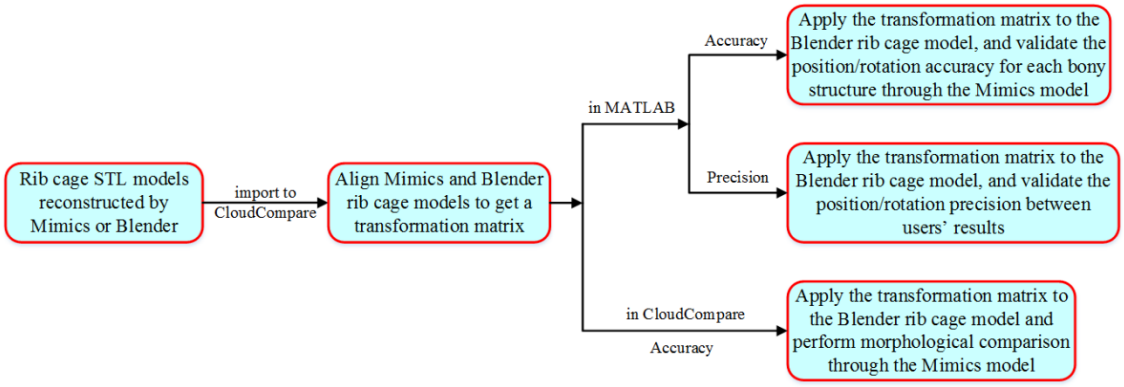

Figure 4.4 Processes of rib cage accuracy and precision validation via different software

4.3.2 Position and Rotation Validation Using MATLAB

After applying the transformation matrix mentioned in section 4.3.1 to each bone in MATLAB, I can validate the accuracy and the precision of the rib cage reconstruction. To validate the position accuracy and precision, I compute the positions and rotations for each bone (with respect to the global coordinate system), including the vertebrae, ribs and the sternum, in the gold standard Mimics models and the participant reconstruction models. It is worth mentioning that the accuracy validation aims to identify the accuracy of our software and the precision validation aims to study the reproducibility of our software.

For validating the accuracy of the positions and rotations, I calculate the geometric centroid (three positions) and the orientations (three rotations) for each bone, including 180 vertebrae, 360 ribs and 15 sternums for all the 15 datasets reconstructed by 5 participants.

In addition, I calculate the root mean square (RMS) error for the positions and the rotations of each bone for the accuracy validation, and the RMS error equation can be written as follows:

$$\text{RMS error} = \sqrt{\frac{\sum_{i=1}^{n}(\hat{y}_i - y_{i,k})^2}{n}} \tag{4.1}$$

where $\hat{y}_i$ is the *i*-th bone's geometric centroid of the gold standard model (Mimics model), y_i is the *i*-th bone's geometric centroid of the *k*-th participant's model, and *n* is the total number of bones for the accuracy validation.

For validating the precision of the positions and rotations, I compute the root mean square of the standard deviation (RMSSD) error and the 95% CI (confidence interval) for each bone. The RMSSD [71], used to describe the absolute precision errors (reproducibility), can be calculated by the following equation,

$$\text{RMSSD} = \sqrt{\frac{\sum_{i=1}^{m}\sum_{i=1}^{n_i}(X_{i,j} - \overline{X_i})^2}{\sum_{i=1}^{m}(n_i - 1)}} = \sqrt{\frac{\sum_{i=1}^{m}(n_i - 1)SD_i^2}{\sum_{i=1}^{m}(n_i - 1)}} \tag{4.2}$$

in which $X_{i,j}$ means the quantitative results (e.g., geometric centroid or rotation angles) of the *j*-th measurement for the *i*-th individual (bone), $\overline{X_i}$ means the average value (e.g., geometric centroid or rotation angles) of the bones, n_i is the total number of measurements for the *i*-th individual (bone), and *m* means a total number of bones computed for the precision validation. Here, I use thoracic vertebrae to demonstrate how to find the *i*, *j*, and *m* in Eq. (4.2). Each dataset possesses 12 thoracic vertebrae; *i* is the 180 vertebrae for 15 datasets, *j* is 5 measurements for each participant, and *m* is a total of 900 vertebrae for precision validation. Additionally, SD_i stands for the standard deviation, of the *i*-th individual (bone) and it can be expressed as,

$$SD_i = \sqrt{\sum_{j=1}^{n_i}\frac{(X_{i,j} - \overline{X_i})^2}{(n_i - 1)}} \tag{4.3}$$

When each bone has the same measurement, then Eq. (4.2) can be simplified to

$$\text{RMSSD} = \sqrt{\sum_{i=1}^{m} \frac{{SD_i}^2}{m}} \tag{4.4}$$

With Eq. (4.4), the 95% CI can be calculated as follows,

$$95\%\ \text{CI} = 2 * \text{RMSSD} = 2 * \sqrt{\sum_{i=1}^{m} \frac{{SD_i}^2}{m}} \tag{4.5}$$

To perform the validation of the rotation accuracy and precision, I first need to define the local coordinate system for each bone. For the vertebrae, previous literature discussed how to define the vertebral coordinate system by using a digitizing probe [72]. Since my study only possesses skeleton bones in Blender software, it is impossible to use a digitizing probe to detect and define the coordinate system in my case. Instead, I adjust the method from [73] so that the local bone coordinate system can be aligned with the global coordinate system in Blender. In Figure 4.5, I pick up three points, which are the two lateral-most P1 and P2, and one anterior-most P3, on the superior endplate of the vertebral body. The x axis (in green) is a normalized vector along $\overrightarrow{P_1P_2}$, and the z axis (in purple) is a normalized vector defined by the cross product of two vectors, $\overrightarrow{P_1P_3}$ and $\overrightarrow{P_1P_2}$. Finally, the y axis (in yellow) is a normalized vector by the cross product of the z axis and the x axis. Then, I can build the local coordinate system for the vertebra. Figure 4.6 shows the positive and negative rotation with respect to the vertebral coordinate system. Each bone possesses three rotation angles, in the frontal, lateral and axial directions, and I take advantage of the Tait-Bryan angles (extrinsic rotations) to deal with the three rotation angles [74]. Blender rotates the object by using the global X-Y-Z coordinate system in order, and the following rotation matrices indicate the orientations with respect to the global X, Y and Z axes,

$$R(X,\alpha) = \begin{bmatrix} 1 & 0 & 0 \\ 0 & cos(\alpha) & -sin(\alpha) \\ 0 & sin(\alpha) & cos(\alpha) \end{bmatrix} \tag{4.6}$$

$$R(Y,\beta) = \begin{bmatrix} cos(\beta) & 0 & sin(\beta) \\ 0 & 1 & 0 \\ -sin(\beta) & 0 & cos(\beta) \end{bmatrix} \tag{4.7}$$

$$R(Z,\gamma) = \begin{bmatrix} cos(\gamma) & -sin(\gamma) & 0 \\ sin(\gamma) & cos(\gamma) & 0 \\ 0 & 0 & 1 \end{bmatrix} \tag{4.8}$$

where the three α, β, and γ rotations represent the frontal, lateral, and axial angles with respect to the global X, Y, and Z axes in Blender. Then, based on the rotation order with respect to the global X-Y-Z axes (fixed frame), the overall rotation matrix becomes

$$R = R(Z,\gamma)R(Y,\beta)R(X,\alpha) =$$

$$\begin{bmatrix} cos(\gamma) & -sin(\gamma) & 0 \\ sin(\gamma) & cos(\gamma) & 0 \\ 0 & 0 & 1 \end{bmatrix} \begin{bmatrix} cos(\beta) & 0 & sin(\beta) \\ 0 & 1 & 0 \\ -sin(\beta) & 0 & cos(\beta) \end{bmatrix} \begin{bmatrix} 1 & 0 & 0 \\ 0 & cos(\alpha) & -sin(\alpha) \\ 0 & sin(\alpha) & cos(\alpha) \end{bmatrix} =$$

$$\begin{bmatrix} cos(\gamma)\,cos(\beta) & -sin(\gamma)cos(\alpha) + cos(\gamma)sin(\beta)sin(\alpha) & sin(\gamma)sin(\alpha) + cos(\gamma)sin(\beta)cos(\alpha) \\ sin(\gamma)\,cos(\beta) & cos(\gamma)cos(\alpha) + sin(\gamma)sin(\beta)sin(\alpha) & -cos(\gamma)sin(\alpha) + sin(\gamma)sin(\beta)cos(\alpha) \\ -sin(\beta) & cos(\beta)sin(\alpha) & cos(\beta)cos(\alpha) \end{bmatrix} \tag{4.9}$$

In the overall rotation matrix *R*, the three angles (α (lateral), β (frontal), and γ (axial)) can be found once the local coordinate system of each vertebra is defined by picking specific locations, P1, P2 and P3. Here, in my study, I utilize the customized MATLAB code to solve for the three rotation angles. With the three rotation angles of the vertebrae, I can compute the RMS errors to validate the accuracy and compute the RMSSD and 95% CI to validate the precision.

For the ribs, most of the previous literature did not mention how to build the coordinate system on ribs, but they employed the best-fit-plane concept instead [39,75]. In other words, I can find a best-fit plane that can best describe and pass the points constructing the rib. An equation to find a best-fit plane is described as follows,

$$z(x,y) = A \cdot x + B \cdot y + C \tag{4.10}$$

where *x*, *y* and *z* are the points on the rib, and A, B, and C are the coefficients of the plane. To solve the coefficients, Eq. (4.10) can be written in a matrix form,

$$\begin{bmatrix} x_1 & y_1 & 1 \\ x_2 & y_2 & 1 \\ & \vdots & \\ x_n & y_n & 1 \end{bmatrix} \begin{bmatrix} A \\ B \\ C \end{bmatrix} = \begin{bmatrix} -z_1 \\ -z_2 \\ \vdots \\ -z_n \end{bmatrix} \tag{4.11}$$

Then, I transpose the *n* by 3 matrix in Eq. (4.11) and multiply both sides by Eq. (4.11) to perform the linear least squares.

$$\begin{bmatrix} x_1 & x_2 \cdots & x_n \\ y_1 & y_2 \cdots & y_n \\ 1 & 1 \cdots & 1 \end{bmatrix} \begin{bmatrix} x_1 & y_1 & 1 \\ x_2 & y_2 & 1 \\ & \vdots & \\ x_n & y_n & 1 \end{bmatrix} \begin{bmatrix} A \\ B \\ C \end{bmatrix} = \begin{bmatrix} x_1 & x_2 \cdots & x_n \\ y_1 & y_2 \cdots & y_n \\ 1 & 1 \cdots & 1 \end{bmatrix} \begin{bmatrix} -z_1 \\ -z_2 \\ \vdots \\ -z_n \end{bmatrix} \tag{4.12}$$

After multiplying and rearranging Eq. (4.12), I obtain the following equation to solve three coefficients (*A*, *B* and *C*),

$$\begin{bmatrix} A \\ B \\ C \end{bmatrix} = \begin{bmatrix} \sum_{i=1}^{n} x_i^2 & \sum_{i=1}^{n} x_i y_i & \sum_{i=1}^{n} x_i \\ \sum_{i=1}^{n} x_i y_i & \sum_{i=1}^{n} y_i^2 & \sum_{i=1}^{n} y_i \\ \sum_{i=1}^{n} x_i & \sum_{i=1}^{n} y_i & \sum_{i=1}^{n} 1 \end{bmatrix}^{-1} \begin{bmatrix} \sum_{i=1}^{n} x_i z_i \\ \sum_{i=1}^{n} y_i z_i \\ \sum_{i=1}^{n} z_i \end{bmatrix} \tag{4.13}$$

The tilting angles, i.e., frontal and lateral angles, of the best-fit plane can be derived by the following equations,

$$\text{Frontal angle (rotation w.r.t. y axis in Figure 4.6)} = atan\left[\frac{-dz(x,y)}{dx}\right] = atan[-A] \tag{4.14}$$

$$\text{Lateral angle (rotation w.r.t. x axis in Figure 4.6)} = atan\left[\frac{dz(x,y)}{dy}\right] = atan[B] \tag{4.15}$$

With Eqs. (4.14) and (4.15), Figures 4.7 (a) and (b) display an example of the frontal and lateral angles from a selected right T1 rib in MATLAB software. It is noted that the axial rotation of the rib cannot be defined by the best-fit plane. Instead, it is defined by the most protruded/posterior points on the same level of ribs. As shown in Figure 4.8, the most

protruded points A and B on the left and right sides of the T1 ribs are connected, and the tilting angle of the connecting line is called the rib hump. The anatomy of each dataset has 12 pairs of ribs, and this implies that each dataset only has 12 rib hump angles. Similar to the vertebrae, I use Eq. (4.1) to calculate the RMS errors of the three rotation angles for accuracy validation, and use Eqs. (4.4) and (4.5) to calculate the RMSSD and 95% CI for precision validation.

For the sternum, less literature discussed how to construct the local coordinate system or mentioned any method to validate its accuracy of the position and the rotation. Hence, I employ a similar concept that I use to define the local coordinate system for the vertebra and apply it to the sternum. Figure 4.9 demonstrates how to define the three points, P1, P2 and P3 on the sternum, where P1 and P2 are located separately on the left and right sides of the second costal notch and P3 is located at the xiphisternal junction. After that, I use Eq. (4.9) to calculate three rotation angles for the sternum, which is similar to the procedures of the vertebrae. For accuracy and precision validation, I compute the RMS error, RMSSD, and 95% CI for the positions and rotations of the sternum. In the next section, I will present detailed results for one dataset and summarize its statistical values for the accuracy (RMS errors) and precision (RMSSD and 95% CI) validation of each bone's positions and orientations.

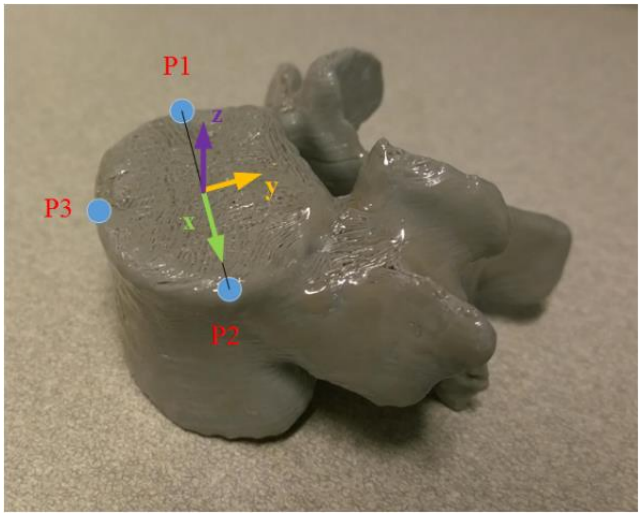

Figure 4.5 Demonstration of the vertebral local coordinate system on the vertebra

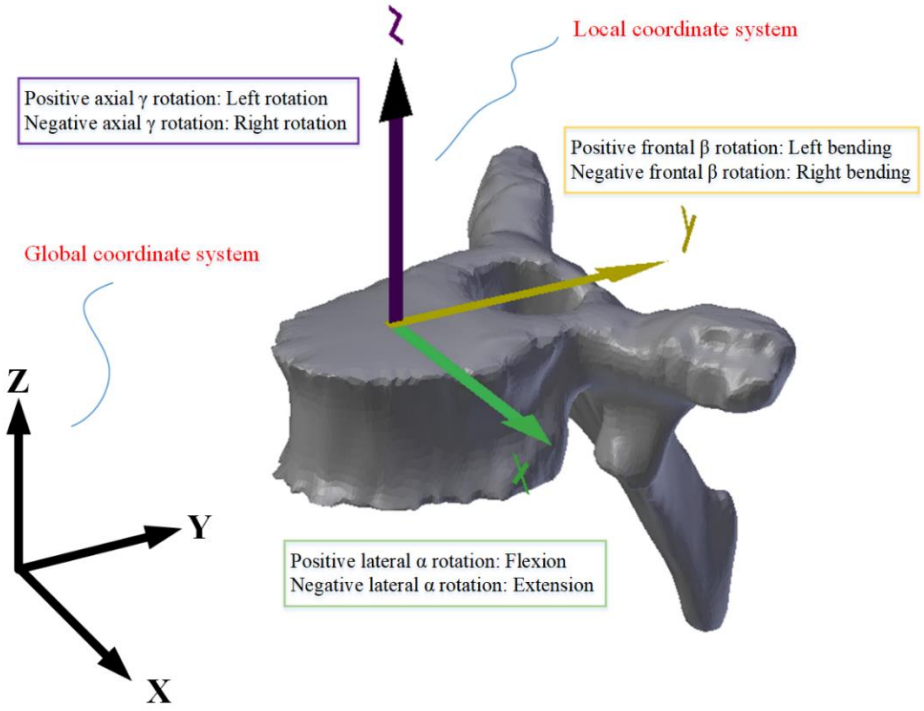

Figure 4.6 Demonstration of the frontal (bending), lateral (flexion or extension) and axial rotation of the vertebra with respect to the global coordinate system in the Blender environment

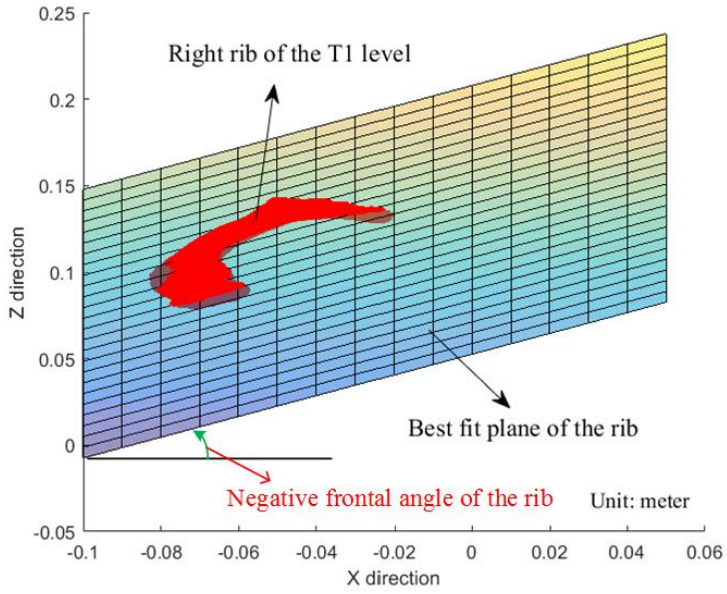

(a) Frontal view

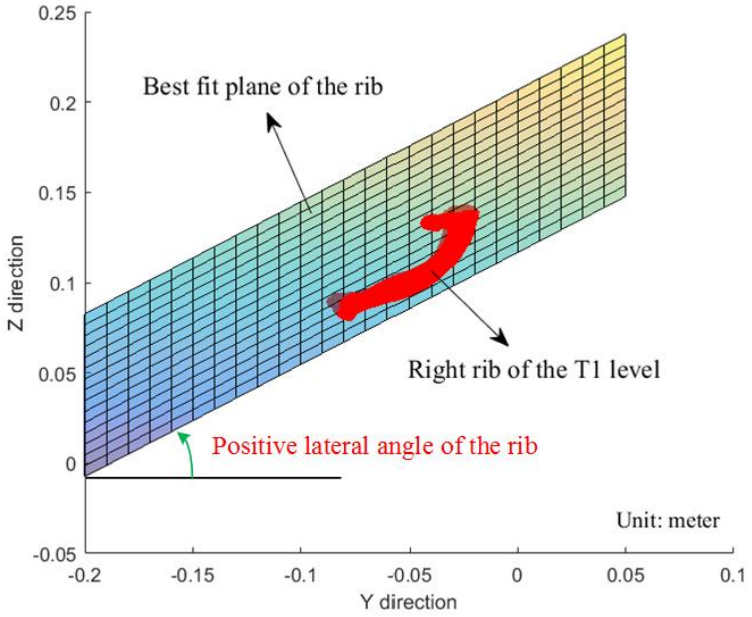

(b) Lateral view

Figure 4.7 Demonstration of the best fit plane and the rib rotation angles in MATLAB

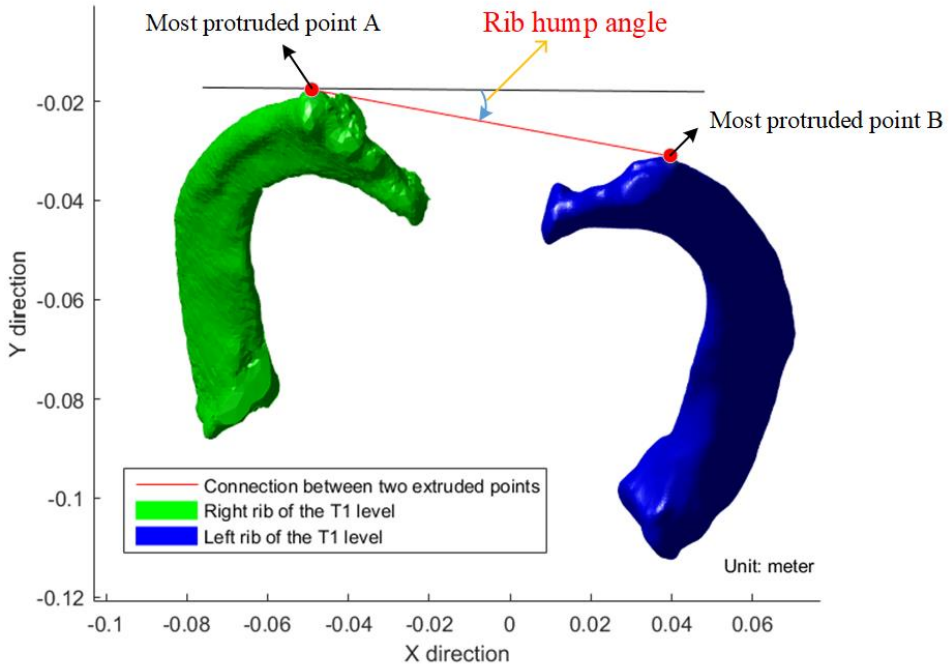

Figure 4.8 Demonstration of the rib hump angle at T1 ribs in a scoliosis patient in MATLAB

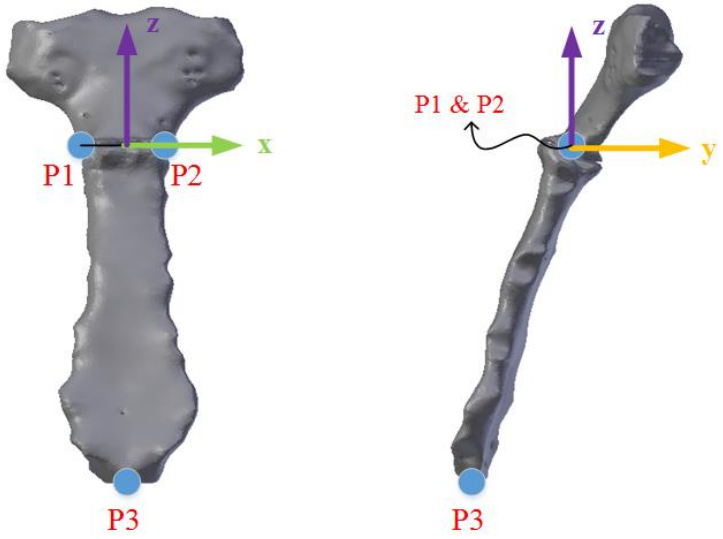

(a) Frontal view (b) Lateral view

Figure 4.9 Demonstration of the local coordinate system on the sternum for rotation validation

4.3.3 Results of Rib Cage Validation Using MATLAB

In this section, I mainly present the statistical results for each bone segment (vertebrae, ribs and sternum), and the interpretation of the results will be given in the discussion section. Herein, I only highlight Dataset 5 (who has the most severe spine deformity) in detail to illustrate the posture accuracy between the gold standard and my software, and the posture precision (reproducibility) among the five participants. Tables 4.4 through 4.9 display the postures (three positions and three rotations) of the vertebrae, ribs and the sternum separately for Dataset 5, which are reconstructed by the gold standard CT method and reconstructed by our software operated by the five participants. The raw data from Tables 4.4 through 4.9 can be further presented as statistical results for Dataset 5 in the following paragraphs.

For the rib cage reconstruction accuracy of Dataset 5, the RMS errors (computed by Eq. (4.1)) of the positions of the vertebrae in the X, Y and Z directions are 1.01, 2.00, and 0.86 mm respectively and the 3D RMS error is 2.40 mm. The RMS errors of the rotations

of the vertebrae in the frontal, lateral, and axial directions are 2.30, 2.42, and 2.06 degrees respectively. For the ribs, the RMS errors are 2.89, 4.09, and 2.97 mm in the X, Y, Z directions for the positions, and the 3D RMS error is 5.81 mm. The RMS errors are 1.93, 2.25, 1.97 degrees in the frontal, lateral, and rib-hump rotations for the ribs. For the sternum, the RMS errors are 0.58, 2.70, and 2.73 mm in the X, Y, and Z directions, and the 3D RMS error is 3.89 mm; the RMS errors are 1.62, 0.61, and 1.77 degrees in the frontal, lateral, and axial rotations. For the reconstruction precision of Dataset 5, the 95% CIs (which is 2 times RMSSD error as proposed in Eq. (4.5)) of the vertebrae are 0.73, 1.24, and 0.72 mm in the X, Y, and Z directions, and 2.22, 2.28, and 3.01 degrees in the frontal, lateral and axial rotations. The 95% CIs of the ribs are 3.76, 4.78, and 2.99 mm in the X, Y and Z directions with a 3D RMSSD error of 3.37 mm, and 2.17, 2.25, and 2.09 degrees in the frontal, lateral, and rib-hump rotations. The 95% CIs of the sternum are 1.26, 0.65, and 0.88 mm in the X, Y and Z directions with a 3D RMSSD error of 0.83 mm, and 1.50, 1.11, and 3.92 degrees in the frontal, lateral, and axial rotations.

For the reconstruction accuracy (comparison between the gold standard and the five participants) of the 15 datasets performed by the five participants, the RMS errors of the specific bone segments are listed in Table 4.10. The 3D RMS error of the position is 2.29 mm for the vertebrae, 4.47 mm for the ribs, and 3.53 mm for the sternums. As can be seen from the above results, the position accuracy of the vertebrae is better than that of the ribs and the sternums. However, the rotational accuracy of the sternum is better than those of the vertebrae and the ribs.

For the reconstruction precision (comparison among the five participants) of the 15 datasets, the RMSSD errors of the specific bone segments are listed in Table 4.11. The 3D RMSSD error of the position is 1.21 mm for the vertebrae, 2.81 mm for the ribs, and 1.03 mm for the sternums. These results disclose that the reconstruction precision in the vertebrae is better than that in the ribs but is slightly inferior to that in the sternum for the positions and rotations.

Table 4.4 Positions of twelve vertebrae in Dataset 5

Unit: mm	Mimics			Participant 1			Participant 2		
Level	X	Y	Z	X	Y	Z	X	Y	Z
T1	-29.9	34.9	66.7	-29.3	36.2	65.8	-28.6	36.5	65.9
T2	-25.7	42.6	56.8	-23.8	43.5	56.5	-24.8	43.9	55.4
T3	-20.0	51.9	46.8	-19.2	54.4	46.9	-19.4	55.8	47.1
T4	-11.7	61.9	38.6	-11.9	64.5	38.8	-12.1	64.4	38.5
T5	-1.5	70.1	30.9	-1.9	73.6	31.8	-2.5	72.6	31.1
T6	9.9	77.7	23.7	9.3	81.2	22.9	8.8	79.7	23.4
T7	20.6	84.6	15.9	20.6	88.3	15.6	19.6	86.7	15.8
T8	30.7	89.9	6.3	29.7	92.1	4.5	29.0	92.4	5.1
T9	37.4	93.1	-6.7	35.9	93.5	-7.9	36.2	93.9	-8.3
T10	41.5	92.6	-22.4	40.9	92.9	-23.5	40.1	93.2	-23.2
T11	41.5	86.7	-38.4	40.4	87.6	-39.6	40.7	86.7	-38.9
T12	36.6	76.1	-52.6	35.9	76.7	-52.2	35.7	75.9	-52.3
Unit: mm	Participant 3			Participant 4			Participant 5		
Level	X	Y	Z	X	Y	Z	X	Y	Z
T1	-28.5	36.5	65.9	-29.3	36.0	65.8	-28.4	35.5	66.4
T2	-24.7	43.9	55.3	-23.8	43.8	56.7	-24.8	43.6	55.0
T3	-19.4	55.7	47.1	-19.2	54.4	46.9	-19.5	54.6	47.6
T4	-12.1	64.4	38.4	-11.9	64.5	38.8	-12.1	64.6	38.9
T5	-2.5	72.6	31.2	-2.0	73.7	31.8	-2.3	72.5	30.7
T6	8.8	79.7	23.4	9.2	81.2	22.9	9.1	79.5	23.4
T7	19.6	86.6	15.8	20.6	88.3	15.6	20.0	85.6	16.0
T8	28.9	92.3	5.0	29.7	92.1	4.5	30.0	91.0	5.2
T9	36.1	93.9	-8.3	35.9	93.5	-8.0	36.8	93.2	-7.5
T10	40.1	93.1	-23.2	40.9	92.9	-23.5	40.9	92.6	-22.9
T11	40.7	86.7	-39.0	40.4	87.6	-39.6	39.8	85.7	-38.8
T12	35.6	75.9	-52.4	35.8	76.7	-52.3	35.6	75.4	-52.3

Table 4.5 Rotations of twelve vertebrae in Dataset 5

Unit: deg	Mimics			Participant 1			Participant 2		
Level	Frontal	Lateral	Axial	Frontal	Lateral	Axial	Frontal	Lateral	Axial
T1	-14.0	41.7	-13.7	-14.2	43.3	-12.8	-15.9	44.4	-10.7
T2	-18.5	29.2	-7.0	-20.1	31.0	-7.3	-21.3	31.8	-8.2
T3	-25.2	36.6	-9.3	-26.0	39.4	-6.9	-27.8	39.5	-5.8
T4	-38.6	41.2	-12.1	-39.7	40.2	-10.4	-40.2	37.5	-12.6
T5	-47.5	41.6	-13.6	-48.9	38.0	-11.1	-48.3	38.1	-12.9
T6	-59.6	24.5	2.1	-57.4	20.6	5.4	-59.4	20.6	4.9
T7	-58.2	-4.5	34.1	-54.9	-5.6	36.5	-55.6	-5.7	31.9
T8	-43.4	-9.5	48.9	-37.5	-12.4	50.4	-39.7	-9.2	48.2
T9	-25.0	-17.0	59.9	-21.5	-14.5	58.6	-21.6	-13.7	56.3
T10	-5.5	-16.9	57.9	-2.6	-15.0	58.0	-3.3	-13.8	59.7
T11	16.2	-8.7	49.2	18.7	-7.5	51.7	19.2	-9.5	49.8
T12	35.7	-14.3	45.0	33.7	-16.3	44.6	34.5	-14.4	45.1
Unit: deg	Participant 3			Participant 4			Participant 5		
Level	Frontal	Lateral	Axial	Frontal	Lateral	Axial	Frontal	Lateral	Axial
T1	-12.7	41.1	-12.2	-13.1	42.7	-8.4	-13.2	41.5	-11.4
T2	-19.2	32.6	-6.8	-18.4	32.4	-8.6	-18.6	31.2	-7.4
T3	-25.1	37.9	-5.8	-27.2	37.2	-6.9	-25.7	37.0	-7.3
T4	-40.2	37.4	-10.0	-39.3	37.8	-11.7	-39.1	38.5	-11.2
T5	-46.0	40.1	-14.5	-49.5	38.7	-12.6	-47.3	39.9	-13.5
T6	-57.5	21.5	2.8	-59.7	19.6	6.9	-58.5	21.7	3.9
T7	-57.6	-4.0	37.4	-57.3	-6.9	36.0	-57.3	-5.1	35.6
T8	-38.9	-11.1	48.1	-42.0	-13.3	51.9	-41.2	-11.2	49.3
T9	-22.4	-14.2	61.1	-21.8	-17.1	61.0	-22.9	-16.0	60.3
T10	-1.0	-12.3	61.6	-2.6	-14.2	58.0	-3.0	-14.4	58.8
T11	20.7	-6.5	47.1	20.6	-6.9	48.9	19.1	-7.3	48.1
T12	35.5	-13.5	47.2	34.1	-15.2	47.5	34.9	-14.2	46.2

Table 4.6 Positions of twenty-four ribs in Dataset 5

Unit: mm	Mimics			Participant 1			Participant 2		
Level	X	Y	Z	X	Y	Z	X	Y	Z
T1L/T1R	4.8/-64.8	16.6/26.3	61.8/49.5	6.5/-66.4	15.0/24.4	60.3/48.4	6.3/-65.8	15.8/24.6	60.6/48.8
T2L/T2R	15.9/-68.5	18.3/25.7	51.7/38.0	17.3/-68.5	19.3/28.9	51.3/38.9	17.0/-67.7	19.9/28.5	51.7/39.6
T3L/T3R	25.3/-67.8	21.6/31.4	37.3/17.2	27.9/-70.0	22.4/29.3	36.5/14.9	27.6/-69.2	23.0/30.3	36.9/15.9
T4L/T4R	34.4/-65.1	27.1/37.3	24.6/2.3	36.6/-67.5	23.8/33.9	22.1/0.5	36.3/-66.1	24.5/36.0	22.6/1.7
T5L/T5R	41.9/-60.6	29.9/45.7	11.3/-6.9	43.4/-64.9	28.2/39.8	9.9/-9.3	43.3/-64.1	29.9/42.0	11.1/-8.6
T6L/T6R	49.7/-60.6	32.8/42.7	-2.2/-17.6	48.9/-61.6	35.8/42.2	-0.1/-18.0	48.3/-58.0	39.0/47.1	2.1/-15.5
T7L/T7R	56.7/-58.1	37.3/46.8	-13.4/-24.8	54.3/-54.4	43.4/49.3	-8.9/-23.1	53.7/-53.2	45.8/52.0	-7.2/-21.7
T8L/T8R	63.5/-51.6	43.8/52.6	-25.0/-28.9	60.0/-49.5	50.7/52.4	-19.7/-28.9	59.4/-50.1	53.4/51.8	-17.6/-29.2
T9L/T9R	68.0/-45.5	55.7/59.2	-34.1/-33.0	65.2/-39.7	55.8/60.4	-32.5/-31.0	64.9/-38.6	56.5/61.4	-32.3/-30.1
T10L/T10R	71.1/-35.7	61.1/66.5	-50.0/-38.2	67.2/-32.1	70.2/66.5	-42.9/-37.2	66.8/-38.5	74.1/64.4	-41.4/-40.1
T11L/T11R	69.5/-20.4	69.1/72.8	-62.9/-45.8	65.9/-20.2	78.2/72.1	-57.7/-46.0	65.1/-20.0	79.8/72.8	-56.6/-45.6
T12L/T12R	56.1/6.6	80.3/74.3	-69.2/-47.3	55.0/8.5	81.5/74.0	-68.7/-46.6	55.2/7.9	81.9/74.0	-68.3/-46.9
Unit: mm	Participant 3			Participant 4			Participant 5		
Level	X	Y	Z	X	Y	Z	X	Y	Z
T1L/T1R	6.2/-65.9	15.7/24.6	60.5/48.8	6.9/-66.7	13.7/24.1	59.5/48.0	6.5/-67.1	14.8/24.2	60.4/48.1
T2L/T2R	17.0/-67.8	19.9/28.4	51.7/39.6	17.7/-68.8	19.2/29.5	50.8/38.4	17.4/-69.8	18.2/29.0	51.0/38.0
T3L/T3R	27.7/-69.1	22.9/30.3	36.8/15.9	27.5/-70.6	22.5/27.4	36.5/14.0	28.5/-71.0	21.2/28.9	35.8/13.7
T4L/T4R	36.3/-65.9	24.5/36.0	22.6/1.7	36.4/-69.2	22.0/30.3	21.0/-0.9	37.3/-68.8	24.3/33.5	22.2/-0.3
T5L/T5R	43.3/-64.0	29.9/42.0	11.0/-8.7	43.5/-67.3	24.7/34.6	7.9/-11.1	43.7/-64.2	28.2/40.9	9.6/-8.6
T6L/T6R	48.5/-58.1	39.0/47.1	2.2/-15.5	48.5/-63.3	30.7/37.9	-3.2/-20.1	50.2/-67.0	34.6/36.7	-1.6/-21.0
T7L/T7R	53.7/-53.0	45.8/52.0	-7.1/-21.8	54.5/-57.0	39.1/45.5	-11.4/-25.4	55.4/-54.3	42.7/47.6	-10.1/-23.6
T8L/T8R	59.4/-49.9	53.6/51.7	-17.8/-29.2	59.9/-49.1	44.7/51.7	-23.5/-29.4	61.3/-49.0	51.1/54.5	-19.8/-27.8
T9L/T9R	64.8/-38.7	56.5/61.6	-32.2/-30.0	65.7/-41.5	54.0/56.8	-33.4/-33.4	65.3/-39.8	56.2/61.7	-32.1/-30.4
T10L/T10R	66.8/-38.4	74.1/64.4	-41.4/-40.1	67.631.3	70.2/65.2	-43.7/-38.0	67.8/-20.1	62.3/72.0	-45.2/-30.6
T11L/T11R	65.2/-20.0	79.9/72.7	-56.6/-45.6	67.7/-20.3	73.5/71.0	-60.2/-46.5	65.7/-20.3	79.4/71.7	-57.5/-46.1
T12L/T12R	54.4/7.9	81.7/74.0	-68.6/-46.8	55.0/8.7	81.1/74.0	-68.8/-46.5	55.6/9.4	81.1/73.9	-69.2/-46.2

Table 4.7 Rotations of twenty-four ribs in Dataset 5

Unit: deg	Mimics			Participant 1			Participant 2		
Level	Frontal	Lateral	Rib-hump	Frontal	Lateral	Rib-hump	Frontal	Lateral	Rib-hump
T1L/T1R	16.5/-33.6	28.1/4.1	-10.8	19.1/-36.1	27.5/3.5	-10.7	19.5/-36.8	27.5/3.9	-10.8
T2L/T2R	20.0/-34.9	23.6/10.3	-5.0	19.2/-34.8	23.7/11.1	-4.9	18.8/-33.8	23.8/11.8	-5.0
T3L/T3R	22.4/-49.6	21.4/-15.5	-7.7	23.0/-48.5	21.6/-14.4	-7.8	23.4/-48.6	21.8/-14.5	-7.7
T4L/T4R	22.5/-46.8	23.7/-15.7	-9.3	22.0/-46.3	23.9/-15.0	-9.6	22.0/-46.3	24.1/-15.3	-9.4
T5L/T5R	23.0/-34.4	26.6/-3.3	-9.3	22.8/-33.8	26.8/-3.0	-10.0	22.9/-33.7	26.6/-3.0	-10.7
T6L/T6R	26.0/-24.6	28.2/5.8	-3.9	25.4/-24.0	28.5/6.5	-4.2	25.3/-24.9	28.2/5.7	-4.0
T7L/T7R	24.4/-18.5	29.1/11.9	3.7	25.2/-18.4	29.3/12.5	3.1	25.7/-19.5	29.1/11.2	3.2
T8L/T8R	18.9/-15.2	29.0/18.5	15.7	23.3/-14.7	29.4/19.6	14.0	23.8/-13.8	29.4/20.2	14.8
T9L/T9R	20.3/-14.2	26.3/23.9	25.1	25.7/-14.1	27.6/24.6	21.5	24.1/-13.9	27.6/24.8	24.4
T10L/T10R	25.2/-14.4	24.4/31.4	23.9	27.4/-15.0	24.0/30.8	26.2	27.7/-14.9	23.9/31.0	26.3
T11L/T11R	17.2/-16.1	26.2/28.4	23.2	18.2/-16.6	24.8/28.3	24.2	17.0/-16.5	26.1/28.1	26.2
T12L/T12R	-3.1/-22.8	27.9/9.5	23.4	-1.1/-23.3	18.6/10.0	19.8	3.9/-22.8	18.1/9.0	21.3
Unit: deg	Participant 3			Participant 4			Participant 5		
Level	Frontal	Lateral	Rib-hump	Frontal	Lateral	Rib-hump	Frontal	Lateral	Rib-hump
T1L/T1R	19.4/-36	27.6/4.0	-10.7	18.1/-35.1	27.3/2.8	-10.7	19.5/-36.5	27.7/3.5	-10.6
T2L/T2R	18.1/-33.1	24.0/12.3	-5.1	20.0/-36.2	23.6/10.1	-4.9	19.8/-36.2	23.6/10.4	-4.9
T3L/T3R	23.0/-48.6	21.8/-14.4	-7.8	22.7/-48.1	21.6/-13.9	-6.9	23.1/-48.9	21.3/-14.9	-8.7
T4L/T4R	22.2/-47.0	24.0/-15.8	-9.4	21.5/-44.6	23.7/-13.4	-8.6	22.6/-47.6	23.9/-15.7	-11.1
T5L/T5R	23.2/-33.7	26.7/-3.1	-10.9	21.8/-33.5	27.1/-2.5	-9.8	23.1/-34.1	26.8/-3.5	-8.6
T6L/T6R	25.4/-24.9	28.2/5.8	-4.5	24.7/-23.1	29.1/7.8	-4.1	26.2/-23.1	28.4/6.8	-4.1
T7L/T7R	25.3/-19.0	29.1/11.7	2.9	25.0/-17.5	29.8/14.0	3.7	24.7/-17.7	29.1/12.9	2.7
T8L/T8R	24.4/-13.8	29.4/20.1	13.5	20.7/-15.3	30.1/19.9	13.4	24.4/-15.9	28.8/18.2	14.3
T9L/T9R	24.4/-14.1	27.8/24.5	21.5	25.6/-14.1	28.0/25.1	20.8	28.6/-14.3	26.8/24.1	19.4
T10L/T10R	25.8/-14.9	23.8/30.9	25.9	29.7/-15.0	24.6/30.5	27.9	26.6/-15.4	23.8/30.9	24.6
T11L/T11R	17.9/-16.6	25.6/28.0	26.1	19.1/-17.5	26.4/26.9	22.6	19.1/-15.8	21.2/30.1	21.9
T12L/T12R	-5.0/-22.9	19.2/6.8	20.6	-0.4/-23.2	14.3/9.0	19.5	-2.8/-24.3	22.7/15.1	17.6

Table 4.8 Positions of the sternum in Dataset 5

Unit: mm	Mimics			Participant 1			Participant 2		
Level	X	Y	Z	X	Y	Z	X	Y	Z
Sternum	-34.0	-36.0	30.9	-34.3	-33.6	33.2	-33.0	-33.2	33.5
Unit: mm	Participant 3			Participant 4			Participant 5		
Level	X	Y	Z	X	Y	Z	X	Y	Z
Sternum	-33.8	-33.3	33.9	-34.7	-33.6	33.2	-33.7	-32.8	34.2

Table 4.9 Rotations of the sternum in Dataset 5

Unit: deg	Mimics			Participant 1			Participant 2		
Level	Frontal	Lateral	Axial	Frontal	Lateral	Axial	Frontal	Lateral	Axial
Sternum	-0.1	-37.1	-3.2	-0.9	-37.0	-5.8	-2.8	-37.4	-3.9
Unit: deg	Participant 3			Participant 4			Participant 5		
Level	Frontal	Lateral	Axial	Frontal	Lateral	Axial	Frontal	Lateral	Axial
Sternum	-1.5	-37.5	-2.5	-1.0	-38.4	-1.5	-1.5	-37.0	-0.9

Table 4.10 Accuracy of the specific bone portions of 15 datasets reconstructed by five participants

Bone Accuracy (RMS)	Position X (mm)	Position Y (mm)	Position Z (mm)	Frontal angle (deg)	Lateral angle (deg)	Axial angle (deg)	Rib-hump angle (deg)
Vertebrae	1.09	1.51	1.34	1.83	1.95	2.28	NA
Ribs	2.11	3.24	2.25	1.82	2.03	NA	1.72
Sternums	0.83	2.34	2.51	1.79	1.35	2.01	NA

Table 4.11 Precision of the specific bone portions of 15 datasets reconstructed by five participants

Bone Precision (RMSSD)	Position X (mm)	Position Y (mm)	Position Z (mm)	Frontal angle (deg)	Lateral angle (deg)	Axial angle (deg)	Rib-hump angle (deg)
Vertebrae	0.58	0.84	0.66	1.22	1.29	1.81	NA
Ribs	1.48	1.82	1.56	1.37	1.46	NA	1.20
Sternums	0.68	0.47	0.63	0.91	0.72	1.8	NA

4.3.4 Shape Morphology Validation Using CloudCompare

In this section, I involve the point-cloud software, CloudCompare [69], to validate the accuracy of the shape morphology between the gold standard CT rib cage models and the participants' rib cage models. In CloudCompare, there are two common methods to compare the shape morphology of two objects; one is the cloud to cloud (C2C) distance and the other is the cloud to mesh (C2M) distance. For C2C distance, the program computes absolute distance errors between two objects (which are transformed as two point cloud sets in CloudCompare software), so each error will be presented in a positive value. For C2M distance, the program computes the signed distance between the mesh object and the point cloud set. The Mimics rib cage model, which serves as the gold standard model, will be treated as a mesh object. Each participant's rib cage model needs to be transformed to be the point cloud set by using the function (called sample points on a mesh) in CloudCompare. Figure 4.10 shows the comparison results of C2C and C2M. The reason to perform the shape morphology comparison is that the accuracy of the shape morphology could influence the accuracy of thoracic volume reconstruction, since I reconstruct the thoracic volume based on the inner surface of the rib cage boundary. Figure 4.10 (a) shows an example of using the C2C method to compare the absolute distance error for the rib cage. The right side of the scalar field roughly shows the distribution of each distance error in the point cloud set. The color here implies there are lower errors in the blue-green region and higher errors in the yellow-red region, and most of the distance errors in this figure are

located in the blue-green region. In Figure 4.10 (b), the maximal signed distance value is -6.415mm, which means the point possessing the maximal error is located inside the gold standard model if I align the model with the Mimics model. After comparing Figure 4.10 (a) to Figure 4.10 (b), I can clearly understand whether the shape of the participant's model falls inside or outside the mesh object (Mimics model) through the C2M method instead of the C2C method. However, the mean provided by the C2M method is the signed mean, not the absolute mean, because the positive and negative distance errors offset each other. That is, the mean value computed by the C2M will be less than that of the C2C method, which offers the absolute mean. Therefore, I decide to utilize the C2C method to get the absolute mean error and the RMS error, whereas the C2M method is used to derive the mean absolute maximal errors for the participants' rib cage models. The validation includes the bone segments, i.e., whole thoracic rib cage, 12 thoracic vertebrae, 12 pairs of ribs, and the sternum. As mentioned in section 4.3.1, each participant's model needs to be aligned with the gold standard Mimics model. Before applying the C2C or C2M method, I transform the whole thoracic rib cage into a 10-million point cloud set, 12 thoracic vertebrae into a 5-million point cloud set, 12 pairs of ribs into a 5-million point cloud set, and the sternum into a 1-million point cloud set.

Once the C2C and C2M comparisons are completed, CloudCompare can provide us with the results of the distance errors, such as the signed maximal error, absolute mean error, and the RMS error. In the next section, I will demonstrate the shape morphology of one case in detail via CloudCompare and summarize the results for different bone segments in all of the 15 datasets reconstructed by the five participants.

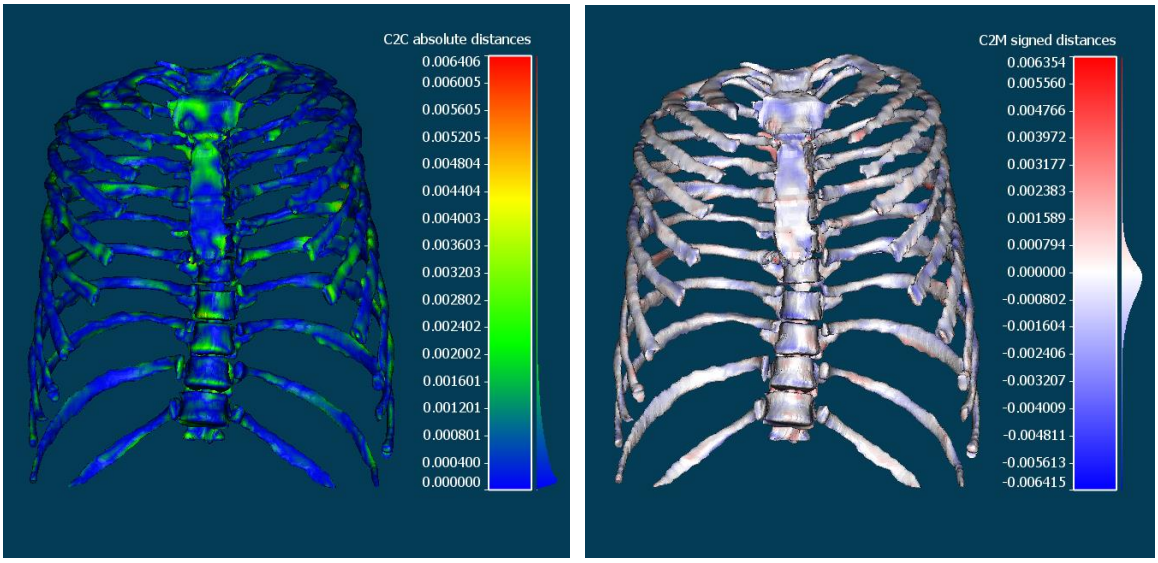

(a) Cloud (participant's model) to cloud (gold standard model) distances

(b) Cloud (participant's model) to mesh (gold standard model) distances

Figure 4.10 Demonstration of the cloud to cloud (C2C) and cloud to mesh distance (C2M) comparison in the CloudCompare environment in meters

4.3.5 Results of Rib Cage Morphology Validation Using CloudCompare

For the shape morphology validation, the rib cage anatomy is divided into three bone segments, including 12 thoracic vertebrae, 24 ribs, and 1 sternum. Figure 4.11 demonstrates the shape morphology results of the three bone segments and the whole rib cage of Dataset 5 reconstructed by the five participants. The values on the scalar field are the signed distance errors between the gold standard CT model and the participant's model. As can be seen, the signed distance error can be a positive or negative value. Take Figure 4.11 (a) for example; red color highlights the positive distance error which means the participant's point (the point cloud set) is located outside the gold standard model (the mesh object). On the contrary, the blue color shows the negative distance error which means the participant's point is located inside the gold standard model. Also shown is the statistical analysis of the absolute mean, RMS, and the mean absolute maximal errors, as presented in Table 4.12. The absolute mean error and the RMS error are calculated through the C2C method, and the absolute maximal errors are obtained through the C2M method. It is worth mentioning that the signed mean error of Dataset 5 is 0.085 mm and this implies that the dataset is well aligned and scaled between the participants' models and the gold standard Mimics model.

For all of the 15 datasets reconstructed by the five participants, Table 4.13 summarizes the morphology accuracy results, including absolute mean errors, mean absolute maximal errors, and the RMS errors of the vertebrae, ribs, and sternum. The results of the absolute mean and the RMS errors show that the ribs possess higher reconstruction errors compared to the vertebrae or the sternum, whereas the sternum has the lowest errors. Those errors could result from manual operation by the participants, because the visualization of the rib's structure is poor when viewed from the lateral X-rays. In fact, the overlapping problem of the right and left ribs can lead to difficulty in clearly identifying the ribs' structure for the operators.

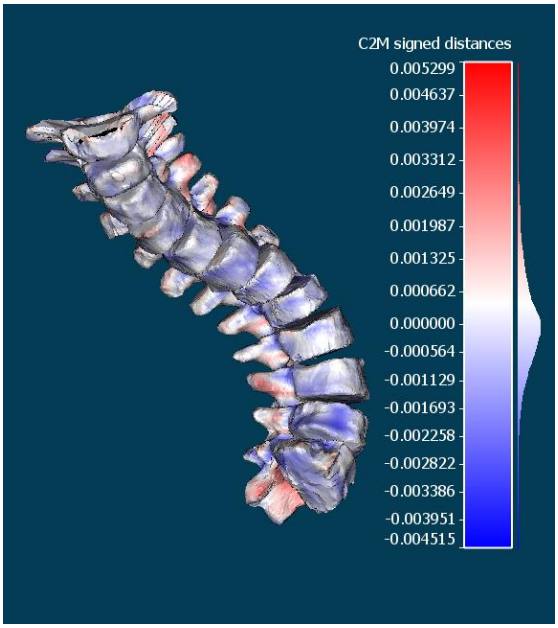

(i) Vertebrae

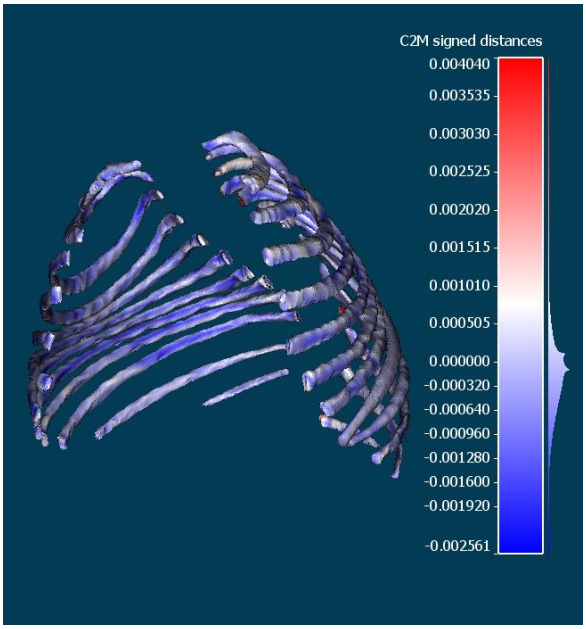

(ii) Ribs

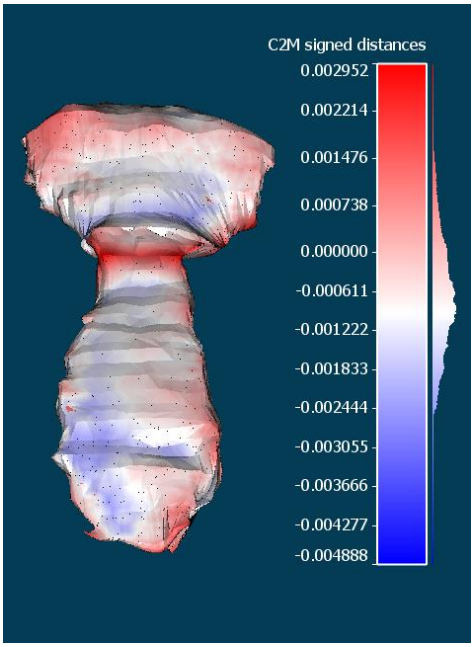

(iii) Sternum

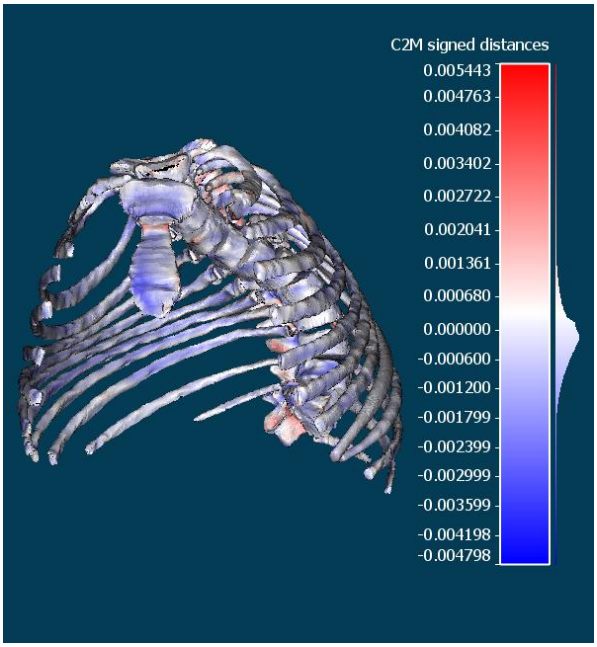

(iv) Whole rib cage

(a) Rib cage morphology result of Participant 1

The scalar field shows the distance error between the gold standard CT model and the participant's model in meters.

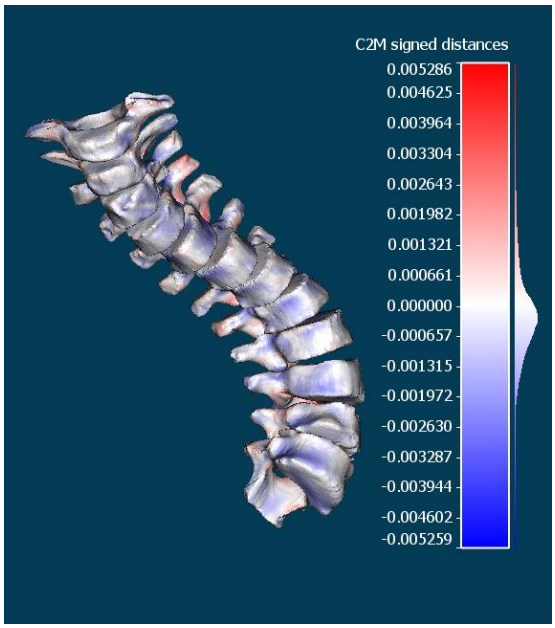

(i) Vertebrae

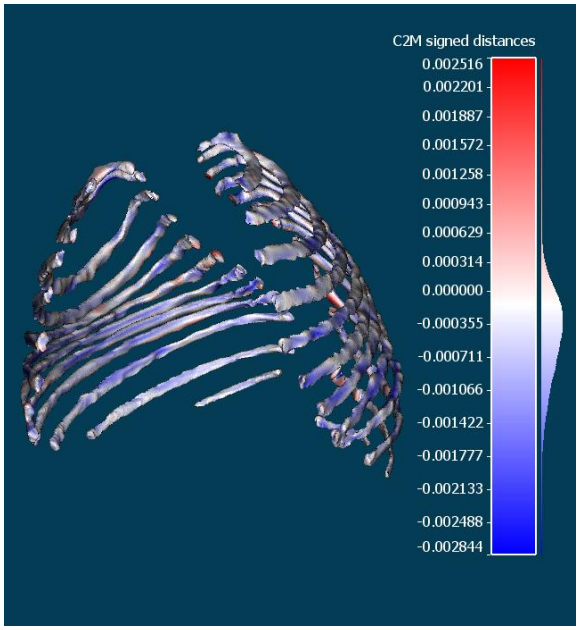

(ii) Ribs

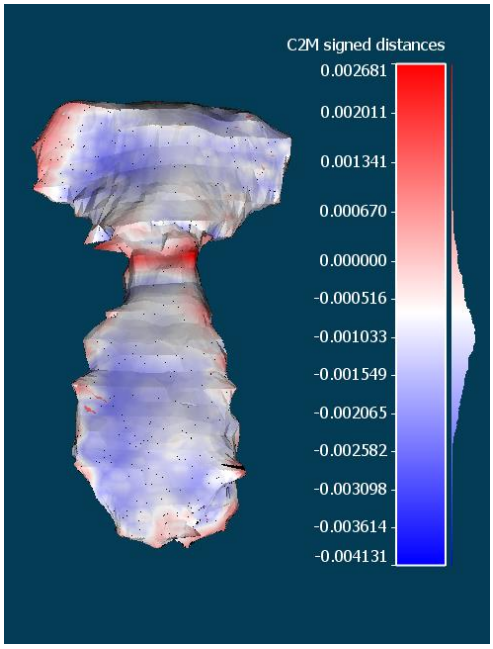

(iii) Sternum

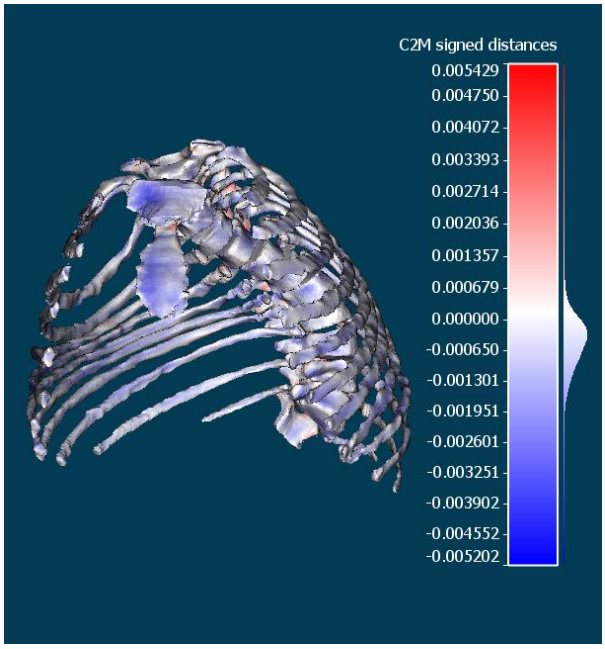

(iv) Whole rib cage

(b) Rib cage morphology result of Participant 2

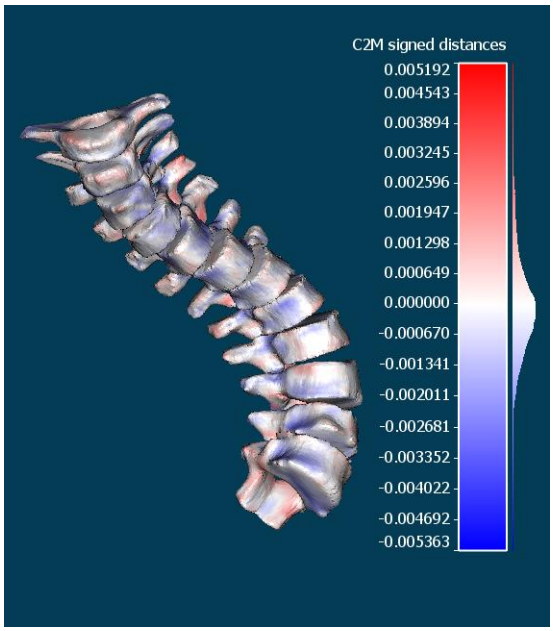

(i) Vertebrae

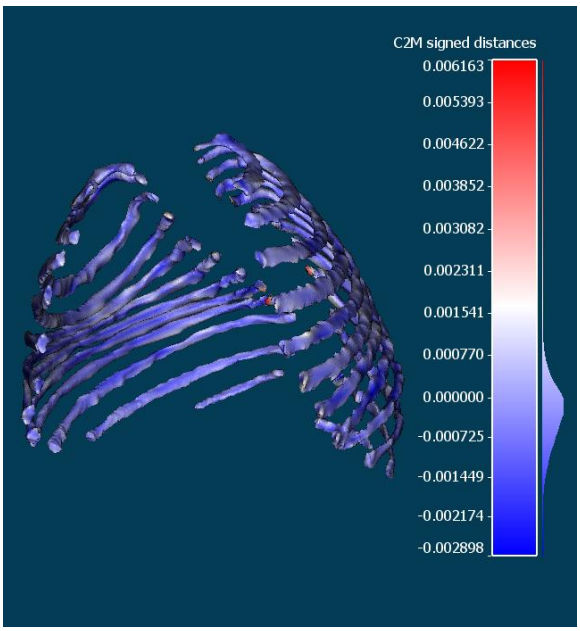

(ii) Ribs

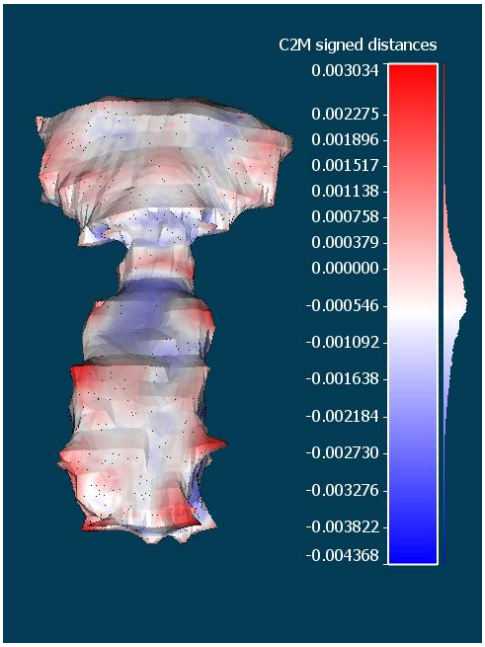

(iii) Sternum

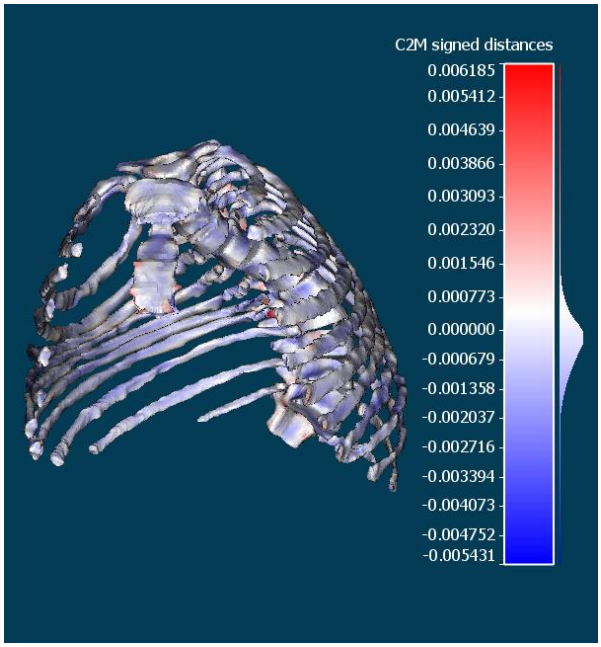

(iv) Whole rib cage

(c) Rib cage morphology result of Participant 3

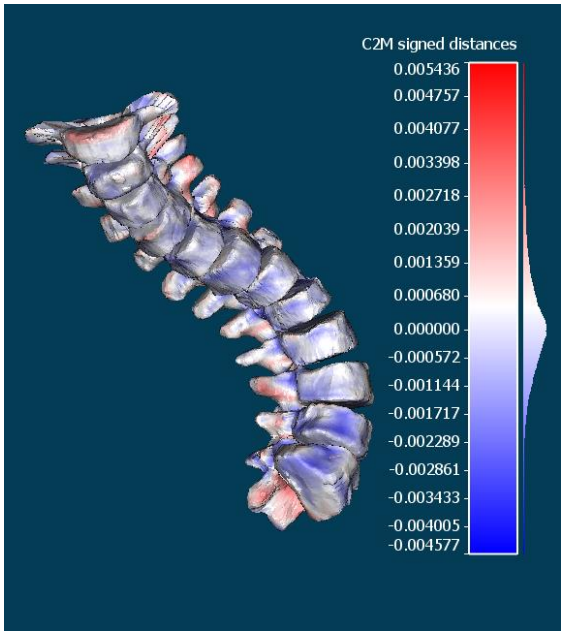

(i) Vertebrae

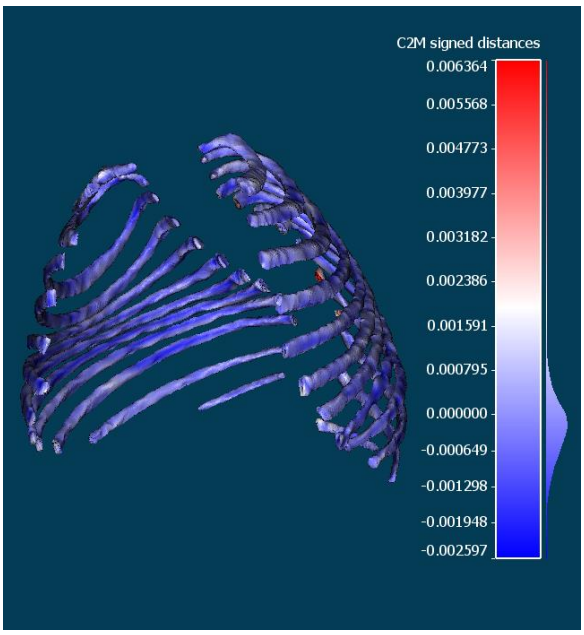

(ii) Ribs

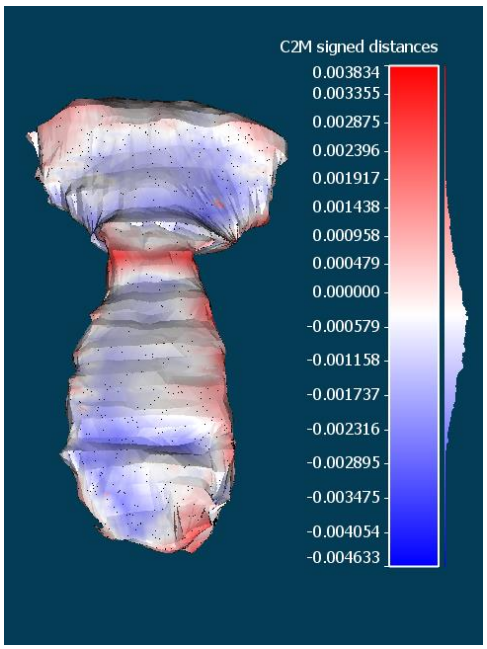

(iii) Sternum

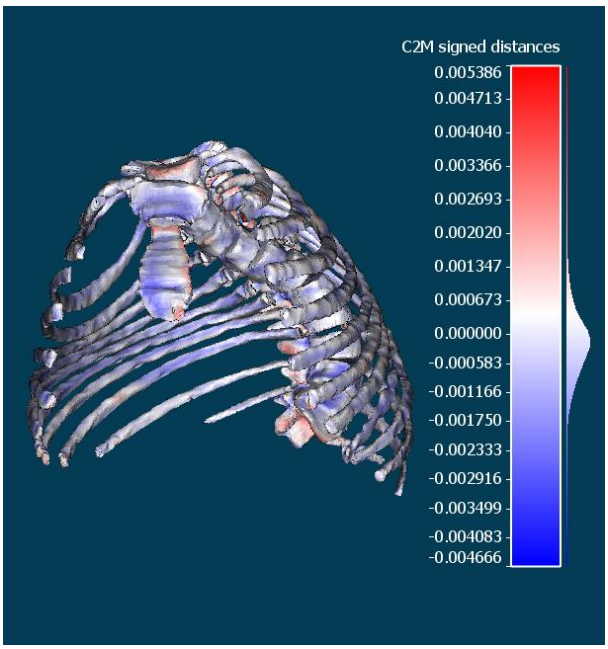

(iv) Whole rib cage

(d) Rib cage morphology result of Participant 4

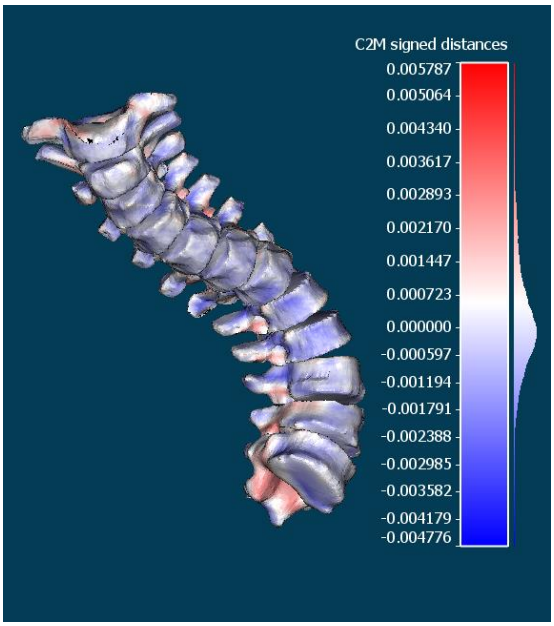

(i) Vertebrae

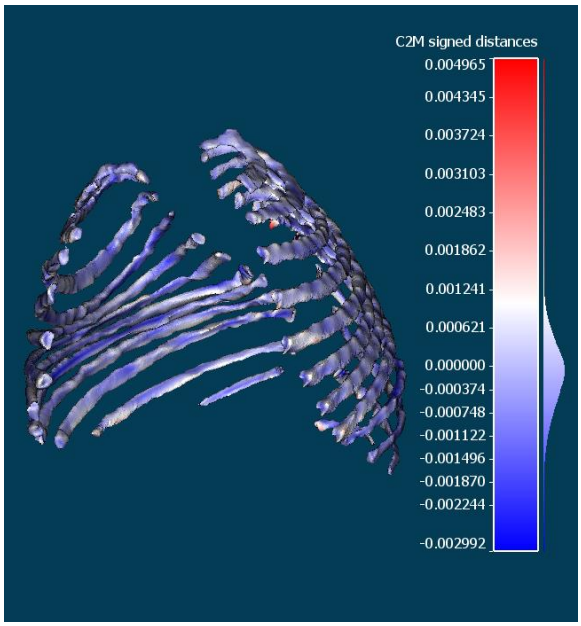

(ii) Ribs

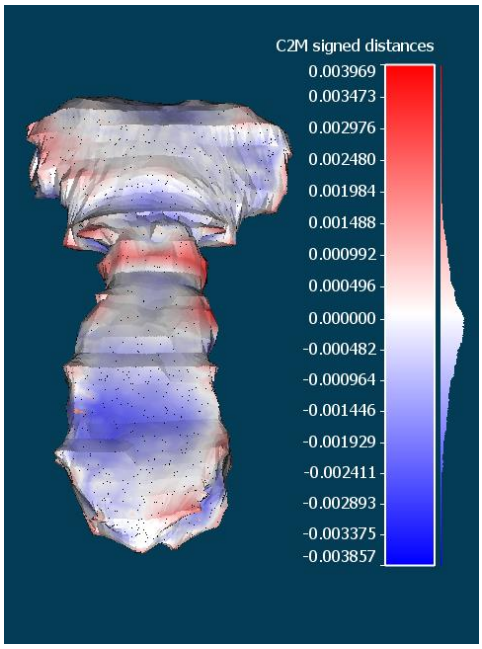

(iii) Sternum

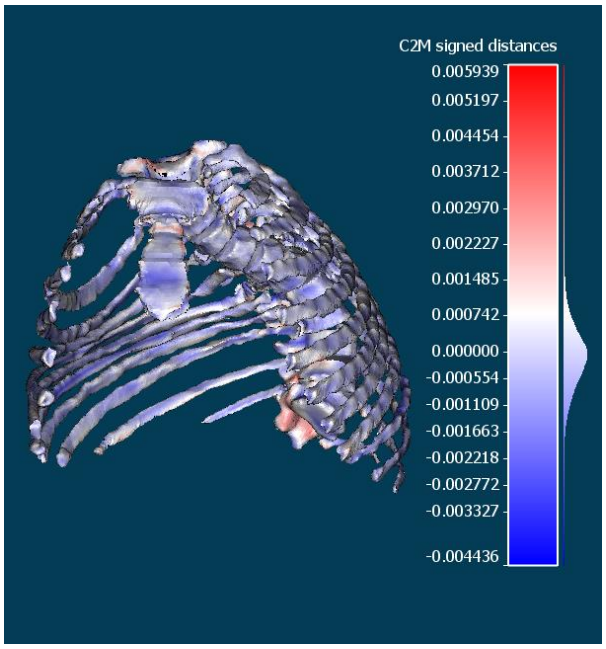

(iv) Whole rib cage

(e) Rib cage morphology result of Participant 5

Figure 4.11 Shape morphology analysis of the thoracic vertebrae, ribs, sternum and the whole rib cage for Dataset 5 using cloud to cloud method in CloudCompare in meters

Table 4.12 Results of the shape morphology accuracy of the specific rib cage regions in Dataset 5

Shape Accuracy (unit: mm)	Absolute Mean Error	Absolute Maximal Error	RMS Error
Vertebrae	0.89	5.43	1.20
Ribs	1.32	4.88	1.53
Sternum	0.92	4.40	1.14

Table 4.13 Results of the shape morphology accuracy of the specific rib cage regions in fifteen datasets

Shape Accuracy (unit: mm)	Absolute Mean Error	Mean Absolute Maximal Error	RMS Error
Vertebrae	1.38	4.31	1.51
Ribs	1.65	4.87	1.94
Sternum	1.29	3.73	1.44

4.3.6 Discussion

The reason to study the accuracy, precision and shape morphology of the rib cage in this section is that the reconstruction results of the positions, rotations and shape morphology of each bone can affect the structure (outer surface) of the rib cage. My method needs to have a rib cage and then reconstruct thoracic volume based on the rib cage boundary. Hence, if the rib cage boundary is not reconstructed accurately, the outcome of the thoracic volume reconstruction will be affected.

For the vertebrae, previous literature [34,36,38,68,76–81] heavily focused on improving the shape morphology of the vertebral structure, and some literature investigated the accuracy [68] and the precision [82,83] of the thoracic vertebrae position or rotation. For accuracy, I compare my results with the results from Glaser et al. [68], and their RMS errors of the positions are 0.5, 0.8, and 0.75 mm (versus ours: 1.09, 1.51, and 1.34 mm) in the X, Y, and Z directions with a 3D RMS of 1.2 mm (versus ours: 2.29). Their RMS errors of the rotations are 0.75, 1.25, and 1.9 degrees (versus ours: 1.83, 1.95, and 2.28 degrees) in the frontal, lateral, and axial rotations. For precision, I summarize the RMSSD of the positions and rotations gained from the previous literature in Table 4.14. It is worth mentioning that the global X and Y directions in previous research [38,68,82,83] were different from ours, so I adjust their local vertebral coordinate system in order to make a comparison. Actually, it was difficult to compare the results of different datasets and conclude whose method was better, especially when my datasets included 11 subjects with moderate to severe spine deformity and 4 subjects without spine deformity. Based on my current datasets, the precision results are comparable to the previous literature for the thoracic vertebrae reconstruction. As for the shape morphology accuracy of the vertebrae, I list the statistical results from the previous literature. As can be seen in Table 4.15, our accuracy of the shape morphology of the thoracic vertebrae is also comparable to other studies.

Table 4.14 Comparison of the precision of the postures of the thoracic vertebrae

RMSSD	Position			Rotation			Notes
	X	Y	Z	Frontal	Lateral	Axial	
Dumas et. al [82]	1.9 mm	0.9 mm	2.0 mm	1.5°	2.0°	2.0°	11 patients with idiopathic scoliosis
Humbert et al. [38]	0.55 mm	0.6 mm	0.4 mm	1.2°	1.15°	1.95°	40 thoracic and lumbar vertebrae from T11-L5 of 11 patients
Moura [84]	0.5 mm	0.5 mm	0.4 mm	1.2°	1.3°	3.3°	10 moderate scoliosis patients
Zhang et al. [83]	2.2 mm	1.8 mm	2.4 mm	1.8°	2.3°	2.8°	132 thoracic vertebrae from 15 scoliosis patients
Present study	**0.58 mm**	**0.84 mm**	**0.66 mm**	**1.22°**	**1.29°**	**1.81°**	**180 thoracic vertebrae from 15 datasets**

Table 4.15 Comparison of the accuracy of the shape morphology of the thoracic vertebrae

Literature (unit: mm)	Absolute Mean Error	Mean Absolute Maximal Error	RMS Error	Notes
Aubin et al. [34]	2.6	NA	NA	17 vertebrae from T1-L5 level of one cadaver
Mitulescu et al. [76]	1.5	19.7	2.0	58 thoracic and lumbar vertebrae from 14 scoliosis patients
Delorme et al. [36]	3.44	NA	5.25	52 vertebrae from T6-T12 levels of 14 scoliosis patients
Le Bras et al. [77]	0.9	5.6	1.2	12 dry thoracic vertebrae

Benameur et al. [78]	1.48	6.44	1.5	51 thoracic vertebrae from 13 idiopathic scoliosis patients
Pomero et al. [79]	1.4	15.8	1.8	Patients' data is the same as Mitulescu et al. [76]
Benameur et al. [80]	1.3	4.64	1.85	51 thoracic vertebrae from 13 idiopathic scoliosis patients
Kadoury et al. [81]	1.1	4.0	1.35	5 thoracic vertebrae from T10-T12 levels of 2 scoliosis patients
Humbert et al. [38]	1.3	NA	NA	40 thoracic and lumbar vertebrae from T11-L5 of 11 patients
Glaser et al. [68]	1.05	4.73	1.32	36 thoracic and 15 lumbar vertebrae from three synthetic scoliotic phantoms
Present study	**1.38**	**4.31**	**1.51**	**180 thoracic vertebrae from 15 datasets**

For the ribs, less literature mentioned how to reconstruct them systematically, and the statistical analysis methods used for accuracy and precision of ribs were different [40,44,58,63,85]. Some literature [40,85] focused on the reconstruction of the geometric shape of the ribs instead of investigating their positions or rotations. For the precision of the ribs' rotations, it is worth mentioning that our inter reproducibility (95% CI) of the frontal and lateral angles are 2.74 and 2.91 degrees, versus 5.2 and 5.5 degrees in [63]. Also, the inter reproducibility of our rib-hump angles is 2.39 degrees, which is better than the 5 degrees in [58] and [63]. The results presented in Section 4.3.3 show that the highest reconstruction accuracy and precision errors occur along the ribs.

For the sternum, I calculate the geometric centroid of the sternum and validate its accuracy and precision. A local coordinate system is constructed to compute the three orientations with respect to the global coordinate system by using MATLAB. Additionally, I rely on the CloudCompare to compare the shape morphology between the gold standard Mimics models and the five participants' models. There is still a lack of literature

discussing how to reconstruct the sternum and validate its reconstruction accuracy or precision; however, in my study, the reconstruction accuracy of the sternum's rotations is better than that of the vertebrae and the ribs, and the precision of the sternum's posture is better than that of the vertebrae or the ribs as well.

4.4 Thoracic Volume Validation

In the following section, the processes to reconstruct the thoracic volume models using the image processing software as the gold standard models are described. I utilize the gold standard models to validate the accuracy of the thoracic volume models, which are reconstructed by different users. Additionally, in order to compare the computational thoracic volume obtained by my program with the existing equations for computing thoracic volume using X-rays, I adjust our thoracic volume models and the CT scan models to satisfy the different thoracic volume boundaries defined by the previous researchers. Finally, the validation results are discussed and interpreted.

4.4.1 Validation of Thoracic Volume Accuracy through Gold Standard CT Scan Technique

The participants reconstruct the 3D thoracic volume of the fifteen datasets after reconstructing the thoracic rib cages in the Blender environment. As mentioned in Chapter 3, the thoracic volume can be computed through Blender. In Figure 4.12, I separately show the rib cage and thoracic volume of Dataset 5 reconstructed by Mimics and by the five participants.

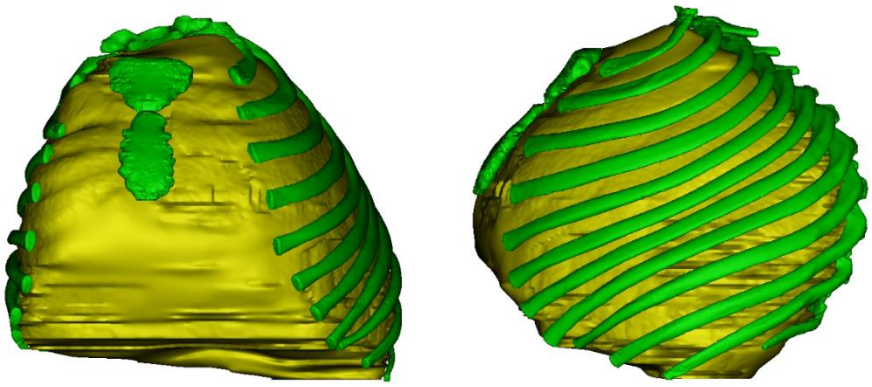

(a) Gold standard thoracic volume model (yellow) by Mimics software

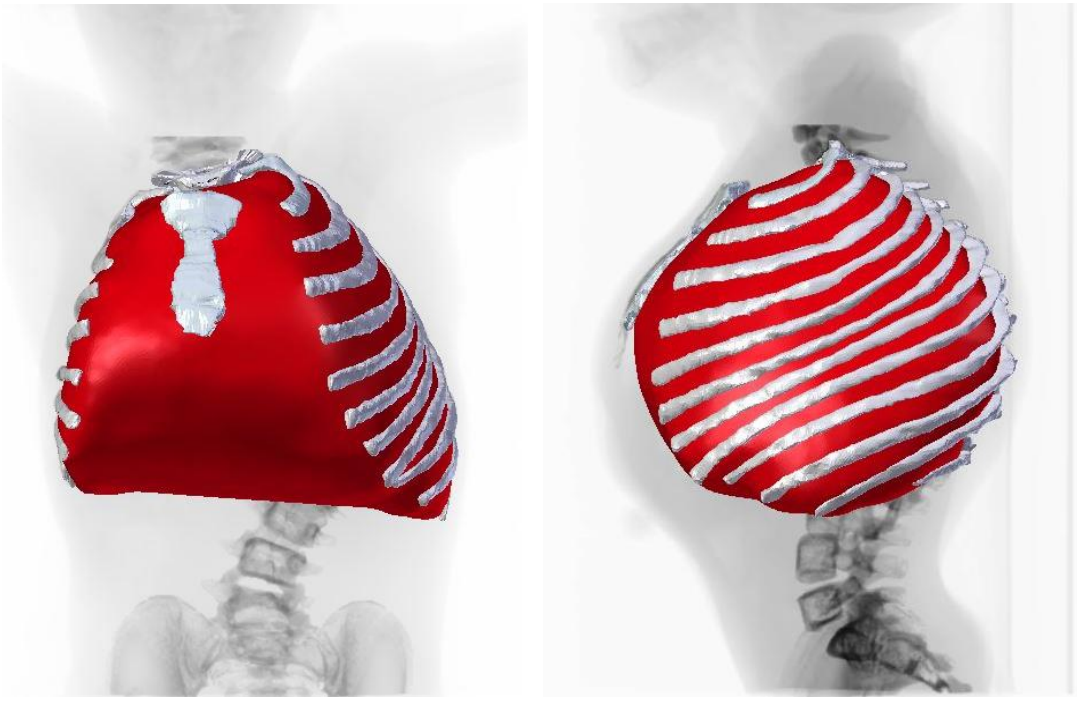

(b) Thoracic volume model (red) by Participant 1

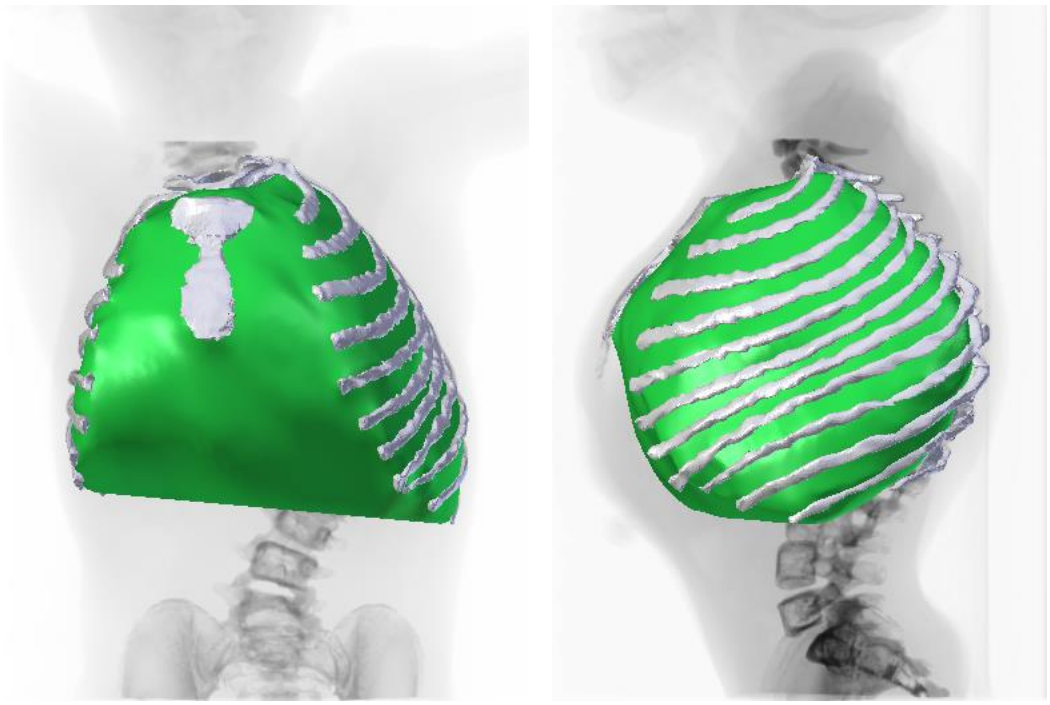

(c) Thoracic volume model (green) by Participant 2

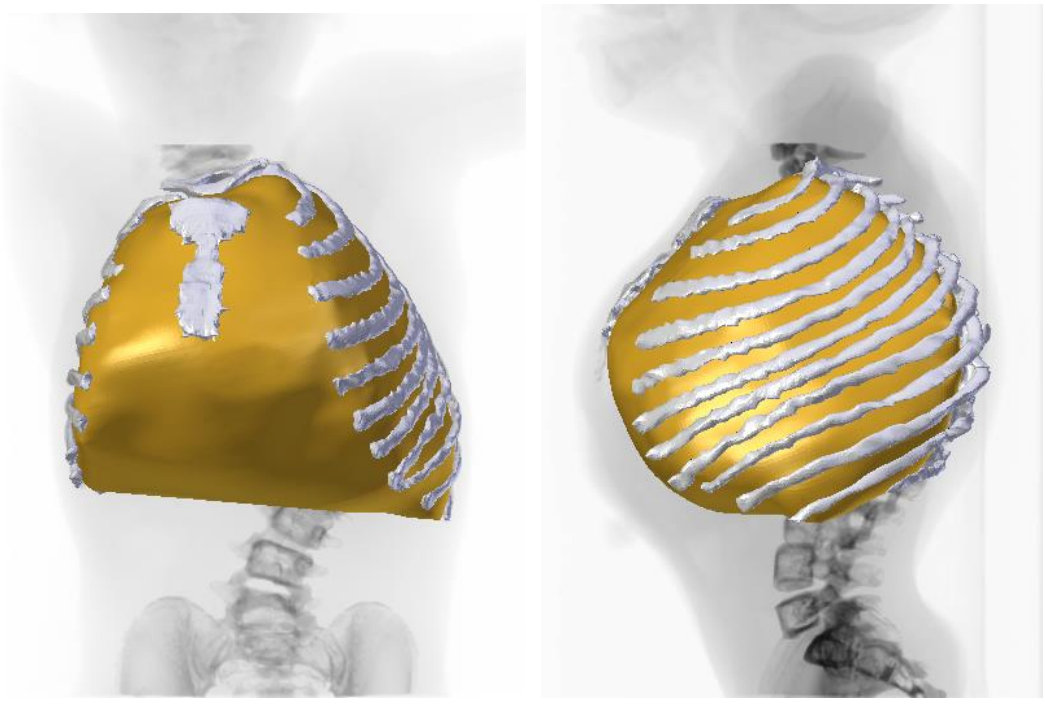

(d) Thoracic volume model (orange) by Participant 3

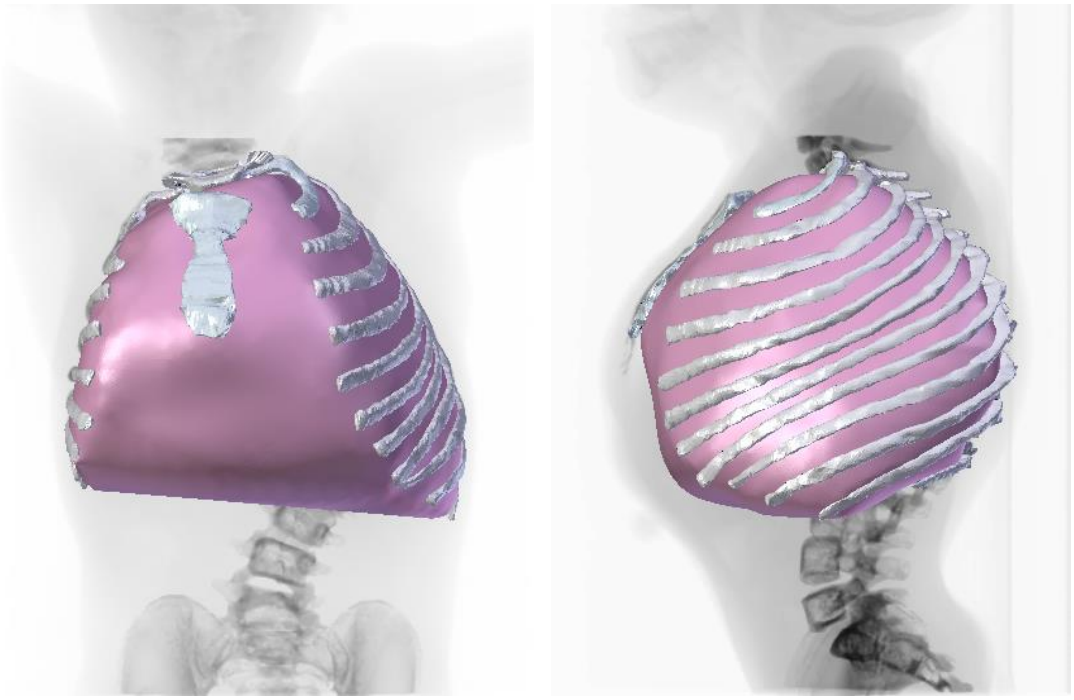

(e) Thoracic volume model (pink) by Participant 4

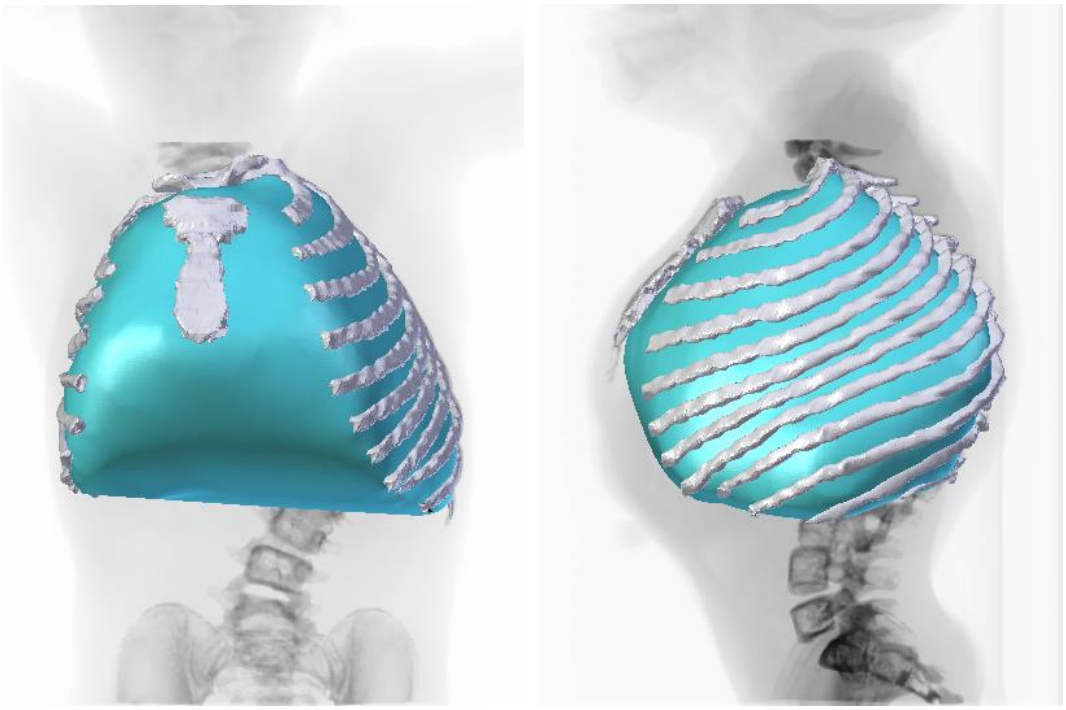

(f) Thoracic volume model (blue) by Participant 5

Figure 4.12 Thoracic volume of Dataset 5 reconstructed by Mimics using CT scan and by our customized program using biplanar X-rays

In order to standardize the measurement of the pulmonary function parameters and provide reliable clinical data, the American Thoracic Society [49] defined a standard protocol to deal with the quality requirement for performing the pulmonary function test by the breath testing equipment (e.g., spirometer or body plethysmography). This society suggests that the equipment of the pulmonary function, like spirometer or body plethysmography, should be capable of measuring the volume with an accuracy of ±3%. Hence, I apply this concept to the acceptable thoracic volume reconstruction error between our developed software and the CT scan (which serves as the gold standard to validate the accuracy of the developed software). I thus judge the thoracic volume accuracy using a ±3% standard. Table 4.16 lists all thoracic volume measured by the five participants in Blender and by the CT scan in Mimics. There were 75 thoracic volumes measured by five participants; 16 of them fell outside the ±3% error, and the others fell inside the ±3% error. The thoracic volume accuracy of all fifteen datasets measured by the five participants is 1.88% with a standard deviation (*SD*) of 1.29%. For adults, the average thoracic volume reconstruction error of the five participants is 1.46% (*SD* 1.14%) and it is 2.35% (*SD* 1.31%) for children. Since the mean error of our validation is within ±3%, the thoracic volume measurement through our developed software fulfills the protocol proposed by the American Thoracic Society. This result implies the accuracy of the software is good for diagnosis and risk assessment in clinical usages [71]. Also, the mean thoracic volume error for all fifteen datasets reconstructed by the five participants is 95cc (*SD* 94cc). In previous literature, Courvoisier et al. [58] used three subjects to compare the reconstruction accuracy of their program with the CT scan, and their mean thoracic volume error is 110cc. By comparison, our program produces less error and has more potential to provide useful clinical information.

The purpose of using two-way ANOVA without replication is to determine whether there is a significant difference in the thoracic volume values between the CT scan and the five participants. The null hypothesis is that no significant difference exists between the CT scan's results and the five participants' results. With the help of the *p*-value, I can understand whether the null hypothesis is rejected or not. With a result of $F(5,70) = 0.69$

and $p = 0.63$ in Table 4.17, it is clear that there is no significant difference between the CT scan's results and the participants' results for thoracic volume calculation due to the *p*-value > 0.05; thus, I fail to reject the null hypothesis. This indicates that the thoracic volumes of fifteen datasets reconstructed by a CT scan or by our program have no significant difference, so our thoracic volume accuracy is satisfactory. It is worth mentioning that there is a significant difference between each dataset's thoracic volume due to $F(14,70) = 11262.8$ and $p < 0.001$, as shown in Table 4.17.

Next, I use Excel to calculate 95% confidence intervals (CI) of the thoracic volume error (which is compared to a gold standard CT result). Table 4.18 presents the mean error of the thoracic volume, standard deviation, margin of error, the upper 95% confidence bound and the lower 95% confidence bound in this study. The outcome implies that 95% of the time the mean thoracic volume error will fall between 1.58% (73cc) and 2.17% (116cc) no matter who operates the thoracic volume estimator to measure the thoracic volume for any dataset. Furthermore, I investigate the reproducibility of the thoracic volume estimator, and the reproducibility can be used to interpret the precision error of the software. Normally, reproducibility analysis includes an intra-observer and an inter-observer. Since our participants only reconstructed each dataset once, I only discuss the inter-observer reproducibility. The inter-observer reproducibility is calculated according to the recommendation of ISO-5725 [86]. For the inter-observer reproducibility of thoracic volume measurements by all participants, the 95% confidence interval (CI) is calculated. The mean thoracic volume of the fifteen datasets computed by all participants is 6124cc (*SD* 4424cc). Then, I calculate the inter-observer reproducibility of the thoracic volume with a 95% CI and the result is 209cc, which is 3.42% determined by our program. This outcome shows the inter-observer reproducibility of the thoracic volume estimator is reproducible and clinically relevant [58]. Finally, I compare the thoracic volume reproducibility (95% CI for the thoracic volume) results with the results from Courvoisier et al. [58] and Aubert et al. [63]. Our inter-observer reproducibility of the thoracic volume measurement produces a better outcome which is 209 cc with a 95% CI and this result is better than 449 cc in [58] and 294 cc in [63].

Table 4.16 Validation of thoracic volume accuracy with usability testing

Dataset No.	TV by CT scan (cc)	TV by Tester 1 (cc)	% error of Tester 1	TV by Tester 2 (cc)	% error of Tester 2	TV by Tester 3 (cc)	% error of Tester 3	TV by Tester 4 (cc)	% error of Tester 4	TV by Tester 5 (cc)	% error of Tester 5
1	1005	965	-4.02%	981	-2.39%	994	-1.06%	989	-1.56%	973	-3.18%
2	1885	1801	-4.46%	1825	-3.14%	1842	-2.24%	1822	-3.33%	1835	-2.61%
3	1425	1415	-0.65%	1434	+0.61%	1469	+3.09%	1440	+1.07%	1457	+2.23%
4	1560	1624	+4.11%	1631	+4.51%	1599	+2.50%	1605	+2.86%	1603	+2.77%
5	2012	1957	-2.75%	1949	-3.16%	1991	-1.05%	1994	-0.89%	2046	+1.67%
6	3262	3238	-0.75%	3308	+1.41%	3265	+0.07%	3299	+1.12%	3254	-0.25%
7	3462	3614	+4.37%	3540	+2.23%	3535	+2.09%	3613	+4.35%	3592	+3.74%
8	9069	9123	+0.59%	9013	-0.62%	9287	+2.41%	9088	+0.21%	9100	+0.35%
9	6454	6321	-2.07%	6362	-1.43%	6464	+0.15%	6365	-1.38%	6645	+2.96%
10	6761	7040	+4.13%	6823	+0.92%	6752	-0.14%	6756	-0.08%	6652	-1.62%
11	13850	13622	-1.65%	13393	-3.30%	13567	-2.04%	13717	-0.96%	13690	-1.16%
12	12791	12706	-0.67%	12589	-1.58%	12728	-0.49%	12660	-1.03%	12873	+0.64%
13	10741	10731	-0.09%	10645	-0.90%	10656	-0.79%	10804	+0.58%	10580	-1.50%
14	11163	10654	-4.57%	11253	+0.80%	11261	+0.88%	11257	+0.84%	11292	+1.15%
15	6491	6660	+2.60%	6728	+3.66%	6654	+2.52%	6630	+2.15%	6672	+2.79%

TV stands for thoracic volume

Tester stands for participant

Table 4.17 Two-factor analysis of variance (ANOVA) for thoracic volume reconstruction results

ANOVA: Two-Factor Without Replication						
Source of Variation	*SS (Sum of Square)*	*df (degree of freedom)*	*MS (Mean Square)*	*F (F statistic)*	***P-value***	*F critical*
Datasets	1649324233	14	1178088744	11262.8	2E-111	1.84
CT scan & five participants	36133.57	5	7226.71	0.69	**0.63**	2.35
Error	732201.53	70	10460.02			
Total	1650092568	89				

Table 4.18 95% confidence interval of thoracic volume accuracy by five participants compared with gold standard CT scan model

Mean error of the thoracic volume	95 cc	1.88%
Alpha (significant level)	0.05	0.05
Standard deviation of the thoracic volume	94 cc	1.29%
Number of datasets	75	75
Margin of error	21.6 cc	0.30%
Lower bound	73 cc	1.58%
Upper bound	116 cc	2.17%

4.4.2 Comparison with Three Equations for Measuring Thoracic Volume Using an X-ray Technique

Kovach et al. [54] assumed the thoracic volume was a paraboloid shape, so they only needed to retrieve the frontal X-rays of the patients to derive their thoracic volume. In Figure 4.13, they defined the measurable parameters on the frontal X-ray; the equation to compute the thoracic volume is expressed as follows,

$$V_K = \frac{\pi}{2} ab^2 \tag{4.16}$$

where V_K = paraboloid shape of the thoracic volume in milliliters

a = distance from the top of the lung to the bottom of the lung in centimeters

b = length of one-half of the base of the two lungs in centimeters

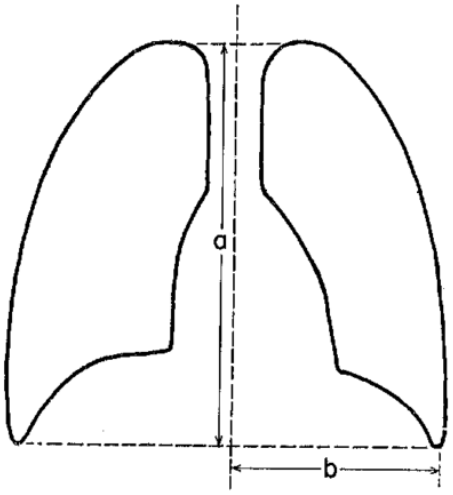

Figure 4.13 Definition of thoracic volume boundary on the frontal X-ray by Kovach (redrawn from [54])

Figure 4.14 shows the thoracic volume boundary for Dataset 14 on the fluoroscopy image based on Kovach's definition. It is worth mentioning that the lungs on the simulated fluoroscopy image look whiter, as can be seen in this figure. With the parameters and the boundary of the thoracic volume, I measure all parameters on the simulated frontal fluoroscopy image of the fifteen datasets and list them in Table 4.19.

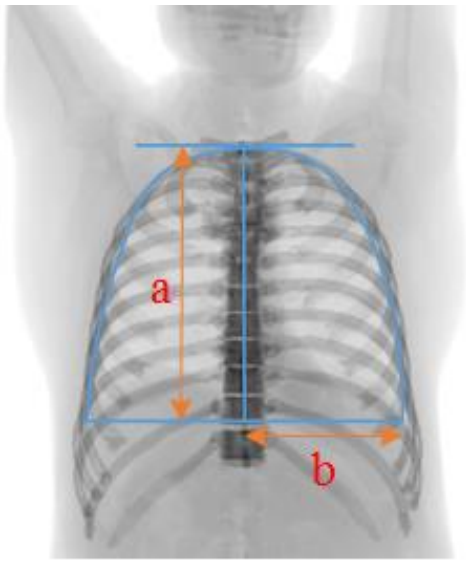

Figure 4.14 Thoracic volume boundary for Dataset 14 defined by Kovach on a frontal fluoroscopy image

Next, I adjust the boundary of the thoracic volume for CT scan models which will become the gold standard models. Here, I use Dataset 14 as an example to demonstrate how parameters a and b are identified on the frontal fluoroscopy image. Also, I use Dataset 14 to demonstrate how 3D thoracic volume looks in Mimics and my thoracic volume estimator based on Kovach's definition of the thoracic volume boundary. Figure 4.15 (a) shows Dataset 14's CT scan models after adjustment. Figure 4.15 (b) presents the result after using the thoracic volume estimator to reconstruct the thoracic volume of Dataset 14 by orthogonal fluoroscopy images and subtracting the extra volumes below the bottom edge of the lungs in the Blender environment based on the boundary of thoracic volume described in [54]. All parameters and percentage error of our method and Kovach's method are listed in Table 4.19. When compared with gold standard CT scan models, the mean error of the thoracic volume measured by our program is 2.52%, with 2.16% for eight adults and 2.92% for seven children. Kovach's method obtains a mean error of 13.29%, with 9.9% for eight adults and 17.16% for seven children.

Table 4.19 Comparison of the thoracic volume accuracy between our customized program and Kovach's method

Dataset No.	Thoracic volume by CT scan (cc)	Thoracic volume by our method (cc)	% error of our method	a (cm)	b (cm)	Thoracic volume by Kovach's method (cc)	% error by Kovach's method
1	791	756	4.40%	11.36	7.57	1024	29.41%
2	1673	1616	3.36%	12.17	7.89	1190	28.88%
3	1092	1069	2.15%	12.22	7.33	1032	5.47%
4	1413	1466	3.71%	12.01	8.35	1316	6.90%
5	1270	1228	3.40%	10.25	8.34	1119	11.84%
6	2923	2854	2.37%	18.93	8.94	2375	18.74%
7	2312	2288	1.05%	13.55	9.39	1875	18.89%
8	6624	6753	1.94%	26.50	13.17	7215	8.92%
9	5971	5757	3.59%	24.62	11.80	5388	9.77%
10	5516	5320	3.56%	23.34	12.14	5406	2.00%
11	13369	12921	3.35%	33.92	14.63	11401	14.72%
12	6918	6896	0.32%	20.91	13.47	5958	13.87%
13	10036	9831	2.05%	29.83	13.79	8914	11.18%
14	8146	8278	1.62%	24.83	15.19	8997	10.44%
15	3797	3831	0.89%	18.67	11.84	4111	8.28%

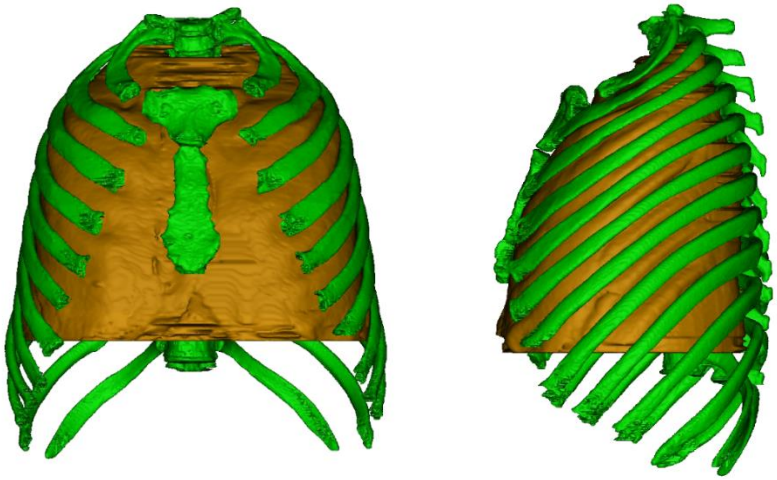

(a) Frontal and lateral views of the thoracic volume (orange) after adjustment in Mimics

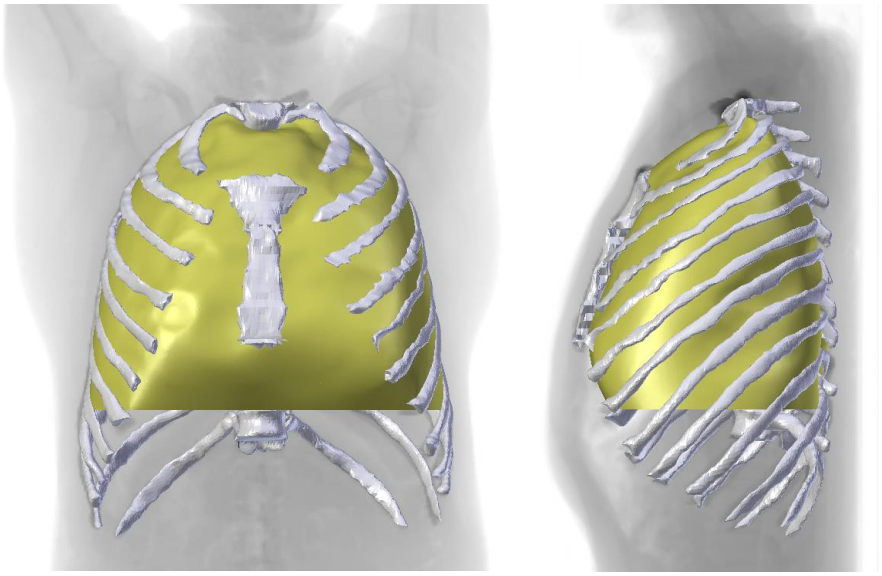

(b) Frontal and lateral views of the thoracic volume (yellow) after adjustment in Blender

Figure 4.15 Thoracic volume boundary for Dataset 14 based on the definition in [54] in the Mimics and Blender environment

Barnhard et al. [15] divided the thoracic volume into five sections and they considered each segment to be an elliptical cylindroid shape. Figure 4.16 demonstrated the five sections of the thoracic volume. The researchers explained how they divided the chest

boundary into five sections on both frontal and lateral X-rays, and the detailed steps were as follows:

1. Outline the boundaries of the lungs by following the inner border of the chest wall.
2. Divide the superior portion of the rib cage into two sections that are 2.5 cm apart (section I and section II in Figure 4.16).
3. Draw a horizontal line at the higher dome of the diaphragm.
4. Equally divide the large area into two parts with another horizontal line to form section III and section IV and the last area will be section V.

After following these steps, I can measure the parameters (i.e., height, width, and depth) of each section on both X-rays. Then, the formula they used to compute the thoracic volume was written as,

$$V_B = V_I + V_{II} + V_{III} + V_{IV} + V_V = \sum_{i=1}^{5} \frac{\pi}{4} \times w_i \times h_i \times d_i \quad (4.17)$$

where V_B = elliptical cylindroid shape of the thoracic volume in milliliters

w = transverse diameter from the leftmost to the rightmost of each section in centimeters

h = height of each section in centimeters

d = anterior-posterior diameter of each section in centimeters

In Figure 4.16, I use Dataset 14 to display Barnhard et al.'s definition of thoracic volume which was equivalent to the summation of five sections' volumes inside the chest wall boundary. I follow their method to measure all parameters on frontal and lateral fluoroscopy images, and then utilize Eq. (4.17) to calculate all thoracic volumes for the fifteen datasets. The lower boundary of their thoracic volume is the base of section V, which is the bottom-most edge of the lungs. It is worth mentioning that the thoracic volume boundary defined by Barnhard et al. is similar to the one by Kovach et al. Therefore, the adjusted models reconstructed by Mimics and by the thoracic volume estimator shown in Figure 4.15 can be employed again to make the comparison of accuracy here. That is, the mean error of the thoracic volume reconstruction using our method can be directly compared with the results by Barnhard et al. After measuring the parameters on the biplanar fluoroscopy images for the fifteen datasets as shown in Table 4.20, I find the accuracy of

Barnhard's method is 11.05% for the mean error when compared with gold standard CT scan models, and the mean error for the adult cohorts and the child cohorts are 5.2% and 17.74% separately.

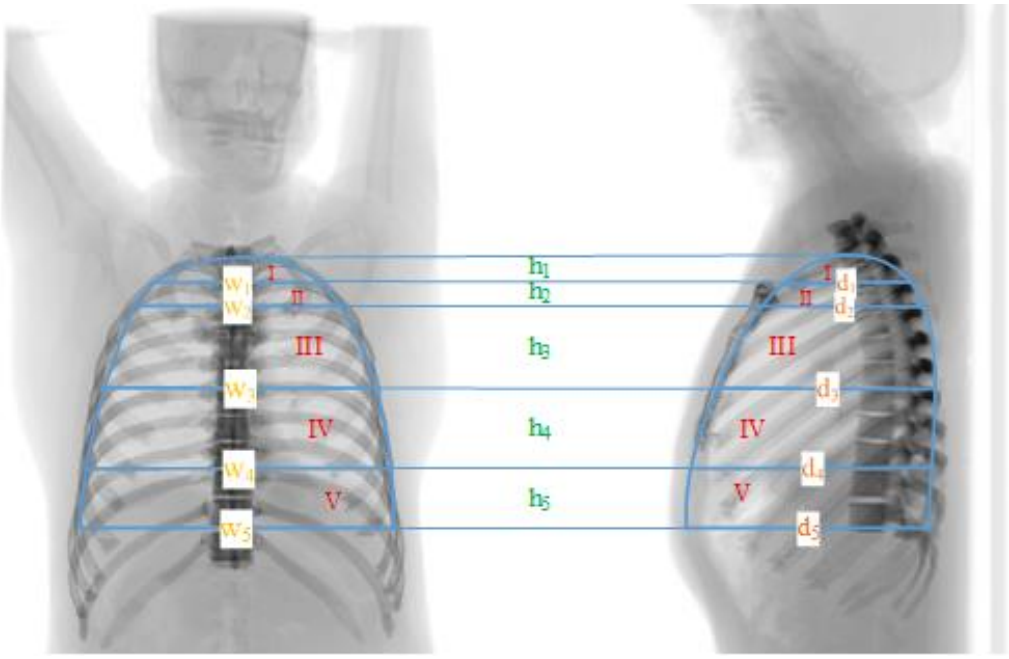

Figure 4.16 Thoracic volume boundary for Dataset 14 on frontal and lateral fluoroscopy images based on Barnhard's definition [3]

Table 4.20 Thoracic volume accuracy by Barnhard's method

Dataset No.	w_1	h_1	d_1	w_2	h_2	d_2	w_3	h_3	d_3	w_4	h_4	d_4	w_5	h_5	d_5	TV by Barnhard method (cc)	% error by Barnhard method
1	10.7	2.5	6.0	13.4	2.5	8.0	13.7	1.7	8.9	14.4	1.7	8.8	15.1	2.9	8.5	756	4.40%
2	12.2	2.5	8.6	14.9	2.5	12.5	15.5	1.4	13.8	16.2	1.4	14.4	15.8	4.3	13.1	1616	3.36%
3	10.0	2.5	6.8	12.9	2.5	10.3	14.0	2.3	11.9	14.3	2.3	11.5	14.7	2.7	9.9	1069	2.15%
4	11.3	2.5	7.7	14.2	2.5	9.7	15.5	2.2	12.1	16.1	2.2	12.2	16.7	2.6	11.9	1466	3.71%
5	9.3	2.5	9.5	12.8	2.5	13.8	14.3	1.2	15.2	15.2	1.2	15.7	16.7	2.9	15.5	1228	3.40%
6	14.0	2.5	8.4	16.4	2.5	11.0	17.5	3.5	13.9	18.0	3.5	15.2	17.9	7.0	12.7	2854	2.37%
7	13.5	2.5	10.2	17.3	2.5	13.4	17.7	2.2	14.8	18.0	2.2	16.0	19.1	6.4	16.1	2288	1.05%
8	14.0	2.5	7.9	19.2	2.5	8.4	22.9	7.6	14.2	24.6	7.6	17.1	26.3	6.2	15.8	6753	1.94%
9	13.8	2.5	7.3	18.4	2.5	10.2	21.6	5.3	13.6	23.8	5.3	15.8	23.6	9.1	15.4	5757	3.59%
10	13.0	2.5	7.7	15.9	2.5	9.1	19.5	5.0	13.8	22.7	5.0	16.0	24.3	8.3	17.0	5320	3.56%
11	15.4	2.5	9.6	20.1	2.5	12.3	27.2	9.2	19.7	29.4	9.2	21.5	29.3	10.5	19.7	12921	3.35%
12	17.0	2.5	11.6	21.7	2.5	13.3	24.5	5.0	17.7	25.7	5.0	21.3	26.9	5.9	20.9	6896	0.32%
13	17.9	2.5	10.4	22.4	2.5	13.7	24.7	7.7	19.1	26.7	7.7	19.7	27.6	9.5	17.8	9831	2.05%
14	17.1	2.5	9.8	21.2	2.5	12.0	25.7	6.9	17.1	27.6	6.9	19.9	30.4	6.1	18.3	8278	1.62%
15	15.5	2.5	8.0	19.3	2.5	10.4	22.2	3.8	13.0	23.0	3.8	14.1	23.7	6.0	13.9	3831	0.89%

TV stands for thoracic volume; all parameters on fluoroscopy images are in centimeters

Stolle et al. [56] regarded the thoracic volume as a combination of the semi-ellipsoid volume and the elliptical truncated cone volume. Figure 4.17 depicted the geometric shape of the defined thoracic volume. The top portion is the semi-ellipsoid volume, and the equation to calculate the volume of this portion is [56]:

$$V_{top} = \frac{\pi}{3} cH(a + b + \frac{b^2}{a}) \tag{4.18}$$

As for the elliptical truncated cone, the equation to calculate its volume is expressed as:

$$V_{bottom} = \frac{2}{3}\pi c \frac{b^2 h}{a} \tag{4.19}$$

Hence, the thoracic volume will be the summation of Eq. (4.18) and Eq. (4.19), which becomes:

$$\mathrm{V_S} = V_{top} + V_{bottom} = \frac{\pi}{3} c \left[H \left(a + b + \frac{b^2}{a} \right) + \frac{2b^2 h}{a} \right] \tag{4.20}$$

where $\mathrm{V_S}$ = thoracic volume in milliliters

a = half thoracic width at the bottom base in centimeters

b = half thoracic width at the level of aortic apex in centimeters

c = half thoracic depth at the bottom base in centimeters

h = height from the aortic arch to the top of the thoracic volume boundary in centimeters

H = height from the top of an aortic arch to the bottom line of the thoracic volume in centimeters

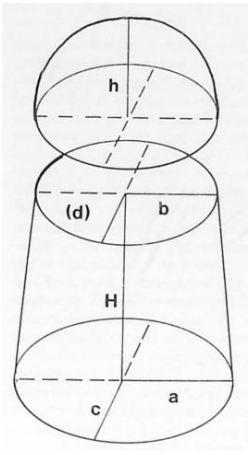

Figure 4.17 Three-dimensional shape of the thoracic volume (copied from [56])

With the thoracic volume boundary of Dataset 14 demonstrated in Figure 4.18, I adjust the CT scan models by Mimics to be our gold standard models. Figure 4.19 shows that the boundary of the thoracic volume for the CT scan models (Dataset 14) is adjusted based on the definition by Stolle et al. I utilize frontal and lateral fluoroscopy images to reconstruct the thoracic volume with our customized add-on program in Blender by subtracting the extra volume outside the thoracic volume outline that I display in Figure 4.18. From Table 4.21, I find that the mean error of our reconstruction method is 2.54%, with a mean error of 2.19% and 2.93% for eight adults and seven children respectively in comparison with the CT scan models. Stolle et al.'s method yields the mean error of 19.55% with a mean error of 12.17% for adults and a mean error of 27.99% for children.

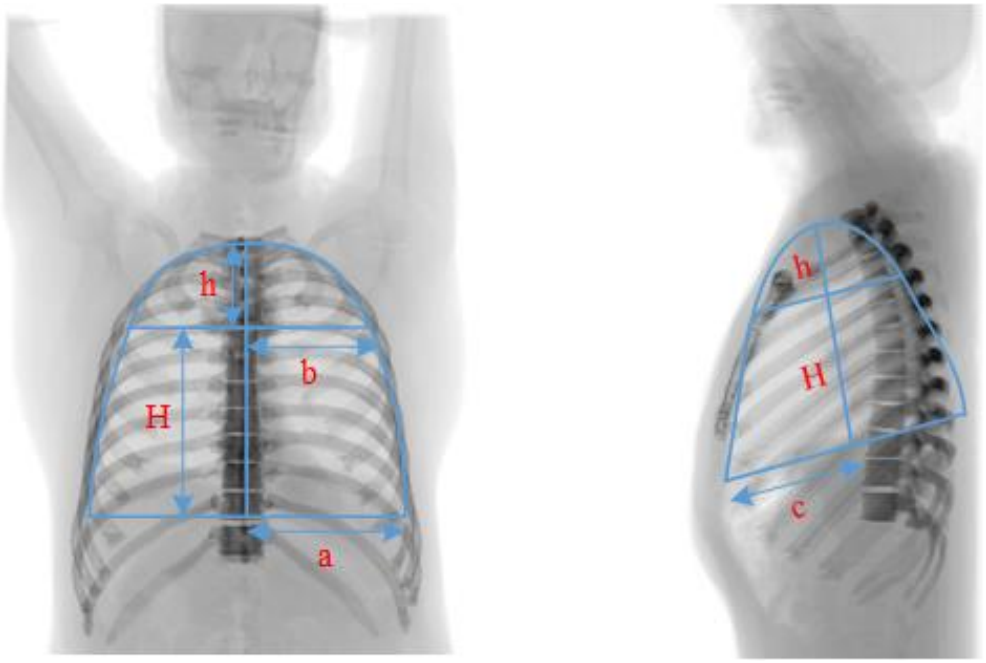

Figure 4.18 Boundary of the thoracic volume for Dataset 14 on frontal and lateral fluoroscopy images defined by Stolle [56]

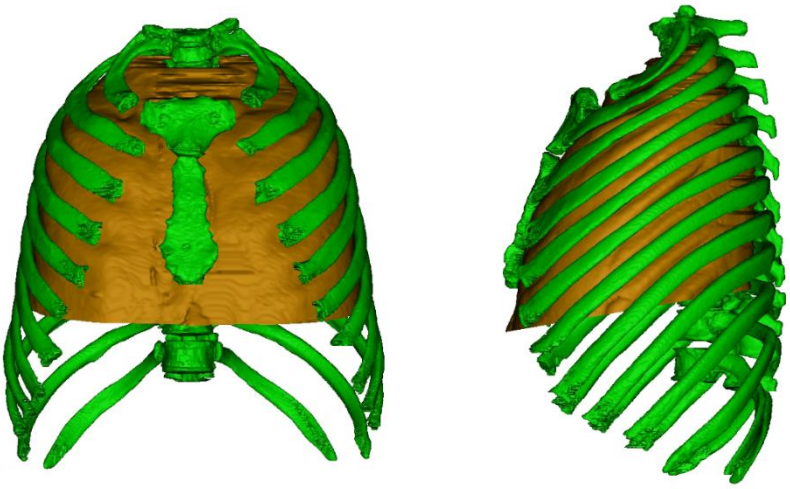

(a) Frontal and lateral views of the thoracic volume (orange) after adjustment in Mimics

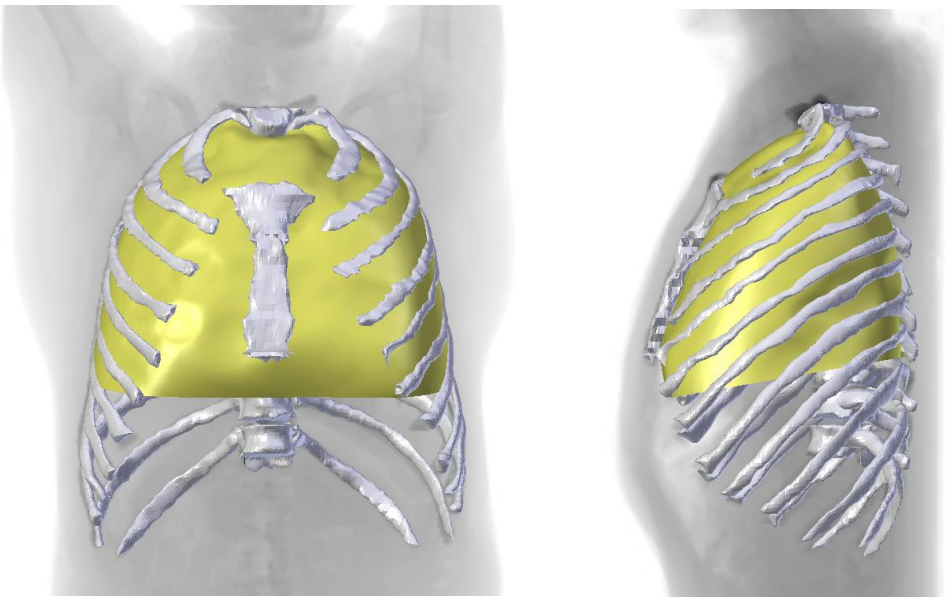

(b) Frontal and lateral views of the thoracic volume (yellow) after adjustment in Blender

Figure 4.19 Thoracic volume boundary for Dataset 14 based on the definition in [56] in the Mimics and Blender environment

Table 4.21 Comparison of the thoracic volume accuracy between our customized program and Stolle's method

Dataset No.	Thoracic volume by CT scan (cc)	Thoracic volume by our method (cc)	% error by our method	a (cm)	b (cm)	c (cm)	H (cm)	h (cm)	Thoracic volume by Stolle's method (cc)	% error by Stolle's method
1	809	771	4.74%	8.44	6.71	4.89	6.98	3.94	946	16.91%
2	1053	1074	1.99%	8.35	7.20	7.05	6.08	3.15	1265	20.05%
3	989	974	1.50%	7.69	6.31	5.74	7.39	3.25	1054	6.55%
4	1008	1053	4.48%	8.64	7.48	6.77	6.69	3.84	1423	41.17%
5	1322	1267	4.16%	9.17	6.60	8.50	7.01	3.60	1584	19.82%
6	2702	2618	3.11%	9.38	8.99	7.23	12.20	5.52	3213	18.89%
7	2311	2323	0.52%	9.95	9.59	8.53	12.22	5.12	3988	72.56%
8	6319	6388	1.08%	14.01	11.64	8.85	16.56	9.80	7174	13.52%
9	5372	5197	3.25%	12.84	10.28	8.46	17.29	6.32	5724	6.55%
10	5508	5648	2.54%	12.83	9.94	9.34	15.54	7.29	5727	3.98%
11	10366	9929	4.22%	15.61	13.31	10.77	18.39	4.14	9412	9.20%
12	6843	6777	0.96%	14.66	12.18	11.75	14.65	6.45	8265	20.79%
13	8615	8457	1.84%	14.16	12.48	9.72	17.69	6.83	8307	3.58%
14	6294	6481	2.96%	15.09	12.38	10.42	14.52	6.35	7362	16.97%
15	3548	3524	0.68%	12.56	11.19	8.07	11.68	6.09	4354	22.74%

4.4.3 Discussion

In section 4.4.1, the thoracic volume accuracy reconstructed by the five participants was validated through the CT scan model reconstructed by Mimics. The mean error of the thoracic volume was 95cc (*SD* 94cc) or 1.88% (*SD* 1.29%) for all participants measured by our thoracic volume estimator, and this result was more accurate than [58] (which was 110cc for the mean thoracic volume error). All thoracic volume accuracy is lower than 5% error in our study as shown in Table 4.16. The reconstruction accuracy for a cohort with eight adults was 1.46% (*SD* 1.14%), which caused less error compared to a cohort with seven children (2.35% with *SD* 1.31%). For children, this result was acceptable due to their smaller thoracic volume, especially for severe scoliosis patients. That is, a 5% error only causes 100 cc deviation from the actual thoracic volume value if we consider a child with a thoracic volume of 2000 cc. This kind of error is clinically acceptable for a small thoracic volume [49]. In the statistical analysis, the two-way ANOVA analysis without replication displayed the fact that there was no significant difference between the CT scan result and the five participants' results for the thoracic volume calculation. This phenomenon indicated that the thoracic volume measurement by our developed program is reliable and replicable whoever operates the program after training. In addition, I calculated the 95% confidence interval for the mean error, margin of mean error, and upper and lower boundary of 75 thoracic volumes reconstructed by the five participants (each participant reconstructed 15 datasets once). This process could predict the range of the thoracic volume accuracy if other users operate our software in the future. The result showed that there was a 95% probability for the thoracic volume error (compared to the CT scan result) to be found in the range between 1.58% (i.e., 73cc) and 2.17% (i.e., 116cc). This finding satisfied the protocol proposed by the American Thoracic Society [49], which defined the acceptable accuracy error (±3%) for the measurement error. Besides, I used ISO standards to study the reproducibility of our developed software, and my primary focus was on the inter-observer reproducibility due to our user testing settings. After calculating the 95% confidence interval of 75 thoracic volumes computed by the five participants, the inter-observer reproducibility of the thoracic volume was 205cc, which was 3.35% with a 95%

confidence interval determined by our thoracic volume estimator. Courvoisier et al. [58] recruited three operators to use their program to measure the thoracic volume for 22 adolescent scoliosis patients. They also conducted the inter-observer reproducibility study in their article. Their result was 449cc for the thoracic volume and the 95% confidence interval was 8% determined by the EOS® commercial imaging system [58]. When comparing our inter-observer reproducibility results with those from Courvoisier et al., I found the performance of our inter-observer reproducibility (precision error) was superior. Overall, our thoracic volume estimator attains good accuracy and precision for the thoracic volume reconstruction, because the accuracy (less than 3% error) satisfies the suggestion by the American Thoracic Society and the precision (RMSSD is 105cc) is better than the previous study. Thus, it can be applied in diagnosis and monitoring in clinical usages.

Thoracic volume can also be segmented and reconstructed by using CT scans, and I utilize my thoracic volume definition to reconstruct the gold standard thoracic volume models with the help of Mimics software. Even though a CT scan can be employed to reconstruct the thoracic volume, its reconstruction time is longer than the time that our developed program takes. The five participants in my research spent an average of about 23 minutes reconstructing one thoracic volume. Unfortunately, the CT scan has high dose radiation and this might trigger cancer issues for the patients in the future. Therefore, traditional X-rays are still routinely adopted to diagnose the spine deformity symptoms in hospitals.

In Section 4.4.2, I compared my thoracic volume reconstruction method with three different methods found in the literature using plain X-rays to estimate the thoracic volume inside the chest wall. Due to different definitions of the thoracic volume boundary made by different researchers [15,54,56], I needed to modify the portion of the CT scan in accordance with their definitions for the comparison of thoracic volume accuracy. The results indicated that the overall mean error of my thoracic volume reconstruction method for the fifteen datasets was lower than 3% with the help of the thoracic volume estimator. However, the three research articles which directly utilized their derived equations to calculate the thoracic volume possessed a mean error larger than 3% (Kovach: 13.29%,

Barnhard: 11.05%, and Stolle: 19.55%) when compared to the CT scan results. Furthermore, among the fifteen datasets of different ages, five datasets have spine scoliosis symptoms, one has the kyphosis diagnosis, and five have combined scoliosis and kyphosis symptoms. However, the previous methods I compared to only focused on how to use their derived equations to measure the thoracic volume for the people without any spine deformity symptoms. Therefore, this may explain why the previous methods were not accurate enough to estimate the thoracic volume for spine deformity patients, especially severe spine patients.

4.5 Conclusion

I implemented a study to validate the reconstruction of the rib cage and thoracic volume through our thoracic volume estimator. Five participants were recruited and trained to operate our program, including a graphical user interface and thoracic volume add-on Blender package, and to reconstruct the thoracic rib cage and thoracic volume via frontal and lateral X-rays in Blender software. Their results of the rib cage and thoracic volume reconstruction were collected to validate the reconstruction accuracy and precision of the developed software. The reconstruction accuracy was validated by comparing the gold standard CT scan models reconstructed by Mimics software with those models reconstructed by the participants through the developed software. The reconstruction precision was validated between the participants' models to study the reproducibility of the thoracic volume estimator.

75 thoracic rib cages reconstructed by the five participants were used to validate the accuracy and the precision of each reconstructed bone, including the vertebrae, ribs, and sternum. For the accuracy validation, I computed the statistical data, i.e., RMS errors of the positions and rotations, for each bone. Furthermore, CloudCompare provided the statistical results, such as the absolute mean error, mean absolute maximal error, and the RMS error of each bone group, which were used to validate the accuracy of the shape morphology for different bone segments (vertebra, rib, and sternum). For the precision validation, the statistical data, i.e., the RMSSD and 95% CI, was computed to investigate

the reproducibility and stability of the thoracic volume estimator. Those statistical results show that our reconstruction ability of the vertebrae in the postures and the shape morphology is comparable to the previous literature. For the ribs, even though the results indicate that the rib's reconstruction errors are higher than the vertebrae or sternum, their inter-observer reproducibility is better than the previous studies. However, for the sternum, the accuracy and precision were seldom mentioned in previous literature, but the reconstruction accuracy of the sternum was better than the vertebrae and the ribs in my study.

For thoracic volume validation, my reconstruction method was firstly compared with the gold standard method (a CT scan). The mean error of the thoracic volume accuracy was below 3% for all participants, which met the accurate requirement for the pulmonary function test instrument proposed by the American Thoracic Society. In the statistical analysis, the two-way ANOVA analysis without replication presented that there was no significant difference between the thoracic volume values computed by CT scan data and by the thoracic volume estimator using orthogonal fluoroscopy images; this confirms the reliability and consistency of our developed program. For the inter-observer reproducibility (precision) study, the comparison between our results and the previous literature led to the conclusion that the thoracic volume reconstruction performance through our thoracic volume estimator was superior. Besides, I compared my thoracic volume reconstruction method with the three previous methods which also used radiographs to estimate the thoracic volume. The previous methods directly used the parameters which were easily measurable on the X-rays of the subjects without spine deformity problems and the thoracic volume could be quickly determined through their published equations. After comparing their methods with my reconstruction method, I found that their thoracic volume results were not accurate enough to estimate the thoracic volume for spine or non-spine deformity subjects. In conclusion, my reconstruction method (thoracic volume estimator) offers a reliable and reproducible way to measure the thoracic volume for spine or non-spine cohorts via orthogonal X-rays.

Chapter 5

Application of the Thoracic Volume Estimator to Monitor Thoracic Volume Variation in Early Onset Scoliosis Patients and Adult Idiopathic Scoliosis Patients

The thoracic volume estimator we develop to reconstruct patient-specific rib cages and thoracic volumes via biplanar X-rays can be applied to monitor the variation between pre-treatment and post-treatment. Consequently, Chapter 5 demonstrates the usage of the developed graphical user interface and Blender add-on package to reconstruct the rib cage and thoracic volume for pediatric and adult scoliosis population. Six early onset scoliosis patients undergoing growing rod surgery need to periodically have an examination. The rods must be lengthened every half year to release the spine so that it can extend, and we need to understand the change in the thoracic volume in different examination periods. Subsequently, ten adult idiopathic scoliosis patients who received bracing or surgical treatments during their adolescence were recruited to track the respiratory function with the help of a pulmonary function test. The correlation between thoracic volume and the parameters in pulmonary function tests is studied. Lastly, a conclusion is made based on my findings in pediatric and adult scoliosis patients.

5.1 Overview

In clinical settings, doctors classify pulmonary disorders into two categories: obstructive lung disease and restrictive lung disease. The former is characterized by the airway obstruction which is associated with several disorders like chronic bronchitis, asthma, bronchiectasis, and emphysema [87]. The latter is caused by different conditions where one of the triggers is tied to the spine deformity. In general, a pulmonary function test (PFT) [88] is used to evaluate and diagnose lung function, and physicians depend on the test results to identify the disease patterns of the patients (obstructive or restrictive lung disease). In the PFT, some parameters including total lung capacity (TLC), vital capacity (VC), and residual volume (RV) can infer the lung volume and lung capacity, as can be seen in Figure 5.1. Other respiratory parameters, such as forced vital capacity (FVC) and forced expiratory volume in the first second (FEV1), are often employed to assess the pulmonary mechanics for the spine patients. Restrictive lung disease patients have difficulty fully expanding during inhalation. For distinguishing restrictive lung disease from obstructive lung disease, one criterion is to judge if a decrease in TLC below 5% of the predicted value occurs. Besides, FVC and FEV1 both decrease proportionally in restrictive lung disease, but the FEV1/FVC is generally normal (>80%) [89]. However, pediatric spine patients, especially under the age of 5, might not be able to follow the instructions to accurately perform the PFT [2,89]. Therefore, it is still challenging for doctors to examine children's respiratory function during the spine deformity therapies.

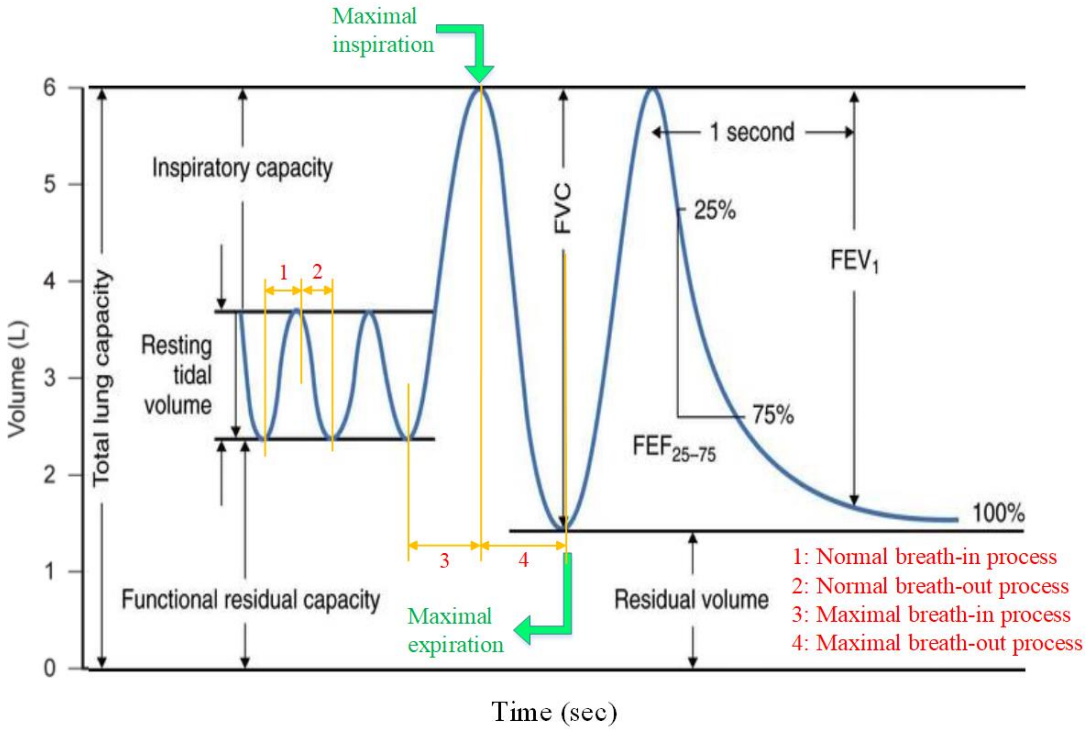

Figure 5.1 Pulmonary function test parameters (Redrawn from [90])

Scoliosis is an abnormal lateral curvature of the spine which involves not only the side to side curvature (in the frontal view) but also an axial rotation of the vertebrae. This disorder affects approximately 3% of the population [91]. A sagittal Cobb angle with 10 degrees or more is the criterion for doctors to diagnose scoliosis symptoms [92]. The measurement of the Cobb angle is to identify the upper and lower ends (endplates) of the spine curvature which tilt most severely and it is demonstrated in Figure 5.2 [93]. Cobb angles can be classified into two different levels, moderate level with Cobb angle of 10-39 degrees and severe level with a ≥40-degree Cobb angle [94]. Scoliosis is characterized by the axial rotations of the vertebrae and is typically classified as either congenital or idiopathic scoliosis. The cause of idiopathic scoliosis is still unknown, and it may occur at the infantile (0-3 years), juvenile (3-10 years), adolescent (10-18 years) or adult (above 18 years) age depending on when the scoliosis symptom presents [95]. For children, idiopathic early onset scoliosis typically occurs before age 10 with a Cobb angle larger than 10 degrees [96]. Early onset scoliosis (EOS) not only affects a child's growth alignment but

it also potentially impairs pulmonary function by decreasing the thoracic volume which is the space available for lungs to expand [61]. Scoliosis with a Cobb angle of more than 40 degrees is commonly associated with impaired pulmonary function and back pain [97], and cardiorespiratory failure is detectable with a severe Cobb angle greater than 90 degrees [98,99]. Therefore, the purposes of surgical interventions, such as a growing rod surgery, are to prevent further deterioration and to correct the spinal deformity which affords the growing child a pathway for normal growth and development. EOS is a complex, three-dimensional disease that accounts for <1% of the entire scoliosis population [96].

For treatments in EOS patients, there is a wide range of options from conservative care to corrective surgery. If the severity of the EOS is less than a 40-degree Cobb angle, doctors will select the conservative treatment, such as physical bracing or casting [100]. If the Cobb angle is larger than 45 degrees in a developing child, it is recommended to involve the growing rod surgery in the surgical intervention [101]. The growing rod surgery is commonly involved in the correction of the pediatric spine deformity. Surgeons insert telescoping growing rods and lengthen the rods about one centimeter every six months. The lengthening procedures allow the growth of the spine and maintain the spine correction for pediatric patients. When the patient's iliac crest on the pelvis is mature and fused based on the Risser classification [102], doctors consider the vertebral growth is complete. Thus, the growing rod instrument is removed and a spinal fusion operation is performed. If EOS patients are left untreated, this may lead to progression of the spinal curve, respiratory complications, early cardiopulmonary failure, and increased mortality due to the decrease in thoracic volume for lung expansion [103–106]. However, the challenge is to determine when is the good timing to intervene with the EOS patients. Especially, it is difficult to track the pulmonary function variations of the EOS patients periodically. In contrast, CT scan and X-ray techniques can both be used to measure the lung volume or thoracic volume, but the former is riskier to monitor the pulmonary function status due to its relatively high-dose radiation. In the previous chapter, I proved that our thoracic volume estimator is accurate enough to measure the thoracic volume (with below 3% accuracy). Therefore, the

thoracic volume measurement via our thoracic volume estimator using X-rays can be a potential surrogate to be applied in the clinical setting.

In Section 5.2, I use our previously developed program to follow up the rib cage and thoracic volume variations for EOS patients pre-operatively and post-operatively. An investigation will be conducted into whether the growing rod surgery can enlarge the thoracic volume through periodically lengthening the implanted growing rod. Moreover, I further investigate the correlation between thoracic volume and spine parameters, including Cobb angles and thoracic kyphotic height, as well as the influence of the growing rod surgery on thoracic volume. Additionally, I examine and discuss the thoracic volume variation when taking the normal growth into account and see if the thoracic volume is increased by the growing rod surgery.

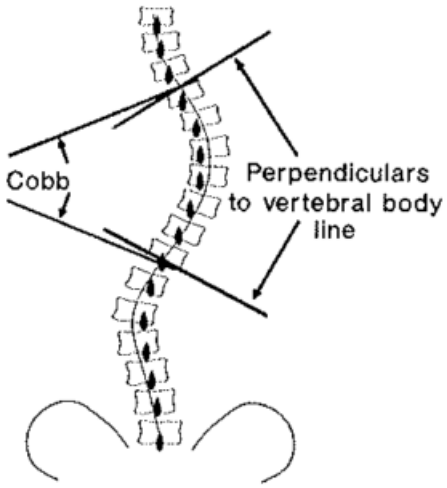

Figure 5.2 Measurement of a Cobb angle in frontal view [93]

Idiopathic scoliosis can also happen in the adolescent and adult population, and the treatments include both bracing and surgery. Restrictive lung disease often happens in scoliosis patients, especially with severe spine deformities [23,98]. However, the relationship between thoracic volume and pulmonary function is not broadly discussed, and different anatomic abnormalities in spine deformities (e.g., scoliosis, kyphosis, and

osteoporosis) or different age population can lead to varying results [23,107,108]. For scoliosis symptoms, the previous literature has shown that the deformity of the thoracic rib cage may have detrimental effects on the respiratory function in adolescent [23,109–111] or adult idiopathic scoliosis patients [104,112]. For adolescent idiopathic scoliosis, Newton et al. [109] found that increasing spine deformity in adolescent idiopathic scoliosis is associated with the reduced pulmonary function in their 631 patients. They identified that pulmonary function impairment happened in some adolescent idiopathic scoliosis patients with moderate spine curvature. Ledonio et al. [23] had a 2-year thoracic volume follow-up in adolescent idiopathic scoliosis patients with severe Cobb angles (68.5 degrees on average) before and after surgical treatments; they found pre-operative to post-operative changes in total lung capacity and thoracic volumes were strongly correlated while pre-surgical total lung capacities were low. Aaro and Ohlund [110] conducted studies of the thoracic rib cages by CT scan and observed a negative correlation between scoliotic deformity (Cobb angle) and PFT parameters, including TLC, VC, and functional RV in 33 adolescent scoliosis patients. Johnston et al. [111] concluded the preoperative PFT's parameters, including FVC and FEV1, were correlated to the severity of scoliosis (Cobb angle) through 858 adolescent idiopathic scoliosis patients. For adult idiopathic scoliosis, Weinstein et al. [112] indicated that idiopathic scoliotic curves progressively increased during the adult life, especially when the thoracic Cobb angle measured between 50 and 80 degrees. Also, the clinically relevant respiratory impairment occurred when the severe curve exceeded 100 degrees. Pehrsson et al. [104] had a 20-year follow up for 24 surgically untreated adult idiopathic scoliosis patients and found 6 patients with predicted vital capacity below 45% and scoliotic curve larger than 110 degrees portrayed developing respiratory failure during the follow up. Pehrsson et al. [113] also pointed out the thoracic rib cage gradually takes up a better position to promote an increased lung volume 25 years after surgical or bracing treatments. In their study, they did not find a significant correlation between VC and FEV1 and scoliotic angles before and after any treatment, but there was a correlation between pre-operative scoliotic angles and percentage predicted VC and FEV1. It is worthwhile to mention that they considered the growth of alveoli is complete

by the age of 8, so the reduced VC before treatments was unlikely due to reduced lung tissue, but due to restricted thoracic rib cage instead. In addition, physical bracing or corrective surgery can be associated with the improvement of pulmonary function in those who have idiopathic scoliosis. [23,53,113–115]. Overall, the neglect of any treatment for idiopathic scoliosis patients may result in the progression of the spine curvature eventually and further cause pulmonary complications and the reduction of life expectancy due to the decreasing size of the thoracic cavity/volume [103,116,117].

In Section 5.3, I hypothesize that the thoracic volume can be used to infer the respiratory function in adult idiopathic scoliosis patients. Thus, I aim to correlate thoracic volume to the parameters in PFTs in adult idiopathic scoliosis patients after they received spine treatments during their adolescence, either with physical bracing or spinal fusion surgery. The relationship between thoracic volume/pulmonary function and the spine parameters is discussed, and the results are also compared with those gained from EOS patients.

5.2 Early Onset Scoliosis Patients

5.2.1 Rib Cage Reconstruction and Thoracic Volume Measurement of Six Pediatric Patients

In this study, six EOS pediatric patients, three boys and three girls (range, 1-10 years), with severe pre-operation Cobb angles (range, 49-87 degrees) were recruited and the University of Minnesota IRB determined this study was not human subject research. The general information of the patients was listed in Table 5.1. These six children were subjected to several 2D radiographs throughout the entire procedure of the growing rod interventions. Only one of them has undergone the spinal fusion surgery so far, and the other five are still undergoing their lengthening procedures (LPs). In order to reconstruct their rib cages and thoracic volumes in 3D, I selected each EOS patient's X-rays from three different examination periods, including the pre-operation (pre-op), one LP post-operation (post-op), and the latest LP post-op. With the help of the thoracic volume estimator, Figure 5.3

shows the frontal and lateral X-rays, reconstructed rib cages in white, and simulated thoracic volume in yellow for six EOS patients in the Blender environment. The image in Figure 5.3 (a)(i) presents the reconstructed rib cage and thoracic volume before the growing rod operation in Patient 1. Figure 5.3 (a)(ii) exhibits the variations in the third period of the growing rod lengthening-procedure (LP3) after the operation, and Figure 5.3 (a)(iii) in the fifth period of the growing rod lengthening-procedure (LP5) after the operation. The normal interval between the LP3 and LP5 is one year. In other words, the lengthening procedures are performed at six-month intervals. Traditionally, patients undergo lengthening procedures through a small incision on an outpatient basis. It is worth noting that Figure 5.3 (d)(iii) displays the situation after the fusion operation, which is performed once the doctors assess the spine is mature. Table 5.2 includes the data of the EOS patients regarding the level of the implant growing rods, T1 to T12 thoracic height, and primary Cobb angles at different examination periods, and all such information can be identified according to the frontal and lateral X-rays. I also present the reconstructed thoracic volumes and the thoracic volume variation in Table 5.2.

Table 5.1 Information of pediatric spine patients before surgical treatments

Patient No.	First-time visiting age (year)	Gender
1	6	M
2	6	M
3	1	F
4	10	F
5	6	F
6	3	M

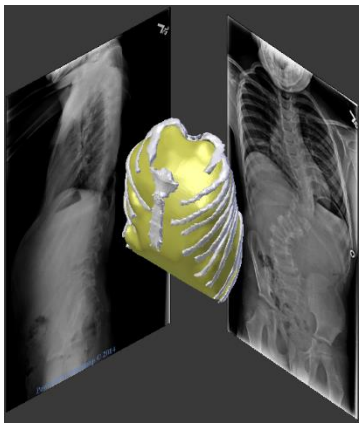

(i) Pre-operation

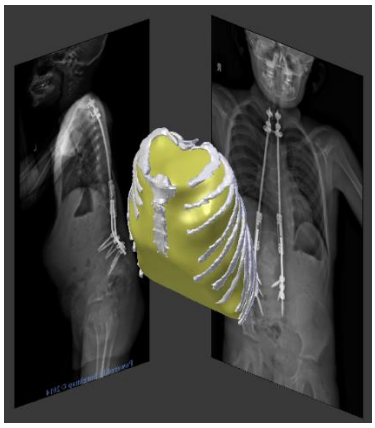

(ii) Post-operation LP3

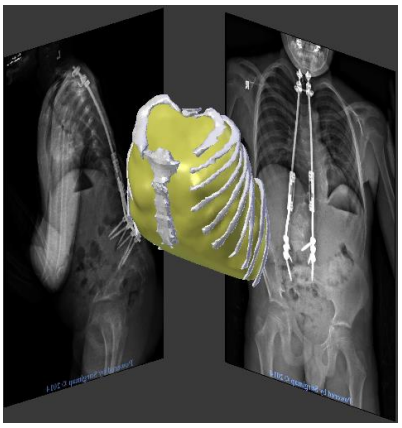

(iii) Post-operation LP5

(a) Patient 1

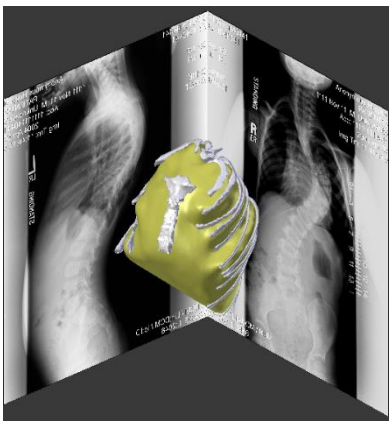

(i) Pre-operation

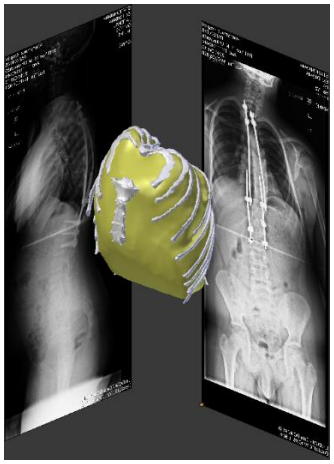

(ii) Post-operation LP4

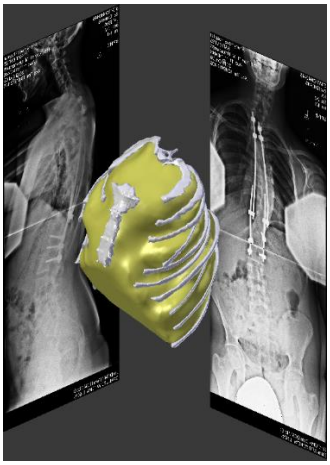

(iii) Post-operation LP8

(b) Patient 2

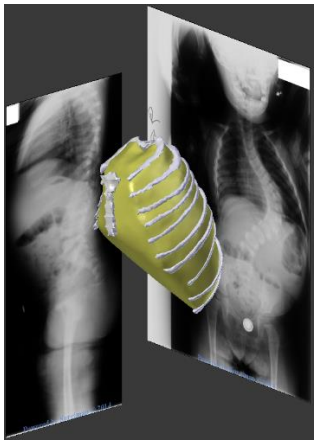

(i) Pre-operation

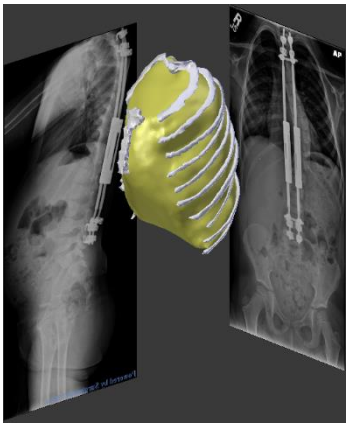

(ii) Post-operation LP5

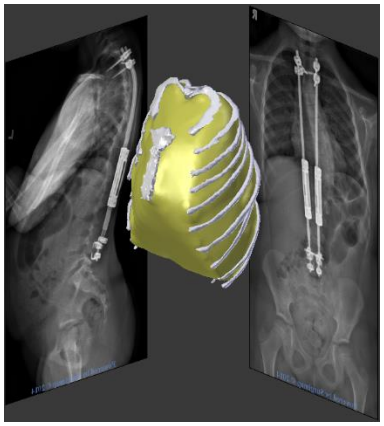

(iii) Post-operation LP10

(c) Patient 3

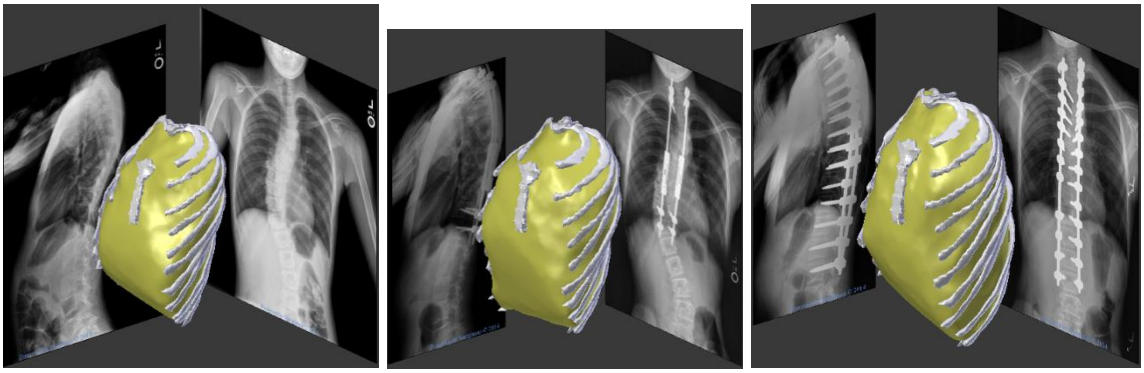

(i) Pre-operation (ii) Post-operation LP3 (iii) Post-operation fusion

(d) Patient 4

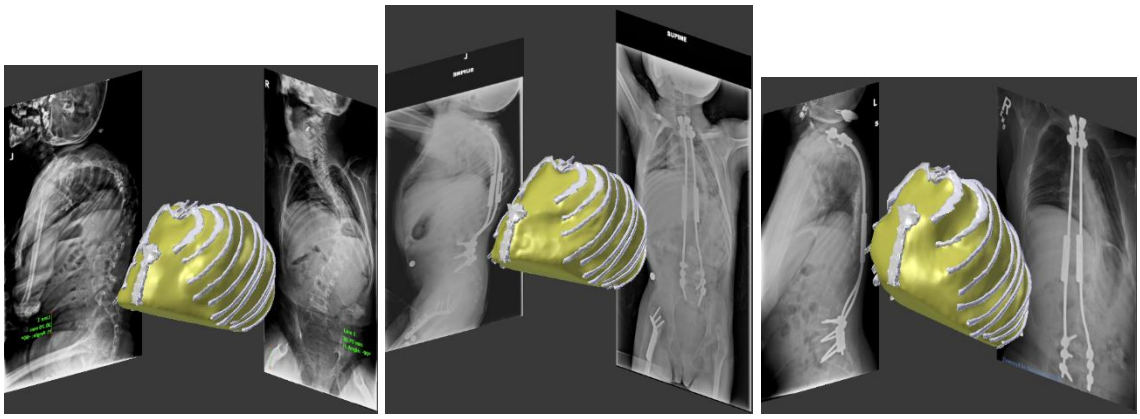

(i) Pre-operation (ii) Post-operation LP1 (iii) Post-operation LP5

(e) Patient 5

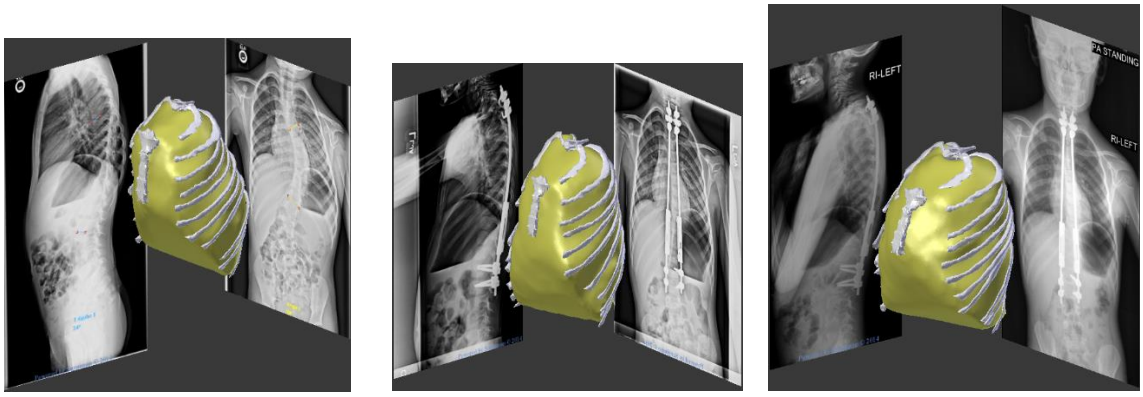

(i) Pre-operation (ii) Post-operation LP1 (iii) Post-operation LP4

(f) Patient 6

Figure 5.3 Reconstruction of thoracic rib cages and thoracic volumes for six EOS patients

Table 5.2 Pre-operation and post-operation information of EOS patients

ID	Patient 1			Patient 2		
Procedure	**Pre-operation**	**Post-operation LP3**	**Post-operation LP5**	**Pre-operation**	**Post-operation LP4**	**Post-operation LP8**
Age	6	7	9	6	8	10
Growing rod implant level	-	T1-S1	T1-S1	-	T2-T12	T2-T12
Primary thoracic curve	T8-T12	T8-T12	T8-T12	T5-T12	T5-T11	T5-T11
Primary Cobb angle (degrees)	63	47	47	78	27	52
% Cobb angle decrease change	-	25.4%	25.4%	-	65.4%	33.3%
Thoracic T1-T12 height (mm)	183.6	209.0	221.0	154.4	180.2	204.9
Thoracic volume (cc)	2726	3424	4231	1640	2297	3212
% Thoracic volume change	-	25.6%	55.2%	-	40.1%	95.9%

ID	Patient 3			Patient 4		
Procedure	**Pre-operation**	**Post-operation LP5**	**Post-operation LP10**	**Pre-operation**	**Post-operation LP3**	**Post-operation Fusion**
Age	1	3	6	10	11	12
Growing rod implant level	-	T2-L4	T2-L4	-	T2-T12	T2-L3
Primary thoracic curve	T6-T12	T7-T12	T7-T12	T2-T7	T2-T7	T2-T7
Primary Cobb angle (degrees)	85	34	23	49	48	34
% Cobb angle decrease change	-	60.0%	72.9%	-	2.0%	30.6%
Thoracic T1-T12 height (mm)	152.0	163.7	177.7	201.0	207.0	224.0
Thoracic volume (cc)	1726	1858	2080	3332	3575	4450
% Thoracic volume change	-	7.6%	20.5%	-	7.3%	33.6%

ID	Patient 5			Patient 6		
Procedure	**Pre-operation**	**Post-operation LP1**	**Post-operation LP5**	**Pre-operation**	**Post-operation LP1**	**Post-operation LP4**
Age	6	7	10	3	4	6
Growing rod implant level	-	T1-L5	T1-L5	-	T1-L3	T1-L3
Primary thoracic curve	T4-T12	T4-T12	T5-T12	T6-T12	T4-T10	T4-T10
Primary Cobb angle (degrees)	87	74	77	59	26	22
% Cobb angle decrease change	-	14.9%	11.5%	-	55.9%	62.7%
Thoracic T1-T12 height (mm)	125.0	145.0	182.0	184.0	187.5	218.0
Thoracic volume (cc)	1821	2005	2870	2689	2730	3623
% Thoracic volume change	-	10.1%	57.6%	-	1.5%	34.7%

5.2.2 Results

In Figure 5.4, I present the tendency of the thoracic volume variation between three examination visits for six EOS patients. As can be seen in the figure, the thoracic volumes of the six EOS patients increase through the growing rod surgical treatments and the multiple lengthening procedures. Hence, the EOS patients can benefit from the growing surgery and their spines can extend along the implant rods. In order to study the relationship between thoracic volume and the spine parameters, I correlate the Cobb angle and thoracic height from T1 to T12 level with the reconstructed thoracic volumes. Based on Table 5.2, I draw two scatter graphs with a regression line in Figure 5.5; Figure 5.5 (a) shows the relation between T1-T12 height and thoracic volumes, and Figure 5.5 (b) indicates the relation between the Cobb angle and thoracic volume. Apparently, there is a strong positive correlation ($r = 0.93$; $p < 0.01$) between thoracic height and thoracic volume as can be seen

in Figure 5.5(a). Glotzbecker et al. [108] also observed a significant correlation between thoracic height and pulmonary function indices in EOS patients, including total lung capacity, forced vital capacity, and forced expiratory volume in the first second. They suggested that the thoracic height can be used as a weak indicator to infer the pulmonary function in EOS patients. Conversely, I cannot observe any significant correlation ($r = -0.43$; $p = 0.07$) between the primary Cobb angle and the thoracic volume in Figure 5.5(b). In Redding and Mayer's paper [107], they also found no correlation between lung function and Cobb angles in their EOS patients.

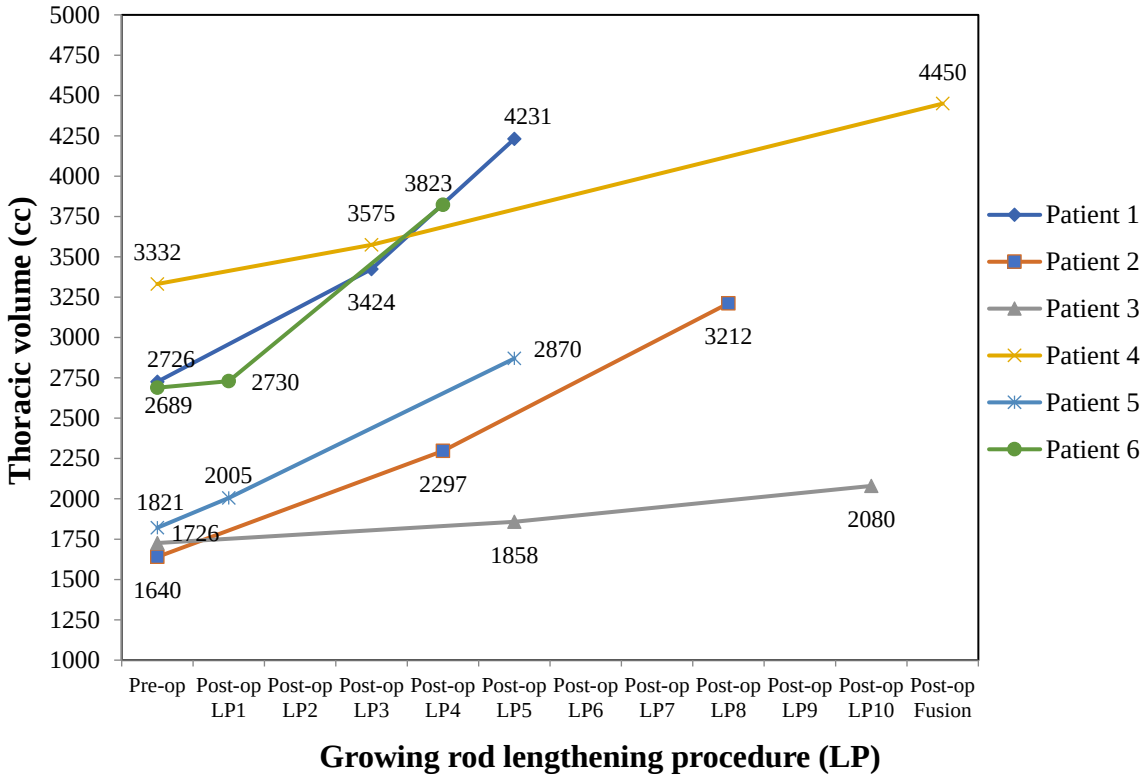

Figure 5.4 Thoracic volume variations in different rod lengthening procedures

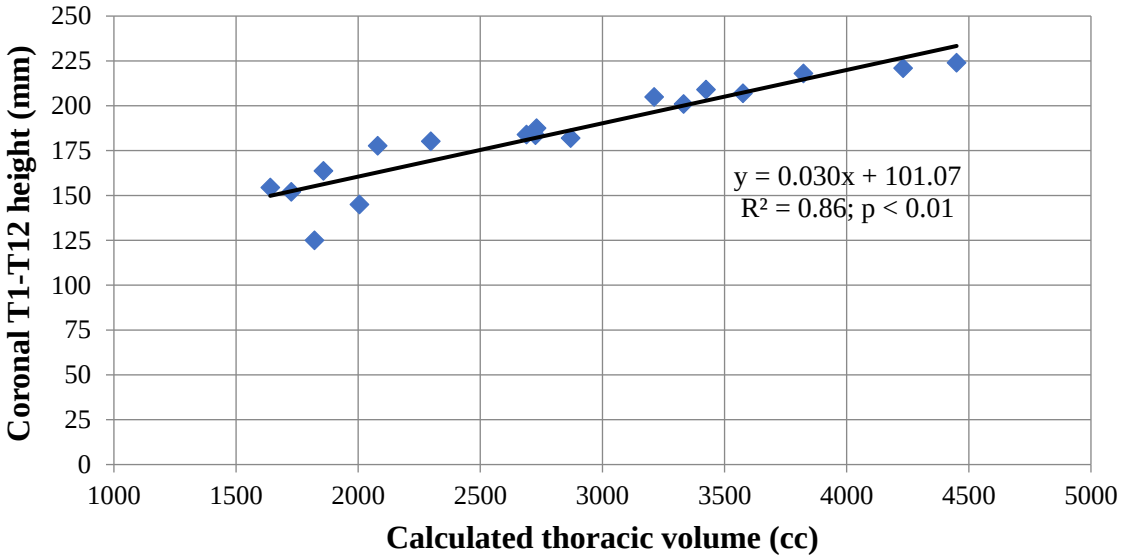

(a) Correlation between thoracic height (T1-T12) and thoracic volume

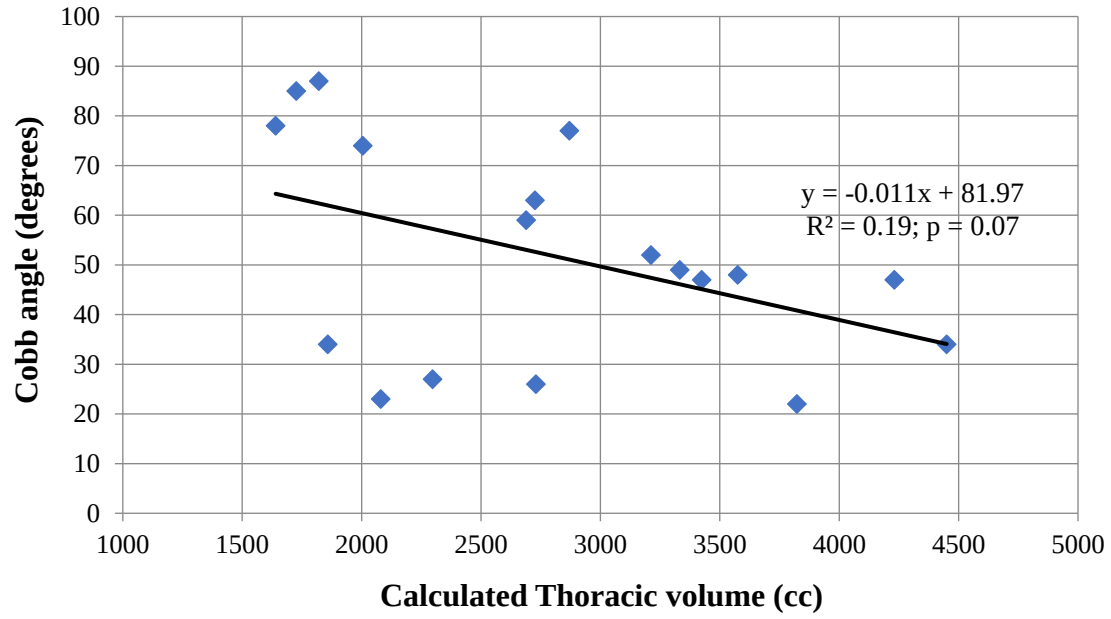

(b) Correlation between Cobb angles and thoracic volume

Figure 5.5 Correlation of thoracic volume with spine parameters during growing rod surgical treatments

5.2.3 Discussion

Depending on the previous results, it seems that the EOS patients can benefit from the growing rod surgery without considering the growth rate of the children. Nevertheless, what if we take the normal growth into consideration, will the growing rod surgery still contribute to the thoracic volume increase in EOS patients? When might be the best timing for EOS patients to undergo the growing rod surgery? To dig into these interesting questions, I first collect the growth pattern of the children. Gillingham et al. [118] revealed that the growth rate from T1 to T12 (thoracic height) levels is the largest between birth and age 5 years, averaging >1.25 cm per year, and then becomes decelerated between ages 5 and 10, and finally becomes accelerated again between ages 10 and 15. In 1990, Dimeglio and Bonnel [16] studied the growing rate of the thoracic volume at different ages. In Figure 5.6, I summarize the growth rate of the thoracic volume in children between new born and age 15 for boys and girls in [16]. All slope markers in this figure are the percentage of the thoracic volume when compared to the final thoracic volume value at age 15. Due to the known growing rate of the children's thoracic volume, I can calculate the thoracic volume increase due to the growing rod surgery. I subtract the normal growth rate from the thoracic volume variation rate I acquired in Table 5.2 using the equation expressed as

$$\mathrm{TVP}=\frac{(m_a - m_b)}{m_b} - \frac{(n_a - n_b)}{n_b} \tag{5.1}$$

where TVP stands for thoracic volume percentage, m_b and m_a stand for the pre-operative thoracic volume and post-operative thoracic volume measured by the developed software respectively; n_b and n_a represent the normal growth rate at pre-operative age and at post-operative age respectively in Table 5.3.

The postoperative thoracic volume and preoperative thoracic volume can be measured via our developed program, and the normal growth rate of children's thoracic volume is referred to in Table 5.3. With the help of Eq. (5.1), the influence of the children's growth on the thoracic volume variation can be removed. Table 5.3 shows the thoracic volume variation of six pediatric patients after growing rod surgery and different lengthening

procedures. Through Eq. (5.1), I compute the thoracic volume variation due to the growing rod surgery, and the result is also shown in Table 5.3. It is easy to identify that the growing rod surgery does increase the thoracic volume in Patients 1, 2, and 5 between pre-operation and post-operation examination periods. However, it seems that the growing rod surgery does not directly affect the thoracic volume in Patients 3 4, and 6 when considering the effect of the normal growth rate. There are two potential interpretations about these phenomena. The first one is that the growth rate in different age periods is different. In Figure 5.6, I divide the growth rate into three main periods based on the reference [16] and indicate the slope in these three periods. The blue slopes in this figure show the normal growth rate of the thoracic volume in boys and girls, and the three green vertical lines for each patient indicate three different thoracic volumes at different ages. It is obvious that the growth rate of the thoracic volume between age 10 to age 15 is the fastest, and the growth rate between age 0 and age 5 is secondary; the growth rate between age 5 and age 10 is slow compared with the other two periods. This fact illustrates that the growing rod surgery benefits Patients 1, 2, and 5 due to the slow normal growth rate of the thoracic volume between age 5 and age 10. As for Patients 3, 4, and 6, their growing rod surgery and the following lengthening procedures occur mostly at the second-fastest growing period and at the fastest growing period respectively. As a result, the thoracic volume changes for these three patients mainly result from children's normal growth. The second potential interpretation is that the growing pattern shown in Figure 5.6 is for normal children without spine disease, so it may not be suitable to apply to children with spine deformities. It is very likely that the growth rate of the thoracic volume is slower in young scoliosis patients than in normal children. The thoracic volume variation may increase due to the growing rod surgery while considering the slow pattern of growth rate in pediatric spine patients. However, Figure 5.6 is the only data available in the literature. The growing rod surgery can make sure the scoliosis curve is partially corrected and it has the potential to release the thoracic space to prevent the pulmonary function disease (e.g., restrictive lung disease), which is triggered by spine deformity.

As for the best timing for EOS patients to undergo the growing rod surgery, it is still under debate. In this discussion, I have no intention to suggest doctors perform the growing rod surgery between age 5 and 10, but instead I want to point out a large contribution of the growing rod surgery to the thoracic volume increase during that period. It is worth mentioning that the growth of lungs stops approximately at age 8, so some doctors recommend the best timing to perform the growing rod surgery for EOS patients is before 8 years of age [119]. Potentially, if the growing rod surgery is performed when patients are too young, the rods might have a higher chance to be broken due to children's growth [106]. However, without any intervention for the progressive spine curvature, the limitation of the thoracic cavity/volume will possibly constrain the expansion of the lungs, and can adversely cause restrictive lung disease or thoracic insufficiency syndrome in pediatric patients [120].

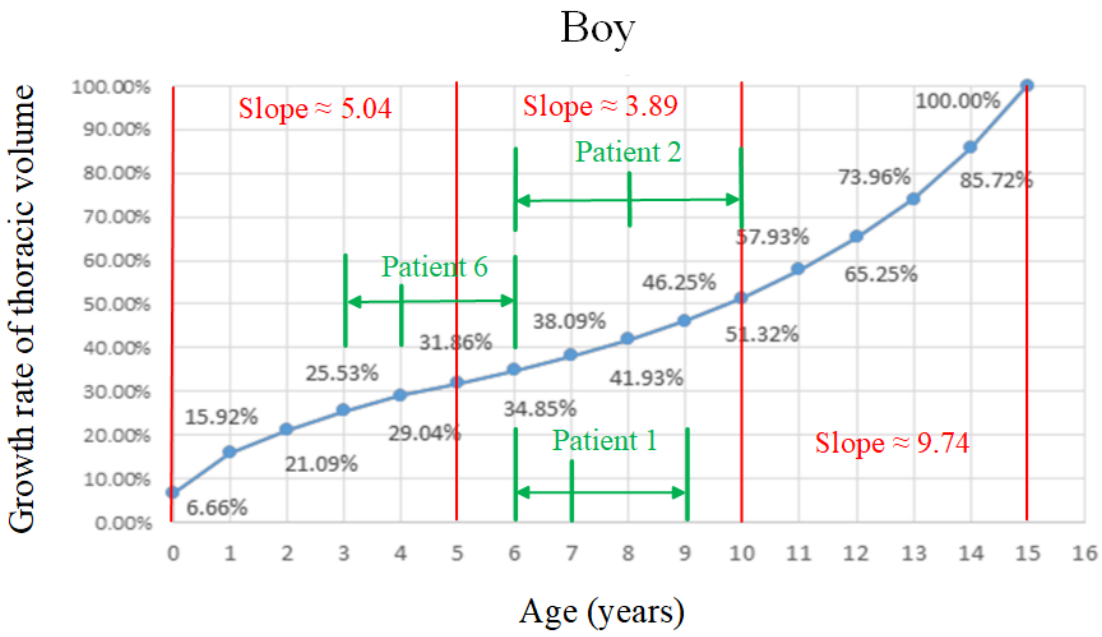

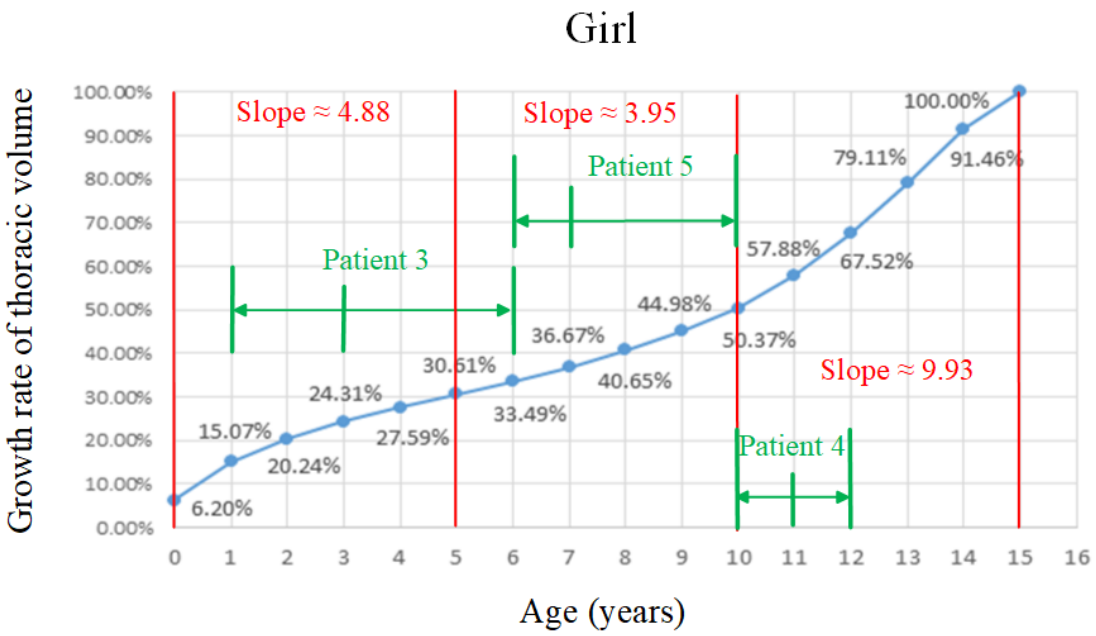

Figure 5.6 Growth rate of the thoracic volume for boys and girls (Redrawn from [16])

Table 5.3 Thoracic volume variation due to growth and growing rod treatments

ID	**Patient 1 (boy)**			**Patient 2 (boy)**		
Procedure	**Pre-operation (Age 6)**	**Post-operation LP3 (Age 7)**	**Post-operation LP5 (Age 9)**	**Pre-operation (Age 6)**	**Post-operation LP4 (Age 8)**	**Post-operation LP8 (Age 10)**
Thoracic volume (cc)	2726	3424	4231	1640	2297	3212
% Thoracic volume change ($\frac{m_a - m_b}{m_b}$)	-	25.6%	55.2%	-	40.1%	95.9%
% Normal thoracic volume growth rate of children between different ages ($\frac{n_a - n_b}{n_b}$)	-	9.3%	32.7%	-	20.3%	47.3%
% Thoracic volume change due to the growing rod surgery	-	16.3%	22.5%	-	19.8%	48.6%

ID	Patient 3 (girl)			Patient 4 (girl)		
Procedure	**Pre-operation (Age 1)**	**Post-operation LP5 (Age 3)**	**Post-operation LP10 (Age 6)**	**Pre-operation (Age 10)**	**Post-operation LP3 (Age 11)**	**Post-operation Fusion (Age 12)**
Thoracic volume (cc)	1726	1858	2080	3332	3575	4450
% Thoracic volume change ($\frac{m_a - m_b}{m_b}$)	-	7.6%	20.5%	-	7.3%	33.6%
% Normal thoracic volume growth rate of children between different ages ($\frac{n_a - n_b}{n_b}$)	-	61.3%	122.2%	-	14.9%	34.0%
% Thoracic volume change due to the growing rod surgery	-	-53.7%	-101.7%	-	-7.6%	-0.4%

ID	Patient 5 (girl)			Patient 6 (boy)		
Procedure	**Pre-operation (Age 6)**	**Post-operation LP1 (Age 7)**	**Post-operation LP5 (Age 10)**	**Pre-operation (Age 3)**	**Post-operation LP1 (Age 4)**	**Post-operation LP4 (Age 6)**
Thoracic volume (cc)	1821	2005	2870	2689	2730	3623
% Thoracic volume change ($\frac{m_a - m_b}{m_b}$)	-	10.1%	57.6%	-	1.5%	34.7%
% Normal thoracic volume growth rate of children between different ages ($\frac{n_a - n_b}{n_b}$)	-	9.5%	50.4%	-	13.7%	36.5%
% Thoracic volume change due to the growing rod surgery	-	0.6%	7.2%	-	-12.2%	-1.8%

5.3 Adult Scoliosis Patients

In this section, the developed program is employed to reconstruct the rib cage and thoracic volume for ten adult scoliosis patients using biplanar X-rays. I hypothesize the thoracic volume can be used to infer the pulmonary function for spine deformity patients. Based on the calculation of the thoracic volumes in patients, I correlate the parameters in the pulmonary function test with the measured thoracic volume. Subsequently, the findings about the relationship between thoracic volume and the two spine indices, thoracic T1-T12 height and Cobb angle, are discussed and compared to those findings in early onset scoliosis patients in Section 5.2.2.

5.3.1 Rib Cage Reconstruction and Thoracic Volume Measurement of Ten Adult Scoliosis Patients

Ten adult scoliosis patients (9 females, 1 male) with different treatments during their adolescence were recruited via Mayo Clinic to perform the pulmonary function test at a minimum 20-year follow-up. This study was approved by the Mayo Clinic IRB. All patients were subjected to 2D radiography using the EOS® imaging system [48], which could film the posterior-anterior and lateral radiographs simultaneously. The mean age of the subjects was 44 years (range, 34 to 54 years) with a mean Cobb angle of 45.9 degrees (range, 30 to 70 degrees). In addition, the mean height was 167.8 cm (±8.8cm) and the mean weight was 84.7kg (±19.3kg). Six patients underwent physical bracing, and four patients had spinal fusion surgery in their adolescence. The detailed information of the pulmonary function parameters in the PFT, Cobb angle, and the calculated thoracic volume are listed in Table 5.4. With the help of the developed semi-automatic program, patient-specific thoracic rib cages and the thoracic volumes of ten adult scoliosis patients are reconstructed through posterior-anterior and lateral X-rays. The reconstructed thoracic rib cages (white) and the calculated thoracic volume (yellow) for ten adult scoliosis patients are shown in Figure 5.7.

Table 5.4 Pulmonary function tests and thoracic volume information in ten adult scoliosis patients

Patient No.	Age (year)	Gender	Height (cm)	Thoracic height (cm)	Cobb angle (degs)	Cobb angle location	Treatment	TLC (cc)	VC (cc)	RV (cc)	FVC (cc)	FEV1 (cc)	Thoracic volume (cc)
1	49	F	177.5	22.6	60	T7-T12	Brace	5760	3500	2270	3420	2500	8434.7
2	38	F	159.6	24.4	36	T5-T12	Brace	4320	2200	2120	2160	1660	6485.5
3	35	F	157.2	22.5	36	T6-T11	Brace	4010	2730	1290	2660	2310	6106.9
4	49	F	165.6	22.7	70	T11-L4	Brace	4350	2740	1610	2680	2180	6518.4
5	50	F	164.1	23.6	30	T4-T12	Surgery	5860	3300	2560	3260	2070	7257.1
6	44	F	163.9	23.7	34	T9-L3	Surgery	5520	3610	1910	3580	2720	6378.2
7	44	F	166.1	22.8	40	T7-L2	Surgery	4400	3010	1390	3100	2430	5054.7
8	54	M	187.1	25.6	71	T6-L3	Surgery	5920	3760	2160	3590	2810	8989.9
9	45	F	171.2	23.8	54	T6-T12	Brace	4660	3100	1560	2950	2340	6348.9
10	34	F	166.1	24.9	41	T7-L2	Brace	3990	2540	1440	2450	1870	4872.4

Total lung capacity (TCL), vital capacity (VC), residual volume (RV); forced vital capacity (FVC); forced expiratory volume in the 1 second (FEV1)

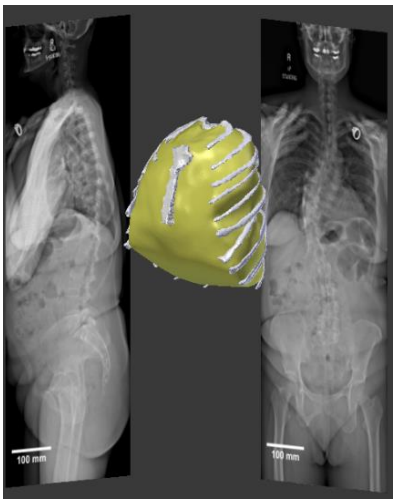

(a) Patient 1

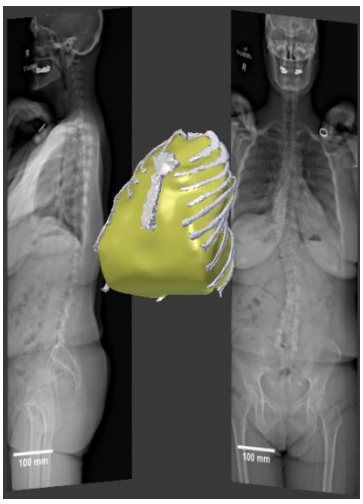

(b) Patient 2

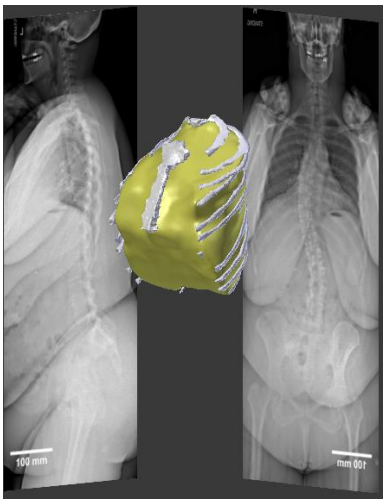

(c) Patient 3

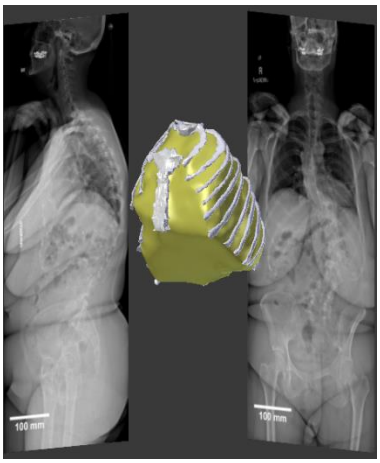

(d) Patient 4

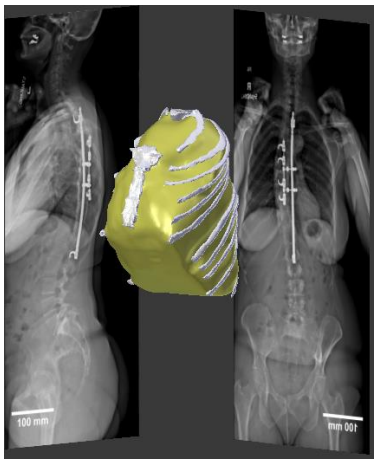

(e) Patient 5

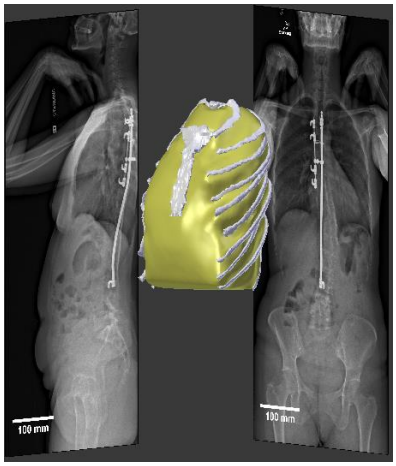

(f) Patient 6

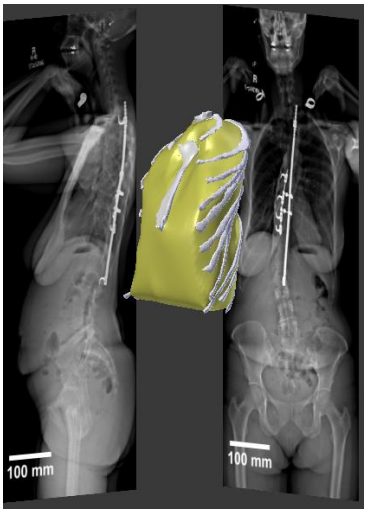

(g) Patient 7

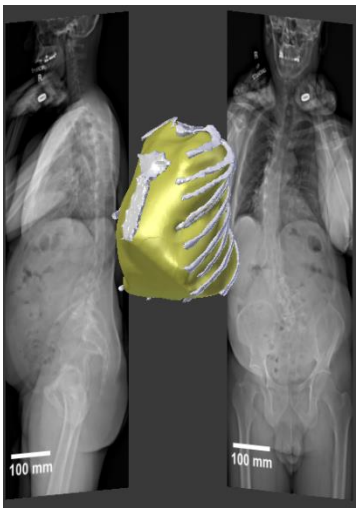

(h) Patient 8

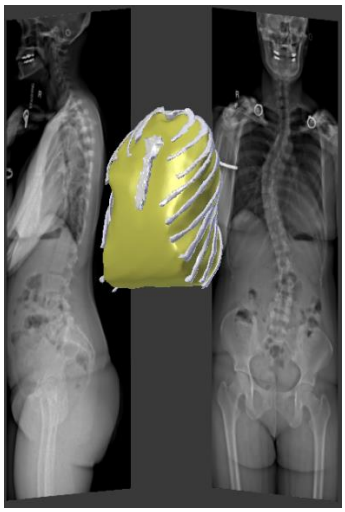

(i) Patient 9

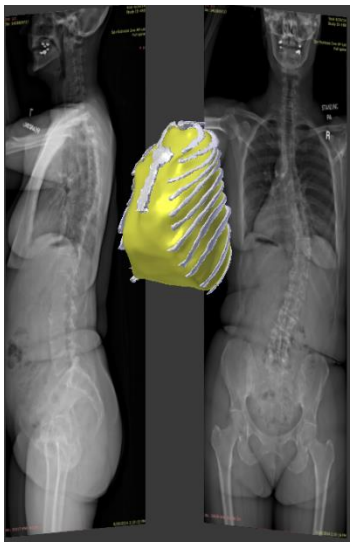

(j) Patient 10

Figure 5.7 3D Reconstruction of the thoracic rib cage (white) and thoracic volume (yellow) in ten adult scoliosis patients

5.3.2 Results and Discussion

Based on the ten adult scoliosis patients' Cobb angles, four patients are considered to have moderate scoliosis (< 40-degree Cobb angle), and six patients severe scoliosis (≥ 40-degree Cobb angle). I found that TLC is correlated with the computed thoracic volume ($r = 0.82$; $p < 0.005$) as shown in Figure 5.8(a). In fact, TLC is larger in the surgical cohort (mean 5425cc) compared to the physical bracing cohort (mean 4514cc). Additionally, the computed thoracic volume is correlated to VC ($r = 0.67$; $p < 0.05$) and RV ($r = 0.74$; $p < 0.05$) separately, as can be seen in Figures 5.8 (b) and 5.8 (c). On the contrary, I do not observe any close correlation between thoracic volume and either FVC ($r = 0.60$; $p = 0.06$) or FEV1 ($r = 0.48$; $p = 0.16$). Also, FVC and FEV1 in all the subjects are typically within the normal range. In this study, I hypothesize that smaller thoracic volume will decrease the space available for lung expansion and thoracic volume can be an indication of the pulmonary function. The results disclose a positive correlation between thoracic volume and TLC, and a correlation between thoracic volume and two spine parameters, including VC and RV. Due to the limited data, I do not know whether different interventions, bracing

or surgery, have any impact on the pulmonary function and the thoracic volume variations before and after the interventions for our adult scoliosis cohorts.

To explore the relationship between thoracic volume and the spine parameters in adult scoliosis patients, I correlated the Cobb angle and thoracic height from T1 to T12 level with the reconstructed thoracic volumes. Figure 5.9 (a) shows no correlation between thoracic height and thoracic volume ($r = 0.60$; $p = 0.07$), and Figure 5.9 (b) also shows no correlation between Cobb angles and thoracic volume ($r = 0.21$; $p = 0.57$). Keeping in mind the results gained in Section 5.2.2, I also cannot observe any correlation between thoracic volume and Cobb angles in adult scoliosis patients. However, the correlation between thoracic volume and thoracic height (T1-T12) is different for EOS patients and for adult scoliosis patients. To further investigate the difference and to see if any relationship between spine parameters and pulmonary function parameters presents, I correlate the pulmonary function parameters (including TLC, VC, FVC, FEV1, and RV) with the Cobb angle and with the thoracic T1-T12 height separately for adult scoliosis patients. Unfortunately, there is no correlation between any pulmonary function parameters and thoracic height, and similar results also appear in the Cobb angle. It seems that the single one-dimensional spine parameter (e.g., thoracic height, thoracic width, and Cobb angles) cannot be directly used to predict the pulmonary function or the thoracic volume in scoliosis patients. In literature, Johnston et al. [111] observed a significantly negative correlation between pulmonary function and main thoracic Cobb angles in adolescent scoliosis patients. However, Pehrsson et al. [113] and Johari et al. [121] did not acquire significant correlation between pulmonary function and Cobb angles in adolescent scoliosis patients. There has been little research conducted on the correlation between the pulmonary function and the thoracic height in adolescent scoliosis patients [115]. For adult scoliosis patients, Akazawa et al. [122] discovered a moderate negative correlation between pulmonary function and main Cobb angles, but Pehrsson et al. [113] found no correlation. However, none of the previous literature studied the relationship between the pulmonary function and thoracic height for adult scoliosis patients. In general, the correlation between

pulmonary function parameters and the spine parameters is still under debate, and scoliosis population of different ages and different individuals can generate different conclusions.

In Chapter 4, I introduced previous research using X-rays to estimate and measure the space of the thoracic volume/cavity [15,54,56,60,115,123], and those works derived the equations to represent the thoracic volume through several spine variables, including thoracic height, frontal thoracic width, and lateral thoracic width, which could be easily measured via X-rays. However, after validating their method to calculate the thoracic volume, I found their thoracic volume accuracy was inferior to ours. Herein, I found Cobb angles cannot be viewed as an indicator to predict the thoracic volume in both EOS and adult scoliosis patients, and thoracic height can be used to infer the thoracic volume for EOS patients only. From these observations, I believe the thoracic volume cannot be simply estimated or measured relying on single or multiple one-dimensional spine parameters on routine X-rays; these parameters include Cobb angles and the thoracic T1-T12 height, because the correlation is distinct in different scoliosis patients. However, pulmonary function in spine deformity patients can be predicted through our thoracic volume estimator.

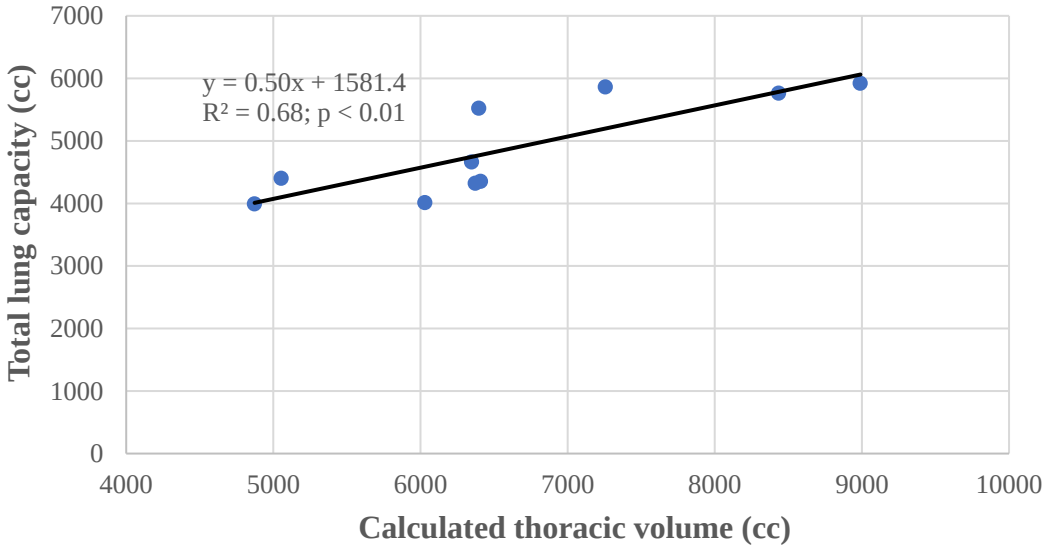

(a) Correlation between total lung capacity and thoracic volume

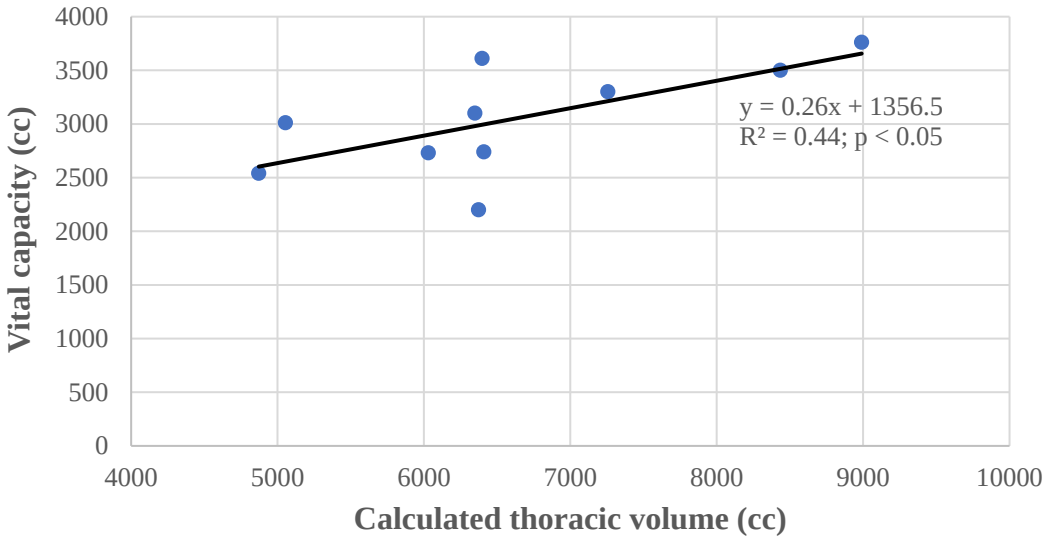

(b) Correlation between vital capacity and thoracic volume

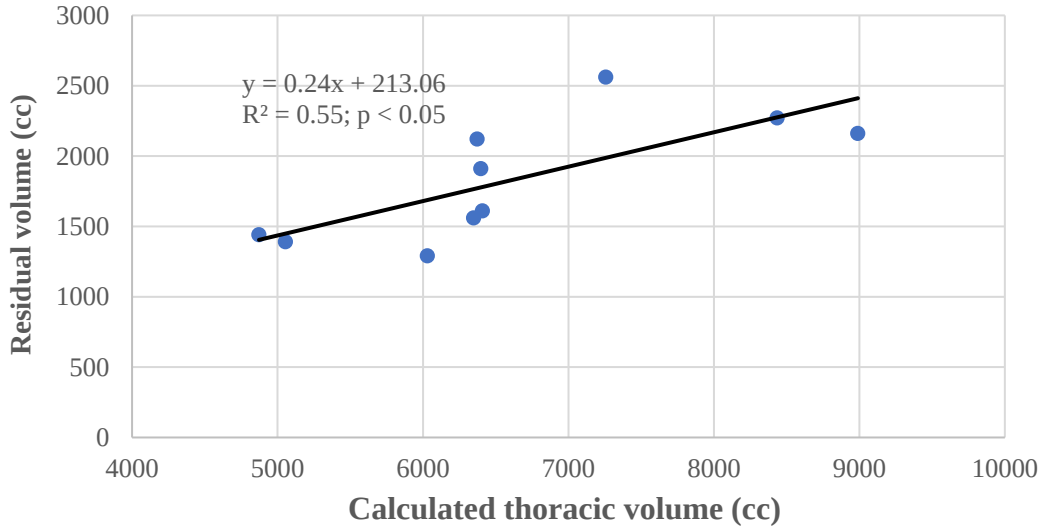

(c) Correlation between residual volume and thoracic volume

Figure 5.8 Correlation between pulmonary function parameters and thoracic volume in ten adult scoliosis patients with different treatments during adolescence

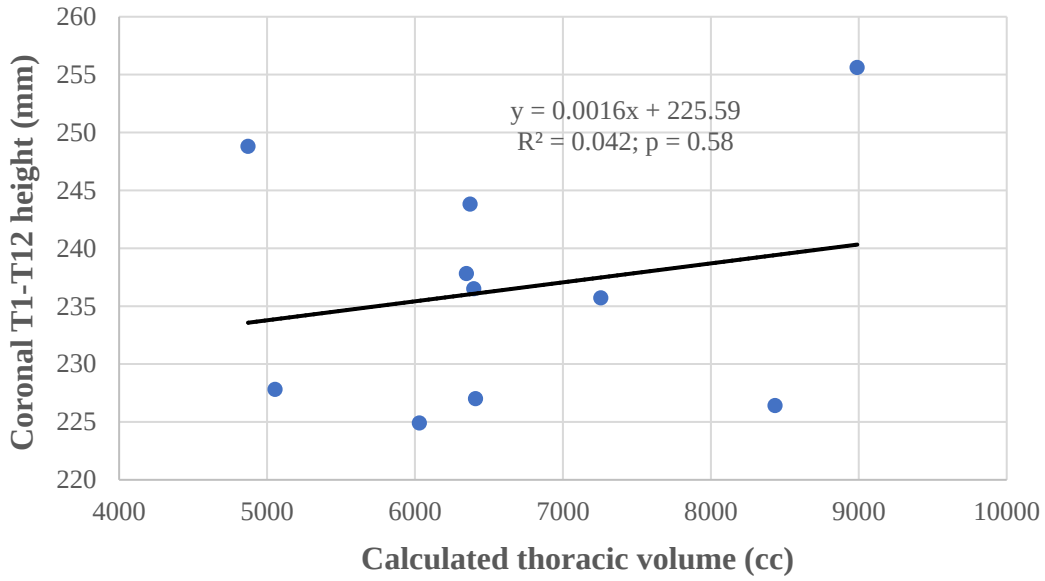

(a) Correlation between thoracic volume and thoracic height (T1-T12)

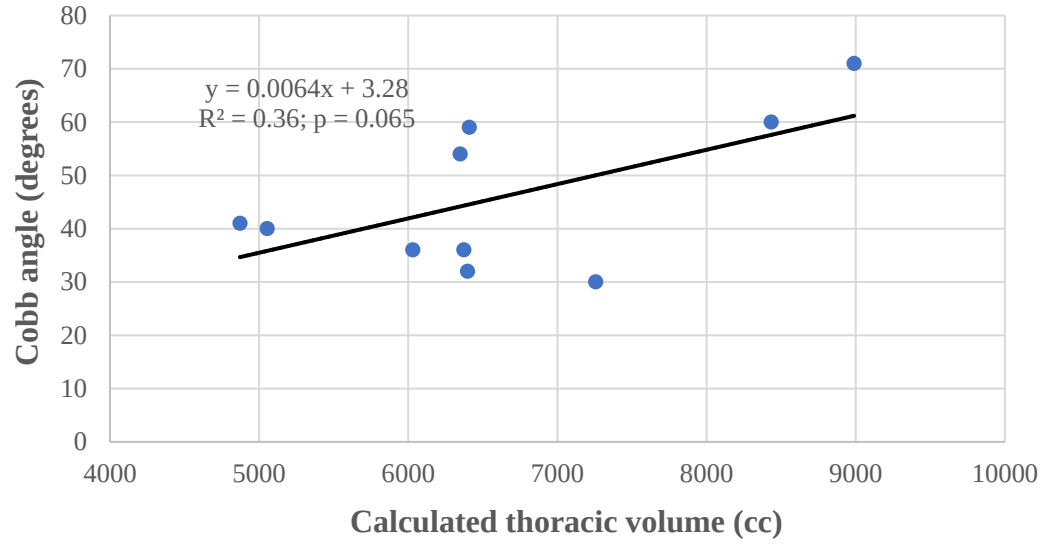

(b) Correlation between thoracic volume and Cobb angles

Figure 5.9 Correlation of thoracic volume with spine parameters in ten adult scoliosis patients with different treatments during adolescence

5.4 Conclusion

In this chapter, I utilized the developed software to reconstruct patient-specific rib cages and measure the thoracic volume through routine frontal and lateral X-rays for EOS and adult scoliosis patients. As I mentioned in the previous chapter, CT scan data can also be used to reconstruct and calculate the thoracic volume; however, the high radiation dose of the CT scan is the main concern for doctors [3], so it is not routinely or periodically used to follow up on patients' spine deformity change and thoracic volume variation, especially in pediatric spine patients.

For EOS patients, most of the existing literature concluded that the efficiency of the growing rod surgery benefits the pediatric EOS patients in pulmonary function and enlarges the thoracic volume for lung expansion [105,124,125], but they did not take the normal growth rate of the children into consideration. To investigate these perspectives, I took advantage of our developed software to monitor the difference of the thoracic volume variation in EOS patients. At first glance, we noticed the thoracic volume grew when the patients underwent the growing rod surgery and the following lengthening procedures. I further eliminated the thoracic volume change resulting from the normal growth rate of the children and identified that the thoracic volume increase of some EOS patients might be caused by the normal growth rate. Moreover, the patients among age 5 to 10 gradually extended their thoracic volumes mainly because of the growing rod surgery and the following lengthening procedures. On the contrary, the thoracic volume augmentation in EOS patients during age 0-5 and age 10-15 was mostly contributed to by their growth rate. However, the thoracic rib cage of the EOS patients might not grow as fast as normal children, so eliminating the normal thoracic volume growth rate from our calculated thoracic volumes might underestimate thoracic volume improvement due to the growing rod surgery. Besides, there are still some advantages which can be generated by the growing rod surgical intervention. For example, it not only corrects the spine curvature of the EOS patients, but also allows the pathological spine to grow smoothly along the implant rods. Most importantly, the growing rod surgery is associated with significant improvement of the pulmonary function for EOS patients [124,125]. Our thoracic volume

reconstruction will benefit doctors when they repeatedly measure the thoracic volume and follow up on its changes for EOS children with different rod lengthening procedures after the surgical treatments.

As for the adult scoliosis patients, I correlated pulmonary function to the thoracic volume to propose that thoracic volume measurement could be a surrogate to indicate the pulmonary function of the spine patients. My findings showed a strong positive correlation between total lung capacity and thoracic volume, and a significant correlation between vital capacity/residual volume and thoracic volume in adult scoliosis patients with different treatments during their adolescence. Also, my findings revealed thoracic volume can be a useful indicator to predict lung function in spine deformity patients, especially the pediatric patients who are unable to accurately perform PFTs.

For both EOS and adult scoliosis patients, I investigated the relationship between spine parameters, including thoracic T1-T12 height and Cobb angles, and the thoracic volume. Those results implied there is no correlation between Cobb angles and the thoracic volume in both spine populations; however, there existed an inconsistent result for the correlation of the thoracic height with the thoracic volume. I noticed that thoracic T1-T12 height and the thoracic volume were significantly correlated in EOS patients but not in adult scoliosis patients. In Chapter 4, I reviewed and validated the thoracic volume accuracy of our software by comparing our measurement with those equations generated by the spine parameters (e.g., thoracic height and thoracic width) on the X-rays. I prove my method is better than other methods which directly used the spine parameters to calculate the thoracic volume. Combining the conclusion drawn in Chapter 4, I am certain that it is not accurate or realistic to only count on the one-dimensional spine parameters, such as thoracic height, thoracic width, and Cobb angles, to estimate the thoracic volume or even the pulmonary function for the spine deformity patients. Until now, plain radiographs are still routinely used by orthopedic doctors to diagnose the spine deformity. Our 3D reconstruction of the thoracic volume via orthogonal frontal and lateral radiographs can potentially serve as a surrogate to predict the pulmonary function of the spine patients in clinical practices.

Chapter 6

A Quantitative Study of the Relationship between Wedging Vertebrae and Thoracic Volume Using Osteoporosis and Scheuermann's Kyphosis Virtual Patients

In this Chapter, I propose a simulation workflow that can be duplicated and transferable to construct virtual patients with different spine deformity symptoms. Then osteoporosis and Scheuermann's kyphosis symptoms are used to demonstrate how to follow this workflow to build virtual patients. With the help of the virtual patients, I quantitatively study the effect of the wedging vertebrae (local vertebral deformity) on thoracic volume for osteoporosis and Scheuermann's kyphosis. In general, the wedging deformity originates from vertebral compression fractures for osteoporosis symptoms, while the deformity only causes multiple wedging shapes along the thoracic spine for Scheuermann's kyphosis. With clinical-based assumptions, virtual patients are utilized to simulate osteoporosis and Scheuermann's kyphosis. The virtual patients are simulated based on subjects without spine deformity problems. The rib cages of the subjects are reconstructed either by CT scan techniques or through our developed software using biplanar X-rays (which was described in Chapter 3), and their baseline thoracic volumes are measured according to the reconstructed rib cage. The subject's normal rib cages and thoracic volumes serve as the baseline to create virtual patients with different wedging deformity numbers and kyphosis angles and to identify the thoracic volume variation. Subsequently, the application of the virtual patients in the orthopedic field is discussed.

6.1 Overview

In recent decades, the application of the virtual patient has been widely used in clinical or educational practice among residents, surgeons, or other medical professionals because the virtual patient is cost-effective and time-efficient [126]. The Food and Drug Administration (FDA) collaborated with the Foundation of Research on Information Technologies in Society (IT'IS Foundation, Zürich, Switzerland) to produce a virtual family, which is a set of anatomical computer-added design (CAD) models of adults and children [127,128], and those CAD models are used in electromagnetic, thermal, and computer fluid dynamics simulations. However, the definition of virtual patients or models has varied across recent years as additional researchers tried to categorize the terminology of virtual patients. In general, virtual patients can be classified into seven major types including: case presentation, interactive patient scenarios, virtual patient game, high fidelity software simulation, human standardized patients, high fidelity manikins, and virtual standardized patients [129]. The virtual patients discussed in this study can be classified as interactive patient scenarios, whose application includes clinical reasoning, surgical planning, and disease diagnosis.

Osteoporosis-related kyphosis is a kind of spine disorders triggered by the vertebral compression fracture. Normally, it is diagnosed by kyphosis angle larger than 50 degrees with a 20% or higher loss of vertebral body height due to the reduction of the bone density and quality, and this symptom often appears in the elderly population, especially women after menopause [130]. An estimated 1.5 million vertebral compression fractures happen every year in the U.S., and 25% of postmenopausal women are influenced during their lifetime [131]. On average, women live longer in the U.S., and the lifetime risk of a clinically diagnosed vertebral fracture is about 5% among white men and 16% among white women, three times higher than men [130,132]. According to the database from the World Health Organization, osteoporosis symptoms affect up to 49 million individuals in the nine industrialized countries, including USA, UK, Canada, France, Germany, Spain, Italy, Japan, and Australia [133]. The adverse health effect for osteoporosis patients is the vertebral compression fracture along the spine, which often results in immobility and back

pain. Severe osteoporosis with a kyphosis angle larger than 55 degrees can lead to impairment in pulmonary function [134], and the relationship between the wedging fracture and the pulmonary function is a negative correlation [135–137]. Leech et al. [135] built a regression equation to generate the relating %FVC (forced vital capacity) and the number of the wedging fractures along the spine. Some researchers studied the correlation of the compression fracture and mortality in women with osteoporosis [138–140], and it was discussed that the women suffering from vertebral wedging fractures have 15% higher rate of mortality than those women do not [131]. To avoid progressive wedging, kyphosis angles and back pain, physicians will recommend patients undergo invasive surgery, such as kyphoplasty or vertebroplasty [141,142], which includes injecting bone cement to reinforce the fractured vertebral body. If left untreated, the vertebral wedging fracture may cause not only a greater risk of new fractures in different vertebral levels but also complications in the pulmonary function system. What's worse, the wedging fracture is associated with elevated mortality risk. Despite that, the effect of the wedging fractures on the thoracic volume variation is still unclear. In the case study of this chapter, I investigate the connection between the vertebral wedging fracture and the thoracic volume through the virtual osteoporotic patients.

In 1920, Scheuermann [143] first described the Scheuermann's kyphosis as a rigid hyperkyphosis associated with wedging vertebrae often among the thoracic spine (upper back). Similar to osteoporosis, Scheuermann's kyphosis is another spine disorder combining local vertebral body wedging problems with a global spine deformity in the lateral view. However, in contrast to osteoporosis, the wedging deformity seldom leads to a fracture in the vertebral body. Scheuermann's kyphosis is a type of developmental kyphosis that happens during growth, so it is easily diagnosed among adolescents, usually between ages 12 and 15 [144,145]. There are two critical criteria to diagnose Scheuermann's kyphosis. One criterion is that three or more consecutive wedging vertebrae with the wedging angle of at least 5 degrees can be discovered along the thoracic spine [146]. The other one is through kyphosis angle; normal kyphosis angle measured from T1 to T12 vertebrae is between 20 and 45 degrees, but the kyphosis angle in Scheuermann's

patients is over 45 degrees [145,147,148]. Thus, the curvature of the spine looks like a round shape with a bent-over posture on the lateral chest X-ray. The reported incidence of Scheuermann's kyphosis ranges from 1% to 8% of the general population [147–149]. Scheuermann's kyphosis affects persons of any gender; some articles concluded that there is no specific gender prevalence [147,150,151], but others thought it is more common in males [149,152].

The wedged vertebrae cause a progressive spine curvature (i.e., thoracic kyphosis angle) and a foreshortened thoracic length. The majority of literature followed up the variation of Scheuermann's kyphosis patients during physical or surgical treatments [153–157], but very few studied or monitored the pulmonary function in Scheuermann's kyphosis patients. Bradford [153] investigated the results of the surgical treatment by the posterior spine arthrodesis technique, and they also performed the pulmonary function test for eleven patients whose kyphosis angles ranged from 50 to 128 degrees. Nevertheless, they only followed up the pulmonary function of five patients after surgery, and they found out patients with decreased pulmonary function preoperatively did improve their respiratory system postoperatively based on their limited data. Murray et al. [152] concluded that the Scheuermann's kyphosis patient with a severe global deformity (larger than 100-degree kyphosis angle) could suffer from restrictive lung disease, which is triggered by the limited space of the thoracic volume for lung expansion. Abbi et al. [158] found out the significantly decreased pulmonary function, including total lung capacity, forced vital capacity and forced expiratory volume in 1 second, in the patients with severe kyphosis angle, but the number of the severe patients (kyphosis angle larger than 90 degrees) is limited. Physical bracing will be recommended if the progressive kyphosis angle is less than 60 degrees [152]. However, operative surgery is advocated by doctors when the progressive kyphosis angle is over 65 degrees with back pain [152,159] or over 75 degrees without back pain [159–161]. Realizing the effect of the wedging deformity on thoracic volume and spine curve can be one of the beneficial decision-making factors for physicians to do surgical planning as well as determining the timing of intervention. Making use of the virtual Scheuermann's kyphosis patients, I can quantitatively study the

influence of the wedging deformity of the vertebrae on the thoracic volumes and the spine curvature.

6.2 Workflow for Building Virtual Spine Patients and Calculating Virtual Thoracic Volume

Virtual patients have been applied to clinical usage to help surgeons predict and monitor the inclination of the disease, visualize the anatomy of the human, or develop a surgical planning strategy before entering the operation room. Here, I propose a four-step simulation workflow in Figure 6.1 which can be transferable to clinical applications to simulate and predict the inclination of the thoracic volume in spine deformity patients. In the first step, physicians can use different techniques to scan the subject, such as CT scan, MRI, and X-rays, in order to construct the baseline model of the subject's rib cage and thoracic volume. After scanning, those image data are used to reconstruct the subjects' rib cages and thoracic volumes as the baseline models via commercial software (Mimics© [19]), free open source software (3D-Slicer [21]), or our developed software. The second step focuses on what type of spine symptoms (e.g., scoliosis, osteoporosis, Scheuermann's kyphosis, lumbar lordosis, or spondylosis) are found; then certain medical assumptions are made related to that clinical finding. The third step is to follow the assumptions made in the second step, and simulate the rib cages of the virtual spine patients based on the baseline rib cage model. In the last step, the thoracic volumes of the virtual patients are constructed and measured based on the internal boundary of the virtual rib cages obtained in the third step. The following Sections 6.3 and 6.4 demonstrate how to implement the workflow presented here to build virtual patients and study two different types of spine disease.

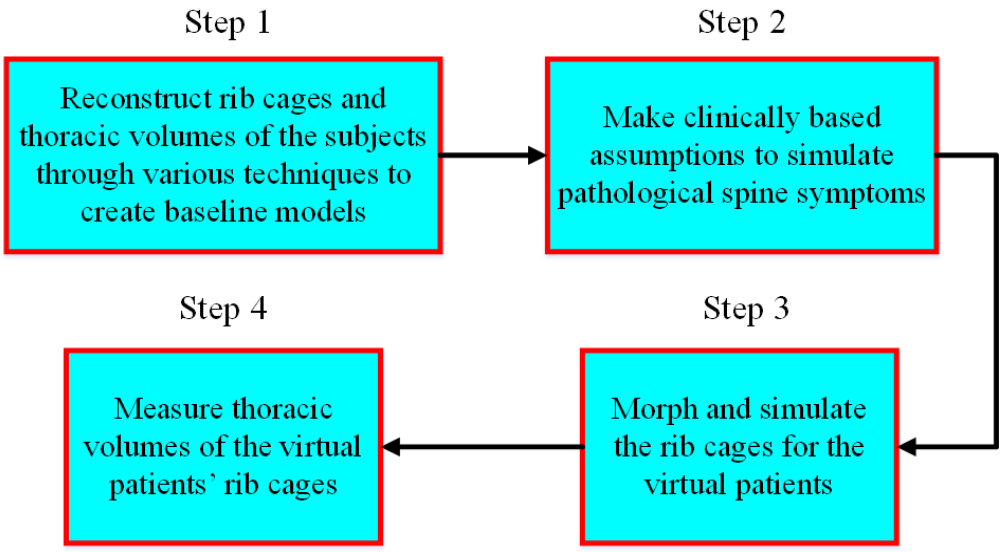

Figure 6.1 Workflow for simulating virtual patients with different spine deformities

6.3 Virtual Osteoporosis Patient Modeling

In this section, the data of Table 6.1 for six subjects without spine deformities is gathered, and I take the rib cages of the six subjects as baseline models to simulate the virtual patients. Before the simulation, some important assumptions need to be addressed based on the clinical syndrome of the osteoporosis. Then I expand the reconstructed rib cages of six elders by using different body scales and kyphosis angles to produce a total of 126 virtual osteoporosis patients with different thoracic volume capacities.

6.3.1 Information of Six Subjects

There are six subjects involved in the virtual osteoporosis study. The University of Minnesota IRB determined this study was not human subject research. After gaining the CT DICOM images (DICOM stands for Digital Imaging and Communications in Medicine, which is a standard to store and transmit medical images enabling the integration of medical imaging devices) of the six subjects, their rib cages are segmented and reconstructed by Mimics© software, and the thoracic volumes are also measured in the

Mimics environment. All bone structure, including 12 thoracic vertebrae, 24 ribs, and 1 sternum, is exported as ASCII STL files. The six subjects consist of two elders and four cadavers without spine deformity disorders, and their rib cages and thoracic volumes serve as the baseline models which is the first step of the workflow in Figure 6.1. Table 6.1 shows their age, gender, initial kyphosis angle and thoracic volume. Subjects 1, 2, 5, and 6 are datasets obtained from the Visible Heart Lab at the University of Minnesota, and the other two are collected from the University of Minnesota Medical Center. It is worthwhile to point out that Subject 3 possesses the abnormal kyphosis angle but there is no wedging fracture along his thoracic spine.

Table 6.1 Information of six subjects serving as osteoporotic baseline models

Subject	Age	Gender	Kyphosis Angle (degrees)	Thoracic Volume (cc)
Subject 1	54	M	32.1	6761
Subject 2	62	M	29.8	13850
Subject 3	69	M	53.7	12791
Subject 4	74	M	42.3	10741
Subject 5	75	M	26.2	11163
Subject 6	87	F	35.4	6491

6.3.2 Assumptions and Methods

Once the baseline rib cage model for each subject is segmented and reconstructed by Mimics, the next key features involve making assumptions to virtually construct the rib cages for virtual osteoporosis patients. Depending on the clinical information for osteoporosis symptoms, the following assumptions and methods can be utilized to simplify the virtual models:

(1) Thoracic kyphosis angle is defined as the angle measured from the superior endplate of the T1 level to the inferior endplate of the T12 level in the lateral plane, as shown in Figure 6.2.

(2) I assume the vertebral compression deformity (wedging) angle is 15 degrees for the vertebra along the thoracic spine.

Figure 6.3 demonstrates one normal T8 vertebra and one T8 vertebra with a wedging deformity angle of 15 degrees using the Armature method in Blender software.

(3) All consecutive endplates remain parallel to each other even if the wedging fracture occurs.

In Figure 6.4, I show two consecutive vertebrae, T5 and T6. When T6 vertebra sustains compression fracture at the top of the vertebral body, T5 vertebra will correspondingly react to the incline of the superior endplate of T6 vertebra and keep parallel to it.

(4) Global thoracic spine deformities and local vertebral wedging deformities only happen in the sagittal plane.

That is, I do not consider the cases possessing osteoporosis (deformity in the lateral plane) and other spine symptoms, such as scoliosis (deformity in the coronal plane) symptoms.

(5) When the thoracic spine progressively bends and deforms due to the compression wedging fracture, the sternum and the ribs move relative to the spine curvature, but there is no local deformity occurring in ribs and sternum.

(6) The wedging fracture in the T1 vertebra is not considered, because the wedging fracture seldom happens at the T1 level.

Even if it occurs, its deformity has little influence on the thoracic volume change.

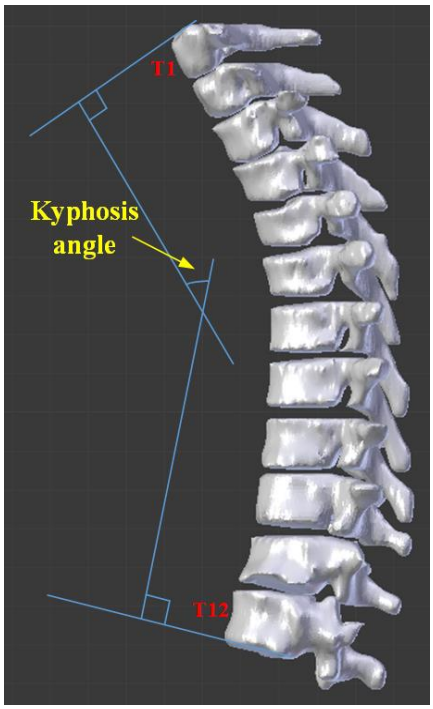

Figure 6.2 Range of kyphosis angle

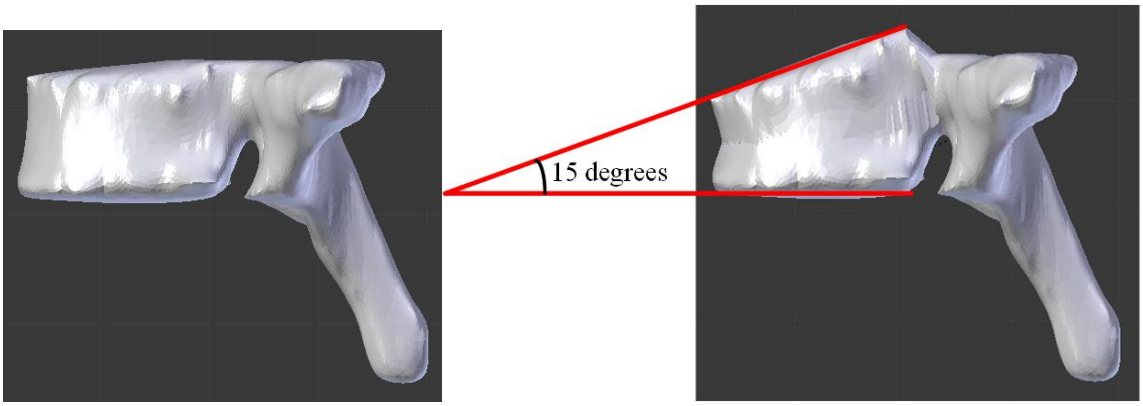

(a) Normal T8 vertebra (b) Wedging T8 vertebra

Figure 6.3 Normal vertebra versus wedging vertebra with a 15-degree wedging angle

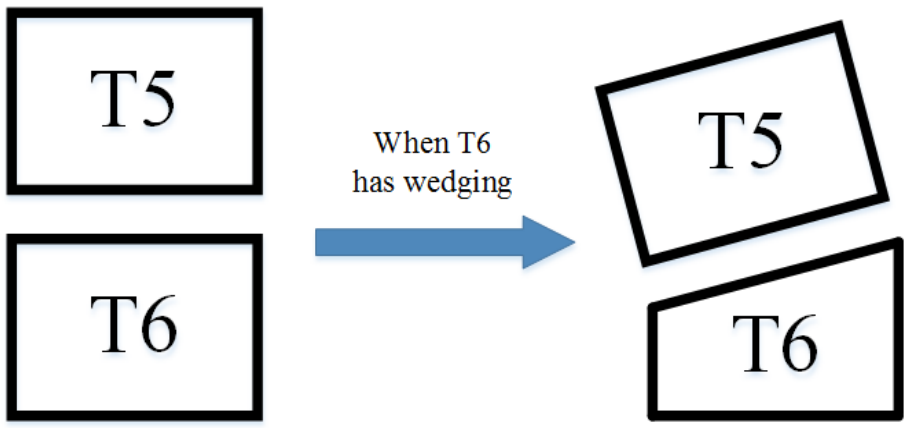

Figure 6.4 Relative position and rotation of two consecutive vertebrae during a wedging fracture

6.3.3 Generation of Virtual Osteoporosis Patients

As described in the workflow of Figure 6.1, I can virtually morph the vertebra to simulate the compression wedging fracture and to construct the virtual patients with the help of the previous assumptions. In Blender software, one build-in function to imitate human skeletons is called Armature bone (virtual bone), which can be used to simulate the osseous (wedging) fracture. To morph the wedging deformity of the vertebra, I divide each vertebra into top and bottom portions which are bonded with two Armature bones. Figure 6.5 (a) displays one wedging vertebra bonded with two Armature bones (the bottom Armature bone is labeled as bone 1 and the top one as bone 2). When the top Armature bone (bone 2) is rotated, the top portion of the vertebral body will collapse due to the bonding and this results in a wedging fracture phenomenon. By manipulating the Armature bones in Blender, I can simulate the deformity of the wedging vertebra. In addition, each intervertebral disc is bonded with one Armature bone, too. Therefore, from the thoracic vertebrae (T1 to T12 vertebrae) and the intervertebral discs, I get 35 consecutive Armature bones in total to simulate the wedging fracture for osteoporosis patients as can be seen in Figure 6.5 (b). To quantitatively study the effect of the wedging vertebrae on thoracic volume, I start building the wedging vertebra from the T12 level to the T2 level with only

one wedging angle of 15 degrees. Subsequently, the kyphosis angle increases 15 degrees more for each virtual modeling case. In Figures 6.6 and 6.7, I respectively present the rib cage and thoracic volume of Subject 1 as the baseline model and eleven virtual patients' rib cages developing from the baseline model with one wedging vertebra (highlighted in blue), and further measure their virtual thoracic volumes (highlighted in yellow) within the boundary of virtual rib cages (highlighted in white). In order to readily observe the bending tendency of the thoracic spine in virtual patients, I only demonstrate all vertebrae, sternum, and right ribs in Figure 6.6. Next, I construct two consecutive wedging vertebrae from the T12 level to the T2 level with wedging angle of 15 degrees for both wedging vertebrae. With two wedging vertebrae along the thoracic spine, the kyphosis angle increases by 30 degrees for each virtual modeling case. Figure 6.8 displays the baseline rib cages of Subject 1 and ten virtual patients with two wedging vertebrae, and I highlight the wedging vertebrae in blue to help recognize the wedging locations. Figure 6.9 demonstrates the baseline thoracic volume and ten virtual thoracic volumes. Except for Subject 3, all other baseline subjects' kyphosis angles are within the normal range. Hence, I only disclose the baseline model of Subject 3 and the simulated virtual patients in Appendix A.1.

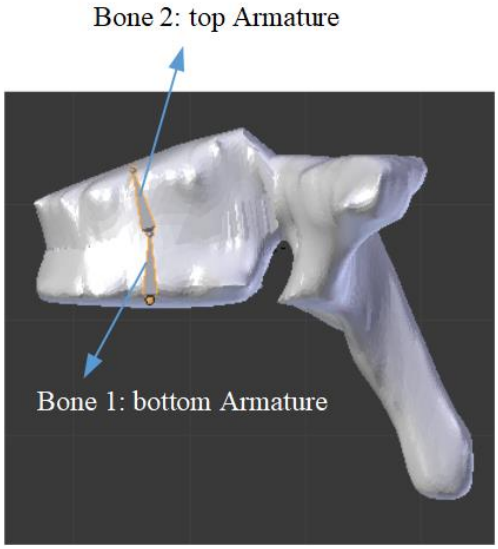

(a) Vertebra with two Armature bones (b) Rib cage with 35 Armature bones

Figure 6.5 Demonstration of Armature structure in specific bone and rib cage

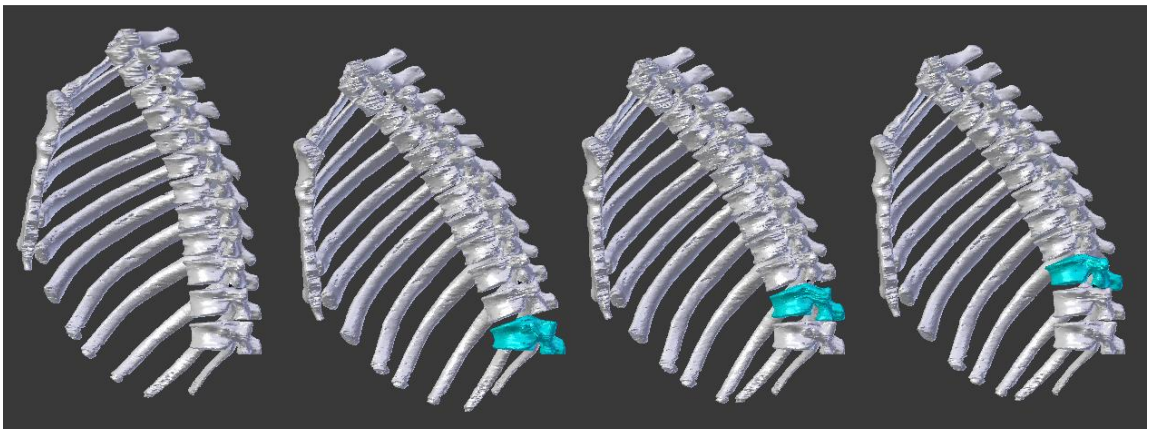

(a) Baseline (b) T12 wedging (c) T11 wedging (d) T10 wedging

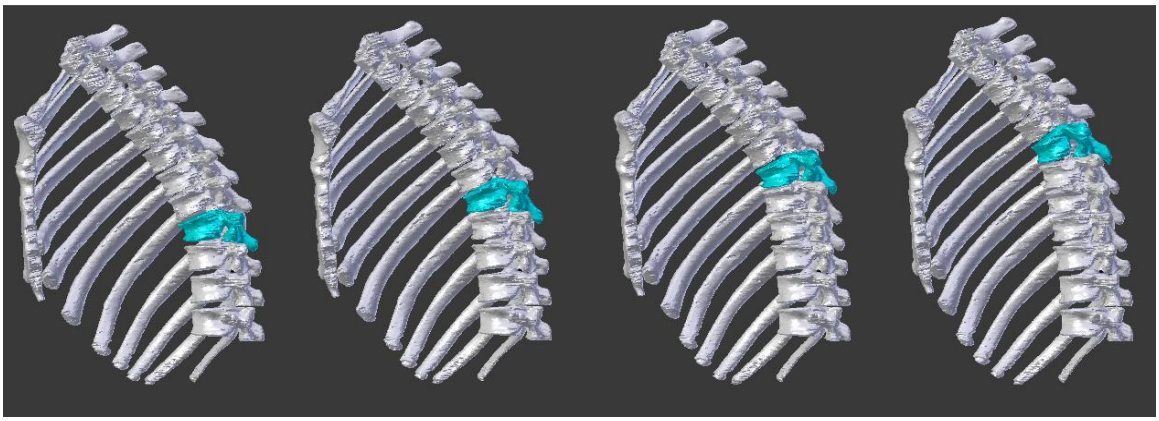

(e) T9 wedging (f) T8 wedging (g) T7 wedging (h) T6 wedging

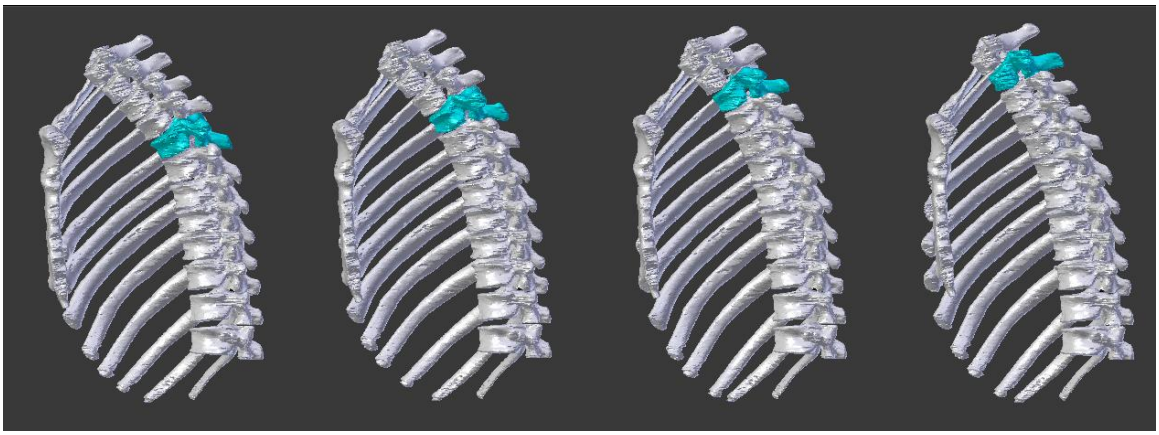

(i) T5 wedging (j) T4 wedging (k) T3 wedging (l) T2 wedging

Figure 6.6 Rib cages of the baseline model (i.e., Subject 1) and eleven virtual osteoporosis patients with one wedging vertebra

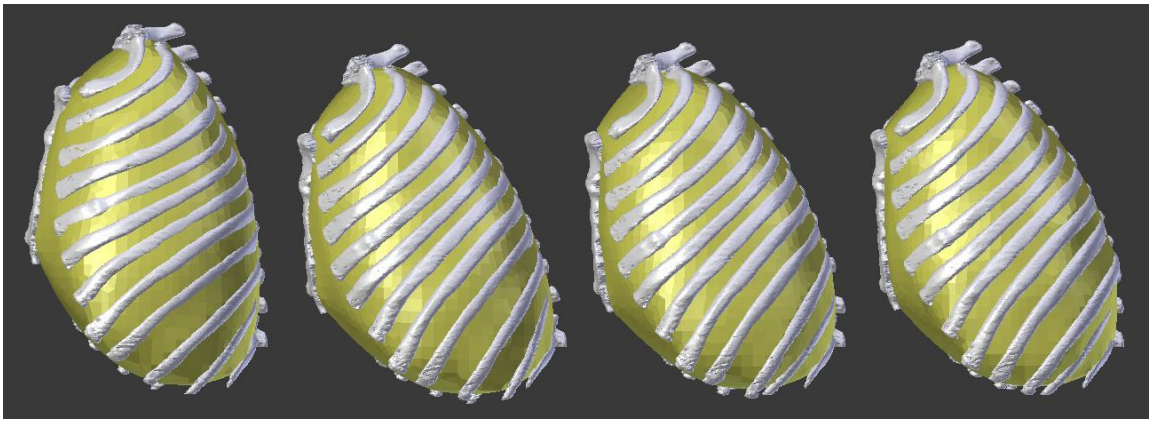

(a) Baseline (b) T12 wedging (c) T11 wedging (d) T10 wedging

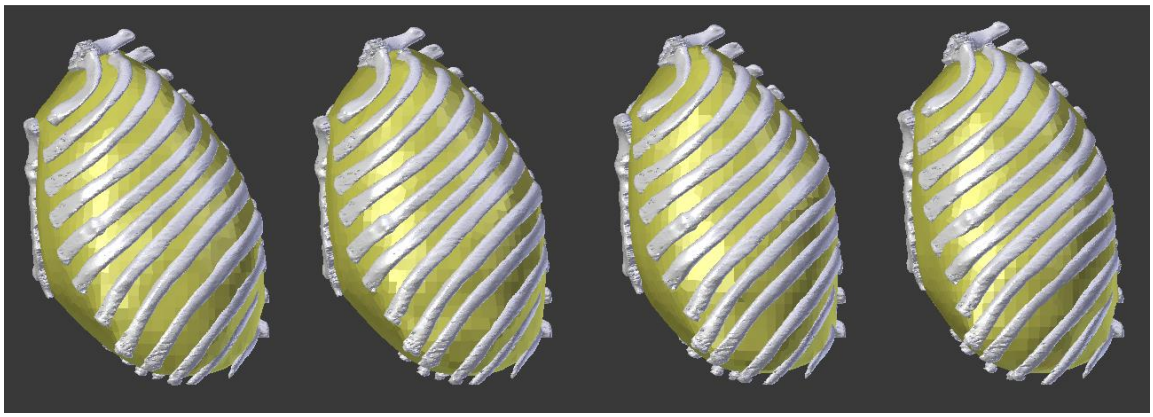

(e) T9 wedging (f) T8 wedging (g) T7 wedging (h) T6 wedging

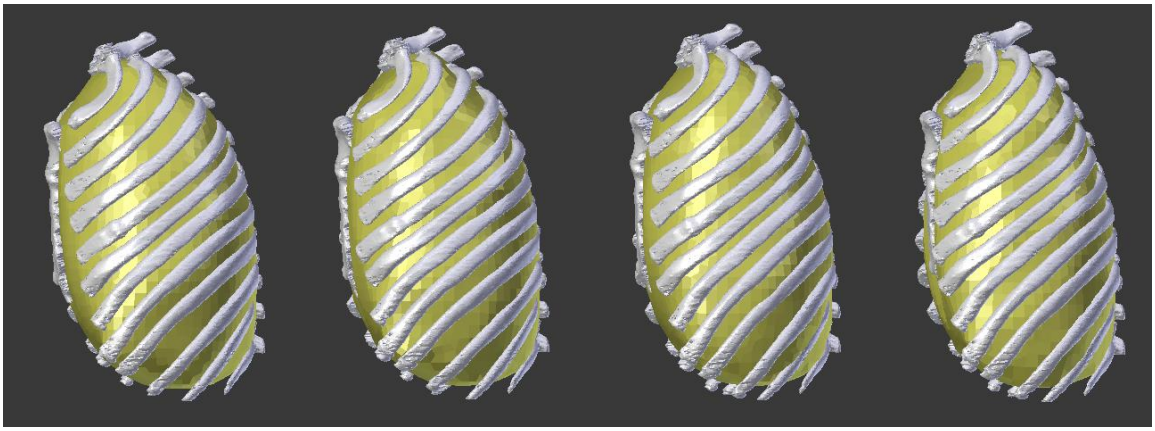

(i) T5 wedging (j) T4 wedging (k) T3 wedging (l) T2 wedging

Figure 6.7 Thoracic volumes of the baseline model (i.e., Subject 1) and eleven virtual osteoporosis patients with one wedging vertebra

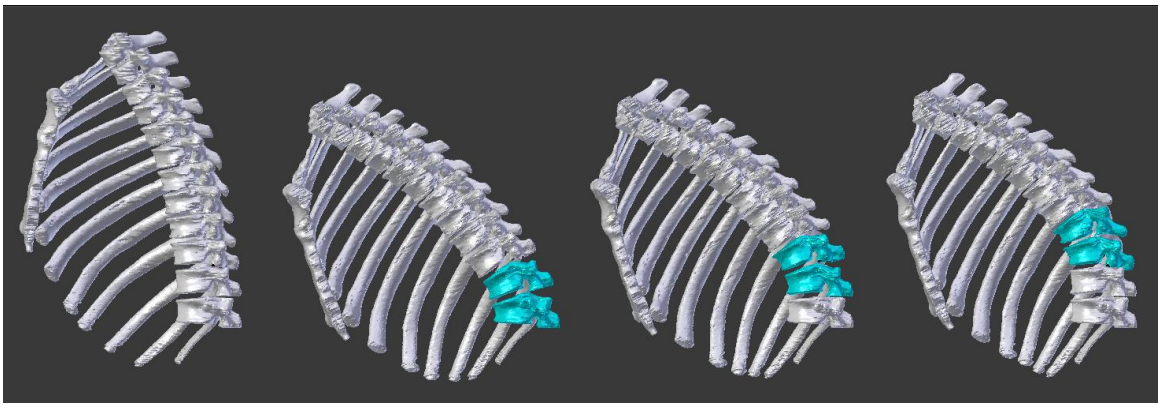

(a) Baseline (b) T12&T11 wedging (c) T11&T10 wedging (d) T10&T9 wedging

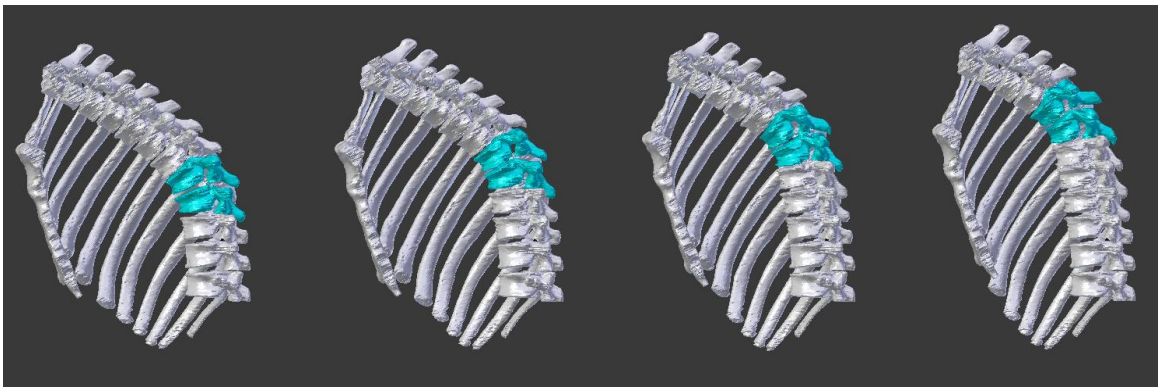

(e) T9&T8 wedging (f) T8&T7 wedging (g) T7&T6 wedging (h) T6&T5 wedging

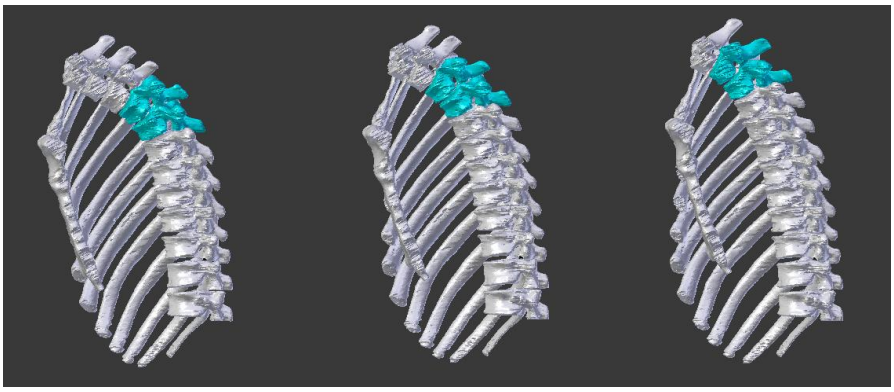

(i) T5&T4 wedging (j) T4&T3 wedging (k) T3&T2 wedging

Figure 6.8 Rib cages of the baseline model (i.e., Subject 1) and ten virtual osteoporosis patients with two wedging vertebrae

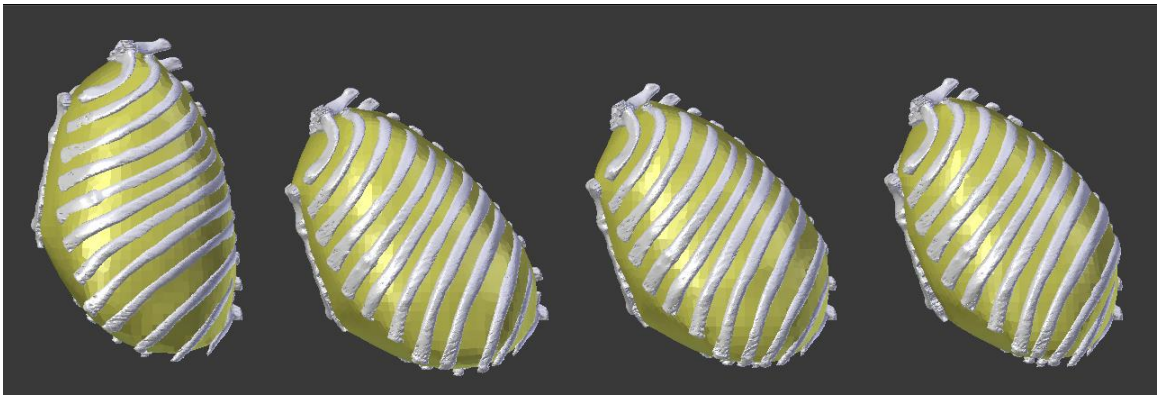

(a) Baseline (b) T12&T11 wedging (c) T11&T10 wedging (d) T10&T9 wedging

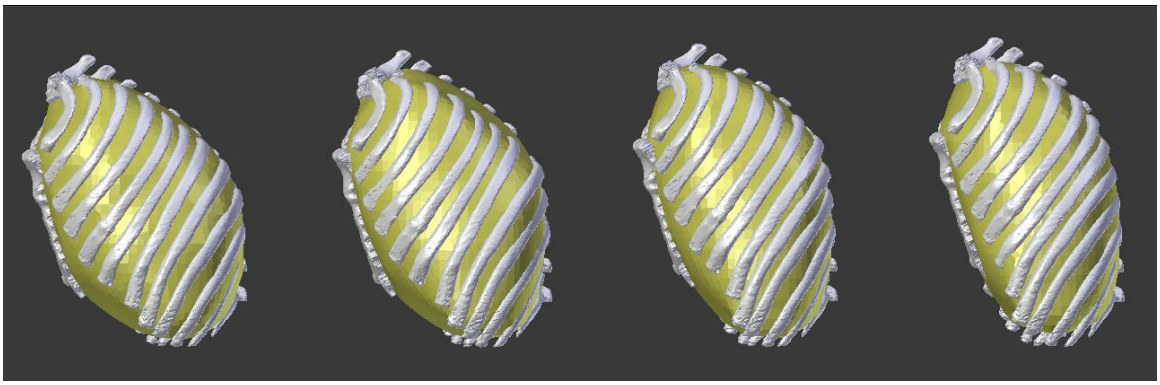

(e) T9&T8 wedging (f) T8&T7 wedging (g) T7&T6 wedging (h) T6&T5 wedging

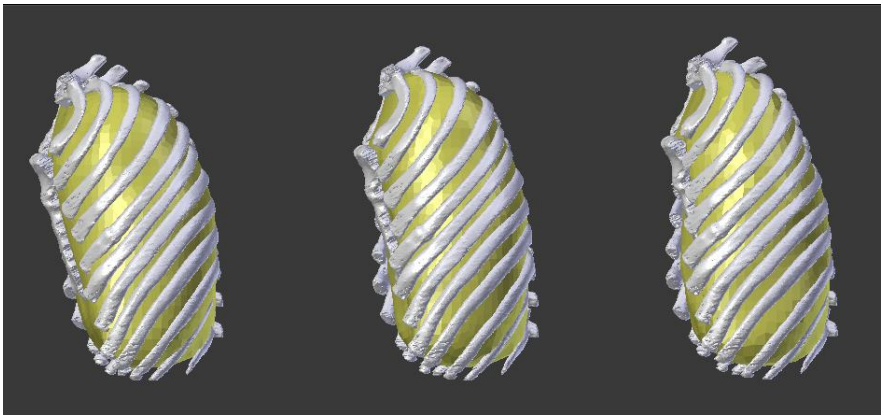

(i) T5&T4 wedging (j) T4&T3 wedging (k) T3&T2 wedging

Figure 6.9 Thoracic volumes of the baseline model (i.e., Subject 1) and ten virtual osteoporosis patients with two wedging vertebrae

6.3.4 Results

I summarize the tendency of the thoracic volume variation in Figure 6.10 and 6.11 for one and two wedging deformities along the thoracic spine separately. Tables 6.2 and 6.3 separately report the baseline thoracic volumes and the percentage change of the virtual thoracic volumes compared to the baseline thoracic volumes for one wedging and two wedging deformities. In addition, Table 6.2 shows that if there is only one wedging vertebra (15 degrees) along the thoracic spine, the average reduction in thoracic volume from baseline thoracic volume to the virtual thoracic volume of T2 wedging vertebra is averagely 19.1% in sixty-six virtual osteoporosis patients. Further, if two consecutive wedging

vertebrae occur in the thoracic spine, the average reduction in thoracic volume from baseline thoracic volume to the virtual thoracic volume of T2&T3 wedging vertebrae becomes 31.8% on average as seen in Table 6.3. With the help of one hundred and twenty-six virtual osteoporosis patients evolving from six baseline subjects with different kyphosis angles and different body scales, it is clear that if any wedging deformity occurs along the thoracic spine, the thoracic volume will be less than the baseline model without any wedging vertebra. More importantly, the wedging deformity occurring in the upper thoracic spine significantly decreases more thoracic volume than the wedging deformity located at the lower thoracic spine. On the whole, virtual osteoporosis simulation clarifies that increasing the wedging number not only affects the local and global spine deformity but also decreases the thoracic volume for lung expansion in elderly osteoporosis patients.

Table 6.2 Baseline thoracic volume (TV) and percentage change of TV in virtual osteoporosis patients with one wedging vertebra

	Subject 1		Subject 2		Subject 3		Subject 4		Subject 5		Subject 6	
Wedging level	TV (cc)	TV change (%)	TV (cc)	TV change (%)	TV (cc)	TV change (%)	TV (cc)	TV change (%)	TV (cc)	TV change (%)	TV (cc)	TV change (%)
Baseline / Virtual	6761	0.0	13850	0.0	12791	0.0	10741	0.0	11163	0.0	6491	0.0
T12	6621	-2.1	13808	-0.3	12562	-1.8	10699	-0.4	11058	-0.9	6387	-1.6
T11	6525	-3.5	13599	-1.8	12254	-4.2	10602	-1.3	10887	-2.5	6244	-3.8
T10	6415	-5.1	13357	-3.6	11964	-6.5	10498	-2.3	10663	-4.5	6076	-6.4
T9	6332	-6.4	13143	-5.1	11692	-8.6	10361	-3.5	10410	-6.7	5895	-9.2
T8	6202	-8.3	12943	-6.5	11334	-11.4	10105	-5.9	10072	-9.8	5712	-12.0
T7	6059	-10.4	12659	-8.6	11024	-13.8	9841	-8.4	9717	-13.0	5557	-14.4
T6	5950	-12.0	12408	-10.4	10761	-15.9	9485	-11.7	9390	-15.9	5403	-16.8
T5	5824	-13.9	12275	-11.4	10589	-17.2	9390	-12.6	9138	-18.1	5269	-18.8
T4	5781	-14.5	12161	-12.2	10432	-18.4	9334	-13.1	8943	-19.9	5142	-20.8
T3	5710	-15.5	11811	-14.7	10297	-19.5	9224	-14.1	8770	-21.4	5019	-22.7
T2	5650	-16.4	11675	-15.7	10197	-20.3	9104	-15.2	8630	-22.7	4912	-24.3

Table 6.3 Baseline thoracic volume (TV) and percentage change of TV in virtual osteoporosis patients with two wedging vertebrae

	Subject 1		Subject 2		Subject 3		Subject 4		Subject 5		Subject 6	
Wedging level	TV (cc)	TV change (%)	TV (cc)	TV change (%)	TV (cc)	TV change (%)	TV (cc)	TV change (%)	TV (cc)	TV change (%)	TV (cc)	TV change (%)
Baseline / Virtual	6761	0.0	13850	0.0	12791	0.0	10741	0.0	11163	0.0	6491	0.0
T12&T11	6537	-3.3	13556	-2.1	12388	-3.2	10629	-1.0	10900	-2.4	6278	-3.3
T11&T10	6366	-5.8	13271	-4.2	12103	-5.4	10423	-3.0	10556	-5.4	6005	-7.5
T10&T9	6149	-9.1	12822	-7.4	11652	-8.9	10125	-5.7	10155	-9.0	5744	-11.5
T9&T8	5900	-12.7	12331	-11.0	11081	-13.4	9697	-9.7	9681	-13.3	5428	-16.4
T8&T7	5665	-16.2	11846	-14.5	10373	-18.9	9025	-16.0	9149	-18.0	5166	-20.4
T7&T6	5442	-19.5	11438	-17.4	10049	-21.4	8672	-19.3	8747	-21.6	4933	-24.0
T6&T5	5214	-22.9	10965	-20.8	9602	-24.9	8336	-22.4	8388	-24.9	4722	-27.2
T5&T4	4987	-26.2	10568	-23.7	9273	-27.5	8170	-23.9	8071	-27.7	4524	-30.3
T4&T3	4821	-28.7	10179	-26.5	8825	-31.0	7975	-25.8	7771	-30.4	4360	-32.8
T3&T2	4672	-30.9	9823	-29.1	8322	-34.9	7717	-28.2	7530	-32.5	4214	-35.1

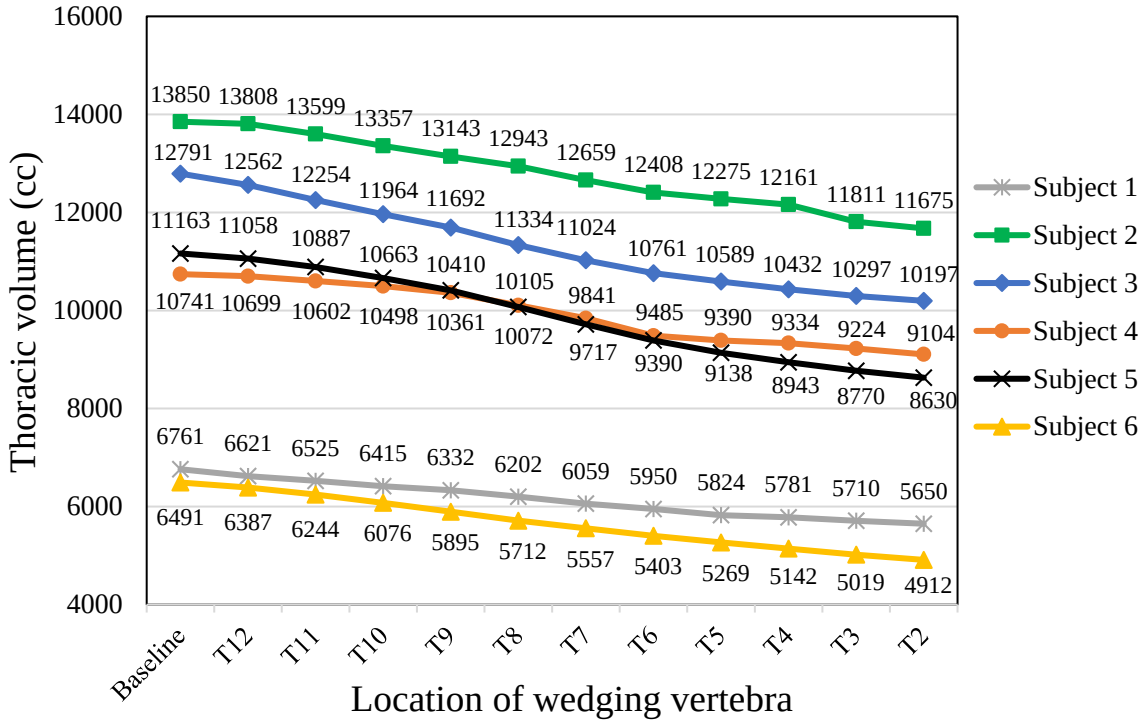

Figure 6.10 Tendency of thoracic volume variation for virtual osteoporosis patients with one wedging deformity along thoracic spine

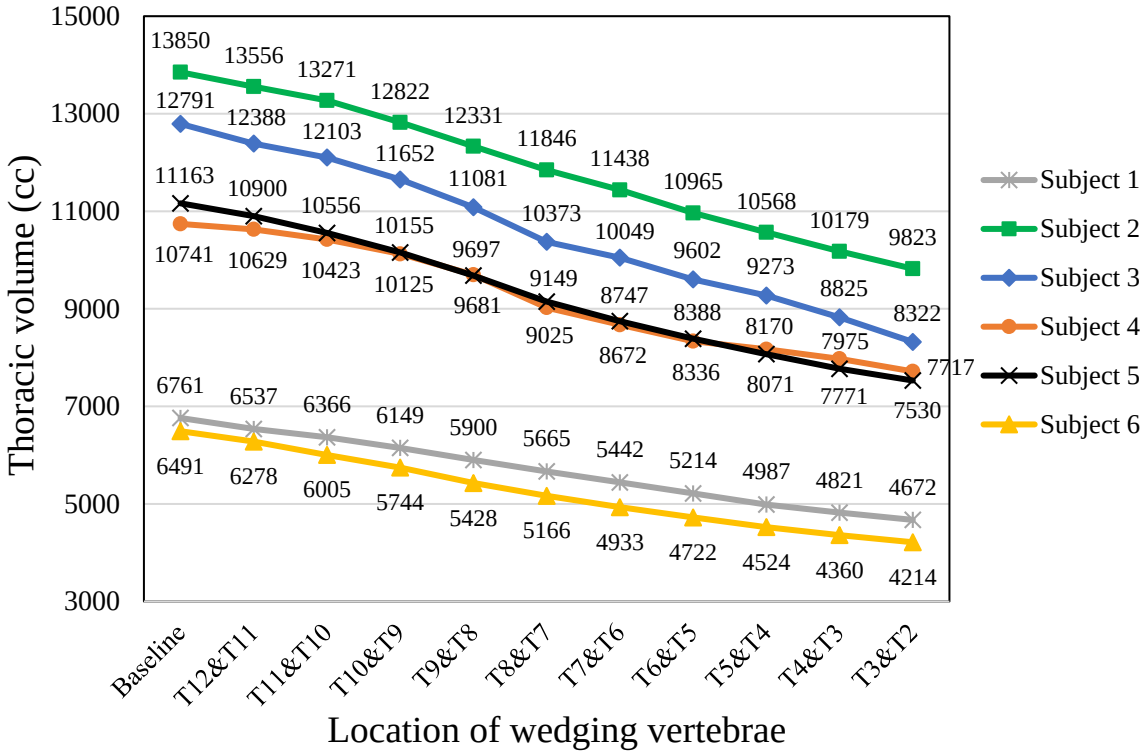

Figure 6.11 Tendency of thoracic volume variation for virtual osteoporosis patients with two wedging deformities along thoracic spine

6.4 Virtual Scheuermann's Kyphosis Patient Modeling

I present five subjects involved in simulating virtual Scheuermann's kyphosis patients, and show the information of the five subjects without Scheuermann's kyphosis disorder. According to the workflow described in Section 6.2, some medically related assumptions need to be made to simplify the process for building virtual patients. Five non-spine deformity adolescents with different body scales and kyphosis angles are utilized to produce a total of thirty virtual Scheuermann's kyphosis patients with different thoracic volume capacities so that I can analyze the tendency of thoracic volume change.

6.4.1 Information of Five Subjects and CREST Model

Due to the limited source of the CT scan data, the frontal and lateral X-rays of five adolescents from the University of Minnesota Medical Center (The University of Minnesota IRB determined this study was not human subject research) were used to simulate the virtual Scheuermann's kyphosis disease. One rib cage model (CREST model) was gathered from the Center for Research in Education and Simulation Technologies at the University of Minnesota [162]. The rib cage model, segmented based on the MRI DICOM images of a healthy fifteen-year-old male, was employed to reconstruct five baseline rib-cage and thoracic-volume models via frontal and lateral X-rays as described in Chapter 3. Thus, the first step of the workflow in Figure 6.1 is completed. The rib cage of the CREST model is shown in Figure 6.12. In addition, the information of the five adolescents, including age, gender, initial kyphosis angle, and initial thoracic volume, is listed in Table 6.4.

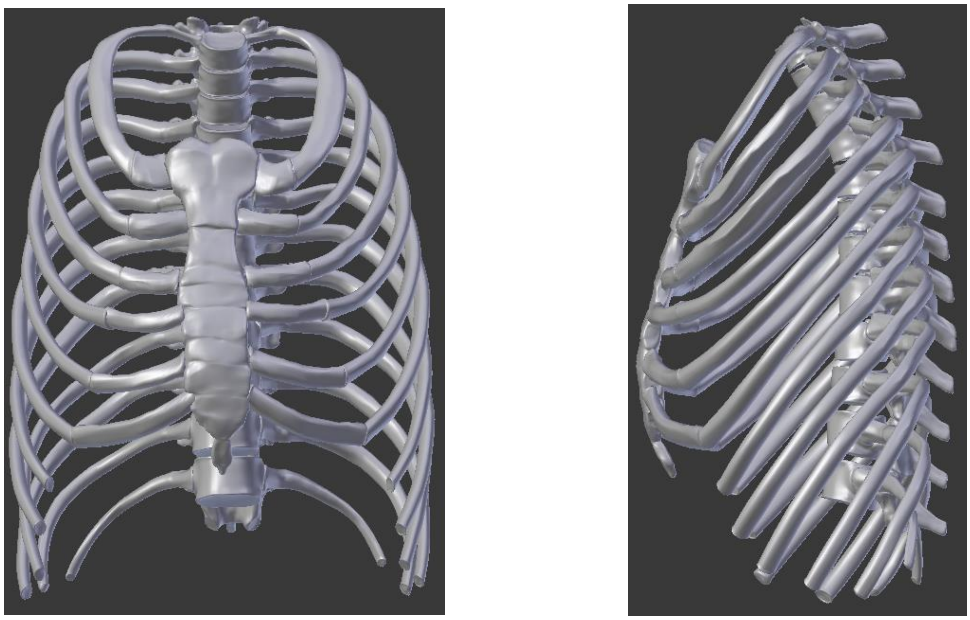

(a) Frontal view (b) Lateral view

Figure 6.12 Rib cage template (CREST model) used for reconstructing five baseline models

Table 6.4 Information of five subjects serving as baseline models

Subject	Age	Gender	Kyphosis Angle (degrees)	Thoracic Volume (cc)
Subject 1	12	F	39	6340
Subject 2	13	M	44.4	6544
Subject 3	15	F	30	6872
Subject 4	15	M	42.6	8065
Subject 5	16	M	45	7103

6.4.2 Assumptions and Methods

To simulate the virtual Scheuermann's kyphosis patients, I need to make assumptions before morphing the five baseline rib cages reconstructed by the CREST model. The assumptions rely on the clinical cases of Scheuermann's kyphosis symptoms, and can ease the complexity in constructing the virtual patients. Some of the assumptions and methods are similar to those for virtual osteoporosis patients, and they are listed as follows:

(1) Thoracic kyphosis angle is measured from superior endplate of T1 vertebra to the inferior endplate of T12 vertebra in the lateral plane.

(2) Depending on the Scheuermann's kyphosis symptoms, I assume the vertebral wedging angle is equal to or larger than 5 degrees for the wedging vertebra and there are at least three consecutive wedging deformities along the thoracic spine when viewed from the lateral X-ray.

Generally speaking, except for the patients with back pain along the spine, physicians do not take any action and only monitor the progression of the wedging vertebrae if the wedging angle is less than 5 degrees.

(3) The wedging deformity above T5 vertebra is not considered, because a wedging deformity between T1 and T4 vertebrae is seldom detected for Scheuermann's kyphosis patients.

In other words, wedging vertebrae are only considered between T5 and T12 levels [163].

(4) The most common apical vertebra along the thoracic spine curve is located between T7 and T9 [151] for Scheuermann's kyphosis, and I choose T9 vertebra as the apex along the thoracic spine. Besides, T9 vertebra is one of the deformities in three consecutive wedging vertebrae.

(5) All consecutive endplates remain parallel to each other while the wedging deformity occurs, so the degree of the wedging angle fully contributes to the increased kyphosis angle.

(6) Global thoracic rib cage deformity and local wedging deformity only occur in the sagittal plane. I do not take into consideration the Scheuermann's kyphosis patients (deformity in the lateral plane) combined with other spine deformity symptoms, like scoliosis (deformity in the coronal plane).

(7) As the thoracic spine gradually deforms due to the wedging deformities, the sternum and the ribs do not locally deform, but they move correspondingly to the deformity of the vertebrae.

6.4.3 Generation of Virtual Scheuermann's kyphosis Patients

In order to generate virtual Scheuermann's kyphosis patients, I implement the workflow of Figure 6.1. Based on the frontal and lateral X-rays of five adolescents, the CREST model is used to reconstruct the rib cage and thoracic volume for five adolescent subjects as five baseline models. As described in Section 6.3.3, we are capable of deforming the vertebral body to simulate a wedging deformity for virtual patients through the Armature bone in Blender. To quantitatively study the impact of the wedging vertebrae on thoracic volume in Scheuermann's kyphosis, I build the wedging vertebrae from T12 level to T5 level having at least three consecutive wedging vertebrae, and T9 is the apex along the thoracic spine in all virtual patients. With the assumptions mentioned above, the five baseline rib

cage models are progressively deformed by 10 degrees from 60 to 110 degrees of kyphosis angle in the sagittal plane. This results in the creation of thirty virtual Scheuermann's kyphosis patients. To generate the virtual patients, I first simulate three consecutive wedging vertebrae from T9 to T11 for virtual 60^0 patients (virtual 60^0 represents 60 degrees of kyphosis angle), and then I add one more wedging vertebra at T12 to force the kyphosis angle to reach 70 degrees (virtual 70^0 patients). For virtual 80^0 patients, there are five consecutive wedging vertebrae from T12 to T8. I continually add one more wedging vertebra until the virtual kyphosis angle reaches 110 degrees which is a serious case but is not commonly found in the literature [154]. In Table 6.5, I list the vertebrae having wedging deformities simulated from Subject 1 and the wedging angles are tabulated as well. The similar data of the other four subjects can be seen in Appendix A.2. Figure 6.13 shows the rib cages of the baseline model (Subject 1) and six virtual patients which are constructed from Subject 1. To identify the wedging locations, the wedging vertebrae are highlighted in blue and apex vertebra (T9) in pink. Figure 6.14 displays the simulated thoracic volumes, all in the lateral view. To prevent both sides of the ribs from overlapping, I only show part of the rib cage, sternum, vertebrae, and right ribs in Figure 6.13. Due to the similarity, I omit the other three subjects but only present the rib cage and thoracic volume of Subject 4, which is the opposite gender to Subject 1, and the simulated virtual patients in Appendix A.2.

Table 6.5 Wedging angles and their locations in virtual Scheuermann's kyphosis patients deriving from Subject 1 baseline

Subject 1	**Wedging location and wedging angles of vertebrae**							
Scheuermann's kyphosis angle	**T12**	**T11**	**T10**	**T9**	**T8**	**T7**	**T6**	**T5**
Baseline (39^0)								
Virtual 60^0		7^0	7^0	7^0				
Virtual 70^0	10^0	7^0	7^0	7^0				
Virtual 80^0	10^0	12^0	7^0	7^0	5^0			
Virtual 90^0	10^0	12^0	12^0	7^0	5^0	5^0		
Virtual 100^0	10^0	12^0	12^0	12^0	5^0	5^0	5^0	
Virtual 110^0	10^0	12^0	12^0	12^0	10^0	5^0	5^0	5^0

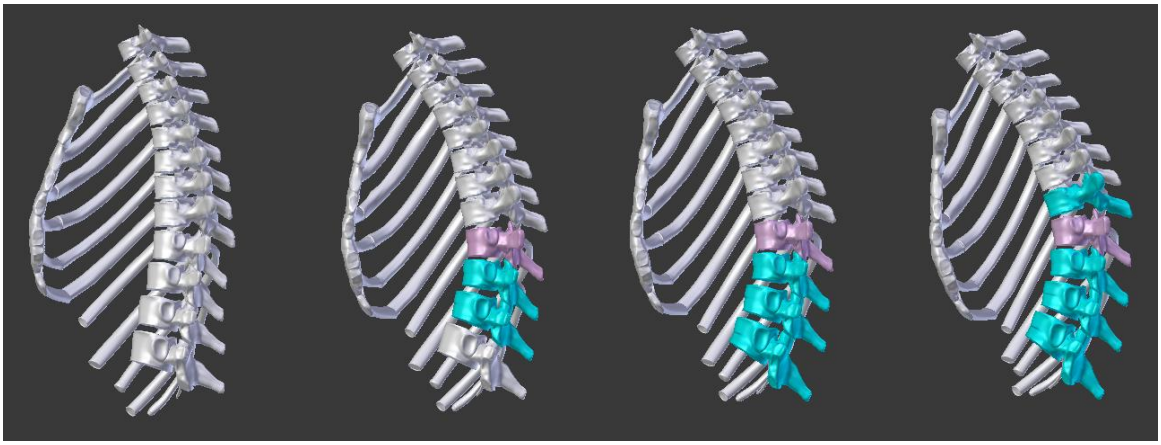

(a) Baseline (b) T11&T9 wedging (c) T12&T9 wedging (d) T12&T8 wedging

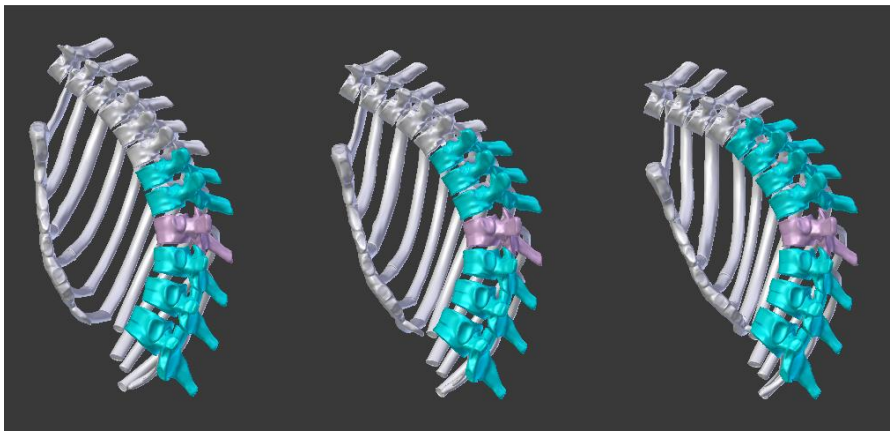

(e) T12&T7 wedging (f) T12&T6 wedging (g) T12&T5 wedging

Figure 6.13 Rib cages of the baseline model (Subject 1) and six simulated virtual Scheuermann's kyphosis patients developed from Subject 1

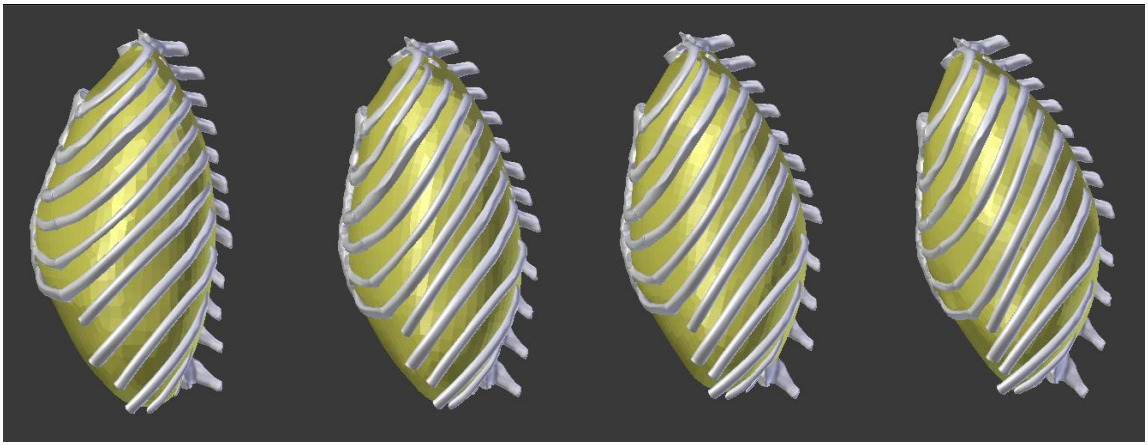

(a) Baseline (b) T11&T9 wedging (c) T12&T9 wedging (d) T12&T8 wedging

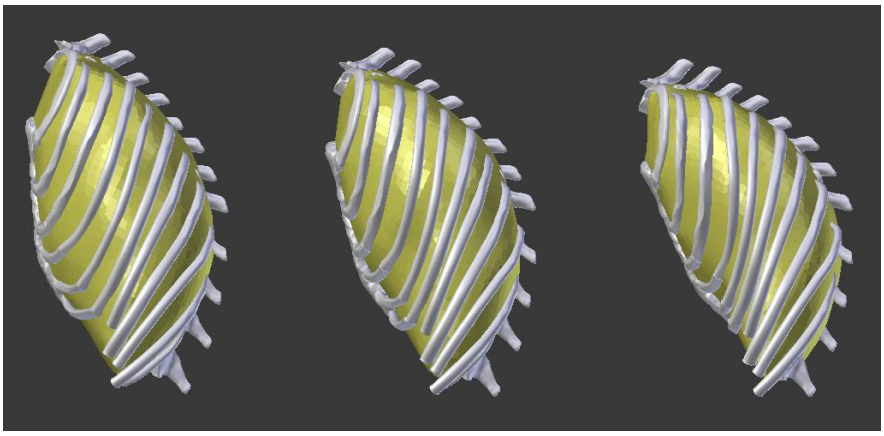

(e) T12&T7 wedging (f) T12&T6 wedging (g) T12&T5 wedging

Figure 6.14 Thoracic volumes of the baseline model (Subject 1) and six simulated virtual Scheuermann's kyphosis patients developed from Subject 1

6.4.4 Results

In Table 6.6, the virtual thoracic volume and the percentage change of different virtual kyphosis angles compared to the normal baseline thoracic volume are presented. Furthermore, the trend line of the thoracic volume variation for all virtual patients with different wedging numbers and wedging angles is revealed in Figure 6.15. Obviously, this figure shows the significant influence of the wedging deformity on thoracic volume change. Compared with the baseline models without wedging deformities, thoracic volumes of virtual Scheuermann's kyphosis patients definitely become lower. The contraction from baseline thoracic volume to virtual 110^0 patients (virtual 110^0 = 110 degrees of kyphosis angle) with eight wedging deformities is on average 21.3% in thirty virtual Scheuermann's kyphosis patients. With the increased wedging angle and increased number of wedging vertebrae, the thoracic kyphosis angle progressively increases, starting from virtual 60^0 patients; the thoracic volume decreases approximately in a linear fashion by a mean of 3.5% for every 10 degrees more of kyphotic progression for thirty virtual Scheuermann's kyphosis patients. Virtual models originating from five baseline subjects with different kyphosis angles and different body scales imply the increased kyphosis angle and wedging deformity number in virtual Scheuermann's kyphosis patients not only

influence the global and local spine deformity, but also reduce the thoracic volume which is the potential space for lung expansion.

Table 6.6 Baseline thoracic volume (TV) and percentage change of TV in virtual Scheuermann's kyphosis models with different kyphosis angles

	Subject 1		Subject 2		Subject 3		Subject 4		Subject 5	
Scheuermann's kyphosis angle	TV (cc)	TV change (%)	TV (cc)	TV change (%)	TV (cc)	TV change (%)	TV (cc)	TV change (%)	TV (cc)	TV change (%)
Baseline / Virtual	6340	0.0	6544	0.0	6872	0.0	8065	0.0	7103	0.0
Virtual 60^0	6006	5.3	6300	3.7	6399	6.9	7657	5.1	6974	1.8
Virtual 70^0	5979	5.7	6219	5.0	6336	7.8	7591	5.9	6844	3.6
Virtual 80^0	5906	6.8	6070	7.2	5998	12.7	7349	8.9	6664	6.2
Virtual 90^0	5713	9.9	5815	11.1	5573	18.9	6999	13.2	6451	9.2
Virtual 100^0	5463	13.8	5543	15.3	5371	21.9	6556	18.7	6173	13.1
Virtual 110^0	5114	19.3	5116	21.8	5218	24.1	6172	23.5	5840	17.8

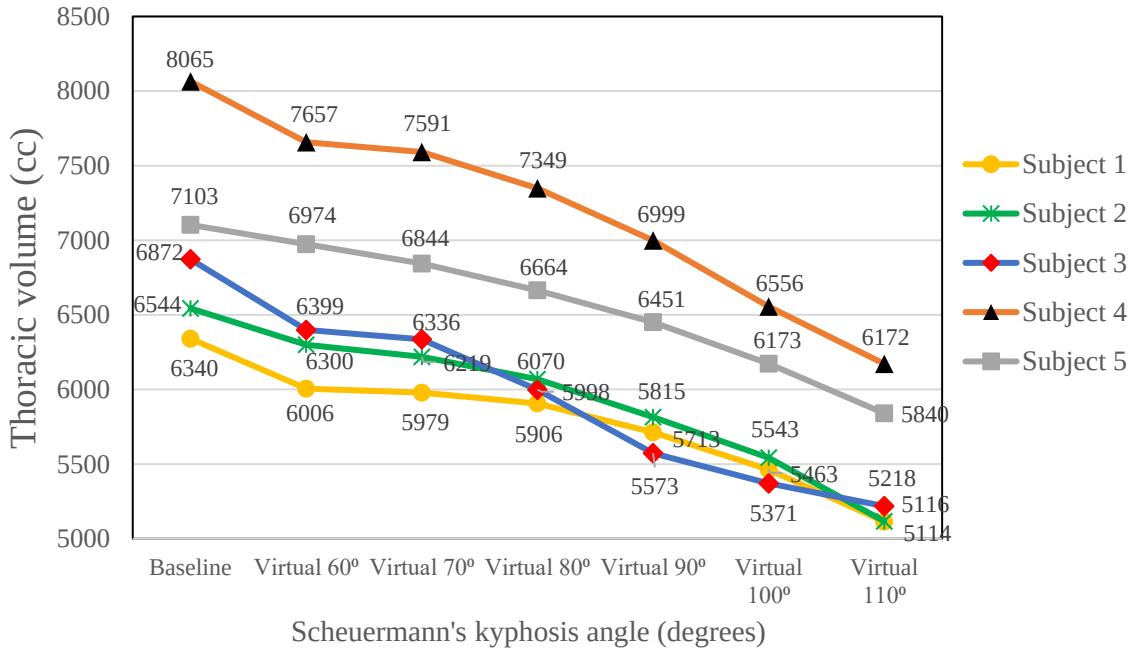

Figure 6.15 Trend line of thoracic volume change for virtual Scheuermann's kyphosis patients with different wedging numbers and wedging angles

6.5 Conclusion

Through 126 virtual osteoporosis patients, I found a strong relationship between compression wedging fractures and thoracic volume. Thoracic volume diminishes when there is a wedging fracture along the thoracic spine, and the wedging fracture also increases the kyphosis angle. Especially, I noticed that the wedging deformity occurring in the upper thoracic spine region is riskier than the wedging deformity located at the lower thoracic spine due to a great loss of the thoracic volume. When more wedging fractures are observed in the thoracic spine, the thoracic volume drops significantly. The limited thoracic volume due to the compression wedging fracture can lead to deterioration in the pulmonary function system in osteoporosis patients [5, 6]. Physicians can use the virtual patients to predict the tendency of the thoracic volume transition, the kyphosis angle, and the severity of the compression wedging fractures, and then further decide the timing to treat the

progressive vertebral body by kyphoplasty or vertebroplasty surgery for osteoporosis patients. From 30 virtual Scheuermann's kyphosis patients, I observed that the more wedging deformities occur in the thoracic spine, the more kyphosis angles progress, and the less thoracic volume the patient possesses. What's worse, the increase in the number of wedging vertebrae and kyphosis angles may possibly damage the pulmonary function, which is are also proven in the previous literature [23, 32]. Understanding the relationship between the wedging deformities and the thoracic volume helps orthopedic doctors make a decision to correct the global and local spine deformities using physical bracing or invasive surgery for Scheuermann's kyphosis patients.

Chapter 7

Discussions and Conclusions

This chapter concludes the findings and contribution of this dissertation and further discusses the potential work in the future.

7.1 Review

This research presented a simulation method and workflow to leverage orthogonal low-dose X-rays to reconstruct patient-specific rib cage and thoracic volume for various spine deformity patients. The method and workflow can benefit medical professionals to efficiently rebuild a patient's pathological rib cage and the volume of the chest wall in 3D. Chapter 3 pointed out the processes (must-do procedures) to develop semi-automatic software to reconstruct the rib cage and thoracic volume through X-rays. The software includes a graphical user interface and an add-on package for Blender® software. The former helps the user easily operate the rib cage reconstruction in the Blender environment and the latter speeds up the thoracic volume reconstruction and increases the accuracy of the thoracic volume. The accuracy of the reconstruction through the developed software was validated through usability testing covered in Chapter 4. The results of the rib cage and thoracic volume reconstructions were compared to those obtained from the gold standard CT scan. In fact, the rib cage reconstruction includes the reconstruction of 12 vertebrae, 24 ribs, and 1 sternum. The results of the thoracic vertebrae reconstruction reveal that the accuracy of the posture (three positions and three rotations) is slightly inferior to [68], but the precision of the posture is slightly superior to the previous literature [82,83]. In addition, the accuracy of the shape morphology of the thoracic vertebrae is comparable to the previous literature [34,36,38,68,76–81] as well. For the thoracic ribs, the

reconstruction results show that the precision of the rotations is superior to the previous literature [58,63]. As for the sternum, less literature discussed or demonstrated its reconstruction. However, it is still worth mentioning that the precision of our sternum reconstruction is better than that of the thoracic vertebra and rib reconstruction. The thoracic volume result from five participants was below 3% error compared to CT scan results, and this satisfies the requirement for measuring humans' pulmonary function recommended by the American Thoracic Society. For further statistical analysis, I employed the two-way ANOVA analysis without replication, and the result shows that there is no significant difference between the thoracic volumes calculated by a CT scan and by our thoracic volume estimator. This reveals the reliability and consistency of the developed software. In the inter-observer reproducibility study, our thoracic volume result was compared to the previous literature [58], and the outcome shows that the accuracy of the thoracic volume reconstruction via the developed program yields superior results. My thoracic volume reconstruction method was compared to the three methods [15,54,56] using equations and the X-rays to measure the thoracic volume. After measuring the thoracic volume, our reconstruction method is lower than 3% error, but the previous methods are all larger than 10% error. This result not only shows that our reconstruction method exceeds those existing methods, but it also concludes that our method provides a more reliable and reproducible technique to calculate the thoracic volume in spine deformity patients.

Chapter 5 demonstrated the application of the developed software for reconstructing thoracic rib cage and volume for early onset scoliosis patients and adult scoliosis patients. For early onset scoliosis patients, they need to undergo multiple imaging examinations and lengthening procedures during growing rod treatments, and the X-rays are the most common way to follow up the pathological spine. I also discussed whether the growing rod surgery contributes to their thoracic volume increase, and the result shows that the answer to this question depends on the age of pediatric patients. Children have distinct speeds of thoracic volume changes at different ages. Generally, the growing rod can assure the children's spines grow smoothly along the implant rods. The adult scoliosis patients

undergo different treatments for the pathological spine during their adolescence. After a 20-year follow-up, I correlated their pulmonary function parameters with the thoracic volume values obtained by the thoracic volume estimator. The result presents that there is a strong positive correlation between the total lung capacity and the thoracic volume, and also a significant correlation between the vital capacity/residual volume and the thoracic volume. These results indicate that our 3D thoracic volume reconstruction by orthogonal biplanar X-rays can potentially serve as an alternative to estimate the pulmonary function of the spine deformity patients in future clinical settings. According to different scoliosis populations, the correlation between several spine parameters and the thoracic volume reflects that the thoracic volume cannot be easily computed or inferred through a one-dimensional spine parameter, which supports the findings in Chapter 4.

Chapter 6 dealt with a quantitative study using the virtual spine patients to investigate the impact of the local wedging deformities or fractures on the thoracic volume. To construct virtual spine patients, I began with several subjects without spine deformity problems. Then, their rib cages and thoracic volumes were reconstructed via our developed thoracic volume estimator introduced in Chapter 3 to serve as the baseline models to further simulate the virtual spine patients. Two spine deformity symptoms: osteoporosis and Scheuermann's kyphosis, were explored and simulated. Some clinical-based assumptions were made to create virtual spine patients to represent actual patients with different pathologies. In the end, 126 virtual osteoporosis patients and 30 virtual Scheuermann's kyphosis patients were created via Blender. From the virtual osteoporosis patients with different locations and numbers of compression fractures, two important conclusions are drawn. One is that when more wedging fractures happen along the thoracic spine, patients will have less thoracic volume. The other one is that the wedging fractures located at a higher level of the thoracic spine cause less thoracic volume than those located at the lower level. These two findings can help orthopedic doctors determine the best timing and treatments for the wedging fractures. In addition, the results from 30 virtual Scheuermann's kyphosis patients demonstrate that different severity levels and numbers of wedging deformities influence the thoracic volume differently. Larger wedging numbers and

wedging angles adversely increase the spine curvature and diminish the thoracic volume. In short, virtual simulated patients can be a cost-effective and time-efficient way to assist orthopedic doctors in visualizing the progressive rib cage deformity and the thoracic volume in specific patients, which will help them decide when and how to intervene and correct a pathological spine.

7.2 Contribution

The following are contributions of this thesis:

1. A new simulation method and workflow for the rib cage and thoracic volume reconstruction through low-dose orthogonal X-rays are developed. The method and workflow can be transferred and replicated to create new medical imaging software to reconstruct the rib cage and thoracic volume for spine patients.
2. A thoracic volume concept and a thoracic volume reconstruction algorithm are proposed, which was not done before, and they provide a surrogate to follow up the respiratory function of the spine deformity patients in a less harmful way (less radiation exposure compared to a CT scan).
3. The application of the thoracic volume estimator is conducted to follow up and compute the thoracic volumes in spine patients, including pediatric and adult scoliosis patients. Through different spine cohorts, it shows that the thoracic volume reconstruction is reliable and accurate compared to directly use a 1-dimensional spine parameter to derive or predict the thoracic volume or lung volume in spine patients.
4. Correlations between the parameters in a pulmonary function test and the thoracic volume in spine patients are explored. These correlation results imply the thoracic volume can be an indicator to infer the total lung capacity in spine patients. The thoracic volume can be an alternative way in future clinical settings to replace the pulmonary function test, especially for those patients who cannot comprehend or follow the instructions during the test.

5. In this study, a workflow to simulate the virtual spine patients through the existing subjects is presented, and the workflow can be adjusted and duplicated for different pathologies. This research is the first one to utilize the concept of the virtual simulated spine patients to quantitatively discover the effect of local compression fractures on thoracic volume variation in osteoporosis patients and the effect of local wedging deformities on thoracic volume changes in Scheuermann's kyphosis patients. No previous literature employed the virtual patients to find out the connection between the wedging vertebrae and the thoracic volume. The simulation results can benefit the orthopedic doctors when they envision the progress of the wedging vertebrae and decide the necessary treatments for the patients.

7.3 Future Work

To make new medical discoveries in the future, there are still some limitations to remove and possible extensions to carry out in this research. The following subsections discuss some of the key elements in detail.

7.3.1 Software Upgrade and Improvement

The future improvements of the current software focus on the following aims:

1. The accuracy of the rib cage reconstruction affects the thoracic volume results, because the rib cage defines the boundary of the thoracic volume. In order to achieve even better accuracy of the rib cage or thoracic volume reconstruction, the morphology and the postures of the rib cage reconstruction can be further improved and refined. For example, the Canny edge detection algorithm [164] can be employed to improve the accuracy of the shape morphology and the postures, especially for the rib reconstruction [57].
2. Current rib cage and thoracic volume reconstruction processes still need users' input and manual operation, which can cause reconstruction errors. In particular, the rib cage (the vertebrae, ribs, and the sternum) reconstruction involves manual operation by the users, so

the reconstruction time for the rib cage is still long, especially for the rib portions of the spine patients. Therefore, the automatic processes of the rib cage reconstruction are necessary to reduce the user operation time and the manual operation errors.

3. When doctors see a spine patient's frontal and lateral X-rays, they normally want to know how severe the spine deformity is. The spine parameters, such as a Cobb angle (for scoliosis patients), a kyphosis angle, a local wedging angle, and the rotation angles of the vertebrae, are vital information to assist doctors in deciding a treatment plan. Hence, those spine parameters can be integrated into the graphical user interface platform or the Blender environment to better facilitate the diagnosis of the spine symptoms.

4. The spine reconstruction in this research incorporates the thoracic rib cage portions, but the reconstruction can extend to the upper and lower spine portions, including the cervical, lumbar, lumbosacral spine and the pelvic portion. The reason for reconstructing the whole skeleton of the spine is to further derive the sagittal vertical axis, which is a plumb line connecting two points between the posterior-superior corner of S1 and the centroid of the C7 vertebral body, as shown in Figure 7.1. The sagittal vertical axis can detect whether the patients possess the imbalance or not. If the sagittal vertical axis does not pass through the two points mentioned above, then it will generate an offset value and result in an imbalance of the human body [165]. This body imbalance can lead to progressive spine curvature in spine patients. As long as the spine curvature changes along the spine, it will possibly vary the thoracic volume. Thus, it would be an interesting topic to explore the effect of the offset value of the sagittal vertical axis on the thoracic volume. Also, the whole spine reconstruction will offer great benefits to the doctor to assess the sagittal imbalance problems of the spine patients.

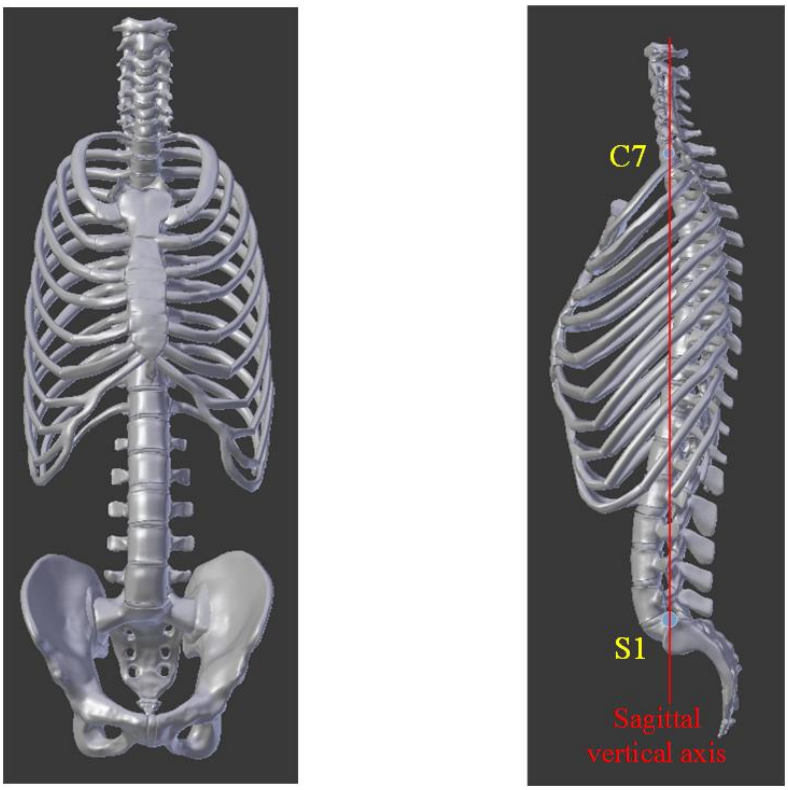

(a) Frontal view (b) Lateral view without showing pelvis

Figure 7.1 Skeleton of whole spine with a demonstration of the sagittal vertical axis

Once the current software is updated and upgraded, it will be necessary to reevaluate the accuracy and the operation time of the updated software by usability testing, as executed in Chapter 4. Also, the reproducibility and repeatability of the software should be studied again. Additionally, the reproducibility study of the software can be reevaluated. Actually, the reproducibility analysis should include an intra-observer and an inter-observer. Due to the time limitation of the users we recruited, the intra-observer reproducibility of the developed software is not conducted in this research. To carry out the intra-observer reproducibility of the developed software in the future, the users will need to reconstruct the rib cage and the thoracic volume for each subject at least twice. The result of two-way ANOVA analysis will disclose whether there is a significant difference between the users and the gold standard CT scan. Besides, 95% of confidence interval

needs to be calculated, because it covers the true population value in 95 of 100 studies performed.

7.3.2 Data Collection from Different Spine Patients for Future Study

In Chapter 5, I correlate the parameters in the pulmonary function test with the thoracic volume, and this study is only performed in adult patients with moderate to severe scoliosis due to the limited data source. In fact, the pulmonary function data from different spine cohorts (subjects old enough to accurately undergo pulmonary function tests) with different severity and spine symptoms (Scheuermann's kyphosis and osteoporosis) can be correlated with the thoracic volume measured by our thoracic volume estimator. The correlation result will further establish the importance and application of the thoracic volume.

As discussed in Chapter 6, I take advantage of the virtual spine patients to study the local wedging deformities. Local wedging deformities present in different spine disorders, such as scoliosis, Scheuermann's kyphosis, and osteoporosis, and they are often associated with the back pain and decreased pulmonary function [166–168]. The orthogonal X-rays from different examination periods of the actual patients with wedging deformity problems can be collected, and the rib cages and the thoracic volumes are reconstructed through the developed software. A validation between the virtual spine models and the actual spine patients with local wedging deformities can be executed to discover how well the virtual models can predict real-life scenarios. In clinical application, the virtual spine models can be employed to assist the surgical planning beforehand.

Bibliography

[1] Bishop, P. J., 1977, "A Bibliography of John Hutchinson," *Med. Hist.*, **21**(4), pp. 384–396.

[2] Escobar, H., and Carver, T. W., 2011, "Pulmonary Function Testing in Young Children," *Curr. Allergy Asthma Rep.*, **11**(6), pp. 473–481.

[3] Brenner, D. J., Elliston, C. D., Hall, E. J., and Berdon, W. E., 2001, "Estimated Risks of Radiation-Induced Fatal Cancer from Pediatric CT," *Am. J. Roentgenol.*, **176**(2), pp. 289–296.

[4] Mettler, F. A., Huda, W., Yoshizumi, T. T., and Mahesh, M., 2008, "Effective Doses in Radiology and Diagnostic Nuclear Medicine: A Catalog," *Radiology*, **248**(1), pp. 254–263.

[5] Gollogly, S., Smith, J. T., and Campbell, R. M., 2004, "Determining Lung Volume with Three-Dimensional Reconstructions of CT Scan Data: A Pilot Study to Evaluate the Effects of Expansion Thoracoplasty on Children with Severe Spinal Deformities," *J. Pediatr. Orthop.*, **24**(3), pp. 323–328.

[6] Cheirsilp, R., Bascom, R., Allen, T. W., and Higgins, W. E., 2015, "Thoracic Cavity Definition for 3D PET/CT Analysis and Visualization," *Comput. Biol. Med.*, **62**, pp. 222–238.

[7] Hurtado, A., and Fray, W. W., 1933, "Studies of Total Pulmonary Capacity and Its Subdivisions. II. Correlation with Physical and Radiological Measurements," *J. Clin. Invest.*, **12**(5), pp. 807–823.

[8] Pratt, P. C., and Klugh, G. A., 1967, "A Method for the Determination of Total Lung Capacity from Posteroanterior and Lateral Chest Roentgenograms," *Am. Rev. Respir. Dis.*, **96**(3), pp. 548–552.

[9] Harris, T. R., Pratt, P. C., and Kilburn, K. H., 1971, "Total Lung Capacity Measured by Roentgenograms," *Am. J. Med.*, **50**(6), pp. 756–763.

[10] Barret, W. A., Clayton, P. D., and Lambson, G. R., 1976, "Computerized

Roentgenographic Determination of Total Lung Capacity," *Am. Rev. Respir. Dis.*, **113**(2), pp. 239–244.

[11] O'Brien, R. J., and Drizd, T. A., 1983, "Roentgenographic Determination of Total Lung Capacity: Normal Values from a National Population Survey," *Am. Rev. Respir. Dis.*, **128**(5), pp. 949–952.

[12] Fumey, M. H., Nickerson, B. G., Birch, M., McCrea, R., and Kao, L. C., 1992, "A Radiographic Method for Estimating Lung Volumes in Sick Infants," *Pediatr. Pulmonol.*, **13**(1), pp. 42–47.

[13] Cala, S. J., Kenyon, C. M., Ferrigno, G., Carnevali, P., Aliverti, A., Pedotti, A., Macklem, P. T., and Rochester, D. F., 1996, "Chest Wall and Lung Volume Estimation by Optical Reflectance Motion Analysis," *J. Appl. Physiol.*, **81**(6), pp. 2680–2689.

[14] Nozoe, M., Mase, K., and Tsutou, A., 2011, "Regional Chest Wall Volume Changes During Various Breathing Maneuvers in Normal Men," *J. Japanese Phys. Ther. Assoc.*, **14**(1), pp. 12–18.

[15] Barnhard, H. J., Pierce, J. A., Joyce, J. W., and Bates, J. H., 1960, "Roentgenographic Determination of Total Lung Capacity: A New Method Evaluated in Health, Emphysema and Congestive Heart Failure," *Am. J. Med.*, **28**(1), pp. 51–60.

[16] Dimeglio, A., and Bonnel, F., 1990, *Le Rachis En Croissance*, Springer, Paris.

[17] Zeng, Y., Chen, Z., Ma, D., Guo, Z., Qi, Q., Li, W., Sun, C., Liu, N., and White, A. P., 2014, "The Influence of Kyphosis Correction Surgery on Pulmonary Function and Thoracic Volume," *Spine (Phila Pa 1976)*, **39**(21), pp. 1777–1784.

[18] Aaro, S., and Dahlborn, M., 1981, "Estimation of Vertebral Rotation and the Spinal and Rib Cage Deformity in Scoliosis by Computer Tomography," *Spine (Phila Pa 1976)*, **6**(5), pp. 460–467.

[19] "Mimics Software" [Online]. Available: https://www.materialise.com/en.

[20] "OsiriX Software" [Online]. Available: https://www.osirix-viewer.com/.

[21] "3D Slicer Software" [Online]. Available: https://www.slicer.org/.

[22] Wozniczka, J. K., Ledonio, C. G. T., Polly, D. W., Rosenstein, B. E., and Nuckley, D. J., 2017, "Adolescent Idiopathic Scoliosis Thoracic Volume Modeling : The Effect of Surgical Correction," *J. Pediatr. Orthop.*, **37**(8), pp. e512–e518.

[23] Ledonio, C. G. T., Rosenstein, B. E., Johnston, C. E., Regelmann, W. E., Nuckley, D. J., and Polly, D. W., 2017, "Pulmonary Function Tests Correlated with Thoracic Volumes in Adolescent Idiopathic Scoliosis," *J. Orthop. Res.*, **35**(1), pp. 175–182.

[24] McKinnis, L. M., 2010, *Fundamentals of Musculoskeletal Imaging*, F. A. Davis, Philadelphia.

[25] Eichinger, M., Heussel, C. P., Kauczor, H. U., Tiddens, H., and Puderbach, M., 2010, "Computed Tomography and Magnetic Resonance Imaging in Cystic Fibrosis Lung Disease," *J. Magn. Reson. Imaging*, **32**(6), pp. 1370–1378.

[26] Schlesinger, A. E., Edgar, K. A., and Boxer, L. A., 1993, "Volume of the Spleen in Children as Measured on CT Scans: Normal Standards as a Function of Body Weight," *AJR Am. J. Roentgenol.*, **160**(5), pp. 1107–1109.

[27] Levy, A. R., Goldberg, M. S., Mayo, N. E., Hanley, J. A., and Poitras, B., 1996, "Reducing the Lifetime Risk of Cancer from Spinal Radiographs Among People with Adolescent Idiopathic Scoliosis," *Spine (Phila Pa 1976)*, **21**(13), pp. 1540–1547.

[28] Yazici, M., Acaroglu, E. R., Alanay, A., Deviren, V., Cila, A., and Surat, A., 2001, "Measurement of Vertebral Rotation in Standing versus Supine Position in Adolescent Idiopathic Scoliosis," *J. Pediatr. Orthop.*, **21**(2), pp. 252–256.

[29] Hoad, C. L., and Martel, A. L., 2002, "Segmentation of MR Images for Computer-Assisted Surgery of the Lumbar Spine," *Phys. Med. Biol.*, **47**(19), pp. 3503–3517.

[30] Davatzikos, C., Liu, D., Shen, D., and Herskovits, E. H., 2002, "Spatial Normalization of Spine MR Images for Statistical Correlation of Lesions with Clinical Symptoms," *Radiology*, **224**(3), pp. 919–926.

[31] Simons, C. J., Cobb, L., and Davidson, B. S., 2014, "A Fast , Accurate , and Reliable Reconstruction Method of the Lumbar Spine Vertebrae Using Positional MRI," *Ann. Biomed. Eng.*, **42**(4), pp. 833–842.

[32] Sullivan, S. M., Banghart, P. R., and Anderson, Q., 1995, "Magnetic Resonance Imaging Assessment of Acute Soft Tissue Injuries to the Temporomandibular Joint," *J. Oral. Maxillofac. Surg.*, **53**(7), pp. 763–767.

[33] Nguyen, D. V, Vo, Q. N., Le, L. H., and Lou, E. H. M., 2015, "Validation of 3D Surface Reconstruction of Vertebrae and Spinal Column Using 3D Ultrasound Data – A Pilot Study," *Med. Eng. Phys.*, **37**(2), pp. 239–244.

[34] Aubin, C. E., Dansereau, J., Parent, F., Labelle, H., and de Guise, J. A., 1997, "Morphometric Evaluations of Personalised 3D Reconstructions and Geometric Models of the Human Spine," *Med. Biol. Eng. Comput.*, **35**(6), pp. 611–618.

[35] Mitton, D., Landry, C., Véron, S., Skalli, W., Lavaste, F., and de Guise, J. A., 2000, "3D Reconstruction Method from Biplanar Radiography Using Non-Stereocorresponding Points and Elastic Deformable Meshes," *Med. Biol. Eng. Comput.*, **38**(2), pp. 133–139.

[36] Delorme, S., Petit, Y., de Guise, J. A., Labelle, H., Aubin, C. E., and Dansereau, J., 2003, "Assessment of the 3-D Reconstruction and High-Resolution Geometrical Modeling of the Human Skeletal Trunk from 2-D Radiographic Images," *IEEE Trans. Biomed. Eng.*, **50**(8), pp. 989–998.

[37] Kadoury, S., Cheriet, F., Laporte, C., and Labelle, H., 2007, "A Versatile 3D Reconstruction System of the Spine and Pelvis for Clinical Assessment of Spinal Deformities," *Med. Biol. Eng. Comput.*, **45**(6), pp. 591–602.

[38] Humbert, L., de Guise, J. A., Aubert, B., Godbout, B., and Skalli, W., 2009, "3D Reconstruction of the Spine from Biplanar X-Rays Using Parametric Models Based on Transversal and Longitudinal Inferences," *Med. Eng. Phys.*, **31**(6), pp. 681–687.

[39] Dansereau, J., and Stokes, I. A. F., 1988, "Measurements of the Three-Dimensional Shape of the Rib Cage," *J. Biomech.*, **21**(11), pp. 893–901.

[40] Mitton, D., Zhao, K., Bertrand, S., Zhao, C., Laporte, S., Yang, C., An, K. N., and Skalli, W., 2008, "3D Reconstruction of the Ribs from Lateral and Frontal X-Rays in Comparison to 3D CT-Scan Reconstruction," *J. Biomech.*, **41**(3), pp. 706–710.

[41] Plourde, F., Cheriet, F., and Dansereau, J., 2012, "Semiautomatic Detection of

Scoliotic Rib Borders from Posteroanterior Chest Radiographs," *IEEE Trans. Biomed. Eng.*, **59**(4), pp. 909–919.

[42] Grenier, S., Parent, S., and Cheriet, F., 2013, "Personalized 3D Reconstruction of the Rib Cage for Clinical Assessment of Trunk Deformities," *Med. Eng. Phys.*, **35**(11), pp. 1651–1658.

[43] Marcil, B., Dansereau, J., Labelle, H., and de Guise, J., 1995, "Incorporation of Patient Displacement into a Trunk Reconstruction Technique," *Proceedings of 17th International Conference of the Engineering in Medicine and Biology Society*, pp. 385–386.

[44] Jolivet, E., Sandoz, B., Laporte, S., Mitton, D., and Skalli, W., 2010, "Fast 3D Reconstruction of the Rib Cage from Biplanar Radiographs," *Med. Biol. Eng. Comput.*, **48**(8), pp. 821–828.

[45] Seoud, L., Cheriet, F., Labelle, H., and Dansereau, J., 2011, "A Novel Method for the 3-D Reconstruction of Scoliotic Ribs from Frontal and Lateral Radiographs," *IEEE Trans. Biomed. Eng.*, **58**(5), pp. 1135–1146.

[46] Trochu, F., 1993, "A Contouring Program Based on Dual Kriging Interpolation," *Eng. Comput.*, **9**(3), pp. 160–177.

[47] Laporte, S., Skalli, W., de Guise, J. A., Lavaste, F., and Mitton, D., 2003, "A Biplanar Reconstruction Method Based on 2D and 3D Contours : Application to the Distal Femur," *Comput. Methods Biomech. Biomed. Eng.*, **6**(1), pp. 1–6.

[48] Illés, T., and Somoskeöy, S., 2012, "The EOS^{TM} Imaging System and Its Uses in Daily Orthopaedic Practice," *Int. Orthop.*, **36**(7), pp. 1325–1331.

[49] Miller, M. R., Hankinson, J., Brusasco, V., Burgos, F., Casaburi, R., Coates, A., Crapo, R., Enright, P., van der Grinten, C. P. M., Gustafsson, P., Jensen, R., Johnson, D. C., MacIntyre, N., McKay, R., Navajas, D., Pedersen, O. F., Pellegrino, R., Viegi, G., and Wagner, J., 2005, "Standardisation of Spirometry," *Eur. Respir. J.*, **26**(2), pp. 319–338.

[50] Charles, Y. P., Diméglio, A., Marcoul, M., Bourgin, J. F., Marcoul, A., and Bozonnat, M. C., 2008, "Influence of Idiopathic Scoliosis on Three-Dimensional

Thoracic Growth," *Spine (Phila Pa 1976)*, **33**(11), pp. 1209–1218.

[51] Pierce, R. J., Brown, D. J., Holmes, M., Cumming, G., and Denison, D. M., 1979, "Estimation of Lung Volumes from Chest Radiographs Using Shape Information," *Thorax*, **34**(6), pp. 726–734.

[52] Krayer, S., Rehder, K., Beck, K. C., Cameron, P. D., Didier, E. P., and Hoffman, E. A., 1987, "Quantification of Thoracic Volumes by Three-Dimensional Imaging," *J. Appl. Physiol.*, **62**(2), pp. 591–598.

[53] Wood, K. B., Schendel, M. J., Dekutoski, M. B., Boachie-Adjei, O., and Heithoff, K. H., 1996, "Thoracic Volume Changes in Scoliosis Surgery," *Spine (Phila Pa 1976)*, **21**(6), pp. 718–723.

[54] Kovach, J. C., Avedian, V., Morales, G., and Poulos, P., 1956, "Lung Compartment Determination," *J. Thorac. Surg.*, **31**(4), pp. 452–457.

[55] Loyd, H. M., String, S. T., and DuBois, A. B., 1966, "Radiographic and Plethysmographic Determination of Total Lung Capacity," *Radiology*, **86**(1), pp. 7–14.

[56] Stolle, E., Fröhlich, K., and Luska, G., 1985, "Ein Neues Rechenverfahren Zur Radiologischen Ermittlung Der Totalen Lungenkapazität (TLC)," *Fortschr Rontgenstr*, **143**(11), pp. 583–587.

[57] Koehler, C., and Wischgoll, T., 2010, "Knowledge-Assisted Reconstruction of the Human Rib Cage and Lungs," *IEEE Comput. Graph. Appl.*, **30**(1), pp. 17–29.

[58] Courvoisier, A., Ilharreborde, B., Constantinou, B., Aubert, B., Vialle, R., and Skalli, W., 2013, "Evaluation of a Three-Dimensional Reconstruction Method of the Rib Cage of Mild Scoliotic Patients," *Spine Deform.*, **1**(5), pp. 321–327.

[59] "Orten Company" [Online]. Available: https://orten.proteor.com/.

[60] Kovač, V., Puljiz, A., Smerdelj, M., and Pecina, M., 2001, "Scoliosis Curve Correction, Thoracic Volume Changes, and Thoracic Diameters in Scoliotic Patients After Anterior and After Posterior Instrumentation," *Int. Orthop.*, **25**(2), pp. 66–69.

[61] Lee, P. C., Ledonio, C., Erdman, A., and Polly, D., 2016, "Thoracic Volume Follow-Up for Growing Rod Surgical Treatment in Early Onset Scoliosis Patients," *J. Med.*

Device., **10**(3), p. 030918.

[62] Dworzak, J., Lamecker, H., von Berg, J., Klinder, T., Lorenz, C., Kainmüller, D., Seim, H., Hege, H. C., and Zachow, S., 2010, "3D Reconstruction of the Human Rib Cage from 2D Projection Images Using a Statistical Shape Model," *Int. J. Comput. Assist. Radiol. Surg.*, **5**(2), pp. 111–124.

[63] Aubert, B., Vergari, C., Ilharreborde, B., Courvoisier, A., and Skalli, W., 2016, "3D Reconstruction of Rib Cage Geometry from Biplanar Radiographs Using a Statistical Parametric Model Approach," *Comput. Methods Biomech. Biomed. Eng. Imaging Vis.*, **4**(5), pp. 281–295.

[64] Cerny, P., Marik, I., and Pallova, I., 2014, "The Radiographic Method for Evaluation of Axial Vertebral Rotation - Presentation of the New Method," *Scoliosis*, **9**(1), pp. 1–9.

[65] "Blender Manual" [Online]. Available: https://docs.blender.org/manual/en/dev/.

[66] "Blender 3D Printing Toolbox" [Online]. Available: https://wiki.blender.org/index.php/Dev:Ref/Release_Notes/2.67/Print_Tools.

[67] Delorme, S., Labelle, H., Poitras, B., Rivard, C. H., Coillard, C., and Dansereau, J., 2000, "Pre-, Intra-, and Postoperative Three-Dimensional Evaluation of Adolescent Idiopathic Scoliosis," *J. Spinal Disord.*, **13**(2), pp. 93–101.

[68] Glaser, D. A., Doan, J., and Newton, P. O., 2012, "Comparison of 3-Dimensional Spinal Reconstruction Accuracy: Biplanar Radiographs with EOS versus Computed Tomography," *Spine (Phila Pa 1976)*, **37**(16), pp. 1391–1397.

[69] "CloudCompare Software" [Online]. Available: https://www.danielgm.net/cc/.

[70] Besl, P. J., and McKay, N. D., 1992, "A Method for Registration of 3-D Shapes," *IEEE Trans. Pattern Anal. Mach. Intell.*, **14**(2), pp. 239–256.

[71] Lu, Y., and Fang, J. Q., 2003, *Advanced Medical Statistics*, World Scientific, Singapore.

[72] Crawford, N. R., and Dickman, C. A., 1997, "Construction of Local Vertebral Coordinate Systems Using a Digitizing Probe," *Spine (Phila Pa 1976)*, **22**(5), pp. 559–563.

[73] Cook, D. J., 2009, "Characterization of the Response of the Cadaveric Human Spine to Loading in a Six-Degree-of-Freedom Spine Testing Apparatus," Master's Thesis, University of Pittsburgh.

[74] Skalli, W., Lavaste, F., and Descrimes, J. L., 1995, "Quantification of Three-Dimensional Vertebral Rotations in Scoliosis: What Are the True Values?," *Spine (Phila Pa 1976)*, **20**(5), pp. 546–553.

[75] Wilson, T. A., Rehder, K., Krayer, S., Hoffman, E. A., Whitney, C. G., and Rodarte, J. R., 1987, "Geometry and Respiratory Displacement of Human Ribs," *J. Appl. Physiol.*, **62**(5), pp. 1872–1877.

[76] Mitulescu, A., Skalli, W., Mitton, D., and de Guise, J. A., 2002, "Three-Dimensional Surface Rendering Reconstruction of Scoliotic Vertebrae Using a Non Stereo-Corresponding Points Technique," *Eur. Spine J.*, **11**(4), pp. 344–352.

[77] Le Bras, A., Laporte, S., Mitton, D., de Guise, J. A., and Skalli, W., 2003, "Three-Dimensional (3D) Detailed Reconstruction of Human Vertebrae from Low-Dose Digital Stereoradiography," *Eur. J. Orthop. Surg. Traumatol.*, **13**(2), pp. 57–62.

[78] Benameur, S., Mignotte, M., Parent, S., Labelle, H., Skalli, W., and de Guise, J. A., 2003, "3D/2D Registration and Segmentation of Scoliotic Vertebrae Using Statistical Models," *Comput. Med. Imaging Graph.*, **27**(5), pp. 321–337.

[79] Pomero, V., Mitton, D., Laporte, S., de Guise, J. A., and Skalli, W., 2004, "Fast Accurate Stereoradiographic 3D-Reconstruction of the Spine Using a Combined Geometric and Statistic Model," *Clin. Biomech.*, **19**(3), pp. 240–247.

[80] Benameur, S., Mignotte, M., Labelle, H., and de Guise, J. A., 2005, "A Hierarchical Statistical Modeling Approach for the Unsupervised 3D Biplanar Reconstruction of the Scoliotic Spine," *IEEE Trans. Biomed. Eng.*, **52**(12), pp. 2041–2057.

[81] Kadoury, S., Cheriet, F., and Labelle, H., 2009, "Personalized X-Ray 3-D Reconstruction of the Scoliotic Spine from Hybrid Statistical and Image-Based Models," *IEEE Trans. Med. Imaging*, **28**(9), pp. 1422–1435.

[82] Dumas, R., Blanchard, B., Carlier, R., de Loubresse, C. G., Le Huec, J. C., Marty, C., Moinard, M., and Vital, J. M., 2008, "A Semi-Automated Method Using

Interpolation and Optimisation for the 3D Reconstruction of the Spine from Bi-Planar Radiography: A Precision and Accuracy Study," *Med. Biol. Eng. Comput.*, **46**(1), pp. 85–92.

[83] Zhang, J., Lv, L., Shi, X., Wang, Y., Guo, F., Zhang, Y., and Li, H., 2013, "3-D Reconstruction of the Spine from Biplanar Radiographs Based on Contour Matching Using the Hough Transform," *IEEE Trans. Biomed. Eng.*, **60**(7), pp. 1954–1964.

[84] De Moura, D. C., 2010, "Three-Dimensional Biplanar Reconstruction of the Scoliotic Spine for Standard Clinical Setup," Doctoral Dissertation, University of Porto.

[85] Koehler, C., Wischgoll, T., and Golshani, F., 2010, "Reconstructing the Human Ribcage in 3D with X-Rays and Geometric Models," *IEEE Multimed.*, **17**(3), pp. 46–53.

[86] *International Organization for Standardization 1994-12-25, Accuracy (Trueness and Precision) of Measurement Methods and Results - Part 2: Basic Method for the Determination of Repeatability and Reproducibility of a Standard Measurement Method*, ISO 5725-2, Geneva, Switzerland.

[87] Kumar, V., Abbas, A. K., Fausto, N., and Mitchell, R. N., 2007, *Robbins Basic Pathology*, Elsevier, Philadelphia.

[88] Pellegrino, R., Viegi, G., Brusasco, V., Crapo, R. O., Burgos, F., Casaburi, R., Coates, A., van der Grinten, C. P. M., Gustafsson, P., Hankinson, J., Jensen, R., Johnson, D. C., MacIntyre, N., McKay, R., Miller, M. R., Navajas, D., Pedersen, O. F., and Wanger, J., 2005, "Interpretative Strategies for Lung Function Tests," *Eur. Respir. J.*, **26**(5), pp. 948–968.

[89] Redding, G. J., 2014, "Early Onset Scoliosis: A Pulmonary Perspective," *Spine Deform.*, **2**(6), pp. 425–429.

[90] Grala, M., 2014, "Pulmonology," *The Harriet Lane Handbook*, B. Engorn, and J. Flerlage, eds., Elsevier, Philadelphia, PA.

[91] Shakil, H., Iqbal, Z. A., and Al-Ghadir, A. H., 2014, "Scoliosis: Review of Types of Curves, Etiological Theories and Conservative Treatment," *J. Back Musculoskelet.*

Rehabil., **27**(2), pp. 111–115.

[92] Cobb, J. R., 1948, "Outline for the Study of Scoliosis," *Instr. Course Lect.*, **5**, pp. 261–275.

[93] Stokes, I. A. F., 1994, "Three-Dimensional Terminology of Spinal Deformity," *Spine (Phila Pa 1976)*, **19**(2), pp. 236–248.

[94] Lee, W. T. K., Cheung, C. S. K., Tse, Y. K., Guo, X., Qin, L., Lam, T. P., Ng, B. K. W., and Cheng, J. C. Y., 2005, "Association of Osteopenia with Curve Severity in Adolescent Idiopathic Scoliosis: A Study of 919 Girls," *Osteoporos. Int.*, **16**(12), pp. 1924–1932.

[95] Asher, M. A., and Burton, D. C., 2006, "Adolescent Idiopathic Scoliosis: Natural History and Long Term Treatment Effects," *Scoliosis*, **1**(1), pp. 1–10.

[96] Yang, S., Andras, L. M., Redding, G. J., and Skaggs, D. L., 2016, "Early-Onset Scoliosis: A Review of History, Current Treatment, and Future Directions," *Pediatrics*, **137**(1), pp. 1–12.

[97] Jackson, R. P., Simmons, E. H., and Stripinis, D., 1989, "Coronal and Sagittal Plane Spinal Deformities Correlating with Back Pain and Pulmonary Function in Adult Idiopathic Scoliosis," *Spine (Phila Pa 1976)*, **14**(12), pp. 1391–1397.

[98] Tsiligiannis, T., and Grivas, T., 2012, "Pulmonary Function in Children with Idiopathic Scoliosis," *Scoliosis*, **7**(1), p. 7.

[99] Koumbourlis, A. C., 2006, "Scoliosis and the Respiratory System," *Paediatr. Respir. Rev.*, **7**(2), pp. 152–160.

[100] Carr, W. A., Moe, J. H., Winter, R. B., and Lonstein, J. E., 1980, "Treatment of Idiopathic Scoliosis in the Milwaukee Brace," *J. Bone Jt. Surg. Am.*, **62**(4), pp. 599–612.

[101] Akbarnia, B. A., 2007, "Management Themes in Early Onset Scoliosis," *J. Bone Jt. Surg. Am.*, **89**(suppl_1), pp. 42–54.

[102] Hacquebord, J. H., and Leopold, S. S., 2012, "In Brief: The Risser Classification: A Classic Tool for the Clinician Treating Adolescent Idiopathic Scoliosis," *Clin. Orthop. Relat. Res.*, **470**(8), pp. 2335–2338.

[103] Nachemson, A., 1968, “A Long Term Follow-up Study of Non-Treated Scoliosis,” *Acta Orthop. Scand.*, **39**(4), pp. 466–476.

[104] Pehrsson, K., Bake, B., Larsson, S., and Nachemson, A., 1991, “Lung Function in Adult Idiopathic Scoliosis: A 20 Year Follow Up,” *Thorax*, **46**(7), pp. 474–478.

[105] Thompson, G. H., Akbarnia, B. A., and Campbell, R. M., 2007, “Growing Rod Techniques in Early-Onset Scoliosis,” *J. Pediatr. Orthop.*, **27**(3), pp. 354–361.

[106] Bess, S., Akbarnia, B. A., Thompson, G. H., Sponseller, P. D., Shah, S. A., El Sebaie, H., Boachie-Adjei, O., Karlin, L. I., Canale, S., Poe-Kochert, C., and Skaggs, D. L., 2010, “Complications of Growing-Rod Treatment for Early-Onset Scoliosis: Analysis of One Hundred and Forty Patients,” *J. Bone Jt. Surg. Am.*, **92**(15), pp. 2533–2543.

[107] Redding, G. J., and Mayer, O. H., 2011, “Structure-Respiration Function Relationships Before and After Surgical Treatment of Early-Onset Scoliosis,” *Clin. Orthop. Relat. Res.*, **469**(5), pp. 1330–1334.

[108] Glotzbecker, M., Johnston, C., Miller, P., Smith, J., Perez-Grueso, F. S., Woon, R., Flynn, J., Gold, M., Garg, S., Redding, G., Cahill, P., and Emans, J., 2014, “Is There a Relationship Between Thoracic Dimensions and Pulmonary Function in Early-Onset Scoliosis?,” *Spine (Phila Pa 1976)*, **39**(19), pp. 1590–1595.

[109] Newton, P. O., Faro, F. D., Gollogly, S., Betz, R. R., Lenke, L. G., and Lowe, T. G., 2005, “Results of Preoperative Pulmonary Function Testing of Adolescents with Idiopathic Scoliosis: A Study of Six Hundred and Thirty-One Patients,” *J. Bone Jt. Surg. Am.*, **87**(9), pp. 1937–1946.

[110] Aaro, S., and Ohlund, C., 1984, “Scoliosis and Pulmonary Function,” *Spine (Phila Pa 1976)*, **9**(2), pp. 220–222.

[111] Johnston, C. E., Richards, B. S., Sucato, D. J., Bridwell, K. H., Lenke, L. G., and Erickson, M., 2011, “Correlation of Preoperative Deformity Magnitude and Pulmonary Function Tests in Adolescent Idiopathic Scoliosis,” *Spine (Phila Pa 1976)*, **36**(14), pp. 1096–1102.

[112] Weinstein, S. L., Zavala, D. C., and Ponseti, I. V., 1981, “Idiopathic Scoliosis: Long-

Term Follow-up and Prognosis in Untreated Patients," *J. Bone Jt. Surg. Am.*, **63**(5), pp. 702–712.

[113] Pehrsson, K., Danielsson, A., and Nachemson, A., 2001, "Pulmonary Function in Adolescent Idiopathic Scoliosis: A 25 Year Follow up After Surgery or Start of Brace Treatment," *Thorax*, **56**(5), pp. 388–393.

[114] Kumano, K., and Tsuyama, N., 1982, "Pulmonary Function Before and After Surgical Correction of Scoliosis," *J. Bone Jt. Surg. Am.*, **64**(2), pp. 242–248.

[115] Ogilvie, J. W., and Schendel, M. J., 1988, "Calculated Thoracic Volume as Related to Parameters of Scoliosis Correction," *Spine (Phila Pa 1976)*, **13**(1), pp. 39–42.

[116] Nilsonne, U., and Lundgren, K. D., 1968, "Long-Term Prognosis in Idiopathic Scoliosis," *Acta Orthop. Scand.*, **39**(4), pp. 456–465.

[117] Pehrsson, K., Larsson, S., Oden, A., and Nachemson, A., 1992, "Long-Term Follow-up of Patients with Untreated Scoliosis: A Study of Mortality, Causes of Death, and Symptoms," *Spine (Phila Pa 1976)*, **17**(9), pp. 1091–1096.

[118] Gillingham, B. L., Fan, R. A., and Akbarnia, B. A., 2006, "Early Onset Idiopathic Scoliosis," *J. Am. Acad. Orthop. Surg.*, **14**(2), pp. 101–112.

[119] Canavese, F., and Dimeglio, A., 2013, "Normal and Abnormal Spine and Thoracic Cage Development," *World J. Orthop.*, **4**(4), pp. 167–174.

[120] Campbell, R. M., and Smith, M. D., 2007, "Thoracic Insufficiency Syndrome and Exotic Scoliosis," *J. Bone Jt. Surg. Am.*, **89**(suppl_1), pp. 108–122.

[121] Johari, J., Sharifudin, M. A., Ab Rahman, A., Omar, A. S., Abdullah, A. T., Nor, S., Lam, W. C., and Yusof, M. I., 2016, "Relationship between Pulmonary Function and Degree of Spinal Deformity, Location of Apical Vertebrae and Age Among Adolescent Idiopathic Scoliosis Patients," *Singapore Med. J.*, **57**(1), pp. 33–38.

[122] Akazawa, T., Kuroya, S., Iinuma, M., Asano, K., Torii, Y., Umehara, T., Kotani, T., Sakuma, T., Minami, S., Orita, S., Inage, K., Fujimoto, K., Shiga, Y., Inoue, G., Miyagi, M., Saito, W., Ohtori, S., and Niki, H., 2018, "Pulmonary Function and Thoracic Deformities in Adolescent Idiopathic Scoliosis 27 Years or Longer After Spinal Fusion with Harrington Instrument," *J. Orthop. Sci.*, **23**(1), pp. 45–50.

[123] Grivas, T. B., Burwell, R. G., Purdue, M., Webb, J. K., and Moulton, A., 1991, "A Segmental Analysis of Thoracic Shape in Chest Radiographs of Children. Changes Related to Spinal Level, Age, Sex, Side and Significance for Lung Growth and Scoliosis," *J. Anat.*, **178**, pp. 21–38.

[124] Yoon, W. W., Sedra, F., Shah, S., Wallis, C., Muntoni, F., and Noordeen, H., 2014, "Improvement of Pulmonary Function in Children With Early-Onset Scoliosis Using Magnetic Growth Rods," *Spine (Phila Pa 1976)*, **39**(15), pp. 1196–1202.

[125] Harshavardhana, N. S., Fahmy, A., and Noordeen, H., 2015, "Surgical Results of Magnet Driven Growing Rods (MdGR) for Early-Onset Scoliosis (EOS): Single Center Experience of Five Years," *Spine J.*, **15**(10), pp. S177–S178.

[126] Cook, D. A., Erwin, P. J., and Triola, M. M., 2010, "Computerized Virtual Patients in Health Professions Education: A Systematic Review and Meta-Analysis," *Acad. Med.*, **85**(10), pp. 1589–1602.

[127] Christ, A., Kainz, W., Hahn, E. G., Honegger, K., Zefferer, M., Neufeld, E., Rascher, W., Janka, R., Bautz, W., Chen, J., Kiefer, B., Schmitt, P., Hollenbach, H. P., Shen, J., Oberle, M., Szczerba, D., Kam, A., Guag, J. W., and Kuster, N., 2010, "The Virtual Family-Development of Surface-Based Anatomical Models of Two Adults and Two Children for Dosimetric Simulations," *Phys. Med. Biol.*, **55**(2), pp. N23–N38.

[128] Gosselin, M. C., Neufeld, E., Moser, H., Huber, E., Farcito, S., Gerber, L., Jedensjö, M., Hilber, I., Di Gennaro, F., Lloyd, B., Cherubini, E., Szczerba, D., Kainz, W., and Kuster, N., 2014, "Development of a New Generation of High-Resolution Anatomical Models for Medical Device Evaluation: The Virtual Population 3.0," *Phys. Med. Biol.*, **59**(18), pp. 5287–5303.

[129] Talbot, T. B., Sagae, K., John, B., and Rizzo, A. A., 2012, "Sorting Out the Virtual Patient: How to Exploit Artificial Intelligence, Game Technology and Sound Education Practices to Create Engaging Role-Playing Simulations," *Int. J. Gaming Comput. Simulations*, **4**, pp. 1–19.

[130] Greenberg, M. S., 2006, *Handbook of Neurosurgery*, Thieme, New York.

[131] Alexandru, D., and So, W., 2012, "Evaluation and Management of Vertebral Compression Fractures," *Perm. J.*, **16**(4), pp. 46–51.

[132] Cummings, S. R., and Melton, L. J., 2002, "Epidemiology and Outcomes of Osteoporotic Fractures," *Lancet*, **359**(9319), pp. 1761–1767.

[133] Wade, S. W., Strader, C., Fitzpatrick, L. A., Anthony, M. S., and O'Malley, C. D., 2014, "Estimating Prevalence of Osteoporosis : Examples from Industrialized Countries," *Arch Osteoporos*, **9**(182), pp. 1–10.

[134] Harrison, R. A., Siminoski, K., Vethanayagam, D., and Majumdar, S. R., 2007, "Osteoporosis-Related Kyphosis and Impairments in Pulmonary Function: A Systematic Review," *J. Bone Miner. Res.*, **22**(3), pp. 447–457.

[135] Leech, J. A., Dulberg, C., Kellie, S., Pattee, L., and Gay, J., 1990, "Relationship of Lung Function to Severity of Osteoporosis in Women," *Am. Rev. Respir. Dis.*, **141**(1), pp. 68–71.

[136] Schlaich, C., Minne, H. W., Bruckner, T., Wagner, G., Gebest, H. J., Grunze, M., Ziegler, R., and Leidig-Bruckner, G., 1998, "Reduced Pulmonary Function in Patients with Spinal Osteoporotic Fractures," *Osteoporos. Int.*, **8**(3), pp. 261–267.

[137] Krege, J. H., Kendler, D., Krohn, K., Genant, H., Alam, J., Berclaz, P. Y., Coffey, B., and Loghin, C., 2015, "Relationship Between Vertebral Fracture Burden, Height Loss, and Pulmonary Function in Postmenopausal Women With Osteoporosis," *J. Clin. Densitom.*, **18**(4), pp. 506–511.

[138] Kado, D. M., Browner, W. S., Palermo, L., Nevitt, M. C., Genant, H. K., and Cummings, S. R., 1999, "Vertebral Fractures and Mortality in Older Women: A Prospective Study," *Arch Intern Med*, **159**(11), pp. 1215–1220.

[139] Teng, G. G., Curtis, J. R., and Saag, K. G., 2008, "Mortality and Osteoporotic Fractures: Is the Link Causal, and Is It Modifiable?," *Clin. Exp. Rheumatol.*, **26**(5 SUPPL. 51), pp. S125–S137.

[140] Svejme, O., Ahlborg, H. G., Nilsson, J. A., and Karlsson, M. K., 2012, "Early Menopause and Risk of Osteoporosis, Fracture and Mortality: A 34-Year Prospective Observational Study in 390 Women," *An Int. J. Obstet. Gynaecol.*,

119(7), pp. 810–816.

[141] Heini, P. F., and Orler, R., 2004, "Kyphoplasty for Treatment of Osteoporotic Vertebral Fractures," *Eur. Spine J.*, **13**(3), pp. 184–192.

[142] Edidin, A. A., Ong, K. L., Lau, E., and Kurtz, S. M., 2011, "Mortality Risk for Operated and Nonoperated Vertebral Fracture Patients in the Medicare Population," *J. Bone Miner. Res.*, **26**(7), pp. 1617–1626.

[143] Scheuermann, H. W., 1920, "Kyphosis Dorsalis Juvenilis," *Ugeskr. Laeger*, **82**(12), pp. 385–393.

[144] Fotiadis, E., Kenanidis, E., Samoladas, E., Christodoulou, A., Akritopoulos, P., and Akritopoulou, K., 2008, "Scheuermann's Disease: Focus on Weight and Height Role," *Eur. Spine J.*, **17**(5), pp. 673–678.

[145] "SRS Website" [Online]. Available: https://www.srs.org/professionals/online-education-and-resources/conditions-and-treatments/kyphosis-in-the-adolescent-and-young-adult.

[146] Sorenson, K. H., 1964, *Scheuermann's Juvenile Kyphosis*, Munksgaard, Copenhagen.

[147] Lowe, T. G., 1990, "Current Concepts Review: Scheuermann Disease," *J. Bone Jt. Surg. Am.*, **72**(6), pp. 940–945.

[148] Lowe, T. G., and Line, B. G., 2007, "Evidence Based Medicine: Analysis of Scheuermann Kyphosis," *Spine (Phila. Pa. 1976)*, **32**(19 Suppl), pp. S115–S119.

[149] Boos, N., and Aebi, M., 2008, *Spinal Disorders: Fundamentals of Diagnosis and Treatment*, Springer, Berlin, Heidelberg.

[150] Lowe, T. G., and Kasten, M. D., 1994, "An Analysis of Sagittal Curves and Balance After Cotrel-Dubousset Instrumentation for Kyphosis Secondary to Scheuermann's Disease. A Review of 32 Patients," *Spine (Phila. Pa. 1976)*, **19**(15), pp. 1680–1685.

[151] Papagelopoulos, P. J., Mavrogenis, A. F., Savvidou, O. D., Mitsiokapa, E A Themistocleous, G. S., and Soucacos, P. N., 2008, "Current Concepts in Scheuermann's Kyphosis," *Orthopedics*, **31**(1), pp. 52–58.

[152] Murray, P. M., Weinstein, S. L., and Spratt, K. F., 1993, "The Natural History and

Long-Term Follow-up of Scheuermann Kyphosis," *J. Bone Jt. Surg. Am.*, **75**(2), pp. 236–248.

[153] Bradford, D. S., Moe, J. H., Montalvo, F. J., and Winter, R. B., 1975, "Scheuermann's Kyphosis. Results of Surgical Treatment by Posterior Spine Arthrodesis in Twenty-Two Patients," *J. Bone Jt. Surg. Am.*, **57**(4), pp. 439–448.

[154] Bradford, D. S., Ahmed, K. B., Moe, J. H., Winter, R. B., and Lonstein, J. E., 1980, "The Surgical Management of Patients with Scheuermann's Disease: A Review of Twenty-Four Cases Managed by Combined Anterior and Posterior Spine Fusion," *J. Bone Jt. Surg. Am.*, **62**(5), pp. 705–712.

[155] Sachs, B., Bradford, D., Winter, R., Lonstein, J., Moe, J., and Willson, S., 1987, "Scheuermann Kyphosis. Follow-up of Milwaukee-Brace Treatment," *J. Bone Jt. Surg. Am.*, **69**(1), pp. 50–57.

[156] Soo, C. L., Noble, P. C., and Esses, S. I., 2002, "Scheuermann Kyphosis : Long-Term Follow-Up," *Spine J.*, **2**(1), pp. 49–56.

[157] Koller, H., Juliane, Z., Umstaetter, M., Meier, O., Schmidt, R., and Hitzl, W., 2014, "Surgical Treatment of Scheuermann's Kyphosis Using a Combined Antero-Posterior Strategy and Pedicle Screw Constructs: Efficacy, Radiographic and Clinical Outcomes in 111 Cases," *Eur. Spine J.*, **23**(1), pp. 180–191.

[158] Abbi, G., Lonner, B. S., Toombs, C. S., Sponseller, P. D., Samdani, A. F., Betz, R. R., Shah, S. A., and Newton, P. O., 2014, "Preoperative Pulmonary Function in Patients with Operative Scheuermann Kyphosis," *Spine Deform.*, **2**(1), pp. 70–75.

[159] Wenger, D. R., and Frick, S. L., 1999, "Scheuermann Kyphosis," *Spine (Phila. Pa. 1976)*, **24**(24), pp. 2630–2639.

[160] Tribus, C. B., 1998, "Scheuermann's Kyphosis in Adolescents and Adults : Diagnosis and Management," *J. Am. Acad. Orthop. Surg.*, **6**(1), pp. 36–43.

[161] Arlet, V., and Schlenzka, D., 2005, "Scheuermann's Kyphosis: Surgical Management," *Eur. Spine J.*, **14**(9), pp. 817–827.

[162] "Center for Research in Education and Simulation Technologies at the University of Minnesota" [Online]. Available: http://www.crest.umn.edu/.

[163] Lonner, B., Yoo, A., Terran, J. S., Sponseller, P., Samdani, A., Betz, R., Shuffelbarger, H., Shah, S. A., and Newton, P., 2013, "Effect of Spinal Deformity on Adolescent Quality of Life Comparison of Operative Scheuermann Kyphosis, Adolescent Idiopathic Scoliosis and Normal Controls," *Spine (Phila. Pa. 1976)*, **38**(12), pp. 1049–1055.

[164] Canny, J., 1986, "A Computational Approach to Edge Detection," *IEEE Trans. Pattern Anal. Mach. Intell.*, **8**(6), pp. 679–698.

[165] Glassman, S. D., Bridwell, K., Dimar, J. R., Horton, W., Berven, S., and Schwab, F., 2005, "The Impact of Positive Sagittal Balance in Adult Spinal Deformity," *Spine (Phila Pa 1976)*, **30**(18), pp. 2024–2029.

[166] Aebi, M., 2005, "The Adult Scoliosis," *Eur. Spine J.*, **14**(10), pp. 925–948.

[167] Greene, T. L., Hensinger, R. N., and Hunter, L. Y., 1985, "Back Pain and Vertebral Changes Simulating Scheuermann's Disease," *J. Pediatr. Orthop.*, **5**(1), pp. 1–7.

[168] Ettinger, B., Black, D. M., Nevitt, M. C., Rundle, A. C., Cauley, J. A., Cummings, S. R., and Genant, H. K., 1992, "Contribution of Vertebral Deformities to Chronic Back Pain and Disability," *J. Bone Miner. Res.*, **7**(4), pp. 449–456.

Appendix A:
Virtual Spine Patients with Wedging Deformities

This appendix documents information for baseline models and presents all virtual rib cage and thoracic volume models for osteoporosis and Scheuermann's kyphosis symptoms. Appendix A.1 shows the baseline rib cage and thoracic volume models of Subject 3 along with the developed virtual osteoporosis patients. Appendix A.2 first tabulates the information for baseline models and virtual Scheuermann's kyphosis patients, and then exhibits rib cages and thoracic volumes from baseline models and simulated virtual patients.

A.1 Virtual Osteoporosis Patients

Due to the similarity, I only present the baseline rib cage and thoracic volume of Subject 3 and twenty-one simulated virtual osteoporosis patients from Figures A.1 to A.4.

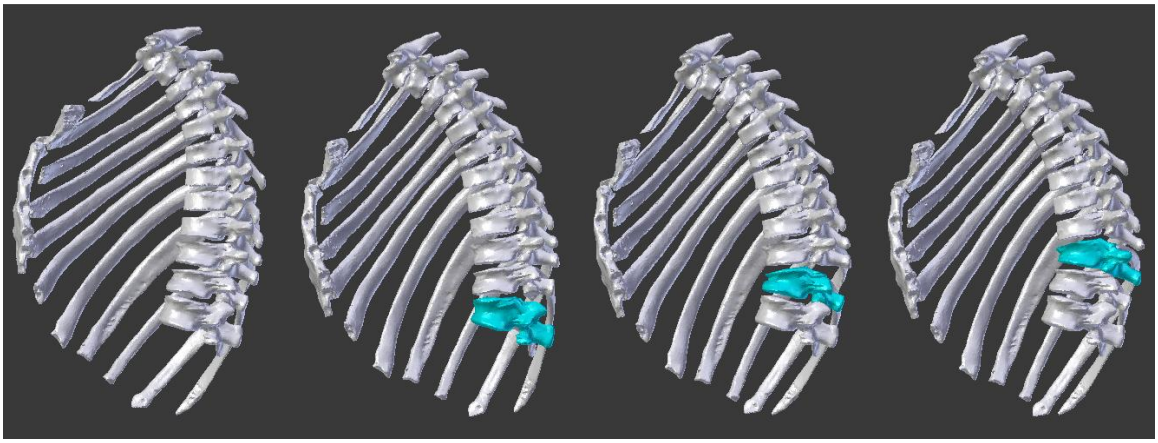

(a) Baseline (b) T12 wedging (c) T11 wedging (d) T10 wedging

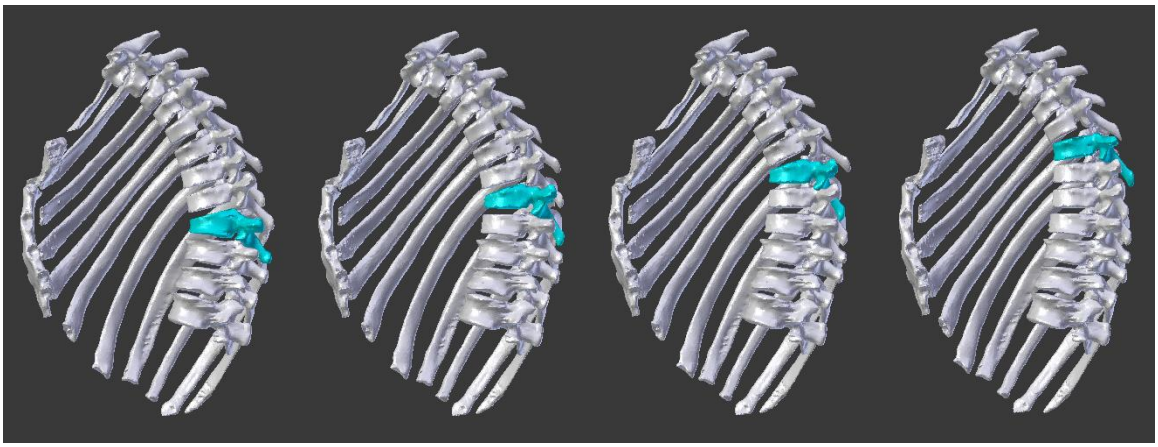

(e) T9 wedging (f) T8 wedging (g) T7 wedging (h) T6 wedging

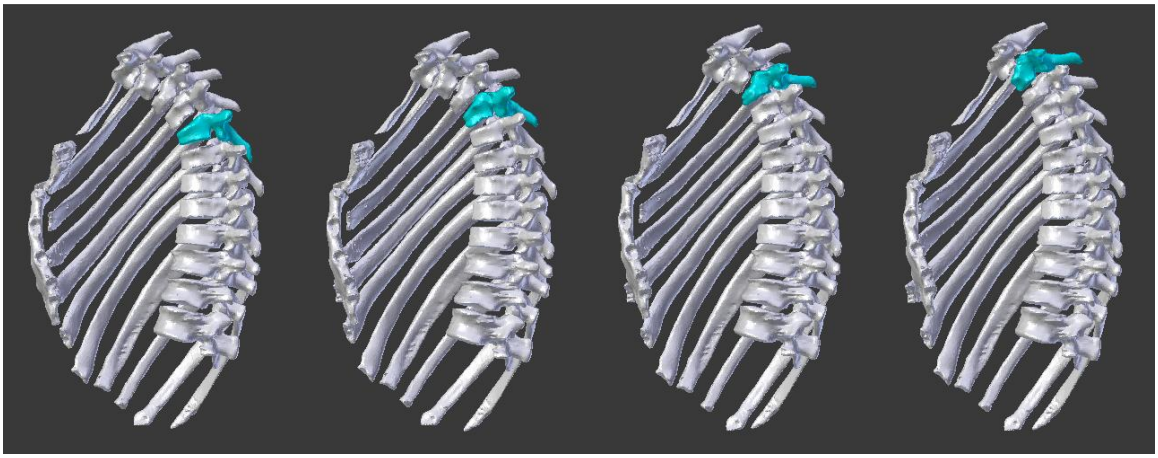

(i) T5 wedging (j) T4 wedging (k) T3 wedging (l) T2 wedging

Figure A.1 Rib cages of the baseline model (i.e., Subject 3) and eleven virtual osteoporosis patients with one wedging vertebra

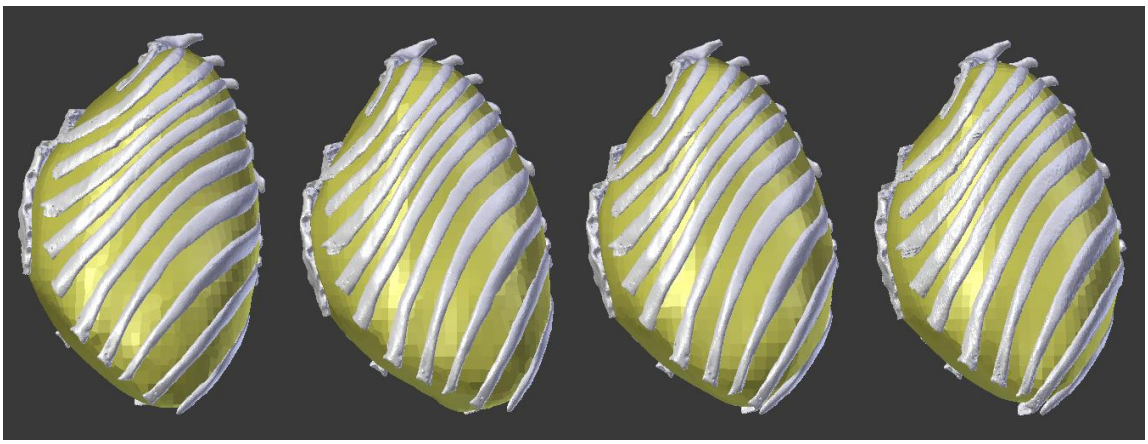

(a) Baseline (b) T12 wedging (c) T11 wedging (d) T10 wedging

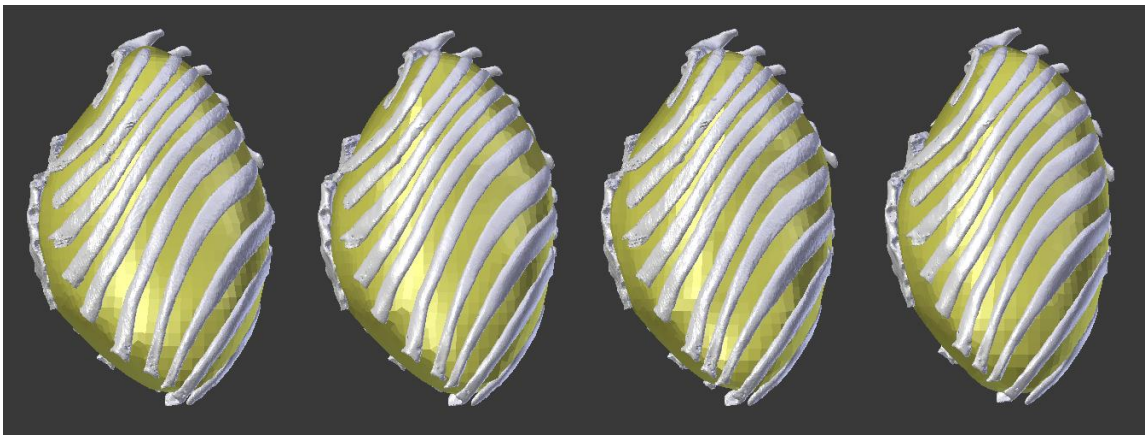

(e) T9 wedging (f) T8 wedging (g) T7 wedging (h) T6 wedging

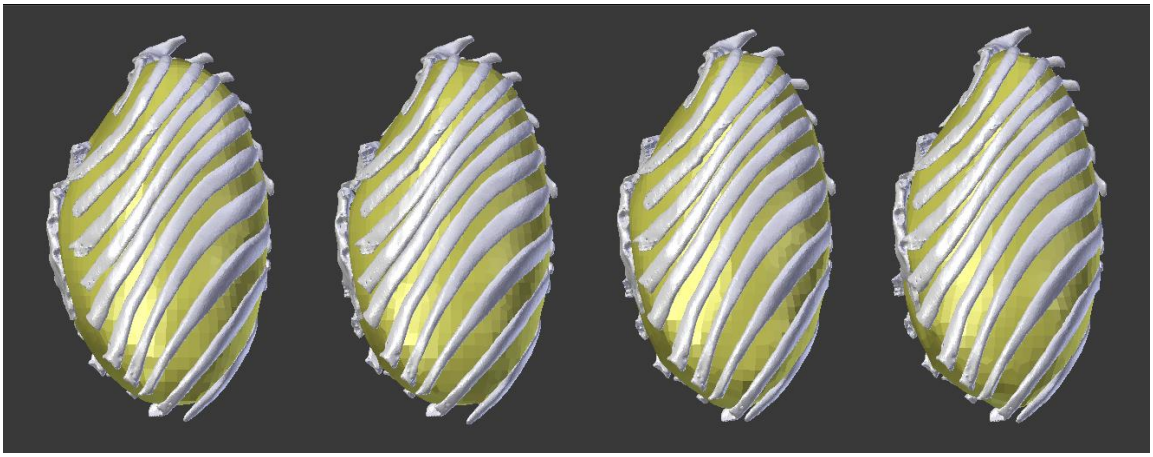

(i) T5 wedging (j) T4 wedging (k) T3 wedging (l) T2 wedging

Figure A.2 Thoracic volumes of the baseline model (i.e., Subject 3) and eleven virtual osteoporosis patients with one wedging vertebra

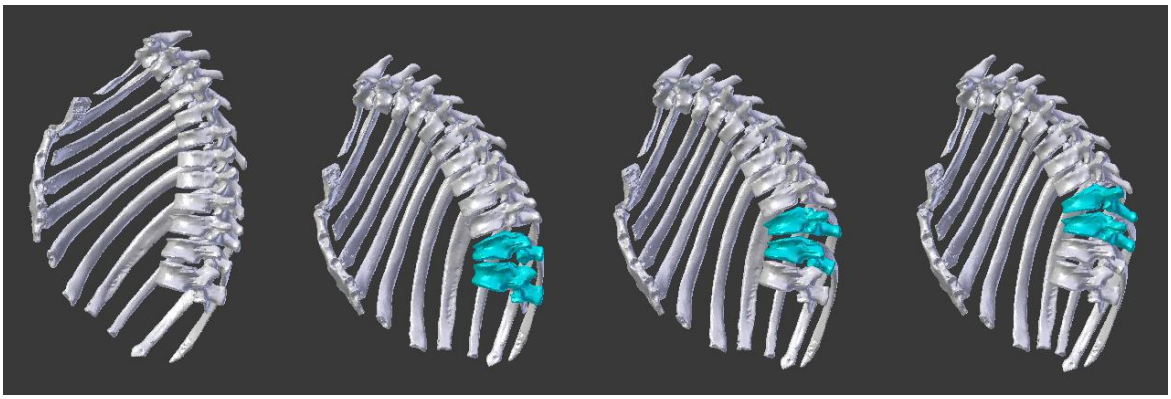

(a) Baseline (b) T12&T11 wedging (c) T11&T10 wedging (d) T10&T9 wedging

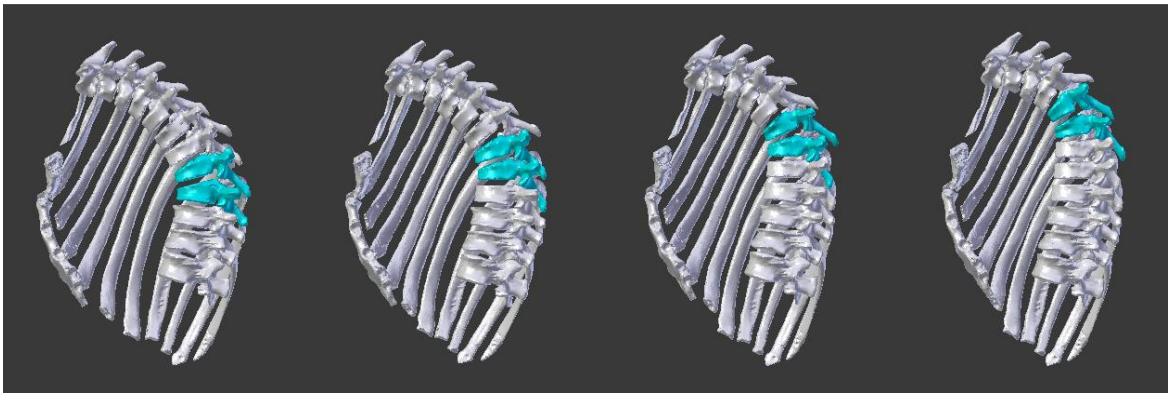

(e) T9&T8 wedging (f) T8&T7 wedging (g) T7&T6 wedging (h) T6&T5 wedging

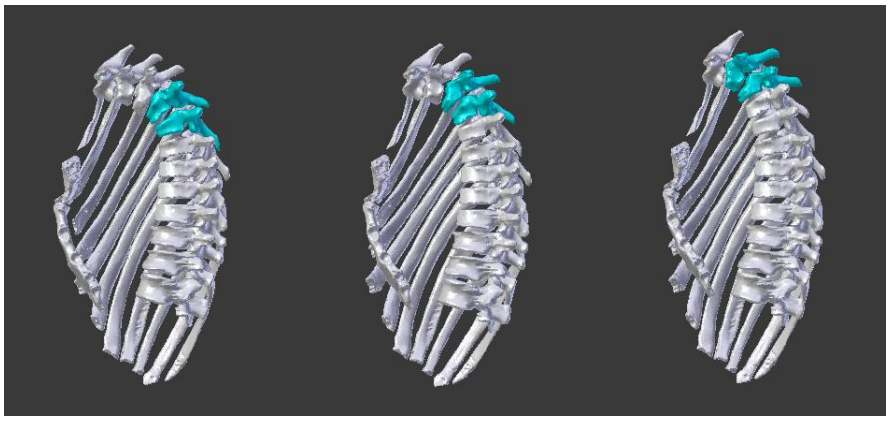

(i) T5&T4 wedging (j) T4&T3 wedging (k) T3&T2 wedging

Figure A.3 Rib cages of the baseline model (i.e., Subject 3) and ten virtual osteoporosis patients with two wedging vertebrae

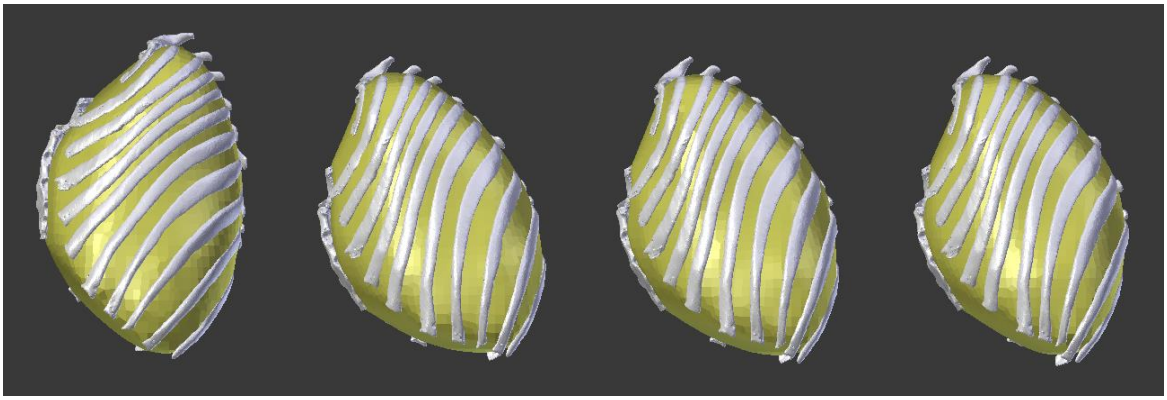

(a) Baseline (b) T12&T11 wedging (c) T11&T10 wedging (d) T10&T9 wedging

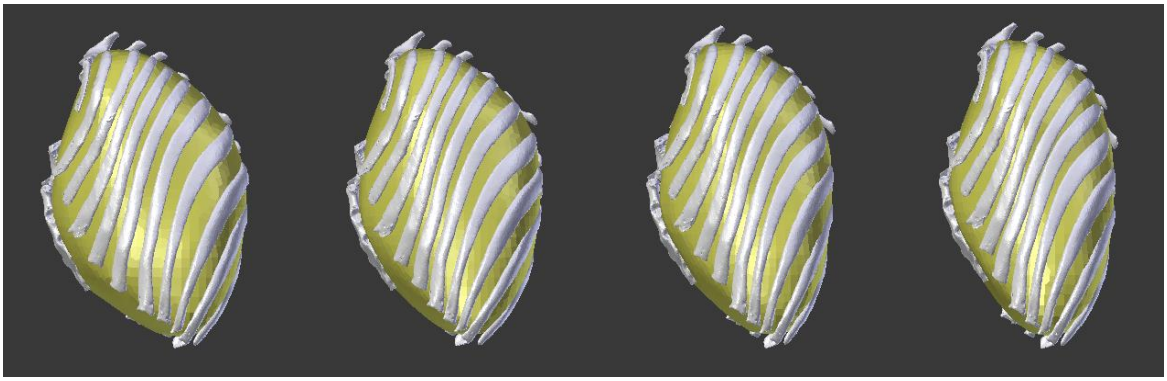

(e) T9&T8 wedging (f) T8&T7 wedging (g) T7&T6 wedging (h) T6&T5 wedging

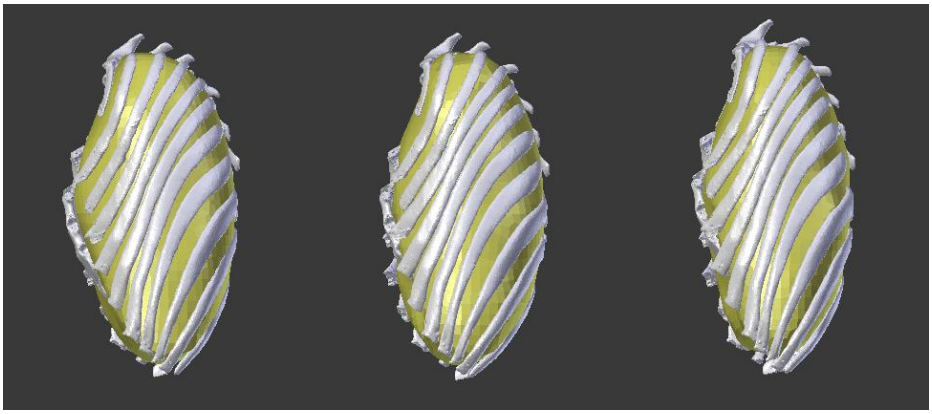

(i) T5&T4 wedging (j) T4&T3 wedging (k) T3&T2 wedging

Figure A.4 Thoracic volumes of the baseline model (i.e., Subject 3) and ten virtual osteoporosis patients with two wedging vertebrae

A.2 Information and Figures of Baseline Model and Virtual Patients for Scheuermann's Kyphosis Symptoms

In Sub-Section 6.4.3, I introduced thirty virtual patients simulated from five baseline models, and I also demonstrated baseline rib cage and thoracic volume of Subject 1 and its simulated virtual patients. Here, the other four baseline models (Subject 2 to Subject 5) and their developed virtual Scheuermann's kyphosis patients with different wedging numbers, wedging locations, wedging angles, and kyphosis angles (from virtual 60^0 to virtual 110^0) are listed from Tables A.1 to A.4. Additionally, Figures A.5 and A.6 display Subject 4's

baseline rib cage and thoracic volume models and six virtual Scheuermann's kyphosis patients.

Table A.1 Wedging angles and their locations in virtual Scheuermann's kyphosis patients deriving from Subject 2 baseline

Subject 2	**Wedging location and wedging angles of vertebrae**							
Scheuermann's kyphosis angle	**T12**	**T11**	**T10**	**T9**	**T8**	**T7**	**T6**	**T5**
Baseline (44.4^0)								
Virtual 60^0		5.2^0	5.2^0	5.2^0				
Virtual 70^0	10^0	5.2^0	5.2^0	5.2^0				
Virtual 80^0	10^0	10.2^0	5.2^0	5.2^0	5^0			
Virtual 90^0	10^0	10.2^0	10.2^0	5.2^0	5^0	5^0		
Virtual 100^0	10^0	10.2^0	10.2^0	10.2^0	5^0	5^0	5^0	
Virtual 110^0	10^0	10.2^0	10.2^0	10.2^0	10^0	5^0	5^0	5^0

Table A.2 Wedging angles and their locations in virtual Scheuermann's kyphosis patients deriving from Subject 3 baseline

Subject 3	**Wedging location and wedging angles of vertebrae**							
Scheuermann's kyphosis angle	**T12**	**T11**	**T10**	**T9**	**T8**	**T7**	**T6**	**T5**
Baseline (30^0)								
Virtual 60^0		10^0	10^0	10^0				
Virtual 70^0	10^0	10^0	10^0	10^0				
Virtual 80^0	10^0	10^0	10^0	10^0	10^0			
Virtual 90^0	10^0	10^0	10^0	10^0	10^0	10^0		
Virtual 100^0	10^0	10^0	10^0	10^0	10^0	10^0	10^0	
Virtual 110^0	10^0	10^0	10^0	10^0	10^0	10^0	10^0	10^0

Table A.3 Wedging angles and their locations in virtual Scheuermann's kyphosis patients deriving from Subject 4 baseline

Subject 4	**Wedging location and wedging angles of vertebrae**							
Scheuermann's kyphosis angle	**T12**	**T11**	**T10**	**T9**	**T8**	**T7**	**T6**	**T5**
Baseline (42.6^0)								
Virtual 60^0		5.8^0	5.8^0	5.8^0				
Virtual 70^0	10^0	5.8^0	5.8^0	5.8^0				
Virtual 80^0	10^0	10.8^0	5.8^0	5.8^0	5^0			
Virtual 90^0	10^0	10.8^0	10.8^0	5.8^0	5^0	5^0		
Virtual 100^0	10^0	10.8^0	10.8^0	10.8^0	5^0	5^0	5^0	
Virtual 110^0	10^0	10.8^0	10.8^0	10.8^0	10^0	5^0	5^0	5^0

Table A.4 Wedging angles and their locations in virtual Scheuermann's kyphosis patients deriving from Subject 5 baseline

Subject 5	**Wedging location and wedging angles of vertebrae**							
Scheuermann's kyphosis angle	**T12**	**T11**	**T10**	**T9**	**T8**	**T7**	**T6**	**T5**
Baseline (45^0)								
Virtual 60^0		5^0	5^0	5^0				
Virtual 70^0	10^0	5^0	5^0	5^0				
Virtual 80^0	10^0	10^0	5^0	5^0	5^0			
Virtual 90^0	10^0	10^0	10^0	5^0	5^0	5^0		
Virtual 100^0	10^0	10^0	10^0	10^0	5^0	5^0	5^0	
Virtual 110^0	10^0	10^0	10^0	10^0	10^0	5^0	5^0	5^0

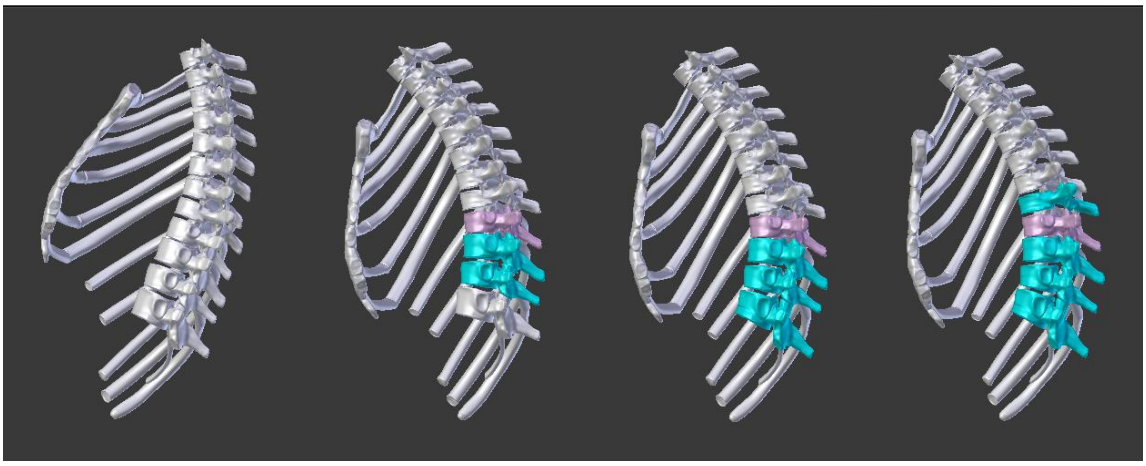

(a) Baseline (b) T11&T9 wedging (c) T12&T9 wedging (d) T12&T8 wedging

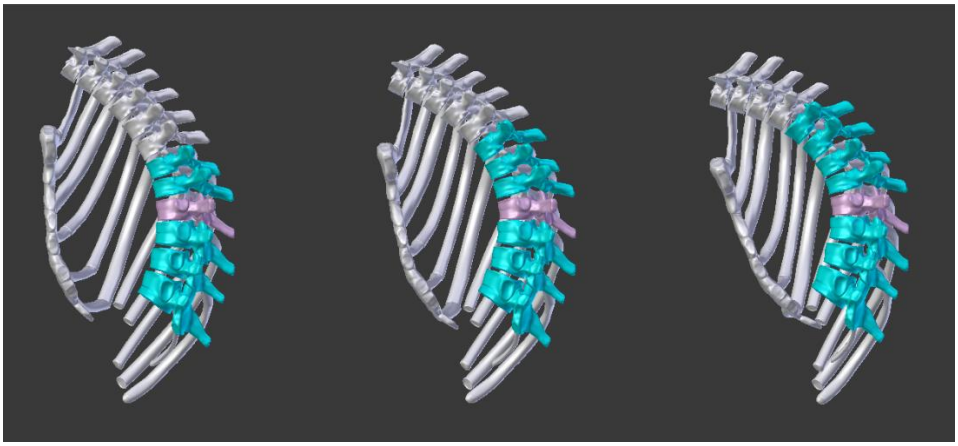

(e) T12&T7 wedging (f) T12&T6 wedging (g) T12&T5 wedging

Figure A.5 Rib cages of the baseline model (Subject 4) and six simulated virtual Scheuermann's kyphosis patients developed from Subject 4

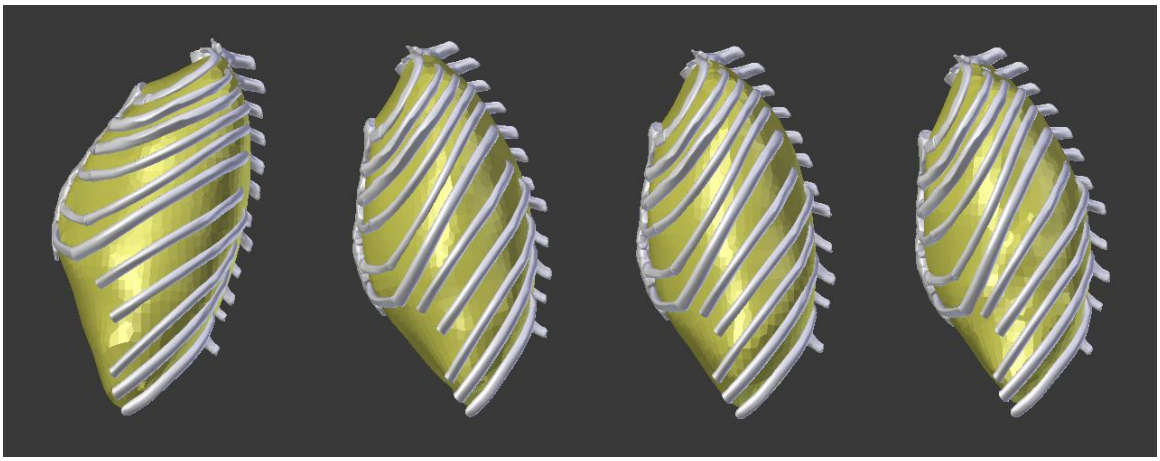

(a) Baseline (b) T11&T9 wedging (c) T12&T9 wedging (d) T12&T8 wedging

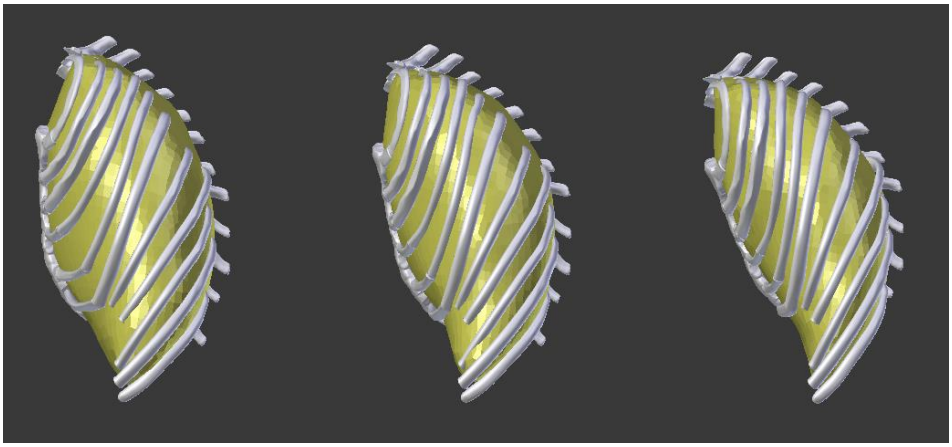

(e) T12&T7 wedging (f) T12&T6 wedging (g) T12&T5 wedging

Figure A.6 Thoracic volumes of the baseline model (Subject 4) and six simulated virtual Scheuermann's kyphosis patients developed from Subject 4